*Journal of*
*Mechanics of*
*Materials and Structures*

# JOURNAL OF MECHANICS OF MATERIALS AND STRUCTURES

http://www.jomms.org

See inside back cover or http://www.jomms.org for submission guidelines.

# PREFACE

Ashkan Vaziri and Mohammad R. K. Mofrad

Many new computational and experimental techniques are currently being developed in the fields of biomechanics and biomaterials, and new applications are emerging, including multiscale theoretical modeling, nanoindentation and nanotribology, single cell mechanics and mechanotransduction, biomolecular mechanics and the synthesis and design of new biomimetic architectures. These recent advances have enhanced the development of engineered materials for nonbiological applications, providing new avenues for diagnosis and treatment of diseases.

In this special issue of *Journal of Mechanics of Materials and Structures*, we have assembled a number of recent studies in the field of mechanics of biomaterials at multiple length scales, ranging from a detailed hierarchical atomistic simulations of proteins to multiscale computational models for mechanics of encapsulated cells. Several review articles are also included which highlight the state of the art in biomechanics and biomaterials.

In "Spontaneous unwinding of a labile domain in a collagen triple helix", Ravikumar et al. present a molecular dynamics simulation of the thermal unwinding behavior of collagen triple helix, showing a possibility for spontaneous local unwinding of collagen at physiological temperatures.

In "Particle collision and adhesion under the influence of near-fields", Zohdi presents a relatively simple but predictive theory for relating the impact velocity needed for adherence of two microscopic particles. This study has direct implications for our understanding of the mechanisms of particle collision in many biomechanical applications.

In "Hierarchical chemo-nanomechanics of proteins: entropic elasticity, protein unfolding and molecular fracture", Buehler develops a multiscale simulation approach to study large deformation and fracture of three protein structures. The results decipher some of the key aspects of mechanical behavior of chemically complex protein materials, including their unfolding behavior and fracture.

In "Micromechanical properties of chondrocytes and chondrons: relevance to articular cartilage tissue engineering", Ofek and Athanasiou provide a comprehensive review of the studies on micromechanical properties of chondrocytes and chondrons. The implications of these studies in understanding the state of human health and disease, as well as their potential applications in developing engineered articular cartilage, are highlighted.

In "Assessment of the mechanical properties of the nucleus inside a spherical endothelial cell based on microtensile testing", Deguchi et al. employ a microtensile experimental setup in addition to detailed finite element simulations to assess the mechanical properties of the nucleus of endothelial cells, providing a quantitative comparison of the mechanical properties of endothelial cells and intact nuclei.

In "Microscale hydrogels for medicine and biology: Synthesis, characteristics and applications", Rivest et al. provide a broad review of the approaches used to synthesize and characterize miscroscale

hydrogels as well as their applications in different biomedical fields, including tissue engineering, drug delivery and biosensors. Potential future applications of these materials are also highlighted.

In "A multilevel numerical model quantifying cell deformation in encapsulated alginate structures", Nair et al. provide a multiscale nonlinear finite element approach to study the mechanics of encapsulated cells. The microscale mechanics of individual cells are linked to the macrolevel mechanics of alginate cell constructs, providing insight into the interaction of tissue scaffold with living cells.

In "Modeling bone resorption using Mixture Theory with chemical reactions", Rouhi et al. present a biphasic mixture model for studying the cellular mechanisms of bone resorption, elucidating the main biochemomechanical factors contributing to the rate of bone resorption.

In "The mechanics of tip growth morphogenesis: what we have learned from rubber balloons", Bernal et al. demonstrate how a tubular rubber balloon offer a useful physical model for studying tip growth morphogenesis. A simple model of tip growth is proposed which provides insight into the underlying mechanisms of the morphogenesis of plants, fungal, and bacterial cells.

In "Continuum-based computational methods in cell and nuclear mechanics", Vaziri et al. provide an overview of the current continuum-based computational models in the field of cell and nuclear mechanics, while recent developments and current trends in multiscale computational models in the field are also highlighted.

In "Quantitative Evaluation of Mechanical Properties of Cell Membranes: An Exact Solution", Baesu et al. propose a simple but effective approach for measuring the mechanical properties of cell membranes. The proposed approach combines atomic force microscopy experimentation with a biomechanical model of the cell membrane to yield mechanical properties of the membrane.

These studies are broad examples of recent advances in some of the most important areas of biomechanics and biomaterials. Our hope is that the articles presented in this special issue will further enhance the increasing interest in these interdisciplinary areas of science, engineering, and medicine.

Finally, we wish to thank Professor Charles R. Steele, Editor-in-Chief of *Journal of Mechanics of Materials and Structures* and Marie-Louise Steele, Associate Editor, for giving us the great opportunity to organize this special issue, and we thank the contributing authors for their excellent papers and also the anonymous reviewers, who helped immensely in shaping this special issue in the current form.

ASHKAN VAZIRI: avaziri@seas.harvard.edu
*School of Engineering and Applied Sciences, Harvard University, 316 Pierce Hall, 29 Oxford St., Cambridge, MA, United States*

MOHAMMAD R. K. MOFRAD: mofrad@berkeley.edu
*Molecular Cell Biomechanics Laboratory, Department of Bioengineering, University of California Berkeley, Berkeley, CA 04720-1762, United States*

# SPONTANEOUS UNWINDING OF A LABILE DOMAIN
# IN A COLLAGEN TRIPLE HELIX

Krishnakumar M. Ravikumar, Jay D. Humphrey and Wonmuk Hwang

We have analyzed thermal unwinding behavior of a biologically relevant collagen mimetic peptide (PDB ID: 1bkv) through molecular dynamics simulations in explicit water. Conformational changes of the triple helix were monitored by introducing a set of local triad vectors and measuring variations in their torsional angles. Although the molecule fluctuates thermally at 273 K, unwinding becomes pronounced at 300 K and 330 K. We found that the region containing Gly-Ile, which is a common cleavage site in collagen, to be an initiation site for unwinding. Our results suggest that local unwinding of collagen is spontaneous at physiological temperatures, and it could be a property utilized for binding by other proteins, such as cleavage enzymes or fibril associated collagens.

## 1. Introduction

Collagen is the most abundant protein in the human body and forms the major component of the extracellular matrix in many tissues and organs [Alberts et al. 2000; Brodsky and Persikov 2005]. It is involved in diverse processes related to growth, maintenance, and remodeling of tissues. Currently more than twenty-seven types of collagens have been identified [Boot-Handford et al. 2003; van der Slot 2005], which can self-assemble into higher-level polymeric structures such as fibrils, fibers, and networks. Mutations in collagen genes can cause several diseases, some of which are fatal [Myllyharju and Kivirikko 2001]. Due to such biological significance, its structure, function, and relationship with other extracellular components have been a major focus of attention during the past six decades.

High-resolution X-ray crystallography of collagen mimetic peptides have provided useful structural insights [Bella et al. 1994; Kramer et al. 2000; 2001]. Collagen molecules have a distinct triple helical structure with three $\alpha$ (polyproline-II-type) chains; three left-handed triple helices are wound together to form a rope-like right-handed superhelix (Figure 1) [Ramachandran and Kartha 1955; Rich and Crick 1961; Brodsky and Persikov 2005]. Individual $\alpha$ chains have a regular amino acid repeating sequence $-(\text{G-X-Y})_n-$, where G is glycine and X,Y are other amino acids. The three chains are staggered by one amino acid along the length of the molecule (Figure 2c), making glycine, the smallest amino acid, always fall in the central part of the triple helix. This, along with the constraint on the backbone imposed by the imino rings in proline (Pro), gives a tight triple helical tertiary structure to the molecule. During posttranslational modifications, prolines in the Y position are specifically hydroxylated into (4R)hydroxyprolines (Hyp). Raines and coworkers have shown that the electron withdrawing effect of the hydroxyl group in Hyp favors an *exo*-ring puckering, giving a stable *trans*-conformation to the Y residue [Holmgren et al. 1998; 1999; Jenkins and Raines 2002; Hodges and Raines 2005] . Gly-Pro-Hyp (GPO) triplets thus form the most stable structural domains [Shah et al. 1996] and are commonly chosen as major constituents of

---

short collagen mimetic peptides. These imino-rich regions have a tighter 7-fold (7/2) helical symmetry (7 amino acids per two helical turns) compared to imino-poor regions which have a 10-fold (10/3) symmetry (10 amino acids per three helical turns) [Kramer et al. 1999]. GPO domains are found at the C-terminal region of collagen and nucleate the triple helix formation [McLaughlin and Bulleid 1998]. Thus, the local sequence of a collagen domain determines its stability, helicity, and functionality.

The complex process of collagen turnover is intricately related to its mechanics [Wright and Humphrey 2002; Tomasek et al. 2002]; for example, mechanical strain affects collagen cleavage [Ruberti and Hallab 2005] and local lability in its structure can help in fibril formation [Kadler et al. 1988]. Functionally, non-GPO domains, being labile and flexible, are cleavage sites for matrix metalloproteinases (MMPs) or binding sites for integrins and heparin [Emsley et al. 2000; Persikov and Brodsky 2002]. Such interactions make collagens crucial members in the feedback loop through which cells can alter their environment to promote homeostasis in tissues. Static and cyclic mechanical loads on collagen substrates can induce differential responses from cells, including cell proliferation, collagen deposition, collagenase activity, and release of growth factors that modulate growth and remodeling of tissues [Carver et al. 1991; Hsueh et al. 1998; MacKenna et al. 2000]. Structurally, collagen cleavage is linked to possible unwinding by collagenases [Chung et al. 2004]. Isolated collagen molecules are known to be unstable at body temperature [Leikina et al. 2002], while collagens cross-linked as a bundle are much more stable. Hence collagen turnover in tissues most likely involves local conformational fluctuations of individual collagen molecules that are sensitive to their thermomechanical environment.

To characterize local conformational variations in collagen, we developed a systematic way of assigning a set of local Cartesian basis triads along the length of the molecule and monitored relative changes in torsional (helical) angles among them. Using molecular dynamics (MD) simulations in explicit water environments, we characterized temperature-dependent changes in the triple helical twist of a collagen mimetic peptide (PDB ID: 1bkv) [Kramer et al. 1999]. This peptide is of special interest, compared to other collagen mimetic peptides, since it contains a biologically relevant 12 amino acid sequence immediately downstream of the unique collagenase cleavage site in human collagen type III. This sequence is known to be important in collagenase specificity [Fields 1991]. We found that the molecule can locally unwind within 1 ns at temperatures of 300 K and above. Importantly, unwinding is initiated around the Gly-Ile bond in the imino-poor region. Such region-specific unwinding could be an initiating event of collagen denaturation or it may facilitate collagenase binding [Fields 1991; Chung et al. 2004]. Our results will thus be useful for developing structure-based physical models for collagen stability and turnover.

## 2. Simulation methods

For MD simulations we used CHARMM [Brooks et al. 1983] version 31b1 with the param22 all-atom force field [MacKerell Jr. et al. 1998]. The crystal structure 1bkv was taken from Protein Data Bank (www.pdb.org) and hydrogens were added using the HBUILD facility in CHARMM [Brünger and Karplus 1988]. The charmm 22 force field does not contain parameters for Hyp which were added from an earlier study [Anderson 2005].

The peptide was solvated by putting it in a water box containing preequilibrated TIP3 water molecules. The box had dimensions $112 \times 37 \times 37$ Å$^3$ with an approximate density of 1080 kg/m$^3$. The box size was
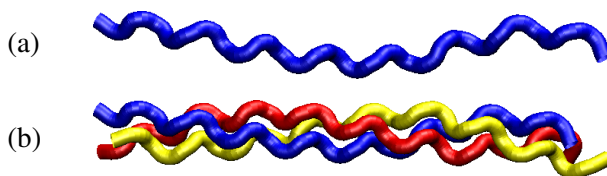
**Figure 1.** Collagen Structure. Each $\alpha$ chain backbone is shown as a tube to reveal its helical twist: (a) a left-handed helical $\alpha$-chain, and (b) a collagen triple helix formed by three $\alpha$-chains in a right-handed manner. Drawings rendered using VMD [Humphrey et al. 1996]; same color schemes used for $\alpha$ chains in Figure 2.
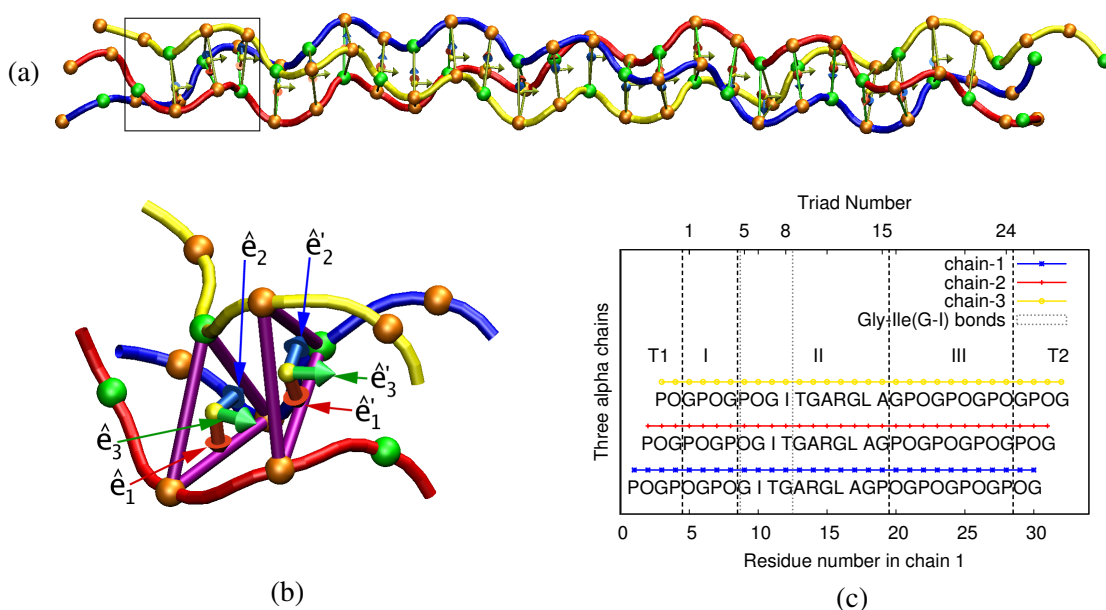


**Figure 2.** Triads along the helix. The three $\alpha$-chains are shown in blue (chain-1), red (chain-2), and yellow (chain-3) (see Figure 1). Spheres are $C_\alpha$ atoms of Gly (green) and X/Y (orange). (a) Overview of 1bkv with the 24 triads. (b) Magnified view of the box in (a). To show face of triangle, molecule is rotated about the vertical axis of the paper plane. Two neighboring triads are denoted $\{\hat{e}_1, \hat{e}_2, \hat{e}_3\}$ and $\{\hat{e}'_1, \hat{e}'_2, \hat{e}'_3\}$. (c) Triad numbers versus amino acid sequence. The horizontal shift of the chains reflects staggered structure in the triple helix; grouped into domains I, II, and III. T1 and T2 are unconsidered regions to eliminate end effects. Triads 5–8, between grey dotted vertical lines, contain Gly-Ile bonds. First proline (P) residue in chain-1 in (c) is shown only for clarity and is invisible in the X-ray crystal structure of 1bkv.

chosen such that its boundaries were at least 11 Å away from the peptide. Periodic boundary conditions were imposed around the solvation box. Water molecules whose oxygen atoms were within a radius of

2.2 Å from heavy atoms in the peptide were deleted during solvation. After solvation, there were 5075 water molecules in the simulation box.

To eliminate close contacts and geometric strain in the system, we used the following energy mini- mization scheme. The peptide molecule was initially fixed and water molecules were minimized for 100 steps by steepest descent (SD) and for 400 steps by adapted basis Newton–Raphson (ABNR) method. As the next step, only the backbone was fixed and side chains along with water molecules were minimized chain by chain for 200 steps and then together for 500 steps by ABNR. The side chains were minimized chain by chain to solvate them better and to eliminate close sidechain-sidechain contacts. Finally, all constraints were removed and the system was minimized for 200 steps using ABNR.

The system was heated from 0 K and then equilibrated at target temperatures for 35 ps, with the peptide harmonically constrained to its original position. The heating rate was 2 K every 0.2 ps to target values ($T = 273$ K, 300 K, and 330 K). After heating, equilibration followed during which temperatures were rescaled if they deviated more than $\pm 2$ K from target temperatures. The final production run was performed for 1 ns using the leap-frog Verlet integration algorithm with a time step of 1 fs at each target temperature with all harmonic constraints removed. The nonbonded pair and image atom lists were updated at each simulation step. A 12 Å cutoff was used for nonbonded interaction energies. Trajectories were stable during production runs, where relative root-mean-square fluctuations of temperature and energy were less than 0.7 % and 0.3 %, respectively.

## 3. Characterization of unwinding

To characterize the conformation of the triple helix, local coordinate triads $\{\hat{e}_1, \hat{e}_2, \hat{e}_3\}$ were generated as follows. We constructed triangles joining the $C_\alpha$ atoms of Gly, X, and Y of adjacent chains along the length of the molecule; see Figure 2a. The centroid of each triangle was chosen as the local coordinate origin and $\hat{e}_1$ was defined as the unit vector along the line joining the centroid to the midpoint of the line segment joining $C_\alpha$ atoms of chain-1 and chain-2. Setting $\hat{e}_3$ perpendicular to the plane fixes $\hat{e}_2 = \hat{e}_3 \times \hat{e}_1$; see Figure 2b. The first two triads and the last two triads were omitted in the analysis to reduce end effects; see Figure 2c. The remaining 24 triads within the middle were grouped into three (I,II,III) sets: domains I (triads 1–4) and III (triads 15–24) are the regular GPO repeats at the N and C termini, while domain II (triads 5–15) is the central imino-poor region.

We characterized orientations of triads using Euler angles [Goldstein 1980]. Let $\mathbf{X} = \{\hat{e}_1, \hat{e}_2, \hat{e}_3\}$ and $\mathbf{X}' = \{\hat{e}_1', \hat{e}_2', \hat{e}_3'\}$ be two adjacent triads; see Figure 2b. Denoting a Cartesian coordinate basis fixed in space as $\mathbf{E} = \{\hat{x}, \hat{y}, \hat{z}\}$, we have $\mathbf{X} = A\,\mathbf{E}$, $\mathbf{X}' = B\,\mathbf{E}$, where $A$ and $B$ are $3 \times 3$ matrices containing the Cartesian components of $\mathbf{X}$ and $\mathbf{X}'$, respectively. We then have

$$\mathbf{X}' = T\,\mathbf{X} \qquad \text{with} \quad T \equiv BA^{-1}. \tag{1}$$

On the other hand, $\mathbf{X}$ and $\mathbf{X}'$ are related by Euler transformation matrices by

$$\mathbf{X}' = R_x R_y R_z \mathbf{X} \qquad \Longrightarrow \qquad T = R_x R_y R_z, \tag{2}$$
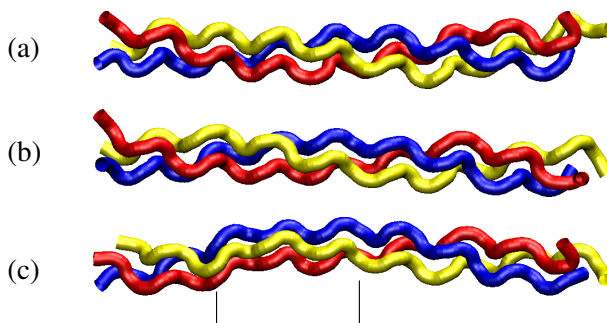
**Figure 3.** Unwinding of collagen. Triple helix at 330 K at: (a) 0 ns, (b) 0.5 ns, and (c) 1 ns. Marked region in (c) shows unwound domain II.

where

$$R_x = \begin{pmatrix} 1 & 0 & 0 \\ 0 & \cos\theta_x & \sin\theta_x \\ 0 & -\sin\theta_x & \cos\theta_x \end{pmatrix}, \qquad R_y = \begin{pmatrix} \cos\theta_y & 0 & \sin\theta_y \\ 0 & 1 & 0 \\ -\sin\theta_y & 0 & \cos\theta_y \end{pmatrix}, \qquad R_z = \begin{pmatrix} \cos\theta_z & \sin\theta_z & 0 \\ -\sin\theta_z & \cos\theta_z & 0 \\ 0 & 0 & 1 \end{pmatrix}.$$

As $A$ and $B$ are easily measurable in a given conformation of the molecule, $T$ can be calculated from Equation (1), which in turn gives Euler angles $\theta_x$, $\theta_y$, and $\theta_z$ by solving Equation (2). If we set $\hat{z}$ along the major axis of the triple helix, changes in $\theta_z$ represent the degree of the helical twist (torsion). This can be seen by plotting the torsional map as the difference $\Delta\theta_z$ between a triad under consideration and a reference triad. For example, if we set the first triad as the reference, $\Delta\theta_z$ will monotonically increase with the triad number for a right-handed triple helix, and the triad that reaches $\Delta\theta_z = 360°$ will define the period of the triple helix. Because $\theta_z$ is the rotation angle of triads with respect to the $z$-axis, our method is not affected by the fact that the triangles in Figure 2a are not exactly perpendicular to the helical axis. For our analysis, we chose the reference point either as the first or the last triads, which gave consistent results. If there was unwinding of the triple helix in a particular region, it would show up as a change in slope of the torsional map; see Figure 4. We also calculated differences in $\theta_z$ between successive triads as another measure by which unwinding can be detected as a dip in the curve; see Figure 5.

## 4. Results

The peptide maintained its stable triple helical structure at 273 K, but unwinding was observed within 1 ns of the production run at 300 and 330 K; see Figure 3. We considered the statistics (average and standard deviation) of the torsional angles during time intervals 0.0–0.2, 0.2–0.4, 0.4–0.6, 0.6–0.8, and 0.8–1.0 ns at different temperatures; see Figure 4. Maximum $\Delta\theta_z$ was approximately 360°, as this peptide has only one helical turn. The torsional map at 273 K gives straight lines because the peptide does not unwind during the 1 ns simulation, see Figure 4a. However, even at such low temperature the G-I region shows some flexibility. Its lower slope (see Figure 4a, right) indicates that this region is less tightly wound compared to other regions. Within the 1 ns simulation time, variation in the profile at 273 K is more like a fluctuation rather than unwinding. Interestingly, the profile for the 0.8–1.0 ns interval shows the slowest growth of $\Delta\theta_z$ until triad 8 (see Figure 4a, right), but in triads 9–15 the slope is steeper than
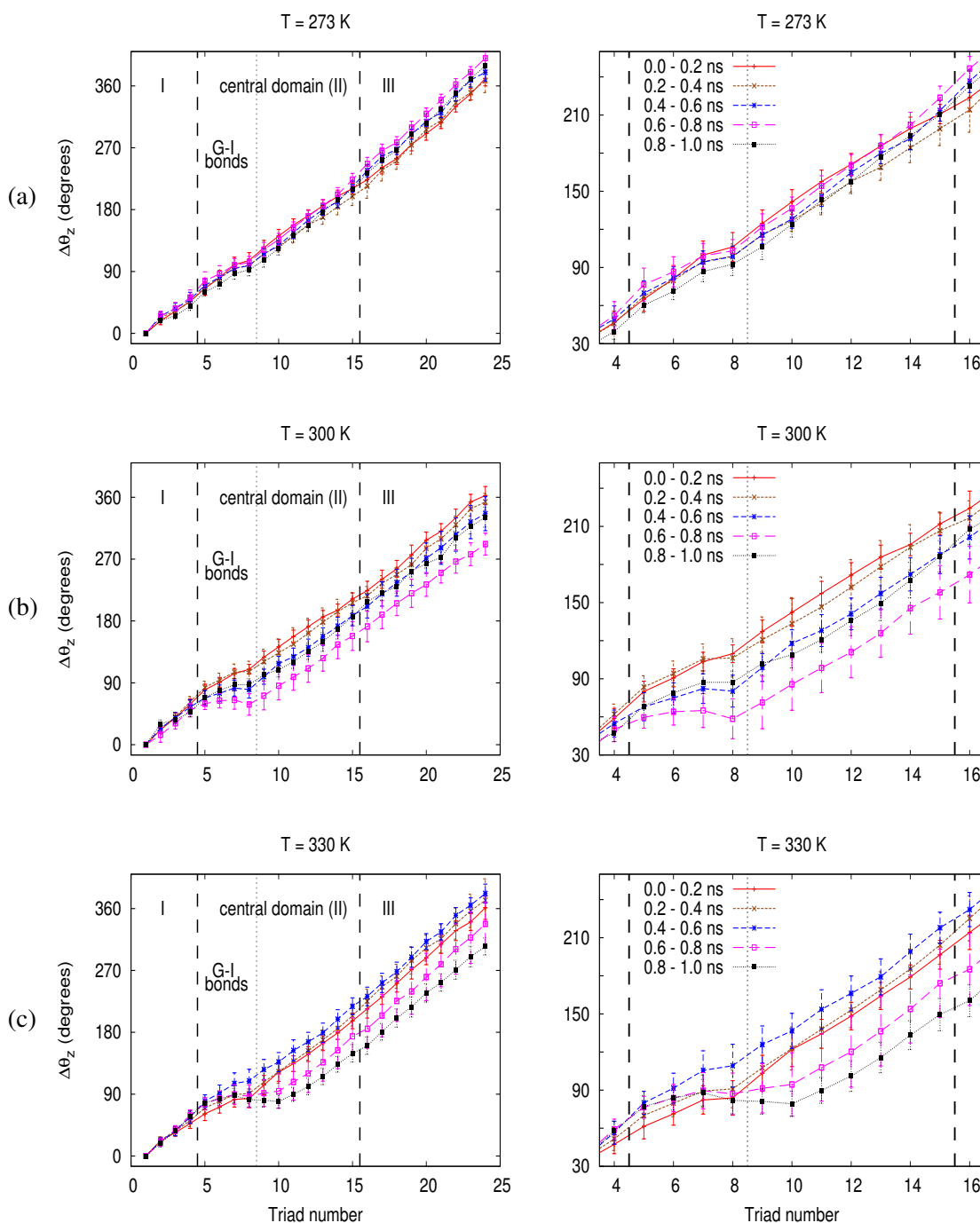
**Figure 4.** Torsional map with triad 1 as reference at (a) 273 K, (b) 300 K, and (c) 330 K. Data points give average value during time interval ± standard deviation: overview on left, close-up of domain II on right. Vertical lines divide different domains.
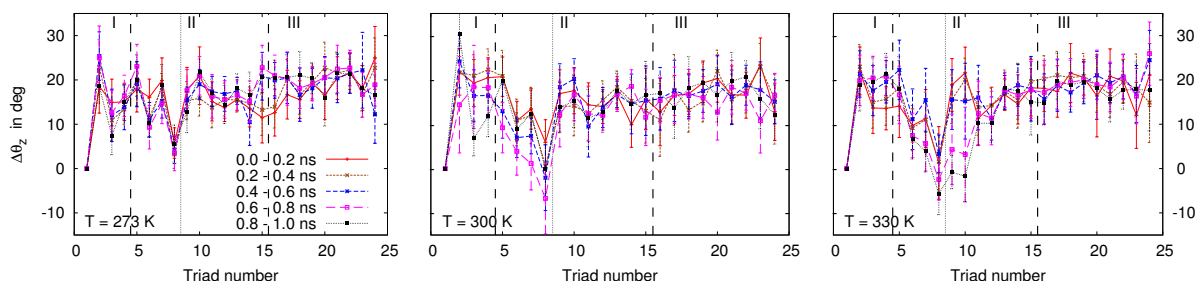
**Figure 5.** Differences in $\theta_z$ between successive triads.

those of other time intervals, so that triad 24 has $\Delta\theta_z$ above that from the 0.0–0.2 ns interval (see Figure 4a, left). This indicates that the unwinding near the G-I region is compensated by an overtwisting of triads 9–15 in domain II, indicative of the fluctuating nature of the imino-poor domain II.

The above trend becomes stronger at 300 K; see Figure 4b. A magnified view of the G-I region (see Figure 4b, right) shows greater fluctuations; unwinding increases until the 0.6–0.8 ns interval, where triad 8 is overunwound (left-handed) with a decreasing $\Delta\theta_z$. During this interval, the change in $\Delta\theta_z$ at triad 24 was 70.6° compared to the interval 0.0–0.2 ns. (This profile was obtained *with respect to* triad 1. In the simulations, triads at both ends rotate in the opposite direction to generate unwinding.) The molecule rewinds again during 0.8–1.0 ns, with a profile similar to the 0.4–0.6 ns interval. Due to the finite simulation time, it is not clear whether the conformation will eventually return to the original or if it will stay partially unwound. Note that overtwisting of triads 9–15 is not present at this temperature, suggesting that triads 1–4 (domain I) and 9–24 (domain II and III, except the G-I region) rotate rigidly relative to each other with the G-I region as a rotational hinge. This is presumably due to shorter relaxation times of the structure at higher temperatures.

At 330 K, initial overtwisting is observed (0.0–0.6 ns), but unwinding manifests at later times. Moreover, it propagates out of the G-I region into triads 9–10 in domain II; see Figure 4c, right. Experimentally, the melting temperature of 1bkv is $\approx$ 293 K [Kramer et al. 2001]. We thus expect that at 330 K the unwinding will proceed eventually into denaturation of the whole molecule. If the molecule becomes heavily disrupted, our approach will become inadequate for characterizing the triple helical conformation. For longer simulations in which unwinding proceeds further, it may be useful to introduce the area of each triangle ( Figure 2) as an additional measure of the integrity of the three-chain bundle.

While Figure 4 identifies local unwinding within the global helicity of the molecule, a sensitive way of monitoring conformational behavior triad-by-triad is by comparing differences in $\theta_z$ along successive triads; see Figure 5. Decreased helicity is evident at 273 K between triads 7 and 8, and overtwisting can be seen to be localized mostly in triad 14–15, at the boundary between domains II and III. Yet, profiles at different time points overlap within standard deviations, thus no clear unwinding behavior is present other than fluctuations. At 300 K a negative value of $\Delta\theta_z$ between triads 7 and 8 again shows an opposite helicity (left-handed), which propagates to the right within domain II at 330 K.

## 5. Concluding discussion

In the present study we have introduced a local triad basis method to monitor delicate conformational changes in collagen triple helix conformation. This approach enabled characterization of local unwinding as an early event preceding denaturation and was sensitive enough to elucidate the lability of the G-I region even at 273 K when unwinding was not noticeable; see Figure 5.

As a comparison, Stultz previously used umbrella sampling to study localized unfolding of 1bkv and an imino-rich peptide [Stultz 2002]. His approach mainly consisted of increasing the radius of gyration of *one* chain near its center of mass, while the atoms outside the *reaction region* were harmonically constrained to their crystallographic coordinates. Although radius of gyration may be a good parameter for the foldedness of globular proteins, it is not suitable for describing conformations of filamentous proteins. It is thus difficult to appreciate the transition state or unfolded conformations obtained in his study as physically meaningful. In contrast, our approach naturally follows the conformational fluctuation of the peptide; it thus offers a higher degree of accuracy and is applicable to characterizing torsional behaviors of other filamentous systems. Other MD simulations on collagen mimetic peptides tested imino-rich structures with simple repeating sequences [Lorenzo and Caffarena 2005; Handgraaf and Zerbetto 2006; Radmer and Klein 2006] and do not address the conformational behavior of imino-poor domains. As a control, we have tested a model collagen which consists only of the GPO repeats. Consistent with experimental results [Bella et al. 1994], we did not observe any unwinding at 300 K (data not shown). We suspect that surface-bound water bridges are involved in the stabilization of the imino-poor region, which are disrupted at higher temperatures. Further analysis of the role of water will be published elsewhere. To our knowledge, the present work is the first to characterize spontaneous unwinding of a collagen triple helix through MD simulations.

Our results indicate that the G-I region within the imino-poor region is most labile and is an initiating site for unwinding; see Figure 4c. The lability of the G-I region might originate from the strongest $\beta$-sheet propensity of the isoleucine residue [Kim and Berg 1993], which prefers an extended backbone conformation. In type III collagen there is an MMP cleavage site [Fields 1991; Lauer-Fields and Fields 2002] (denoted by Gly~Ile) that is upstream of the domain II of 1bkv: -Gly~Ile-Ala-Gly-Ile-Thr-Gly-Aln-Arg-Gly-Leu-Ala-Gly-, where Gly-Ile is the G-I region in 1bkv. This region, which contains two G-I bonds, is thus likely to be highly flexible in collagen III and could unwind at physiological temperatures.

MMPs [Overall 2002] cleave fibrillar collagen (type I, II, or III) only at a specific site (-Gly~Ile or -Gly~Leu-) approximately three-fourths from the amino terminus of the molecule. A distinctive feature of this site is that it is followed by a loose helical region [Fields 1991]. In gelatin — that is, denatured collagen — apart from the unique collagen cleavage site, other Gly-Ile and Gly-Leu bonds are cleaved by collagenases [Welgus et al. 1982], suggesting that MMP specificity in targeting those bonds could be due to their tendency to unwind.

Structurally, the groove of the collagen cleaving domain in MMPs is too narrow to accommodate the triple helix, but can accommodate only one $\alpha$-chain [Chung et al. 2004]. Collagen unwinding is thus a requirement for cleavage, for which the hemopexin-like domain in MMP is believed to unwind collagen [Nagase and Woessner 1999; Overall 2002; Lauer-Fields and Fields 2002; Chung et al. 2004]. While further studies are needed for MMP-mediated collagen unwinding, our results suggest that the cleavage sites can spontaneously unwind via thermal fluctuations even at body temperature. Hence, the function

of a hemopexin-like domain would be to help stabilize the unwound conformation rather than forcibly unwind a domain.

Our view is supported by the report that proteolysis of collagen does not require much energy and can occur in the absence of ATP molecules [Lauer-Fields and Fields 2002]. It is possible that the hinge domain in MMP, which is a polyproline chain, may invade the loose nonhelical strands, further disturbing the helical structure and facilitating cleavage [De Souza et al. 1996]. Spontaneous unwinding also explains why trypsin, though it does not have a hemopexin-like domain to unwind collagen, can still cleave collagen despite with less efficiency [Ryhänen et al. 1983; Lauer-Fields and Fields 2002].

In preliminary simulations, we also observed unwinding of the 'labile domain' in collagen-I (63 residues per $\alpha$ chain) [Miles and Bailey 2001] that is low in imino acid content (data not shown), in accordance with previous experimental results that local relaxation exists in collagen even below melting temperatures [Ryhänen et al. 1983; Kadler et al. 1988]. Strand invasion by Fibril Associated Collagen with Interrupted Triple helices (FACITs) is another example by which spontaneous collagen unwinding likely plays a role – in an intact collagen fiber, nano-particle coated FACIT mimetic peptides associate with the labile domain in the gap region [Mo et al. 2006], presumably due to the spontaneous unwinding of individual collagens. These peptides bind along the fiber after the sample was heat treated to 313 K, indicating extensive damage to the triple helical structure. As local unwinding facilitates binding to other extracellular components (FACITs, fibronectin, etc.) [Engvall et al. 1978] and render flexibility to collagen molecules, it would play a key role in the self-assembly of collagen into fibrils and networks.

Our simulations were performed without any external load on the molecule which provides a bound on its behavior [Chen et al. 1998]. In the extracellular matrix, however, collagen is likely stressed due to cell traction and external loads. Experimentally mechanical load on collagen matrix enhances resistance to degradation and thermal denaturation [Chen et al. 1998; Ruberti and Hallab 2005]. Based on our results we suspect that the resistance is based on a decreased tendency for unwinding under tension. Further extension of our simulation with mechanical loads is under way.

Our results suggest that a collagen molecule can be conceptually divided into *structural* and *functional* domains. The structural domains are composed of imino-rich residues where electro-negativity plays an important role in stability [Holmgren et al. 1998; 1999]. Being highly stable and tightly packed, these domains play a structural role giving shape and strength to the molecule. The imino-poor functional domains are thermally fluctuating metastable regions. By having such domains, degradation of a collagenous matrix can be easy and systematic, which is important in making collagen a highly adaptable material.

## References

[Alberts et al. 2000]  B. Alberts, A. Johnson, J. Lewis, M. Raff, K. Roberts, and P. Walter, *Molecular biology of the cell*, Garland Science, 2000.

[Anderson 2005]  D. Anderson, *Collagen self-assembly: a complementary experimental and theoretical perspective*, Ph.D. thesis, University of Toronto, 2005.

[Bella et al. 1994]  J. Bella, M. Eaton, B. Brodsky, and H. M. Berman, "Crystal and molecular structure of a collagen-like peptide at 1.9 Å resolution", *Science* **266**:5182 (1994), 75–81.

[Boot-Handford et al. 2003]  R. P. Boot-Handford, D. S. Tuckwell, D. A. Plumb, C. F. Rock, and R. Poulsom, "A novel and highly conserved collagen (pro $\alpha$1(XXVII)) with a unique expression pattern and unusual molecular characteristics establishes a new clade within the vertebrate fibrillar collagen family", *J. Biol. Chem.* **278**:33 (2003), 31067–31077.

[Brodsky and Persikov 2005] B. Brodsky and A. V. Persikov, "Molecular structure of the collagen triple helix", *Adv. Protein Chem.* **70** (2005), 301–339.

[Brooks et al. 1983] B. R. Brooks, R. E. Bruccoleri, B. D. Olafson, D. J. States, S. Swaminathan, and M. Karplus, "A program for macromolecular energy, minimization, and dynamics calculations", *J. Comput. Chem.* **4**:2 (1983), 187–217.

[Brünger and Karplus 1988] A. T. Brünger and M. Karplus, "Polar hydrogen positions in proteins: empirical energy placement and neutron diffraction comparison", *Proteins* **4**:2 (1988), 148–156.

[Carver et al. 1991] W. Carver, M. L. Nagpal, M. Nachtigal, T. K. Borg, and L. Terracio, "Collagen expression in mechanically stimulated cardiac fibroblasts", *Circ. Res.* **69**:1 (1991), 116–122.

[Chen et al. 1998] S. S. Chen, N. T. Wright, and J. D. Humphrey, "Heat-induced changes in the mechanics of a collagenous tissue: isothermal, isotonic shrinkage", *J. Biomech. Eng.* **120**:3 (1998), 382–388.

[Chung et al. 2004] L. Chung, D. Dinakarpandian, N. Yoshida, J. L. Lauer-Fields, G. B. Fields, R. Visse, and H. Nagase, "Collagenase unwinds triple-helical collagen prior to peptide bond hydrolysis", *EMBO J.* **23**:15 (2004), 3020–3030.

[De Souza et al. 1996] S. J. De Souza, H. M. Pereira, S. Jacchieri, and R. R. Brentani, "Collagen/collagenase interaction: does the enzyme mimic the conformation of its own substrate?", *FASEB J.* **10**:8 (1996), 927–930.

[Emsley et al. 2000] J. Emsley, C. G. Knight, R. W. Farndale, M. J. Barnes, and R. C. Liddington, "Structural basis of collagen recognition by integrin $\alpha 2\beta 1$", *Cell* **101**:1 (2000), 47–56.

[Engvall et al. 1978] E. Engvall, E. Ruoslahti, and E. J. Miller, "Affinity of fibronectin to collagens of different genetic types and to fibrinogen", *J. Exp. Med.* **147**:6 (1978), 1584–1595.

[Fields 1991] G. B. Fields, "A model for interstitial collagen catabolism by mammalian collagenases", *J. Theor. Biol.* **153**:4 (1991), 585–602.

[Goldstein 1980] H. Goldstein, *Classical mechanics*, 2 ed., Addison-Wesley, 1980.

[Handgraaf and Zerbetto 2006] J.-W. Handgraaf and F. Zerbetto, "Molecular dynamics study of onset of water gelation around the collagen triple helix", *Proteins* **64**:3 (2006), 711–718.

[Hodges and Raines 2005] J. A. Hodges and R. T. Raines, "Stereoelectronic and steric effects in the collagen triple helix: toward a code for strand association", *J. Am. Chem. Soc.* **127**:45 (2005), 15923–15932.

[Holmgren et al. 1998] S. K. Holmgren, K. M. Taylor, L. E. Bretscher, and R. T. Raines, "Code for collagen's stability deciphered", *Nature* **392**:6677 (1998), 666–667.

[Holmgren et al. 1999] S. K. Holmgren, L. E. Bretscher, K. M. Taylor, and R. T. Raines, "A hyperstable collagen mimic", *Chem. Biol.* **6**:2 (1999), 63–70.

[Hsueh et al. 1998] W. A. Hsueh, R. E. Law, and Y. S. Do, "Integrins, adhesion, and cardiac remodeling", *Hypertension* **31**:1 Pt 2 (1998), 176–180.

[Humphrey et al. 1996] W. Humphrey, A. Dalke, and K. Schulten, "VMD: visual molecular dynamics", *J. Mol. Graphics* **14**:1 (1996), 33–38.

[Jenkins and Raines 2002] C. L. Jenkins and R. T. Raines, "Insights on the conformational stability of collagen", *Nat. Prod. Rep.* **19**:1 (2002), 49–59.

[Kadler et al. 1988] K. E. Kadler, Y. Hojima, and D. J. Prockop, "Assembly of type I collagen fibrils *de novo*: Between 37 and 41 degrees C the process is limited by microunfolding of monomers", *J. Biol. Chem.* **263**:21 (1988), 10517–10523.

[Kim and Berg 1993] C. A. Kim and J. M. Berg, "Thermodynamic beta-sheet propensities measured using a zinc-finger host peptide", *Nature* **362**:6417 (1993), 267–270.

[Kramer et al. 1999] R. Z. Kramer, J. Bella, P. Mayville, B. Brodsky, and H. M. Berman, "Sequence-dependent conformational variations of collagen triple-helical structure", *Nat. Struct. Biol.* **6**:5 (1999), 454–457.

[Kramer et al. 2000] R. Z. Kramer, M. G. Venugopal, J. Bella, P. Mayville, B. Brodsky, and H. M. Berman, "Staggered molecular packing in crystals of a collagen-like peptide with a single charged pair", *J. Mol. Biol.* **301**:5 (2000), 1191–1205.

[Kramer et al. 2001] R. Z. Kramer, J. Bella, B. Brodsky, and H. M. Berman, "The crystal and molecular structure of a collagen-like peptide with a biologically relevant sequence", *J. Mol. Biol.* **311**:1 (2001), 131–147.

[Lauer-Fields and Fields 2002] J. L. Lauer-Fields and G. B. Fields, "Triple-helical peptide analysis of collagenolytic protease activity", *Biol. Chem.* **383**:7-8 (2002), 1095–1105.

[Leikina et al. 2002] E. Leikina, M. V. Mertts, N. Kuznetsova, and S. Leikin, "Type I collagen is thermally unstable at body temperature", *Proc. Natl. Acad. Sci.* **99**:3 (2002), 1314–1318.

[Lorenzo and Caffarena 2005] A. C. Lorenzo and E. R. Caffarena, "Elastic properties, Young's modulus determination and structural stability of the tropocollagen molecule: a computational study by steered molecular dynamics", *J. Biomech.* **38**:7 (2005), 1527–1533.

[MacKenna et al. 2000] D. MacKenna, S. R. Summerour, and F. J. Villarreal, "Role of mechanical factors in modulating cardiac fibroblast function and extracellular matrix synthesis", *Cardiovasc. Res.* **46**:2 (2000), 257–263.

[MacKerell Jr. et al. 1998] A. D. MacKerell Jr., D. Bashford, M. Bellott, R. L. Dunbrack Jr., J. D. Evanseck, M. J. Field, S. Fischer, J. Gao, H. Guo, S. Ha, D. Joseph-McCarthy, L. Kuchnir, K. Kuczera, F. T. K. Lau, C. Mattos, S. Michnick, T. Ngo, D. T. Nguyen, B. Prodhom, W. E. Reiher III, B. Roux, M. Schlenkrich, J. C. Smith, R. Stote, J. Straub, M. Watanabe, J. Wiorkiewicz-Kuczera, D. Yin, and M. Karplus, "All-atom empirical potential for molecular modeling and dynamics studies of proteins", *J. Phys. Chem. B* **102**:18 (1998), 3586–3616.

[McLaughlin and Bulleid 1998] S. H. McLaughlin and N. J. Bulleid, "Molecular recognition in procollagen chain assembly", *Matrix Biol.* **16**:7 (1998), 369–377.

[Miles and Bailey 2001] C. A. Miles and A. J. Bailey, "Thermally labile domains in the collagen molecule", *Micron* **32**:3 (2001), 325–332.

[Mo et al. 2006] X. Mo, Y. An, C.-S. Yun, and S. M. Yu, "Nanoparticle-assisted visualization of binding interactions between collagen mimetic peptide and collagen fibers", *Angew. Chem. Int. Edit.* **45**:14 (2006), 2267–2270.

[Myllyharju and Kivirikko 2001] J. Myllyharju and K. I. Kivirikko, "Collagens and collagen-related diseases", *Ann. Med.* **33**:1 (2001), 7–21.

[Nagase and Woessner 1999] H. Nagase and J. F. Woessner, Jr., "Matrix metalloproteinases", *J. Biol. Chem.* **274**:31 (1999), 21491–21494.

[Overall 2002] C. M. Overall, "Molecular determinants of metalloproteinase substrate specificity: matrix metalloproteinase substrate binding domains, modules, and exosites", *Mol. Biotechnol.* **22**:1 (2002), 51–86.

[Persikov and Brodsky 2002] A. V. Persikov and B. Brodsky, "Unstable molecules form stable tissues", *Proc. Natl. Acad. Sci.* **99**:3 (2002), 1101–1103.

[Radmer and Klein 2006] R. J. Radmer and T. E. Klein, "Triple helical structure and stabilization of collagen-like molecules with 4(R)-hydroxyproline in the Xaa position", *Biophys. J.* **90**:2 (2006), 578–588.

[Ramachandran and Kartha 1955] G. N. Ramachandran and G. Kartha, "Structure of collagen", *Nature* **176**:4482 (1955), 593–595.

[Rich and Crick 1961] A. Rich and F. H. C. Crick, "The molecular structure of collagen", *J. Mol. Biol.* **3** (1961), 483–506.

[Ruberti and Hallab 2005] J. W. Ruberti and N. J. Hallab, "Strain-controlled enzymatic cleavage of collagen in loaded matrix", *Biochem. Biophys. Res. Commun.* **336**:2 (2005), 483–489.

[Ryhänen et al. 1983] L. Ryhänen, E. J. Zaragoza, and J. Uitto, "Conformational stability of type I collagen triple helix: evidence for temporary and local relaxation of the protein conformation using a proteolytic probe", *Arch. Biochem. Biophys.* **223**:2 (1983), 562–571.

[Shah et al. 1996] N. K. Shah, J. A. Ramshaw, A. Kirkpatrick, C. Shah, and B. Brodsky, "A host-guest set of triple-helical peptides: stability of Gly-X-Y triplets containing common nonpolar residues", *Biochemistry* **35**:32 (1996), 10262–10268.

[Stultz 2002] C. M. Stultz, "Localized unfolding of collagen explains collagenase cleavage near imino-poor sites", *J. Mol. Biol.* **319**:5 (2002), 997–1003.

[Tomasek et al. 2002] J. Tomasek, G. Gabbiani, B. Hinz, C. Chaponnier, and R. A. Brown, "Myofibroblasts and mechano-regulation of connective tissue remodelling", *Nat. Rev. Mol. Cell Biol.* **3**:5 (2002), 349–363.

[van der Slot 2005] A. J. van der Slot-Verhoeven, *Telopeptide lysyl hydroxylase: a novel player in the field of fibrosis*, Ph.D. thesis, Leiden University, 2005, Available at https://openaccess.leidenuniv.nl/dspace/bitstream/1887/2704/5.

[Welgus et al. 1982] H. G. Welgus, J. J. Jeffrey, G. P. Stricklin, and A. Z. Eisen, "The gelatinolytic activity of human skin fibroblast collagenase", *J. Biol. Chem.* **257**:19 (1982), 11534–11539.

[Wright and Humphrey 2002] N. T. Wright and J. D. Humphrey, "Denaturation of collagen via heating: an irreversible rate process", *Annu. Rev. Biomed. Eng.* **4** (2002), 109–128.

KRISHNAKUMAR M. RAVIKUMAR: krishhere@tamu.edu
*Department of Biomedical Engineering, Texas A&M University, College Station, Texas 77843-3120, United States*

JAY D. HUMPHREY: jhumphrey@tamu.edu
*Department of Biomedical Engineering, Texas A&M University, College Station, Texas 77843-3120, United States*

WONMUK HWANG: hwm@tamu.edu
*Department of Biomedical Engineering, Texas A&M University, College Station, Texas 77843-3120, United States*

# PARTICLE COLLISION AND ADHESION UNDER THE INFLUENCE OF NEAR-FIELDS

T. I. ZOHDI

In many biomechanical applications, the collision of microscopic particles, under the influence of inter-particle near-field forces, is an important step in an overall biophysical process. In this communication, expressions are derived relating the impact velocity needed for two small-scale particles to adhere as a function of particle sizes, material hardnesses, densities and interparticle near-field character.

## 1. Introduction

There are numerous applications in biomechanics where one step in an overall series of events is the collision and possible adhesion of small-scale particles (1–100 microns), under the influence of inter-particle near-fields. For example, in study of atherosclerotic plaque growth, a predominant school of thought attributes the inception of atherosclerotic plaque growth to a relatively high concentration of microscale suspensions (low-density lipoprotein (LDL) particles) in the blood. Atherosclerotic plaque formation involves: (a) adhesion of monocytes (essentially larger suspensions) to the endothelial surface, which is controlled by the adhesion molecules stimulated by the excess LDL, oxygen content, and the intensity of blood flow; (b) penetration of the monocytes into the intima and subsequent tissue inflammation; and (c) rupture of the plaque accompanied by some degree of thrombus formation or even subsequent occlusive thrombosis. For an overall general introduction [Libby 2001a; 2001b; Libby et al. 2002; Libby and Aikawa 2002]. For extensive analyses addressing modeling and numerical procedures, see [Jou and Berger 1998; Berger and Jou 2000; Kaazempur-Mofrad and Ethier 2001; 2003; 2004; Younis et al. 2004; Stroud et al. 2002; Stroud et al. 2000]. For experimentally-oriented physiological flow studies of atherosclerotic carotid bifurcations and related systems, see [Bale-Glickman et al. 2003b; 2003a]. Notably, Bale-Glickman et al. [2003b; 2003a] have constructed flow models which replicate the lumen of plaques excised intact from patients with severe atherosclerosis, which have shown that the complex internal geometry of the diseased artery, combined with the pulsatile input flows, gives exceedingly complex flow patterns. They have shown that the flows are highly three-dimensional and chaotic, with details varying from cycle to cycle. In particular, the vorticity and streamline maps confirm the highly complex and three-dimensional nature of the flow. Despite the large body of work on the subject, the mechanisms in the initial stages of the disease involving the interparticle mechanics have not been extensively studied, although some simple semianalytical qualitative studies have been carried out recently [Zohdi et al. 2004; 2005c], focusing on particle-wall adhesion. Furthermore, particle-to-particle adhesion can play a significant role in the behavior of a thrombus, comprised of agglomerations of particles, ejected by a plaque rupture which can occur in later stages of the disease. The behavior, in

particular the fragmentation of such a particulate-laden thrombus, as it moves downstream, is critical in determining the chances for stroke.

Another biological process where particle interaction and aggregation is important is the formation of certain types of kidney stones, which start as an agglomeration *seed* of particulate materials, for example combinations of calcium oxalate monohydrate, calcium oxalate dihydrate, uric acid, struvite or cystine [Kim 1982; Kahn et al. 1983; 1993; Kahn and Hackett 1984; Coleman and Saunders 1993; Pittomvils et al. 1994; Zohdi and Szeri 2005]. The mentioned examples are only a few of the many biomechanical applications, where the collision of microscale particles, under the influence of near-field forces, which play a considerable role at these scales, form an important step in an overall biophysical process. The objective of this communication is to shed light on some fundamental aspects of collision and adhesion of such particles, which are typically between 1–100 microns. In particular, we isolate and focus on a single aspect of particle adhesion, namely the determination of the impact velocity needed for two small-scale particles to adhere as a function of particle size, material hardness, density and interparticle near-field character. (We neglect fluid effects. This analysis is not meant to be a comprehensive or complete picture of the combined fluid-particle interaction problem.)

## 2. Analysis of a particle collision

We consider the scenario of two impacting particles, isolated from the group in Figure 1. The linear momentum exchange between two identical particles, $i$ and $j$, each traveling with an initial velocity of $v_o$ is opposite directions ($v_i(0) = v_o = -v_j(0)$). For the pair, along the line of impact

$$m_i v_i(0) + m_j v_j(0) = m_i v_i(\delta t) + m_j v_j(\delta t) = 0, \tag{1}$$
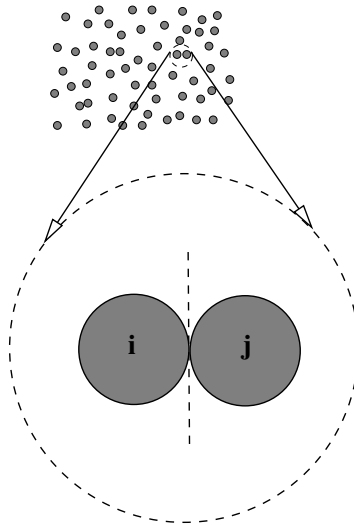


**Figure 1.** Isolating two particles undergoing a collision.

and for an individual

$$m_i v_i(0) + \underbrace{\int_0^{\delta t} I \, dt}_{\bar{I} \delta t} = m_i v_i(\delta t), \tag{2}$$

where $\bar{I}$ is the average impulse acting between particles. The impulse is

$$\bar{I} = \frac{m_i v_i(\delta t) - m_i v_i(0)}{\delta t}. \tag{3}$$

Recall the classical coefficient of restitution, defined as

$$e = \frac{v_j(\delta t) - v_i(\delta t)}{v_i(0) - v_j(0)}, \tag{4}$$

where $e = 1$ is a perfectly elastic (energy preserving) impact and where $e = 0$ is a perfectly plastic (full adhesion) impact.[1] The phenomenological parameter $e$ depends on the severity of the impact velocity, and, implicitly, the pressure in the contact zone. See [Goldsmith 2001] for extensive experimental data or [Johnson 1985] for detailed analytical treatments. For the applications considered, involving particle bonding leading to agglomeration in such particulate media, it is advantageous to construct a coefficient of restitution relations that are pressure based, which idealize bonding as a limiting case as $e \to 0$. For example, empirically motivated relations involving the material's Vicker's hardness to determine whether two particles bond can be found in [Nesterenko et al. 1994]. See [Meyers 1994; Nesterenko 2001] for reviews on bonding criteria.

Specifically, the phenomenological material parameter $e$ depends on $\bar{I}$, and thus implicitly on the impact velocity. An empirically derived condition for whether two surfaces will bond is if the magnitude of the surface pressure ($|P|$) exceeds or attains twice the Vicker's hardness $2H$, that is, if $|P| \geq 2H$. See [Meyers 1994; Nesterenko et al. 1994; 2001] for reviews.[2] We construct an ad hoc model for bonding by approximating the surface pressure as

$$|P| \approx \frac{|\bar{I}|}{a_c},$$

where $a_c$ represents the apparent contact area. Clearly if $e = 1$, the impact is purely elastic with no adhesion, and thus there is no loss in energy, while if $e = 0$ there is a maximum loss in energy. Consistent with Nesterenko's experimental observations on bonding [Nesterenko et al. 1994; Nesterenko 2001], we shall follow the assumption that if the pressure exceeds twice the Vicker's hardness, the two surfaces will bond. Furthermore, we approximate $e$ by a linear scaling with the pressure-to-hardness ratio [Zohdi 460]. Accordingly, a relatively simple constitutive relation for $e$, incorporating the pressure criteria ($|P| \geq 2H$), is

$$e = \frac{v_j(\delta t) - v_i(\delta t)}{v_i(0) - v_j(0)} = \max\left(\left(1 - \frac{|P|}{2H}\right), 0\right) = \max\left(\left(1 - \frac{m_i |v_i(\delta t) - v_i(0)|}{2 H a_c \delta t}\right), 0\right), \tag{5}$$

---

[1]The use of this relation for *charged* particles is valid, provided that we ignore the near-field contributions from particles other than the isolated pair. More general relations, which include the contributions from surrounding particles, can be found in [Zohdi 2005b; 2005a].

[2]The Vicker's hardness is correlated to the yield point for plastic deformation of the material by $H \approx 3\sigma_y$.

where we have used Equation (1), and where $a_c$ is the contact area between two particles. We assume that the contact area is proportional to the cross-sectional area of the particle, $a_c \propto \pi b^2$, thus we can approximate a (proportional) contact area relationship of the form $a_c = k_1 \pi b^2$, where $0 \le k_1 \le 1$ and $b$ is the particle radius. By setting $e = 0$ in Equation (5), we obtain

$$|v_i(\delta t) - v_i(0)| \ge \frac{3k_1 \delta t H}{2\rho b}, \tag{6}$$

where $m_i = \rho \frac{4}{3} \pi b^3$, $\rho$ being the particle mass density. If we have identical adhering ($e = 0$) particles ($v_o = v_i(0) = -v_j(0)$), then $v_i(\delta t) = 0$. Also, the impact time, $\delta t$, is proportional to the size of the particles and the impact velocity, thus we approximate $\delta t = k_2 b / v_o$ ($k_2$ is dimensionless), and we have[3]

$$\frac{2 v_o^2 \rho}{3 H k_1 k_2} \ge 1 \Rightarrow v_o \ge \sqrt{\frac{3 H k_1 k_2}{2\rho}} = k_3 \sqrt{\frac{H}{\rho}}. \tag{7}$$

In other words, the critical velocity for two particles to adhere, based solely on mechanical pressure, is directly proportional to the material's hardness and inversely proportional to its density. Thus, hard, low-density, particles would require extremely high velocities in order to adhere.

## 3. Impact with near-fields present

Now consider the case where interparticle near-field (for example, electrostatic forces, van Der Waals, etc.) interaction is present. As before, for the pair, along the line of impact, we have

$$m_i v_i(0) + m_j v_j(0) = m_i v_i(\delta t) + m_j v_j(\delta t) = 0, \tag{8}$$

however, for an individual we have

$$m_i v_i(0) + \underbrace{\int_0^{\delta t} I \, dt}_{\overline{I} \delta t} + \underbrace{\int_0^{\delta t} E \, dt}_{\overline{E} \delta t} = m_i v_i(\delta t), \tag{9}$$

where $\overline{I}$ is the average impulse acting between the particles due to contact, and where $\overline{E}$ is the average impulse acting between the particles due to interparticle near-field interaction. The impulse is

$$\overline{I} = \frac{m_i v_i(\delta t) - m_i v_i(0)}{\delta t} - \overline{E}. \tag{10}$$

As before, we set $e = 0$ in Equation (5), using the same relations as before, and we now obtain ($v_o \overset{\text{def}}{=} v(0)$)

$$|P| = \frac{|\overline{I}|}{a_c} = \frac{1}{a_c} \left| -\overline{E} - \frac{m v_o}{\delta t} \right| \ge 2H. \tag{11}$$

**Case 1:** If the near-field is attractive between particles ($\overline{E} \ge 0$), we obtain

$$v_o \ge \left( 2 H a_c - |\overline{E}| \right) \frac{\delta t}{m}. \tag{12}$$

---

[3][Johnson 1985] for more detailed treatments of impact duration.

**Case 2:** If the near-field is repulsive between particles ($\overline{E} \leq 0$) and if $|\frac{mv_o}{\delta t}| \geq |\overline{E}|$, we obtain

$$v_o \geq \left(2Ha_c + |\overline{E}|\right)\frac{\delta t}{m}. \tag{13}$$

If the near-field is repulsive between particles ($\overline{E} \leq 0$) and if $|\frac{mv_o}{\delta t}| \leq |\overline{E}|$, we obtain *no adhesion.* If we utilize the previous assumptions in the "$E$-free" case,

(a) $a_c = k_1 \pi b^2$,

(b) $m_i = m_j = m = \rho \frac{4}{3}\pi b^3$ and

(c) $\delta t = k_2 b / v_o$,

the two cases become:

$$\textbf{Case 1}: \quad v_o^2 \geq \frac{3Hk_1k_2}{2\rho} - \underbrace{|\overline{E}|\frac{3k_2}{4\rho\pi b^2}}_{\geq 0} \tag{14}$$

and

$$\textbf{Case 2}: \quad v_o^2 \geq \frac{3Hk_1k_2}{2\rho} + \underbrace{|\overline{E}|\frac{3k_2}{4\rho\pi b^2}}_{\geq 0}. \tag{15}$$

In other words, the critical velocity for two particles to adhere is increased if the near-field is repulsive and decreased if the near-field is attractive. Essentially, the introduction of a near-field produces results which are deviations from the $E$-free term that first appeared in Equation (7):

$$\frac{3Hk_1k_2}{2\rho}.$$

Now consider $\overline{E}$ as a function of the separation distance, and hence $b$ at the moment of contact. For example, consider a simple relation

$$\overline{E}(|r_i - r_j|) = \alpha|r_i - r_j|^{-\beta}, \tag{16}$$

where $r_i$ is the position of the center of particle $i$, $r_j$ is the position of the center of particle $j$ and $0 < \beta < \infty$ and $-\infty < \alpha < \infty$. When $\alpha > 0$, then the resulting force between the particles is attractive, while if $\alpha < 0$, then the resulting force is repulsive. For direct central impact, at contact, this collapses to ($|r_i - r_j| = 2b$)

$$\overline{E}(b) = \alpha(2b)^{-\beta}. \tag{17}$$

We introduce the following (per unit mass$^2$) decomposition for the force imparted on particle $i$ by particle $j$ and vice-versa:

$$\alpha = \overline{\alpha}m_i m_j, \tag{18}$$

where $\overline{\alpha}$ has units of [Newton (meter)$^\beta$]$/kg^2$. The substitution of this near-field form into the equations for the two cases yields ($m_i = m_j = m$):

$$\textbf{Case 1}: \quad v_o^2 \geq \frac{3Hk_1k_2}{2\rho} - \underbrace{b^{(6-\beta)}\frac{4|\overline{\alpha}|\rho\pi k_2 2^{-\beta}}{3}}_{\geq 0} \tag{19}$$

and

$$\textbf{Case 2}: \quad v_o^2 \geq \frac{3Hk_1k_2}{2\rho} + \underbrace{b^{(6-\beta)}\,\frac{4|\overline{\alpha}|\rho\pi k_2 2^{-\beta}}{3}}_{\geq 0}.$$

(20)

Generally, if $\beta < 6$ then the critical velocity needed for adhesion decreases with increasing particle size, while, if the near-field is repulsive, the critical velocity increases with increasing particle size. For example, if $\beta = 2$, (similar to an electrostatic Coloumb-type character), then the critical velocity needed for adhesion decreases with increasing particle size, while the critical velocity increases with increasing particle size, if the near-field is repulsive. However, if $\beta \geq 6$, then the critical velocity needed for adhesion increases with increasing particle size, while the critical velocity decreases with increasing particle size, if the near-field is repulsive.

## 4. Summary

In summary, the objective of this communication was to investigate some fundamental aspects of the collision and adhesion of microscopic particles, such as those frequently encountered in biological applications. Basic relations were derived relating the impact velocity needed for two particles to adhere as a function of fundamental quantities such as the particle sizes, material hardnesses, densities and interparticle near-field character. The assumptions leading to the derivation of primary results, Equations (19) and (20), are easily replaceable with more accurate descriptions, if and when they become available; however, the overall structure can stay, more or less, intact. For example, one central assumption in the derivation of Equations (19) and (20) was the representation of the *charge per unit mass* (Equation (18)). This can be easily replaced with a *per surface area* relation or some other charge/particle-size metric, for example $\alpha_{ij} = f(b_i, b_j)$, where $f(b_i, b_j)$ is a function that correlates the particle sizes to the level of *near-field charge*.

## References

[Bale-Glickman et al. 2003a] J. Bale-Glickman, K. Selby, D. Saloner, and O. Savas, "Experimental flow studies in exact-replica phantoms of atherosclerotic carotid bifurcations under steady input conditions", *J. Biomech. Eng.* (*Trans. ASME*) **125**:1 (2003), 38–48.

[Bale-Glickman et al. 2003b] J. Bale-Glickman, K. Selby, D. Saloner, and O. Savas, "Physiological flow studies in exact-replica atherosclerotic carotid bifurcations", in *Proceedings of 2003 ASME International Mechanical Engineering Congress* (Washington, DC), IMECE2003-41281, American Society of Mechanical Engineers, New York, November 2003.

[Berger and Jou 2000] S. A. Berger and L. D. Jou, "Flow in stenotic vessels", *Annu. Rev. Fluid Mech.* **32** (2000), 347–382.

[Coleman and Saunders 1993] A. J. Coleman and J. E. Saunders, "A review of the physical properties and biological effects of the high amplitude acoustic fields used in extracorporeal lithotripsy", *Ultrasonics* **31**:2 (1993), 75–89.

[Goldsmith 2001] W. Goldsmith, *Impact: the theory and physical behavior of colliding solids*, Dover, Toronto, 2001.

[Johnson 1985] K. Johnson, *Contact mechanics*, Cambridge University Press, 1985.

[Jou and Berger 1998] L. D. Jou and S. A. Berger, "Numerical simulation of the flow in the carotid bifurcation", *Theor. Comp. Fluid Dyn.* **10**:1-4 (1998), 239–248.

[Kaazempur-Mofrad and Ethier 2001] M. R. Kaazempur-Mofrad and C. R. Ethier, "Mass transport in an anatomically realistic human right coronary artery", *Ann. Biomed. Eng.* **29**:2 (2001), 121–127.

[Kaazempur-Mofrad et al. 2003] M. R. Kaazempur-Mofrad, H. F. Younis, S. Patel, A. G. Isasi, C. Chung, R. C. Chan, H. D. P., R. T. Lee, and R. D. Kamm, "Cyclic strain in human carotid bifurcation and its potential correlation to atherogenesis: idealized and anatomically-realistic models", *J. Eng. Math.* **47**:3–4 (2003), 299–314.

[Kaazempur-Mofrad et al. 2004] M. R. Kaazempur-Mofrad, A. G. Isasi, H. F. Younis, , R. C. Chan, D. P. Hinton, G. Sukhova, G. M. LaMuraglia, R. T. Lee, and R. D. Kamm, "Characterization of the atherosclerotic carotid bifurcation using MRI, finite element modeling and histology", *Ann. Biomed. Eng.* **32**:7 (2004), 932–946.

[Kahn and Hackett 1984] S. R. Kahn and R. L. Hackett, "Microstructure of decalcified human calcium oxalate urinary stones", *Scan. Electron Micros.* **150**:II (1984), 935–941.

[Kahn and Hackett 1993] S. R. Kahn and R. L. Hackett, "Role of organic matrix in urinary stone formation: an ultrastructural study of crystal matrix interface of calcium oxalate monohydrate stones", *J. Urology* **150**:7 (1993), 239–245.

[Kahn et al. 1983] S. R. Kahn, B. Finlayson, and R. L. Hackett, "Stone matrix as proteins adsorbed on crystal surfaces: a microscopic study", *Scan. Electron Micros.* (1983), 379–385.

[Kim 1982] K. M. Kim, "The stones", *Scan. Electron Micros.* **1982**:IV (1982), 1635–1660.

[Libby 2001a] P. Libby, "Current concepts of the pathogenesis of the acute coronary syndromes", *Circulation* **104** (2001), 365–372.

[Libby 2001b] P. Libby, "The vascular biology of atherosclerosis", Chapter 30, pp. 995–1009 in *Heart disease: a textbook of cardiovascular medicine*, sixth ed., edited by E. Braunwald et al., Saunders, Philadelphia, 2001.

[Libby and Aikawa 2002] P. Libby and M. Aikawa, "Stabilization of atherosclerotic plaques: new mechanisms and clinical targets", *Nat. Med.* **8**:11 (2002), 1257–1262.

[Libby et al. 2002] P. Libby, P. M. Ridker, and A. Maseri, "Inflammation and atherosclerosis", *Circulation* **105** (2002), 1135–1143.

[Meyers 1994] M. A. Meyers, *Dynamic behavior of materials*, John Wiley & Sons, 1994.

[Nesterenko 2001] V. F. Nesterenko, *Dynamics of heterogeneous materials*, Springer Verlag, 2001.

[Nesterenko et al. 1994] V. F. Nesterenko, M. A. Meyers, H. C. Chen, and J. C. LaSalvia, "Controlled high rate localized shear in porous reactive media", *Appl. Phys. Lett.* **65**:24 (1994), 3069–3071.

[Pittomvils et al. 1994] G. Pittomvils, H. Vandeursen, M. Wevers, J. P. Lafaut, D. De Ridder, P. De Meester, R. Boving, and L. Baert, "The influence of internal stone structure upon the fracture behaviour of urinary calculi", *Ultrasound Med. Biol.* **20**:8 (1994), 803–810.

[Stroud et al. 2000] J. S. Stroud, S. A. Berger, and D. Saloner, "Influence of stenosis morphology on flow through severely stenotic vessels: implications for plaque rupture", *J. Biomech.* **33**:4 (2000), 443–455.

[Stroud et al. 2002] J. S. Stroud, S. A. Berger, and D. Saloner, "Numerical analysis of flow through a severely stenotic carotid artery bifurcation", *J. Biomech. Eng. (Trans. ASME)* **124**:1 (2002), 9–20.

[Younis et al. 2004] H. F. Younis, M. R. Kaazempur-Mofrad, R. C. Chan, A. G. Isasi, D. P. Hinton, A. H. Chau, L. A. Kim, and R. D. Kamm, "Hemodynamics and wall mechanics in human carotid bifurcation and its consequences for atherogensis: investigation of inter-individual variation", *Biomechanics and Modeling in Mechanobiology* **3**:1 (2004), 17–32.

[Zohdi 2005a] T. I. Zohdi, "Charge-induced clustering in multifield particulate flows", *Int. J. Numer. Methods Eng.* **62**:7 (2005), 870–898.

[Zohdi 2005b] T. I. Zohdi, "Modeling and direct simulation of near field granular flows", *Int. J. Solids Struct.* **42**:2 (2005), 539–564.

[Zohdi 2005c] T. I. Zohdi, "A simple model for shear stress mediated lumen reduction in blood vessels", *Biomechanics and Modeling in Mechanobiology* **4**:1 (2005), 57–61.

[Zohdi 460] T. I. Zohdi, "A computational framework for agglomeration in thermochemically reacting granular flows", *P. Roy. Soc. Lond. A Mat.* **2004**:2052 (460), 3421–3445.

[Zohdi and Szeri 2005]  T. I. Zohdi and A. J. Szeri, "Fatigue of kidney stones with heterogeneous microstructure subjected to shock-wave lithotripsy", *J. Biomed. Mater. Res. Part B* **75B**:2 (November 2005), 351–358.

[Zohdi et al. 2004]  T. I. Zohdi, G. A. Holzapfel, and S. A. Berger, "A phenomenological model for atherosclerotic plaque growth and rupture", *J. Theor. Biol.* **227**:3 (2004), 437–443.

T. I. ZOHDI: zohdi@me.berkeley.edu
*Mechanical Engineering, 6117 Etcheverry Hall, University of California, Berkeley, Berkeley, CA 94720-1740, United States*
http://www.me.berkeley.edu/faculty/zohdi/

# HIERARCHICAL CHEMO-NANOMECHANICS OF PROTEINS: ENTROPIC ELASTICITY, PROTEIN UNFOLDING AND MOLECULAR FRACTURE

## MARKUS J. BUEHLER

Proteins are an integral part of nature's material design. Here we apply multiscale modeling capable of providing a bottom-up description of the nanomechanics of chemically complex protein materials under large deformation and fracture. To describe the formation and breaking of chemical bonds of different character, we use a new reactive force field approach that enables us to describe the unfolding dynamics while considering the breaking and formation of chemical bonds in systems that are comprised of several thousand atoms. We particularly focus on the relationship between secondary and tertiary protein structures and the mechanical properties of molecules under large deformation and fracture. Our research strategy is to systematically investigate the nanomechanics of three protein structures with increasing complexity, involving alpha helices, random coils and beta sheets. The model systems include an alpha helical protein from human vimentin, a small protein $\alpha$-conotoxin PnIB from *conus pennaceus*, and lysozyme, an enzyme that catalyzes breaking of glycosidic bonds. We find that globular proteins can feature extremely long unfolding paths of several tens of nanometers, displaying a characteristic sawtooth shape of the force-displacement curve. Our results suggest that the presence of disulfide cross-links can significantly influence the mechanics of unfolding. Fibrillar proteins show shorter unfolding paths and continuous increase of forces until molecular rupture occurs. In the last part of the article we outline how a mesoscale representation of the alpha helical protein structure can be developed within the framework of hierarchical multiscale modeling, utilizing the results of atomistic modeling, without relying on empirical parameters. We apply this model to describe the competition between entropic and energetic elasticity in the mechanics of a single alpha helical protein molecule, at long time scales reaching several microseconds. We conclude with a discussion of hybrid reactive-nonreactive modeling that could help to overcome some of the computational limitations of reactive force fields.

## 1. Introduction

The behavior of biological systems is controlled by a complex interplay of a large set of macromolecules, chemical solvents and external stimuli such as mechanical forces or strain. Cells, for example, represent exceptionally complicated systems that feature heterogeneous structures across many length- and time-scales, including ribosomes, protein networks, microtubules, DNA and the cell membrane. Many structural materials found in nature, such as bone and nacre, display a clever heterogeneous design that includes proteins, inorganic phases and solvents.

To date, the function and mechanical response of biological structures and materials is largely limited to phenomenological concepts that characterize the behavior of biological systems from a macroscopic perspective, by introducing a set of empirical parameters, using a top-down approach. Quantitative theories, in particular those that link the scale of chemistry and molecular properties to the scales of materials, or to the scale of complex biological systems that comprise of several thousands of molecules, are still missing.

This lack of understanding is partly due to difficulties in handling and measuring properties of such tiny structures with dimensions of several nanometers and below, and force levels that are often limited to several pN or nN. Carrying out highly specific experiments with high spatial and temporal resolution at these force levels represents a significant challenge.

Experimental methods developed recently now enable us to investigate the nanoscale behavior of materials using quantitative analysis techniques. For example, nanoindentation, AFM, optical and magnetic tweezers enables scientists to probe the origins of elastic and plastic deformation of materials, with forces in the range of pN to $\mu$N, and at scales approaching that of individual atoms, molecules or cells [Gouldstone et al. 2001; Sun et al. 2001; Dao et al. 2003; Sun et al. 2004]. At the same time availability of computational resources and new theoretical approaches have led to significant advances in addressing nanomechanics from a first principles viewpoint [Marko and Siggia 1995; MacKerell et al. 1998]. Combining experimental with computational or theoretical studies could lead to an alternative to the classical top-down engineering approach, by providing a bottom-up materials description linking small to large [Whitesides and Wong 2006]. The multiscale approach is visualized schematically in Figure 1.

Materials found in nature often feature hierarchical structures ranging from the atomistic and molecular to macroscopic scales [Hulmes et al. 1995; Sasaki and Odajima 1996; Jager and Fratzl 2000; Puxkandl et al. 2002; Aizenberg et al. 2005; Whitesides and Wong 2006]—a variation which renders this class of materials both fascinating and extremely challenging. Examples of such materials include bone, tendon, or nacre. Moreover, many biological materials found in living organisms primarily utilize proteins as fundamental building blocks, creating fascinating materials whose functions range from load bearing and serving as catalysts to intercellular signaling. Proteins are a particularly intriguing class of biopolymers representing a complex three-dimensional folded structure of one or more polypeptide chains. Proteins play a particularly important role in many biological tissues and functions, including tendon, bone, teeth, or cartilage and even in the cardiovascular system. Severe mechanical tensile and shear loading of proteins can occur under physiological conditions, as in joints and in bone. In other cases, extreme mechanical stimulation can lead to malfunction and disease. The properties of proteins represent a complicated and intertwined interplay of mechanics, chemistry and biological function, creating multifunctional, active or *smart* materials out of primarily only 20 distinct building blocks, the naturally occurring amino acids.

Our long-term objective is to contribute to develop a rigorous understanding of the mechanics of complex biological protein materials, while considering atomistic and molecular scales, bridging to larger time and length scales. To reach this goal we develop atomistic models of the nanomechanical properties of globular and fibrillar proteins. In this article we focus on the source of elasticity, deformation and fracture of single protein molecules. We apply a new modeling approach based on reactive force fields that enables us to treat complex chemistry in systems comprising several thousand atoms.
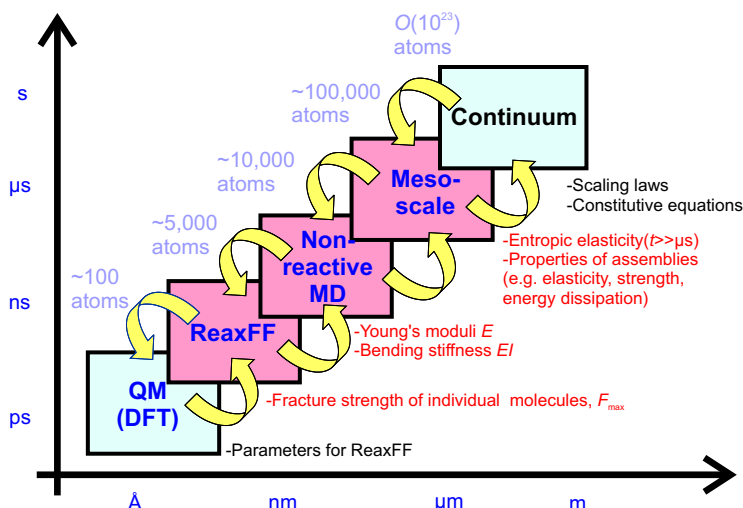
**Figure 1.** Summary of a hierarchical multiscale scheme used to gain an understanding of the behavior of biological materials, across scales in length and time. First principles quantum mechanics (QM) calculations (for example, Density Function Theory, DFT [Springborg 1997]) are carried out to train a reactive force field ReaxFF [van Duin et al. 2001]. The reactive force field is used together with nonreactive force fields [MacKerell et al. 1998] to obtain properties of individual protein molecules and assemblies of several molecules [Buehler 2006a; 2006b]. The results of atomistic calculations can then be coupled to continuum scale models, for example, by using scaling laws [Buehler 2006a; 2006d]. We note that reactive force field calculations are significantly more expensive, which typically limits us to sub-ns time scales. This can influence the observed trajectories, as strain rates may be unrealistically large. This limitation could be overcome by parallelization or development of faster computational resources.

**1.1.** *Nanomechanics of protein materials: laboratory experiments.* When materials are deformed, they display a small regime in which deformation is reversible or elastic. Once the forces on the material are increased, deformation becomes irreversible and can involve fracture. Deformation and fracture of materials is controlled by atom-by-atom processes that are eventually governed by quantum mechanics, or quantum chemistry. The deformation mechanics of brittle materials (for example, ceramics, silicon, glass, some polymers) and ductile materials (for example, copper, nickel) has been subject to extensive and very successful research over the past decades [Buehler and Gao 2006b]. Figures 2(a) and (b) depict a schematic of the fundamental deformation mechanisms in these materials that include crack propagation or dislocation nucleation and interaction [Buehler et al. 2003; 2004; 2005; Hartmaier et al. 2005; Buehler and Gao 2006a].

However, similar mechanisms are not yet well understood for biological materials, and rigorous deformation theories are still missing. Figure 2c depicts a schematic of a hierarchical biological material that consists of a heterogeneous assembly of building blocks. The response of the material depends on the mechanical and interface properties of its building blocks (for example, protein molecules, nanocrystals
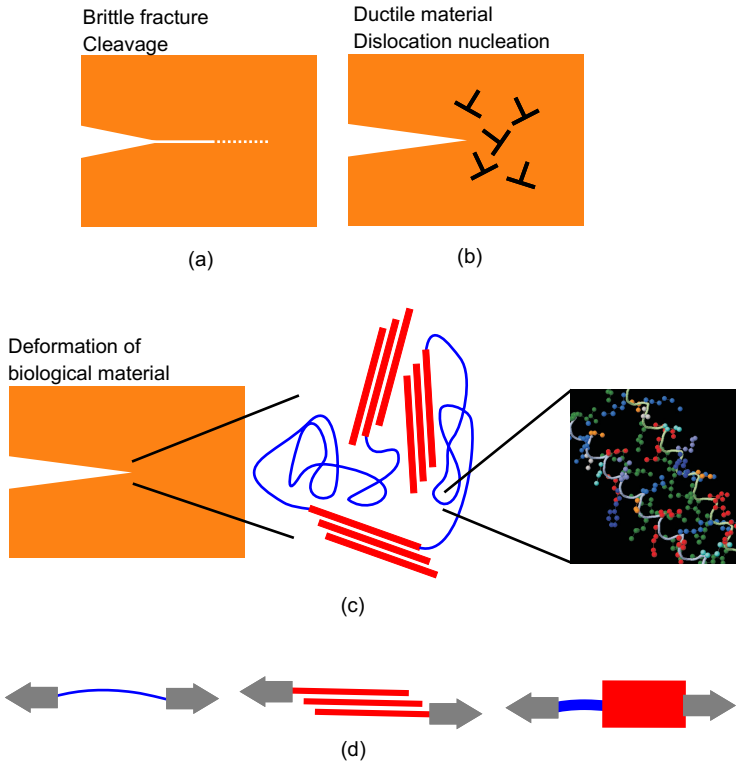
**Figure 2.** Response of different classes of materials to extreme mechanical stimulation. The response of brittle (subplot (a)) and ductile (subplot (b)) materials is relatively well understood, with theories describing crack extension and dislocation nucleation and propagation. However, the response of biological materials to mechanical loading, for example, the response of materials to the large stresses at the tip of a microcrack, remains an active area of research, since little understanding exists about how specific components of hierarchical materials participate in deformation and how they contribute to the macroscopic material properties (subplot (c)). Biological materials feature several layers of complexity, and the key to understanding their behavior is the ability to decipher the response of its building blocks (for example, random coils, beta sheets and assemblies of those, or globular folded structures). Subplot (d) shows a schematic decomposition of the complex three-dimensional structure into its building blocks. Each building block is studied under a variety of different types of mechanical loading conditions. Information from these studies is then used to build models that are capable of describing the entire, realistic material nano-structure of the material.

or other components), as illustrated in Figure 2d. The apparent need to understand the properties of nature's buildings better has motivated systematic investigations of the nanomechanical properties of individual protein molecules.

The nanomechanics of individual proteins has been subject to an intense debate over the last decades that has led to significant advances in understanding the behavior of their mechanical response, leading

to estimates for their Young's modulus, the persistence length or the bending stiffness [Rief et al. 1997; 2000]. For example, in a recent study carried out using optical tweezers researchers have measured the persistence length of individual proteins [Rief et al. 1997; 2000; Mehta et al. 1999; Sun et al. 2001; Schwaiger et al. 2002]. A widely used approach determine the persistence length is to employ optical tweezers to obtain force-stretching curves. The persistence length can be extracted from such experiments by assuming that the elastic response can be described using a worm-like chain (WLC) model. If the contour length and temperature is known, the persistence length is the only parameter in the WLC model [Bustamante et al. 1994; Marko and Siggia 1995] and can thus be determined to fit the experimental results. For example, this approach has also been used to study the persistence length of a type I tropocollagen molecule [Sun et al. 2004]. Similar techniques has also been successfully applied to titin [Rief et al. 1997; 2000; Gao et al. 2001; 2002], DNA and many other biomolecules.

However, forces in experiment are typically limited to a few nN, which approximately equals the strength of covalent bonds. This limits the applicability of such experiments to study the large-strain elastic properties and fracture properties of individual molecules or assemblies of molecules. Further, some experimental techniques are limited in terms of their temporal and spatial resolution. There is indirect experimental evidence of large-deformation and fracture of protein materials, as outlined in several experimental studies of bone, mineralized tendon and tendon [Landis et al. 2002; Nalla et al. 2003; 2005; Ritchie et al. 2004; Gupta et al. 2004; 2005; Peterlik et al. 2006].

## 1.2. *Hierarchical multiscale modeling of protein molecules: reactive versus nonreactive force fields.*
Atomistic and molecular modeling [Wang et al. 2001; Karplus and McCammon 2002; Buehler 2006c] can supplement experiment by providing a highly specific, controlled and fundamental method to describe the nanomechanical properties of biological matter in general, in particular those of proteins.

Atomistic models are capable of simulating the motion of all atoms in a material, with systems comprised of up to several billion particles [Kadau et al. 2004], reaching scales of several micrometers, that are getting close to macroscopic scales where material behavior that can be directly observed in experiment [Buehler 2006a, 2006d]. Atomistic models enable us to probe the macroscopic response of materials, for example, due to mechanical stimulation, based on their fundamental, atomistic ultrastructure, including the complexities of the chemical interactions in the material without introducing empirical parameters. The key input parameter in atomistic modeling are the interatomic forces. Classical molecular dynamics [Leach 2001] force fields suitable to study the properties of proteins include CHARMM, AMBER and DREIDING [Wang et al. 2001; Karplus and McCammon 2002; Li and Arteca 2005] that provide a reasonably accurate representation of the molecular structure and energetics.

MD simulation using an approach referred to as steered MD allows application of atom-specific forces in large molecules. This method has been applied to study the unfolding dynamics of several fibrillar and globular proteins [Gao et al. 2001; 2002; Arteca 2003; Cieplak and Marszalek 2005; Lorenzo and Caffarena 2005]. Some of these simulations have been used to resemble AFM experiments of protein unfolding [Rief et al. 1997; 2000].

Even though molecular simulation has been successfully applied to describe some properties of protein molecules, most classical molecular simulation techniques are limited to describing molecular states close to the equilibrium configuration, and cannot be applied to describe large strain elastic response and fracture of covalent bonds [Wang et al. 2001; Karplus and McCammon 2002; Li and Arteca 2005;

Buehler 2006b]. The reason for these limitations is that these methods are not capable of describing formation or breaking of chemical bonds, as the methods often do not allow a unified treatment of the various chemical interactions with different bonding strength, treating covalent interactions by using harmonic potentials that lead to an infinitely large energy barrier for bond breaking. So far this is only possible by using quantum mechanical methods (for example, [Papamokos and Demetropoulos 2004] describes a study of nanomechanical properties of a small helical protein).

Figure 3 depicts a schematic representation of this behavior, emphasizing on the limitation of classical force fields so that they are not able to describe the transition state A-B during bond breaking or formation, but can only provide a representation of the ground states A or B. An important consequence of this limitation in regards to the mechanics of proteins is that molecular fracture cannot be described, making biological molecules unrealistically strong [Buehler 2006b]. In the remainder of this article we refer to these models as nonreactive force fields.
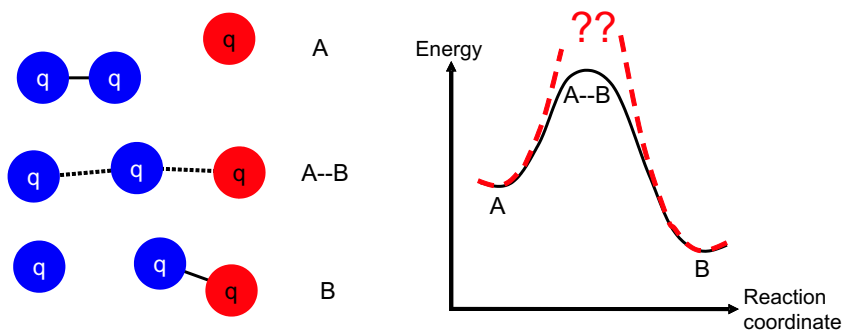


**Figure 3.** The concept of reactive versus nonreactive force fields. The reactive force fields enable describing the transition state energies between two ground states, as it is important for example during chemical reactions, including bond rupture. Nonreactive force fields (dashed line in the right subplot) are only capable of describing the ground states A and B, but not the transition state A-B.

To overcome the limitations of the nonreactive force fields we propose a new generation reactive force field ReaxFF [van Duin et al. 2001] that is capable of describing formation and breaking of chemical bonds, including the flow of charges during chemical reactions. This method enables us to describe the full reactivity of large systems that include several thousand atoms with quantum mechanical accuracy, providing a more realistic description of the large-deformation elastic behavior, including permanent deformation and fracture. The work described in this article is focused on demonstrating the applicability of this new method to describe the unfolding and stretching dynamics of proteins, enabling, for the first time, the description of molecular fracture of molecules comprised of several thousand atoms.

Both reactive and nonreactive models are limited to time scales of several nanoseconds. However, using a combination of hierarchies of simulation methods, vast time and length scales can be captured, a method referred to as multiscale modeling. Multiscale modeling combines a set of computational tools ranging from first principles quantum mechanics and molecular dynamics to reactive force fields and

|  | Force regime | Time scale | Entropic elasticity | Specificity, applicability |
|---|---|---|---|---|
| Experiment (optical tweezer, AFM, etc.) | Typically $< 10$ nN | $\gg$ fs (slow strain rates) | Yes | Difficult, analysis of atomistic processes often not possible |
| Atomistic simulation (reactive and nonreactive force fields) | $0, \ldots, 100$ pN (nonreactive force fields) $0, \ldots, 10$ nN (reactive force fields) | Typically $<$ ns (high strain rates) | No (time scale typically too short, molecular structures rather small) | Highly specific, reveals atomistic processes |
| Mesoscale particle models (for example, bead models) | $0, \ldots, 100$ nN (wide range) | $< \mu$sec, $\ldots$, sec (depending on level of discretization) | Yes | Highly specific, but no atomistic resolution |

**Table 1.** Differences between various experimental and computational methods that allow probing single molecule mechanics.

mesoscale models. The concept of integrating various simulation methods by handshaking to bridge across the scales is schematically represented in Figure 1.

Table 1 includes an overview over various properties that can be probed using nanomechanical experiments and atomistic or molecular simulation, illustrating how the different methods can supplement each other.

**1.3.** *Outline.* The focus of this article is application of reactive atomistic models to describe the large-deformation elastic and fracture behavior of proteins. After this introduction we briefly review the physical foundations of elasticity in biological molecules and biological materials in Section 2. In Section 3 we describe our multiscale modeling approach, including a discussion of the reactive force fields. In Section 4 we review a detailed analysis of three specific applications. First, we describe atomistic and mesoscale studies of stretching a single alpha helix, a building block of other proteins and protein materials including keratin, elastin and intermediate filaments in the cell's cytoskeleton. We continue with a discussion of atomistic modeling of the unfolding dynamics of a crosslinked protein $\alpha$-conotoxin PnIB from *conus pennaceus*. Finally, we discuss the unfolding of lysozyme, a well-studied enzyme that catalyzes breaking of glycosidic bonds. In Section 5 we present a broader discussion on chemical-mechanical interactions in biological materials and methods to bridge full atomistic to larger time and length scales, including coarse-graining techniques. We conclude with a brief outline of how such methods enable us to describe entropic elasticity using molecular dynamics and an example that demonstrates how reactive and nonreactive force fields can be combined in a concurrent multiscale scheme.

## 2. Physical foundations of elasticity: entropic and energetic contributions

Elasticity stems from the collective interactions of atoms, and, thus, it is intimately linked to chemistry. The elastic properties of materials can be expressed as the partial derivative of the free energy density with respect to the strain tensor that characterizes the resistance to deformation. Starting with free energy $A = U - TS$ composed of energetic $U$ and entropic contributions $TS$, we can define the free energy density, that is, free energy per unit volume $V$, via $\Phi = A/V$. The (scalar) stress $\sigma$ and the elastic modulus $E$ are then given by

$$\sigma = \frac{\partial \Phi}{\partial \varepsilon}, \qquad E = \frac{\partial^2 \Phi}{\partial \varepsilon^2}. \tag{1}$$

Note that stress and strain are related by Hooke's law, $\sigma = E\varepsilon$ [Courtney 1990]. Whereas the elasticity of crystalline materials is primarily controlled by energetic changes of the internal energy, in natural and biological materials elasticity can be significantly influenced by entropic contributions. This is because in many crystalline materials the entropic term can be neglected, so that $\Phi$ in Equation (1) can be directly substituted by $U/V$, the internal energy. However, in biopolymers entropic contributions can dominate the elasticity, in particular for small deformations, and therefore $\Phi$ in Equation (1) can be substituted by $-TS/V$.

Dominance of entropic behavior is a well-known phenomenon in many polymers. The contributions to the entropic term to elasticity can be described in several ways, including classical descriptions such as the WLC or the freely jointed Gaussian chain model [Bustamante et al. 1994; Marko and Siggia 1995]. Such descriptions are similar to constitutive models in continuum elasticity, and require input parameters that are typically determined empirically. In contrast to these models, molecular dynamics modeling can provide a first principles based description of entropic elasticity without any additional fitting parameters beyond the atomic interactions. This can be achieved by calculating the bending stiffness using full atomistic simulations.

The persistence length is defined as the molecular length at which entropic contributions to elasticity become important, as the molecule shows significant bending purely due to its thermal energy. A molecule with length far beyond the persistence length will bend, even without application of forces, and assume a conglomerated, wiggly shape. With the bending stiffness of a molecule denoted as $EI$, the persistence length is defined as $\xi_p = EI/(k_B T)$. When the length of molecules, denoted by $L$, is greater than the persistence length, that is, $L \gg \xi_p$, thermal energy can bend the molecule, and entropic elasticity typically plays a role. On the other hand, when $L \ll \xi_p$, entropic effects play a minor role, and energetic elasticity governs. Entropic effects become important and appear in measurements, for example, when one stretches a convoluted molecule.

Assuming that the initial point-to-point distance is $x < L$ (expressing the fact that the molecule is convoluted), the force that resists stretching can be approximated by

$$F(x; L, \xi_p) = \frac{kT}{\xi_p} \left( \frac{1}{4} \frac{1}{(1 - x/L)^2} - \frac{1}{4} + \frac{x}{L} \right). \tag{2}$$

This model is called the WLC or Marko–Siggia equation [Bustamante et al. 1994; Marko and Siggia 1995]. The molecular properties enter this equation in form of the persistence length, which is a function of the bending stiffness. If these properties are known from atomistic calculations, the WLC model

provides a quantitative estimate of entropic elasticity. The WLC model is only valid for deformations sufficiently far away from the contour length, as $F(x)$ diverges when $x \to L$.

Stretching single molecules typically involves a transition between two extreme regimes of sources of elasticity. Entropic elasticity controls the resistance to stretch the molecule when the end-to-end distances below the contour length. When the molecules is stretched to its contour length $x = L$, the entropic contributions decrease to zero and energetic elasticity starts to dominate. Thereafter the force increases proportionally to the stretching distance, according to a specific spring constant that relates distance of stretch and restoring force via

$$F(x; k) = k(x, L)(x - L). \tag{3}$$

Note that this equation is only valid when $x \geq L$, since the molecule can easily buckle under compressive load. When $x < L$, the restoring force assumes values close to zero. Also, note that $k(x, L)$ is a function of the deformation, in general, indicating that the elastic properties can change with deformation, a phenomenon referred to as nonlinear elasticity or hyperelasticity. At the atomistic scale energetic elasticity is characterized by the stretching of atomic, metallic, covalent or ionic bonds that leads to a change in potential energy in the material volume [Buehler 2006b].

## 3. Computational modeling of atomic interactions: from chemistry to mechanics

We provide a brief review of atomistic modeling techniques used for the studies reported in this article. The behavior of molecules is intimately linked to the interactions of atoms, which are governed by the laws of quantum chemistry. In metals, for example, bonding is primarily nondirectional, and can be characterized by positive ions embedded in a gas of electrons. Other materials show much greater chemical complexity, often featuring many different chemical bonds with varying strength.

In biological materials it is vital to consider the interplay of chemical interactions that include (ordered by their approximate strength): covalent bonds (due to overlap of electron orbitals); electrostatic interactions (Coulombic interactions); hydrogen bonds; and weak or dispersive van der Waals (vdW) interactions. We note that electrostatic interactions can be significantly weakened by screening due to electrolytes, which can lead to interactions that are weaker than vdW interactions [Feig and Brooks 2004].

In proteins covalent interactions are primarily responsible for the chemistry within the polypeptide amino acid chains. The three-dimensional folded structure is stabilized by a combination of hydrogen bonding, dispersive interactions and electrostatic interactions. In addition to the weak interactions, the structure of proteins is sometimes stabilized by covalent cross-links, such as disulfide bridges between different amino acids as they can be formed between two cysteine (CYS) residues. Even though some of these interactions are relatively weak (up to 1,000 times weaker than covalent bonding), they play an overarching in stabilizing many biological molecules.

**3.1.** *Atomistic model: classical nonreactive force fields.* Our basic modeling approach is based on the classical force field CHARMM [MacKerell et al. 1998], implemented in the MD program NAMD [Nelson et al. 1996]. The CHARMM force field is widely used in the protein and biophysics community, and provides a reasonably accurate description of proteins. Other popular examples are the AMBER force field [Wang et al. 2001] and the DREIDING force field [Mayo et al. 1990]. Force fields of this type are

typically based on harmonic and anharmonic terms describing covalent interactions, in addition to long-range contributions describing van der Waals (vdW) interactions, electrostatic (Coulomb) interactions, as well as hydrogen bonding. Water molecules are described using the TIP3 water model [Wang et al. 2001].

Since the bonds between atoms are modeled by harmonic springs or its variations, bonds between atoms cannot be broken, and new bonds cannot be formed. Moreover, the charges are fixed and cannot change, and the equilibrium angles do not change depending on stretch. For example, the energy penalty due to stretching of a bond $r_{ij}$ between atoms $i$ and $j$ is given by a harmonic function

$$\varphi(r_{ij}) = \tfrac{1}{2} k_t (r_{ij} - r_0)^2. \tag{4}$$

The harmonic approximation leads to a linear dependence of the stretching force and distance, $F(r_{ij}) \sim k_t r_{ij}$. While such a description is certainly appropriate for small deformation from the equilibrium bond length $r_0$, it fails to describe the correct energy-distance relationship for large deformation (we emphasize that $k_t$ in Equation (4) is not a function of deformation as in the general formulation provided in Equation (3)). Clearly, this is an unrealistic description for the behavior of biological molecules under large stretch.

Typical time steps in nonreactive force fields are chosen to be $\Delta t = 1$ fs. Thus, by carrying out $10^6$-$10^7$ steps one can reach time scales of several nanoseconds.

**3.2.** *Reactive force fields.*  So far, all attempts have failed to accurately describe the transition energies during chemical reactions using more empirical descriptions than relying on purely quantum mechanical (QM) methods [Papamokos and Demetropoulos 2004] (see also Figure 3).

Reactive force fields [Stuart et al. 2000; van Duin et al. 2001; Brenner et al. 2002] represent a new strategy to overcome some of the limitations classical force fields, in particular the fact that these descriptions are not able to describe chemical reactions. In fact, the behavior of chemical bonds at large stretch has major implications on the mechanical response, as it translates into the properties of molecules at large-strain, a phenomenon referred to nonlinear elasticity or hyperelasticity [Buehler et al. 2003; Buehler and Gao 2006a].

Reactive potentials are based on a more sophisticated formulation than most nonreactive potentials. A bond-length to bond-order relationship is used to obtain smooth transition from nonbonded to single, double, and triple bonded systems. All connectivity-dependent interactions (that is, valence and torsion angles) are formulated to be bond-order dependent. This ensures that their energy contributions disappear upon bond dissociation so that no energy discontinuities appear during reactions. The reactive potential also features nonbonded interactions (shielded van der Waals and shielded Coulomb).

Several flavors of reactive potentials have been proposed in recent years [Stuart et al. 2000; van Duin et al. 2001; Brenner et al. 2002; van Duin et al. 2003]. Reactive potentials can overcome the limitations of empirical force fields and enable large-scale simulations of thousands of atoms with quantum mechanics accuracy. The reactive potentials, originally only developed for hydrocarbons [Stuart et al. 2000; van Duin et al. 2001; Brenner et al. 2002], have been extended recently to cover a wide range of materials, including metals, semiconductors and organic chemistry in biological systems such as proteins [van Duin et al. 2003; Strachan et al. 2003; Nielson et al. 2005; Han et al. 2005; Chenoweth et al. 2005; Strachan et al. 2005; Cheung et al. 2005]. Here we use the ReaxFF formulation [van Duin et al. 2001]. We employ

a particular flavor of the ReaxFF potentials as suggested in [van Duin et al. 2001; Strachan et al. 2005], with slight modifications to include additional QM data suitable for protein modeling [Datta et al. 2005].

Key features of the ReaxFF reactive force fields are [van Duin et al. 2001; van Duin et al. 2003; Strachan et al. 2003; Nielson et al. 2005; Strachan et al. 2005; Chenoweth et al. 2005]:

- a bond-length/bond-order relationship is used to obtain smooth transition (Pauling) from nonbonded to single, double, and triple bonded systems;

- all connectivity-dependent interactions (that is, valence and torsion angles) are made bond-order dependent to ensure that their energy contributions disappear upon bond dissociation;

- they feature shielded nonbonded interactions that include van der Waals and Coulomb interactions;

- ReaxFF uses a geometry-dependent charge calculation scheme (similar to QEq [Rappe and Goddard 1991]) that accounts for polarization effects;

- most parameters in the formulation have physical meaning, such as corresponding distances for bond-order transitions, atomic charges and others.

The reactive formulation uses a geometry-dependent charge calculation scheme similar to QEq [Rappe and Goddard 1991] that accounts for polarization effects and modeling of charge flow. This is a critical breakthrough leading to a new bridge between QM and empirical force fields. All interactions feature a finite cutoff of $R_{\text{cut}} = 10 \, \text{Å}$.

Since charge equilibration is carried out at every step, the reactive method can also describe flow of charges during deformation processes of the protein. Such information cannot be obtained from nonreactive force fields. It is apparent that such charge flows may be very significant in biological processes, such as enzymatic reactions, or solvent-protein interactions in general. Even though we will not discuss this aspect in detail, it is an important potential of the reactive force field that could be investigated in future studies.

In ReaxFF the total energy of a system is expressed as the sum of different contributions that account for specific chemical interactions. The total energy is given by

$$E_{\text{system}} = E_{\text{bond}} + E_{\text{vdWaals}} + E_{\text{Coulomb}} + E_{\text{val,angle}} + E_{\text{tors}} + E_{\text{over}} + E_{\text{under}} + E_{\text{res}}.$$

The terms $E_{\text{bond}} + E_{\text{vdWaals}} + E_{\text{Coulomb}}$ are two-body contributions, the terms $E_{\text{val,angle}} + E_{\text{tors}}$ are 3-body and 4-body terms, and $E_{\text{over}} + E_{\text{under}}$ correspond to multibody contributions due to the local chemical environment. The term $E_{\text{res}}$ describes energetic contributions of resonance effects.

ReaxFF is based on the concept of bond-orders that dates back to early work by Abell, Tersoff, Brenner and others [Tersoff 1988; Brenner 1990; Stuart et al. 2000; Brenner et al. 2002]. The basic concept of bond-orders is simple to explain. The key idea is to modulate the bond strength based on the atomic environment, taking advantage of some theoretical chemistry principles.

Consider a pair potential in which the total energy of the system is given by the sum over all pairs of atoms (note the factor 1/2 to avoid double counting):

$$U_{\text{total}} = \frac{1}{2} \sum_{\substack{i=1 \\ i \neq j}}^{N} \sum_{j=1}^{N} \varphi(r_{ij}). \tag{5}$$

Instead of writing $\varphi(r_{ij})$ as a harmonic function (see above), in the Abell–Tersoff approach the interaction between two atoms is expressed as $\varphi(r_{ij}) = \varphi_R(r_{ij}) - M_{ij}\varphi_A(r_{ij})$, where $\varphi_R(r_{ij})$ and $\varphi_A(r_{ij})$ are pair repulsive and attractive interactions, respectively. The parameter $M_{ij}$ that multiplies the attractive interactions represents a many-body interaction parameter. This parameter describes how strong the attraction is for a particular bond, from atom $i$ to atom $j$. Most importantly, the parameter $M_{ij}$ can range from zero to one, and describes how strong this particular bond is, depending on the environment of atom $i$. It can thus be considered a normalized bond-order, following the concept of the Pauling relationship between bond-length and bond-order. Abell suggested that

$$M_{ij} \sim Z^{-\delta}, \tag{6}$$

where $\delta$ depends on the particular system, and $Z$ is the coordination number of atom $i$ that depends on the bond radius.

Equations (5) and (6) immediately lead to a relationship between bond-length, binding energy and coordination, through the parameter $M_{ij}$. The modulation of the bond strength effectively leads to a change in spring constant as a function of bond environment, $k(r) \sim k_0 M(Z, \delta)$. Note that $k_0$ is a reference spring constant, which is modulated by the atomic environment that is essentially dependent on the bond radius. This method has been very successful in describing the interatomic bonding in several materials, for example the C-C bonds in diamond, graphite and even hydrocarbon molecules. It is also the basis for the ReaxFF force field.

The concept of the bond-length/bond-order dependence used in the reactive force field ReaxFF is shown schematically in Figure 4. Table 2 shows a systematic comparison between reactive and nonreactive force fields.

We note that the coordination number is a concept widely used in lattice systems, for example crystals. In organic molecules, the coordination number can be thought of as the amount of covalent bonds that an atom has made.

We refer the reader to specific publications for the derivation and development of reactive force fields [van Duin et al. 2001; van Duin et al. 2003; Strachan et al. 2003; Chenoweth et al. 2005; Strachan et al. 2005; Cheung et al. 2005]. In the remainder of this paper, we focus on the application of this method to describe large-deformation behavior of proteins.

Due to the increased complexities of force field expressions and the charge equilibration step that is carried out at each force calculation, reactive force fields are between 50 and 100 times more expensive than nonreactive force fields, yet several orders of magnitude faster than DFT-level calculations that would be able to describe bond rupture as well.

Typical time steps in reactive force fields are chosen to be $\Delta t = 0.25$ fs. Thus, by carrying out $10^6$-$10^7$ steps, one can reach time scales of approximately one to two nanoseconds. However, since each step of force calculation is significantly more expensive in reactive force fields than in nonreactive formulations, we can typically only reach time scales less than tens picoseconds, leading to large strain rates. This represents a significant limitation of this method that could be overcome, for instance, by parallelization or development of faster algorithms.

The large strain rates and large forces applied to the protein may induce deformation mechanisms that are different from those that would be seen at slower strain rates of $\mu$m/sec, as may, for example, be
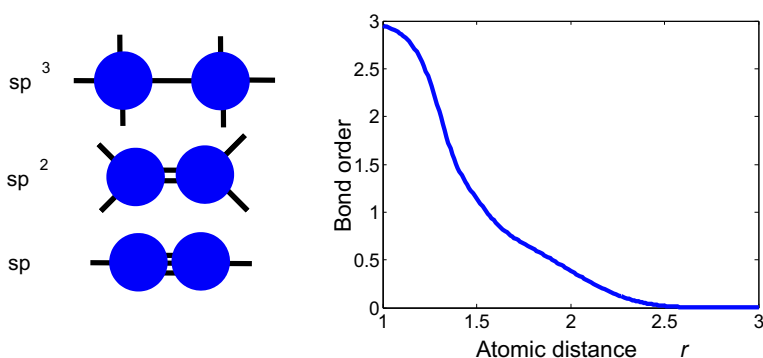
**Figure 4.** This plot illustrates the concept of bond-orders, here in an example for a C-C bond. Depending on the distance between atoms, different bond-orders are obtained through a bond-order mapping function. This enables us to distinguish different quantum chemical states such as $sp^3$ (single bond), $sp^2$ (double bond) and sp (triple bond). The continuous change of bond-orders as a function of distance ensures that reactive force fields are energy continuous, which is critical to carrying out constant energy simulations. At large distances the bond-order vanishes indicating breaking of the covalent bond. In ReaxFF the spring constant that characterizes the strength of atomic bonding is modulated by the bond order leading to vanishing bond strength or dissociation at large stretch.

|  | Nonreactive FFs | Reactive FFs |
|---|---|---|
| Ground state energies (for example, distinguish sp3-sp2-sp...) | Yes (few states) | Yes |
| Excited / transition states (go from one to another ground state; see also Figure 4) | No | Yes |
| Breaking of bonds and continuous energies during reactions | No (sometimes: Morse functions for bond breaking but energetics are often wrong) | Yes |
| Formation of bonds | No | Yes |
| Charge flow during reactions | No | Yes |
| Organo-Inorganic interfaces (or between other materials) | No (mostly) | Yes (bridging FFs) |
| Retyping necessary after reaction | Yes (have C_2,C_3 etc. for different hybridization [Mayo et al. 1990]) | No (atom types are element types [van Duin et al. 2001]) |
| Accessible time scales | Several ns on single CPU easily reached | Typically < ns for single CPU simulation |

**Table 2.** Distinctions between reactive and nonreactive force fields.

used in experiment [Balsera et al. 1997; Rief et al. 1997; Lu et al. 1998; Arteca 2003]. We leave a more systematic investigation of these phenomena to future work.

Even though many biological processes are controlled by the interplay of weak interactions, there exist several examples of material deformation during which fracture of covalent bonds is critical. Specific examples include fracture of bone during which cross-links in the collagen phase or cross-links between hydroxyapatite and collagen may rupture, fracture of cross-links in biopolymers such as highly cross-linked or aged collagen, or large deformation of elastin networks that contain a large number of disulfide bonds [Landis et al. 2002; Nalla et al. 2003; 2005; Ritchie et al. 2004; Gupta et al. 2004; 2005; Peterlik et al. 2006]. Even though the applied stress may be moderate, stress concentrations at, for example, locations of cracks or flaws in the material [Anderson 1991] may induce forces large enough to lead to rupture of covalent bonds.

**3.3.** *Molecular simulation procedure.* The atomic structure of many proteins has been determined according to X-ray diffraction data obtained by experiment. Atomistic structures can often be taken directly from the Protein Data Bank (PDB) and provide reasonably starting structures for atomistic simulation. Typically, charges of atoms and the locations of hydrogen atoms are not included. To add hydrogen atoms and water molecules, and to assign atomic partial charges, we use the *psfgen* program that is part of the NAMD molecular simulation package. The charges of each atom are assigned according to the CHARMM rules, while hydrogen atoms and the protonation states of individual amino acids are assigned according to pH 7. The CHARMM input files (structure and topology files) are then used to perform NAMD calculations. In addition to crystallographic water, we add a skin of water of a few Å surrounding each tropocollagen molecule.

We note that even though the entire molecule is embedded in water at the beginning of the simulation, under large deformation of the molecule, water begins to cluster around certain regions in the protein, leaving other regions exposed to vacuum. Since hydrophobic side chains are typically buried in aqueous environment, charged side chains tend to come together in vacuum, which can induce additional unfolding paths. The effect of these processes on the unfolding dynamics are hard to predict and represent a potential source of error, and need to be considered with caution. A possible remedy to this situation could be using much larger water skins, for example, periodic boxes whose space is completely filled with water molecules. Such models are, however, prohibited with today's computational resources, in particular when reactive force fields are employed.

For reactive calculation, no information about the chemical bonding is necessary, so that the only input parameters are chemical element atom types (C, N, S, H, ...) and the coordinates of all atoms in the system (see also comparison between reactive and nonreactive force fields in Table 2).

Before finite temperature dynamical calculations are performed, we carry out an energy minimization for several thousand steps, making sure that convergence is achieved, thus relieving any potential overlap in vdW interactions after adding hydrogen atoms. In the second step, we anneal the molecule after heating it up to a temperature $T = 300$ K. The heat up rate is $\Delta T = 25$ K every 25 steps, and we keep the temperature fixed after the final temperature $T = 300$ K is achieved (then we apply a temperature control in an NVT ensemble [Leach 2001]). We also ensure that the energy remains constant after the annealing procedure.

For stretching calculations, we typically fix one end of the molecules and apply a force at the other end of the molecule using a method called Steered Molecular Dynamics (SMD). SMD is based on the concept of adding restraint force to groups of atoms by extending the Hamiltonian by an additional restraint potential of the form $k_{SMD}(r - r_\lambda)^2/2$. The SMD approach is implemented in both ReaxFF and NAMD [Nelson et al. 1996; Phillips et al. 2005]. Unless indicated otherwise, we use an SMD scheme with spring constant $k_{SMD} = 10\,\text{kcal/mol/Å}^2$.

While the force is increased, we investigate the response of the molecule due to the applied loading. Typically, we obtain force-versus-displacement data, which is then used to extract the bending stiffness, using continuum mechanical concepts by drawing analogies between the molecular level and continuum mechanical theories [Buehler 2006a; 2006d].

We note that in this paper we typically present simulations only at a single deformation rate, and – due to the higher computational expenses of reactive force fields – at rather short time scales at fractions of nanoseconds. Future studies should focus on a more careful investigation of the rate dependence of the results. This is particularly critical in order to compare the results with experiments. Results of different loading rates could be extrapolated to rates comparable to experimental efforts.

## 4. Computational results

Our focus is to investigate the relationship between protein structure and its mechanical properties. Our strategy is to focus on three protein structures with increasing complexity, involving alpha helices, random coils and beta sheets.

These model systems include alpha-helical (AH) structure, a small protein $\alpha$-conotoxin PnIB from *conus pennaceus*, and lysozyme, a well-studied enzyme that catalyzes breaking of glycosidic bonds. Table 3 summarizes the most significant structural features of these three proteins. Figure 5 shows an overview of the three protein structures considered. This figure illustrates the increase in complexity and distinct structural features in the three proteins studied.

|  | 1GK7 (alpha helix) | 1AKG (conotoxin PnIB) | 194L (lysozyme) |
|---|---|---|---|
| Alpha helices | Yes | Yes | Yes |
| Random coils | — | Yes | Yes |
| Beta-sheets | — | — | Yes |
| Disulfide cross-links | — | Yes | Yes |
| Function: physiological or general | Structural protein | Antagonist | Enzyme |

**Table 3.** Summary of the most significant structural features of the three proteins in this article.

**4.1. *Stretching and bending of a single alpha-helical protein.*** First, we study the elastic, plastic and fracture behavior of a small AH motif. AH motifs constitute the molecular building blocks of coiled structural motifs. We consider a recently crystallized AH protein with PDB ID 1GK7 [Strelkov et al. 2002]. This protein is part of the human vimentin coil 1A fragment with 38 residues that belongs to
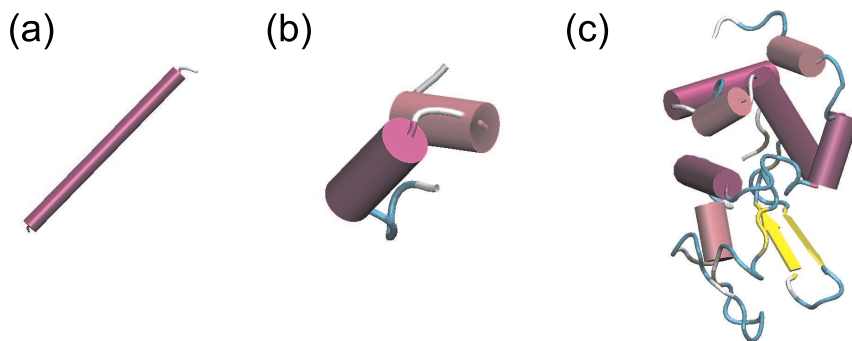
**Figure 5.** Overview over the three protein structures studied in this article. Subplot (a) shows a simple alpha-helical structure (PDB ID 1GK7) [Strelkov et al. 2002], subplot (b) depicts a small protein *α*-conotoxin PnIB from *conus pennaceus* (PDB ID 1AKG) [Fainzilber et al. 1994] and subplot (c) depicts the protein lysozyme, an enzyme that catalyzes cleaving glycosidic bonds (PDB ID 194L) [Vaney et al. 1996]. This sequence of structures is chosen since it represents a systematic increase in complexity of the folded arrangement and existence of structural motifs (alpha helices are drawn as cylinders, random coils as thin curved lines, and beta shears are drawn as yellow arrows). The pure alpha helical structure represents a class of coiled-coil proteins (subplot (a)). Additional polypeptide motifs and covalent cross-links are added in the structure of 1AKG (subplot (b)). Lysozyme (subplot (c)) represents the most complex structure, which features beta sheets, alpha helices, random coils and covalent cross-links.

the intermediate filament family of proteins. The intermediate filaments together with microtubules and actin microfilaments constitute the cytoskeleton, the structural backbone of eukaryotic cells. Vimentin filaments are an important structural feature of eukaryotic cell, serving as cross-links between microtubules and actin filaments, and thus these filaments are subject to severe mechanical loading under physiological conditions of cells, serving as its *safety belt* [Alberts et al. 2002]. The sequence of the protein considered here is GLY SER ASN GLU LYS VAL GLU LEU GLN GLU LEU ASN ASP ARG PHE ALA ASN TYR ILE ASP LYS VAL ARG PHE LEU GLU GLN GLN ASN LYS ILE LEU LEU ALA GLU LEU GLU GLN LEU.

Earlier studies [Arteca and Li 2004; Li and Arteca 2005; Ortiz et al. 2005; Contera et al. 2005] of the response of AH structures to mechanical loading were carried out using nonreactive force fields, with force levels below the critical load that leads to molecular fracture. Some studies were carried out using rather short sequences of AH structures composed of 10 and 20 residues [Li and Arteca 2005], using a soft steered MD approach (SSMD) that allows for a more gentle force application to molecules by redistributing internal energy during pulling [Arteca 2003]. Other molecular simulations were carried out using a coarse grained representation of the helical structure, using a Lennard–Jones model [Cieplak et al. 2002]. Here we focus particularly on the large-deformation regime of such AH structures, including molecular rupture, using a longer sequence of AH structure composed of 39 residues and having a total length of 58 Å.

Our computational experiments are designed to resemble an AFM or optical tweezers experiment, where a continuously increasing force is applied at the ends of the molecule, while the end-to-end distance is measured. This results in force-displacement data that provides information about the mechanical properties. A structural analysis of the protein during deformation enables insight into the atomistic and molecular deformation mechanisms. This computational experiment is realized by using a steered MD scheme, with a thin layer of water surrounding the molecule to represent realistic solvent conditions. The forces are applied at the $C_\alpha$ atom at the first (N-terminus) and last (C-terminus) residue of the AH structure.

Figure 6 depicts the entire force-stretching response of a single AH protein, for a loading rate of 0.0005 Å/iteration. The loading case is depicted in Figure 6a. The results shown in Figure 6b indicate that there are three different deformation regimes, resulting in a strongly nonlinear mechanical response. The first regime is characterized by a relatively strong increase of the force with respect to strain, up to approximately 19% strain or stretch or 10 Å (point A in Figure 6). This regime corresponds to the initial stretching of the intact helical structure.

This initial regime is followed by a plateau-like behavior (between points A and B), during which we observe uncoiling of the helical arrangements, leading to an almost straight polypeptide chain at approximately 129% strain or 75 Å (point B in Figure 6), while the applied force increases only slightly with increased end-to-end distance. This unfolding regime is primarily controlled by continuous *breaking* of H-bonds that provide structural integrity of the AH motif.

Once the helical structure is lost, covalent bonds in the protein backbone are being stretched, leading to a sharp increase of the force with respect to strain, at point C. The molecule fractures at approximately 163% strain or approximately 95 Å, at a maximum force close to 7.8 nN.

Snapshots of the entire deformation process are shown in Figure 7, using a cartoon representation that visualizes the AH structure. The visual representation clearly illustrates breakdown of the AH structure, leading to a flat polypeptide structure at large deformation. Eventually, molecular rupture occurs at large values of force.

The force-stretch information can be used to extract a local, in terms of strain or stretch, Young's modulus $E(L)$, which is given by

$$E(L) = \frac{L_0}{A_C} \frac{\partial F(L)}{\partial L}. \tag{7}$$

In Equation (7), the parameter $L_0$ is the initial, undeformed length of the AH molecule, where $L_0 \approx 58$ Å. Note that Young's modulus is independent of the length $L_0$ of the molecule. The definition in Equation (7) is a consequence of the fact that the stretching force is expressed as a function of stretch $d$ rather than strain ($\sigma = E\varepsilon$ and note that $\varepsilon = (L - L_0)/L_0$).

With $A_C = \pi R_C^2$ and $R_C \approx 7.27$ Å, where the value of $R_C$ is based on an estimate of the cross-sectional distance between the ends of AH side chains across the diameter of the molecule, Young's modulus for deformations up to approximately 18% is approximately 5 GPa. The secant modulus up to point B is approximately 0.8 GPa. The tangent modulus under large deformation (beyond point B up to fracture at point C) is approximately 9.2 GPa. If an additional layer of water molecules surrounding the AH molecule is considered, the effective cross-sectional area increases (the two method to approximate the cross-sectional area of the molecule are shown in the inlay of Figure 7). In this case, $R_C \approx 10.27$ Å, and Young's modulus for small deformation is given by 2.5 GPa, the secant modulus is approximately
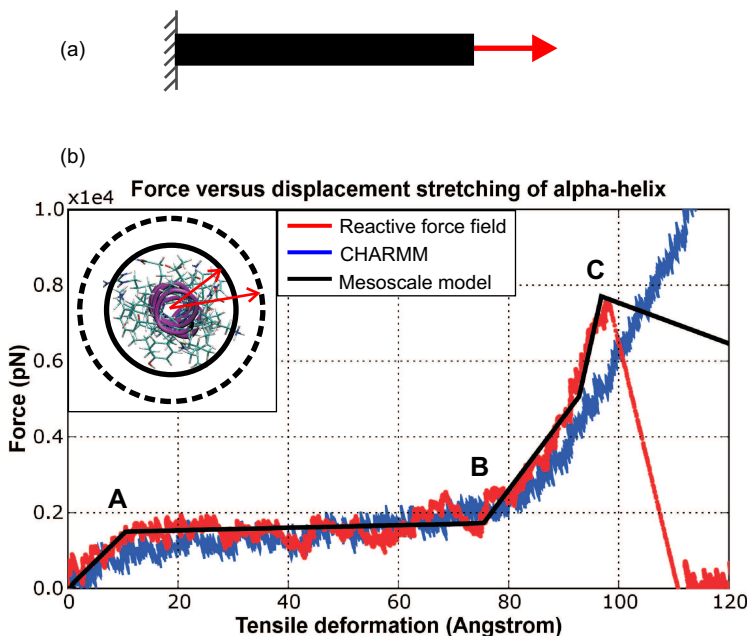
(a)

(b)



**Figure 6.** Stretching of a single alpha-helix with approximately 5.8 nm length, compar-
ing reactive and nonreactive force fields. Both models yield similar force-displacement
curves for small deformation. For large deformation, however, the two models disagree.
The reactive model predicts a fracture strength of approximately 7,800 pN, at approxi-
mately 172% strain. The deformation behavior at strains below 75 Å is characterized by
a homogeneous uncoiling of the helical structure. The initial uncoiling regime is accom-
panied by a slowly increasing force that approaches approximately 2,000 pN. Once the
entire molecule has lost the helical structure, the forces increase significantly until the
molecule fractures. The inlay depicts a view into the molecular axis of the AH protein,
illustrating our method to estimate the cross-sectional area of the molecule. The dashed
circle corresponds to the size estimate considering a thin layer of water molecules as part
of the molecular cross-sectional area. The pulling simulation was carried out over a time
scale of $6.8 \times 10^{-11}$ seconds.

0.4 GPa, and the large-deformation tangent modulus is 4.6 GPa. The fracture tensile stress of the AH
protein is approximately 4.8 GPa. If only the helical core is considered, $R_C \approx 3.64$ Å, and Young's
modulus for small deformation is given by 20 GPa, the secant modulus is approximately 1.6 GPa, and
the large-deformation tangent modulus is 18.4 GPa.

Figure 7 also includes the results obtained using a nonreactive (CHARMM) force field denoted by
a red curve. The prediction by CHARMM is similar to the result obtained using the reactive force
field, albeit forces are slightly smaller than those obtained in the reactive calculation. However, the two
descriptions disagree for large deflections from the initial length, with the most significant difference
being the continuous increase in force even for forces that approach 10 nN and more. This result suggests
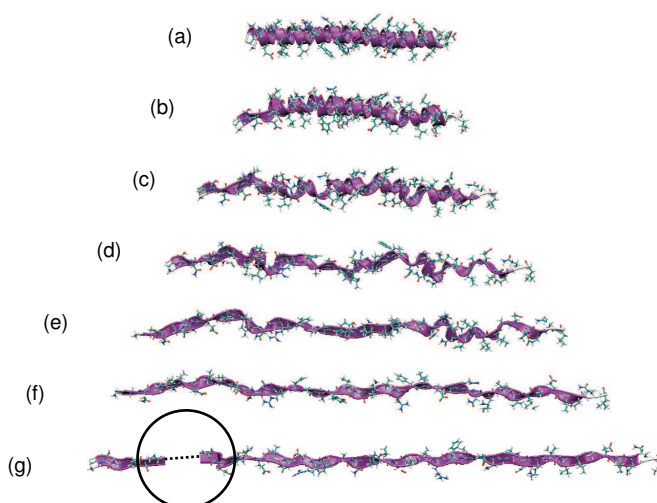
**Figure 7.** Unfolding of an alpha-helix, due to mechanical stimulation along the axial direction. The initial deformation behavior is characterized by homogeneous stretching of the alpha-helical structure (up to point A in Figure 4), followed by continuous uncoiling of the helical structure (between points A and B in Figure 4)). Once the entire molecule has lost the helical structure (see point B in Figure 4), the forces increase significantly until the molecule fractures (see point C in Figure 4). A snapshot right after fracture has occurred is shown in subplot (g). To make the alpha-helical structure (and its disappearance) better visible, we render it using VMD's *Ribbons* method.

that such models are incapable of correctly describing the molecular fracture mechanics of biological molecules.

The total simulation time for the stretching calculation is $6.8 \times 10^{-11}$ seconds. The resulting high strain rates may introduce artificial effects, as the molecule may not be in equilibrium at all times during deformation. However, our results are nevertheless in qualitative agreement with earlier simulation work using nonreactive force fields, as well as experimental efforts [Schwaiger et al. 2002; Akkermans and Warren 2004; Fudge and Gosline 2004; Li and Arteca 2005; Root et al. 2006; Kiss et al. 2006].

Figure 8 shows the results of a bending calculation. Subplot (a) depicts the loading case of a double supported three-point bending test. Figure 8b shows the force versus bending displacement, obtained using the CHARMM force field. The data shown in Figure 8b is collected in a regime where the molecule undergoes pure bending.

The bending simulation is carried out using the identical SMD technique, but using a different spring constant and a much lower strain rate. The loading rate used for this simulation is 0.000002 Å/iteration, with $k_{SMD} = 0.01$ kcal/mol/Å$^2$. These choices reflect the fact that the molecule is much softer under bending than under tension.

This study leads to force information about $F_{\text{appl}}$ versus bending displacement $d$. This information can be used to estimate the bending stiffness, for the case of a double supported beam with a bending
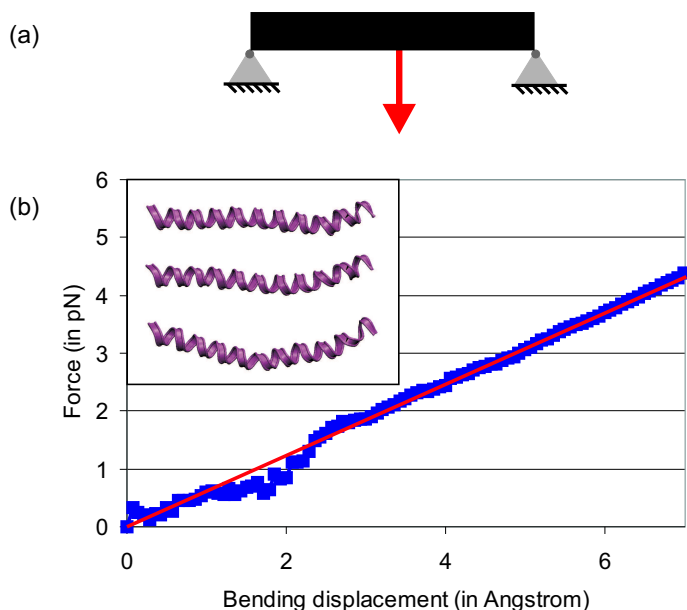
**Figure 8.** Bending of a single alpha-helix with approximately $L \approx 5.8$ nm length. Subplot (a) shows the loading case, and subplot (b) depicts the force increase versus the bending displacement increase. The red line is a linear fit to the data, whose slope is used to determine the bending stiffness according to Equation (8) (the ratio $F/d$ corresponds to the slope measured from atomistic simulation results). The inlay shows a few snapshot as the AH protein undergoes bending deformation. The initial force-displacement regime is slightly noisier. We believe that this is due to thermal fluctuations that disappear once the molecule is under increased tensile load due to the bending.

force applied in the center of the molecule:

$$EI = \frac{F_{\text{appl}}L^3}{48d}. \tag{8}$$

Assuming that the AH protein can be represented by a continuum beam, the resulting bending stiffness of this molecule is $2.27 \times 10^{-29}$ Nm$^2$. This atomistic result is a key input parameter for the development of the mesoscale representation (see Section 5.1). Using the bending stiffness, we estimate the persistence length of the AH protein (at $T = 300$ K) to approximately be 5.5 nm. This result agrees somewhat with experimental studies that found a persistence length of a AH structure on the order of 1-2 nm [Papadopoulos et al. 2006]. The reason for this disagreement could, for example, be rate effects.

We note that the observation that the AH structure vanishes under large deformation is not contracting Astbury's X-ray diffraction based observations in the 1930s that the structure of such proteins changes significantly under stretch [Astbury and Street 1932].

**4.2.** *Unfolding dynamics of globular, cross-linked proteins: 1AKG.* The protein studied in the previous example has a relatively simple structure, consisting of only one alpha helix. Now we consider a protein
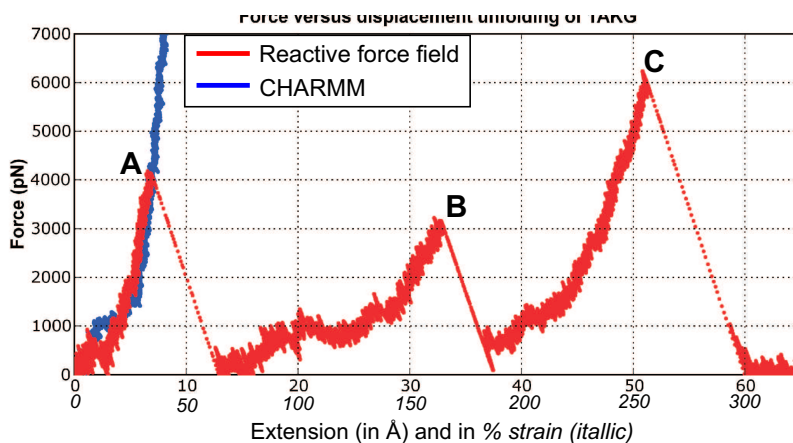
**Figure 9.** Mechanically stimulated unfolding of a small protein PnIB 1AKG, modeling results obtained using CHARMM (red curve) and the reactive force field ReaxFF (blue curve). We apply a slowly increasing force at the N- and C-terminus of the polypeptide. It is apparent that although the ReaxFF and CHARMM descriptions agree for small deformation (below $\approx 7\,\text{Å}$), they disagree strongly for larger deformation. The difference can be explained based on the fact that the CHARMM potential is incapable of describing breaking of the disulfide bonds. The points A–C characterize different stages of deformation; A and B correspond to breaking of the two disulfide bonds, with lower force for the second one. Point C characterizes breaking of the backbone chain. The strength of the backbone chain is slightly larger than the disulfide bonds. The characteristic saw tooth shape is reminiscent of experimental results. However, experiment is somewhat limited with respect to the force levels that can be reached, which makes it difficult to study breaking of strong covalent bonds. The pulling simulation was carried out over a time scale of $2 \times 10^{-11}$ seconds.

that has a slightly more complex structure. We consider a small protein $\alpha$-conotoxin PnIB from a cone-shell species *conus pennaceus* that appears primarily in the Indian Ocean. This protein is an extracellular protein that serves as acetylcholine receptor antagonist. It consists of 16 residues that resemble two distinct building blocks, alpha helices and random coils, which are connected by disulfide cross-links formed at the CYS residue. This protein has recently been crystallized and deposited in the PDB with ID 1AKG [Fainzilber et al. 1994]; the structure is shown in Figure 5b.

To simulate the mechanical stimulated unfolding of the protein, we apply a slowly increasing force at the N-terminus (beginning of the polypeptide chain, in this example the GLY1 residue) and C-terminus of the protein (end of the polypeptide chain, in this example the CYS16 residue).

Figure 9 shows the force-displacement curve during mechanical unfolding of this protein, comparing the predictions made by the CHARMM force field and ReaxFF. Individual rupture events of covalent bonds can be associated with peaks in the force-displacement curve, leading to a characteristic sawtooth shape. The first rupture occurs at approximately 4 nN, and is due to breaking of the disulfide bond between CYS3 and CYS16. The second rupture features a lower rupture force of 3 nN, and is due to
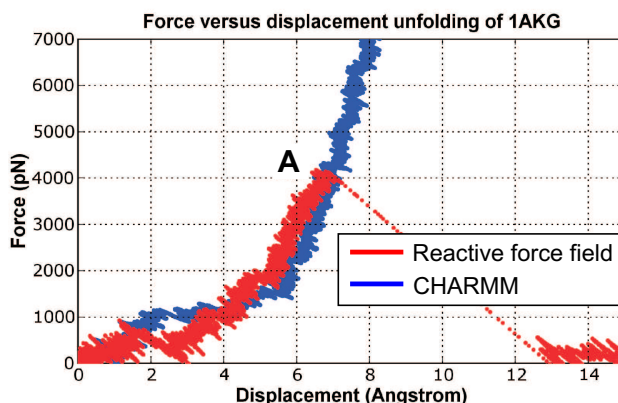
**Figure 10.** Mechanically stimulated unfolding of a small protein PnIB 1AKG. This plot shows a zoom into smaller displacements (same data as shown in the previous figure). It is apparent that although the ReaxFF and CHARMM descriptions agree for small deformation (for displacements below $\approx 17\,\text{Å}$), they disagree strongly for larger deformation, until the first covalent disulfide bond ruptures (*A*).

breaking of the disulfide bond between CYS2 and CYS8. The final rupture of the protein backbone peptide bond occurs at approximately 6 nN, at a larger force than any of the previous breaking events. These results suggest that the disulfide cross-link is weaker than the peptide bond. The total simulation time for the results shown in Figure 9 is $2 \times 10^{-11}$ seconds, which is only a fraction of a nanosecond. As in the previous case, the resulting high strain rates may introduce artificial effects, as the molecule is not in equilibrium at all times during deformation.

Figure 10 shows a more detailed view of this system, focusing in on the small displacements and the first bond rupture event. It is apparent that the reactive force field model and the CHARMM description agree reasonably well for small deformation. The CHARMM model, however, predicts a very different unfolding sequence with forces raising to unrealistically large values. This is an immediate consequence of the nonreactive character of this force field as the forces become arbitrarily large for large bond stretch (see Equation (4)).

Figure 11 depicts several snapshots of the atomic structure as the protein undergoes deformation, for the studies using the reactive force field. Figure 12 depicts a similar sequence of snapshots for the nonreactive CHARMM force field. The sequence of snapshots shown in this figure shows that the covalent cross-links never break, even at large deformation, leading to incorrect prediction of the folding dynamics under large stretch.

From the results shown in Figures 9–12, it is apparent that classical CHARMM-like descriptions are not capable of addressing the various chemical events properly, and lead to incorrect behavior at large deformation. Our results clearly demonstrate the difference between the reactive potential and a classical CHARMM potential in a study of unfolding of a small protein PDB ID 1AKG.

**4.3.** *Unfolding dynamics of a globular, cross-linked protein: lysozyme.* Now we focus on the unfolding mechanics of a more complex protein structure, the enzyme lysozyme. Figure 13 depicts the three-dimensional structure of lysozyme, without (subplot (a)) and with (subplot (b)) the substrate attached.
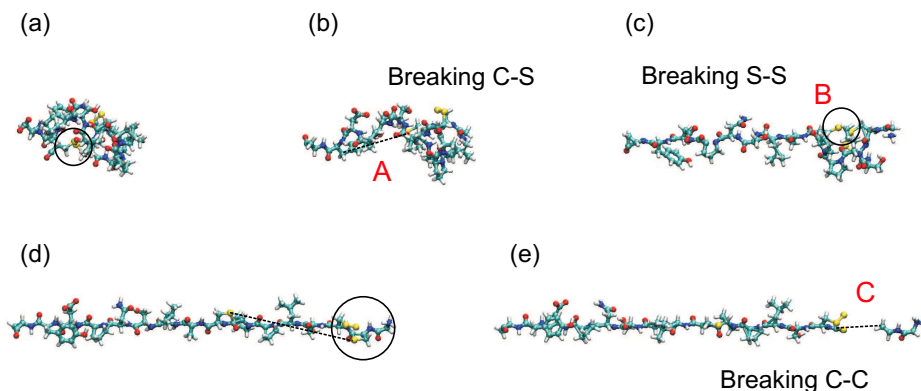
**Figure 11.** Snapshots of mechanically stimulated unfolding of a small protein, simulation carried out using the reactive potential. The plot depicts results obtained using the reactive force field ReaxFF The points A–C represent rupture events and correspond to those shown in Figure 9.
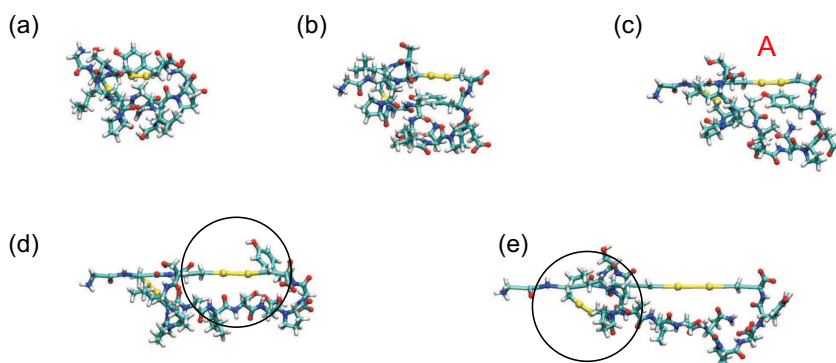


**Figure 12.** Snapshots of mechanically stimulated unfolding of a small protein. Simulation is carried out using the CHARMM potential. It is evident that the disulfide cross-links never rupture (see the disulfide bond indicated with *A* in subplot (c)).

As can be verified in this figure, the substrate binds to the active site of the enzyme. The structure shown in subplot (a) is based on PDB ID 194L [Vaney et al. 1996] (hen egg white lysozyme), and the structure on the right is based on PDB ID 1LJN [Harata and Kanai 2002] (turkey egg lysozyme with a N-acetyl-D-glucosamine substrate). The basis for all calculations discussed subsequently is the crystal structure of lysozyme 194L [Vaney et al. 1996].

Lysozyme represents a more complex structure than those studied in Sections 4.1 and 4.2. In addition to alpha helices and random coils, this protein also contains one beta sheet. Of particular interest to us are the four disulfide cross-links inside the protein, and its participation and influence on the unfolding dynamics of the protein. Lysozyme consists of 129 residues. Disulfide cross-links are present between CYS6 and CYS127, CYS30 and CYS115, CYS64 and CYS80, as well as between CYS76 and CYS94.
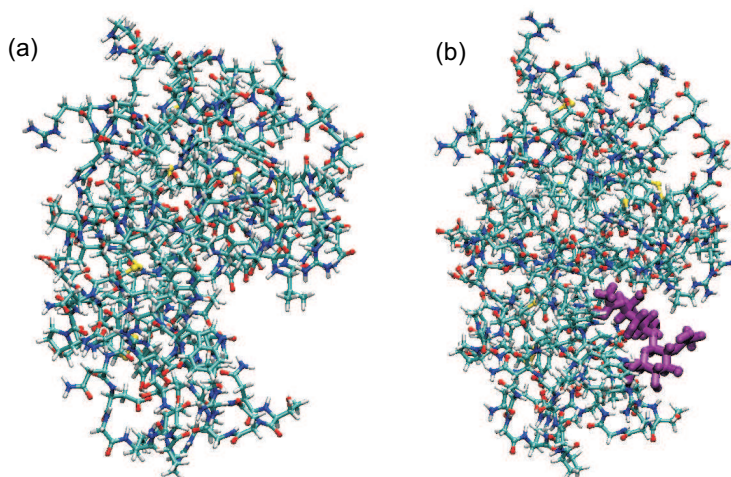
**Figure 13.** This figure depicts the three-dimensional structure of the enzyme lysozyme, without (subplot (a)) and with (subplot (b)) the substrate attached, without showing any water molecules. As can be verified in this figure, the substrate binds to the active site of the enzyme. The structure shown in subplot (a) is based on PDB ID 194L [Vaney et al. 1996] (hen egg white lysozyme), and the structure on the right is based on PDB ID 1LJN [Harata and Kanai 2002] (turkey egg lysozyme with a N-acetyl-D-glucosamine substrate).

Figure 14 depicts the locations of disulfide bonds in lysozyme, where subplot (a) shows a view of the entire protein, and subplot (b) depicts a detailed view on one of the disulfide bonds.

A particular interest of this study is to shed light on the unfolding dynamics such as the sequence of specific unfolding events during deformation [Cieplak et al. 2002].

Figure 15 depicts the force-displacement curve during mechanically stimulated unfolding of lysozyme. The unfolding is induced by applying a slowly increasing force between the N- and C-terminus of the protein, using a steered MD scheme. The force is applied between residues LYS1 and LEU239. The force-displacement scheme indicates two maxima (points A and D) at which the forces approach several nN, corresponding to two cross-link fracture events. The forces during uncoiling of the folded structure is characterized by force levels of approximately 1 nN and 2 nN. We observe a small maximum at approximately 120 Å separation, where the forces reach 2.2 nN.

The initial increase in stretching force is due to breaking of the first covalent disulfide bond (A) at approximately 4.5 nN, followed by its rupture and a regime in which the forces approach an approximately constant value of 1.2 nN (B). This regime is followed by a slight increase to 2.5 nN (C). The second disulfide cross-link breaks at point D, leading to an increase in force similar to that at point A. The first peak (A) is due to breaking of the cross-link between CYS6 and CYS127, and the second peak is due to breaking of the cross-link between CYS30 and CYS115. This result can be explained since these residues are in closest geometric vicinity to the ends of the polypeptide chain, at which the forces are being applied.
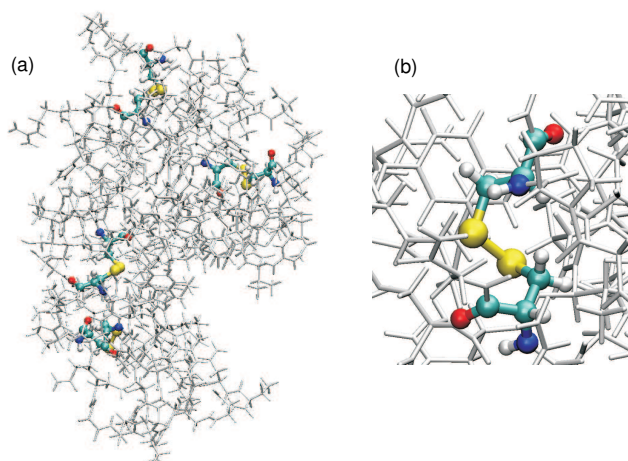
**Figure 14.** Locations of disulfide bonds in lysozyme. Subplot (a) shows a view of the entire protein, highlighting the four disulfide cross-links (in color, and using larger spheres). The substrate binding site can be seen in the lower right part of the protein (similar angular view as that used in Figure 13). Subplot (b) depicts a detailed view on one of the disulfide bonds, including all atoms in the neighboring CYS residues. The yellow atoms are the two sulfur atoms that connect two CYS residues.
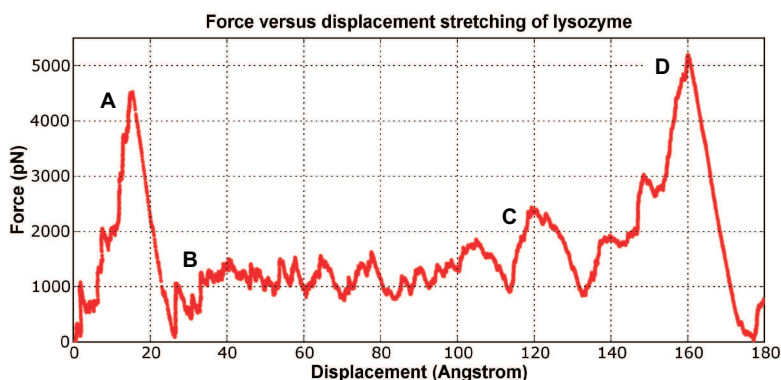


**Figure 15.** Mechanically stimulated unfolding of lysozyme, force versus displacement. The initial increase in stretching force is due to breaking of the first covalent disulfide bond (A) at approximately 4,500 pN, followed by its rupture and a regime in which the forces approach an approximately constant value of 1,200 pN (B). This regime is followed by a slight increase to 2,500 pN (C). The second disulfide cross-link breaks at point D, leading to an increase in force similar to that at point A, but with slightly higher maximum rupture force of approximately 5,200 pN. The first peak (A) is due to breaking of the cross-link between CYS6 and CYS127, and the second peak (D) is due to breaking of the cross-link between residues CYS30 and CYS115. The pulling simulation was carried out over a time scale of $4.5 \times 10^{-11}$ seconds.

Figure 16 depicts snapshots of the different stages during unfolding dynamics of lysozyme. In this simulation, the distance between the ends of the protein (C-alpha atom of the terminal residues) is continuously increased by applying a continuously increasing force. The direction of the force is given by the instantaneous distance vector of the two ends.

The molecular simulation enables us to perform a detailed analysis of the deformation mechanics. We observe that the N-terminus of the protein unfolds first. Once the cross-link that is attached at residues CYS6 and CYS 127 is reached, the force increases significantly due to the resistance of the covalent cross-link (this corresponds to the first peak (A)).

After rupture of the first cross-link, the C-terminus of the protein starts to unfold, and additional unfolding at the N-terminus ceases. This is because the cross-link between residues CYS30 and CYS115 pins this end leading to shutdown of unfolding. Once the C-terminus is pulled so far that the cross-link between CYS30 and CYS115 is reached, the forces increase significantly, leading to uncoiling of the alpha-helical structure that is attached close to the C-terminus. This is confirmed in Figure 16(f-h) by considering the increase of the length of the cylinder that represents the AH structure.

Our simulations reveal that unfolding of lysozyme occurs sequentially, and that peaks that appear in the force-stretch curve are due to sequential breaking of cross-links. Unfolding of this protein is a sequential rather than homogeneous process, as observed in several earlier studies. Smaller force peaks appear when unfolding of domains is observed (see Figure 15, point C).

The key predictions of our reactive simulations are:

- the N-terminus unfolds first, while the C-terminus remains in its folded configuration until the fist disulfide cross-link ruptures;

- large peaks occur at specific end-to-end distances, whenever a covalent cross-link is reached.

## 5. Discussion, conclusion and outlook

The results reported in this article illustrate how reactive force fields can be successfully used to describe the stretching and unfolding dynamics of small proteins, including molecular fracture. Using this computational technique, we have studied the unfolding and stretching dynamics of three proteins with increasing complexity.

Our model provides a reactive treatment of the unfolding problem, considering not only rupture of vdW and H-bonds, but also rupture of covalent bonds. We have demonstrated that in proteins in which disulfide cross links are present, a reactive treatment is essential, and that CHARMM type potentials do not allow a description of the unfolding processes. Including the possibility of bond rupture is essential to describe the unfolding processes correctly, and neglecting such effects may lead to incorrect force-displacement curves as shown in Figures 9 and 10. A nonreactive description may lead to unrealistically large forces and an incomplete unfolding of the protein, even though extremely large forces are applied that exceed several nN.

Our studies show a distinctions in the force-displacement unfolding curves between fibrillar and globular proteins. Whereas stretching a single AH structure suggests a continuous increase of the stretching force with stretching distance followed by molecular rupture, globular proteins feature a sawtooth like force-displacement curve with extremely long unfolding paths, featuring several local maxima that correspond to domain unfolding or cross-link rupture.
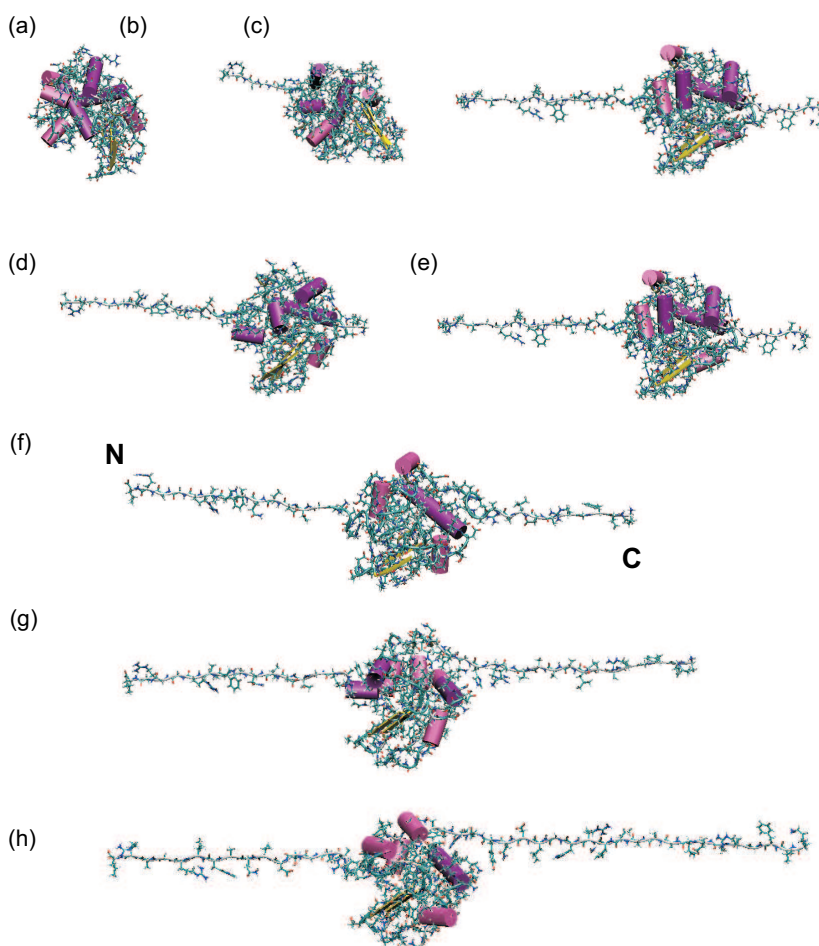
**Figure 16.** Different stages during unfolding dynamics of lysozyme. In this simulation, the distance between the ends of the protein ($C_\alpha$ atom of the terminal residues) is continuously increased by applying a continuously increasing force. The direction of the force is given by the instantaneous distance vector of the two ends. The molecular simulation enables us to perform a detailed analysis of the deformation mechanics. We observe that one end of the protein unfolds first. Once the cross-link that is attached at residue CYS6 is reached, the force increases significantly due to the resistance of the covalent cross-link. After this cross-link is broken and the displacement further increases, the second cross-link is reached (close to residue CYS30) the second end of the protein starts to unfold as well, and the further displacement of the first one ceases. Unfolding of the other end proceeds until another cross-link is reached, which is then followed by significant stretch of the alpha-helical structure that is attached close to the other end. Subplot (h) depicts the configuration slightly before the second covalent cross-link is broken.

Our analysis of unfolding of lysozyme suggests that the activity of the enzyme may be severely impeded if a stretching force is applied at the ends of the polypeptide strand. This is because the binding pocket of the enzyme undergoes a shape change that may make it difficult or impossible to bind the substrate and thus significantly hinder the enzyme's main function to stabilize the transition states of the catalyzed chemical reactions. Our MD modeling further provided an analysis of the temporal sequence of unfolding of different domains, of both lysozyme and the small protein with PDB ID 1AKG.

For both globular proteins studied here (1AKG and 194L), we observe that the force increases rapidly even for modest deformation (see Figures 9 and 15). This may be due a specific molecular design that prevents unfolding of the protein, thus providing additional stability. In both cases, this design objective is realized by placing a covalent cross-link close to the end and the beginning of the polypeptide chain, respectively. The AH protein resembles a different behavior, showing a continuous increase of stress with respect to increasing strain, leading to eventual rupture when the force approaches its maximum. Similar behavior has been reported about the deformation mechanics of individual tropocollagen molecules.

Our reactive studies provide estimates for the fracture strength of an AH protein, including an estimate for Young's modulus and the bending stiffness. Our molecular analyses suggest a persistence length at room temperature of approximately 5.5 nm.

Extreme deformation of structural and functional proteins can be relevant under physiological conditions. Cells, for example, can exert large forces that can exceed several nN. As our studies show, such large force levels can lead to breaking of covalent bonds or other severe deformation with nonlinear elasticity. Thus, sound understanding of the nanomechanical responses of materials may be critical to shed light on associated biological or bioengineering processes. We note that even though cells can exert such large forces, it does not necessarily mean that individual cells sense such large forces. Other critical applications are in fracture of tissue such as bone or skin. Once covalent cross-links are present, covalent bond breaking becomes important under fracture conditions.

Although full atomistic studies provide a fundamental view into the atomistic mechanisms during deformation of matter, it has intrinsic limitations, the most significant of which is related to the high deformation and strain rates, due to the limitations of time scales to several nanoseconds. This may lead to overestimation of the unfolding forces; it has been discussed extensively in earlier work [Balsera et al. 1997; Rief et al. 1997; Lu et al. 1998; Arteca 2003].

**5.1.** *Development of a mesoscale model: entropic elasticity.* To overcome the time- and length-scale limitations, the atomistic simulation results can be used to develop a mesoscale model of the protein structure that features less degrees of freedom, but is capable of capturing the essential physical properties of the molecules. Here we demonstrate how such a model can be applied to the AH protein.

To achieve this, the entire sequence of amino acids that makes up the AH structure is replaced by a collection of beads (see Figure 17a). The beads interact according to a intermolecular multibody potential. The parameters of this bead model are determined from the full atomistic simulation results. Appendix A describes the detailed mathematic formulation of this model. For example, the tensile stiffness parameters are obtained from the stretching calculations. The bending stiffness is obtained from a bending calculation of the single molecule, similar as described in future publications. We leave details about how the parameters are obtained to a future work, and focus on application of this model.
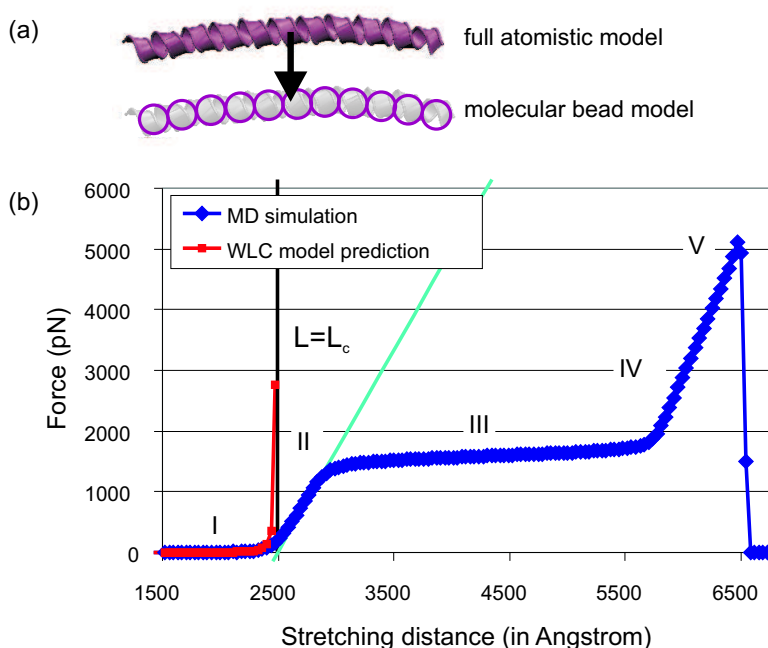
**Figure 17.** Stretching experiment of an alpha helix molecule, with length $L = 249.5\,\text{nm}$, at $300\,\text{K}$, carried out using the mesoscale model. Subplot (a) shows a schematic of the coarse-graining procedure, changing the full atomistic representation arriving at the molecular bead model. Subplot (b) shows the entire force-displacement curve including regime I, entropic elasticity, regime II, energetic elasticity, regime III uncoiling of the AH structure, IV stretching of the backbone bonds, and regime V, molecular fracture. Whereas the WLC model predicts divergence of forces at the contour length, molecular modeling predicts a smooth transition from entropic to energetic elasticity. The plateau regime reached beyond approximately $3{,}000\,\text{Å}$ is due to unfolding of alpha helical structures. The long stretching distances are a consequence of the fact that the molecule is extremely long. Conformations at different stages are shown in Figure 20.

Figure 17b depicts the force-versus stretching curve for this case, showing five regimes: (I) entropic elasticity, (II) energetic elasticity due to homogeneous stretching of the AH structure, (III) uncoiling of the AH structure, (IV) stretching of backbone bonds, followed by (V) molecular rupture. Figure 18 shows a detailed view of the entropic regime, comparing the WLC model given in Equation (2) with the molecular modeling results. Figure 19 depicts several snapshots as the molecule undergoes tensile deformation.

These results show that the mesoscale representation of the molecule is capable of modeling entropic contributions to elasticity, at large time scales reaching several microseconds. Our results confirm the hypothesis that the molecular mechanics is controlled by a transition from entropic to energetic elasticity.

**5.2.** *Hybrid reactive-nonreactive models.* Reactive force fields can be computationally very expensive. In some cases, the region of atoms where a reactive treatment is actually needed is quite localized. A
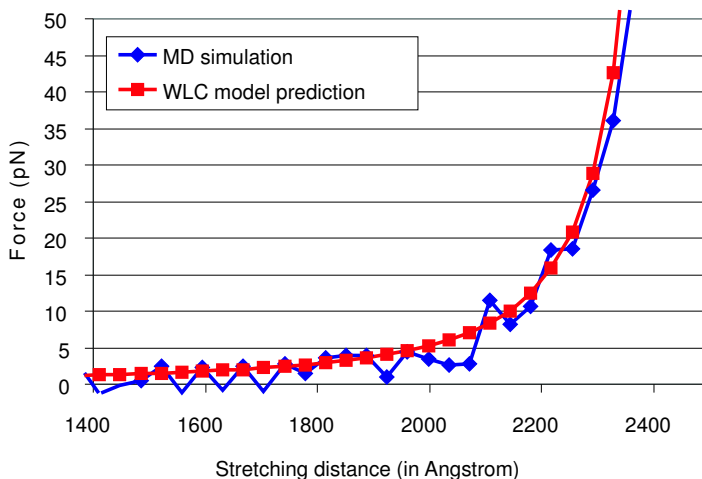
**Figure 18.** This plot shows a zoom into entropic elasticity before the molecule is completely stretched to its contour length, including a quantitative comparison with the WLC model. The contour length is indicated in the plot as a straight line.

prominent example for such a case are enzymes, where reactions are largely limited to the active site where the substrate is attached (see, for example, the substrate binding site shown in Figure 13b) [Wang et al. 2001].

To reduce the computational cost of reactive force fields, we can use a spatial decomposition scheme, similar to the scheme used in QM/MM approaches [Wang et al. 2001; Cui et al. 2002]. These methods, however, have limitations with respect to the number of atoms that can be treated and difficulties associated with terminating quantum mechanical regions and their handshaking to the empirical force field.

As an alternative approach to the QM/MM methods, we suggest a concurrent coupling of ReaxFF [van Duin et al. 2001] and DREIDING [Mayo et al. 1990]. DREIDING is a nonreactive force field similar to CHARMM. The central idea is to use a smooth transition of force contributions along a spatial decomposition, as shown schematically in Figure 20. We have implemented this algorithm in the CMDF framework [Buehler et al. 2006]. The CMDF framework is a simulation framework that is capable of integrating various simulation methods, facilitating multiscale and multiparadigm modeling [Buehler et al. 2005].

Different algorithms can be used to determine the reactive region. Here we have used a simple approach that is based on selection a set of specific atoms that are required to be embedded in a reactive domain. During the simulation, a spherical region surrounds these atoms whose quantum numbers are dynamically updated. Regions of reactive atoms are linked to a nonreactive force field using the concept of mixed Hamiltonians. The reactive region is updated every $N_\Omega$ steps with typical values $N_\Omega = 10$-20.

Figure 20a depicts the concept of handshaking reactive and nonreactive force fields using force mixing, slowing transitioning from one force field to another. The figure depicts the theoretical method of smoothly transitioning from one force field to another. The specific transition is characterized by two
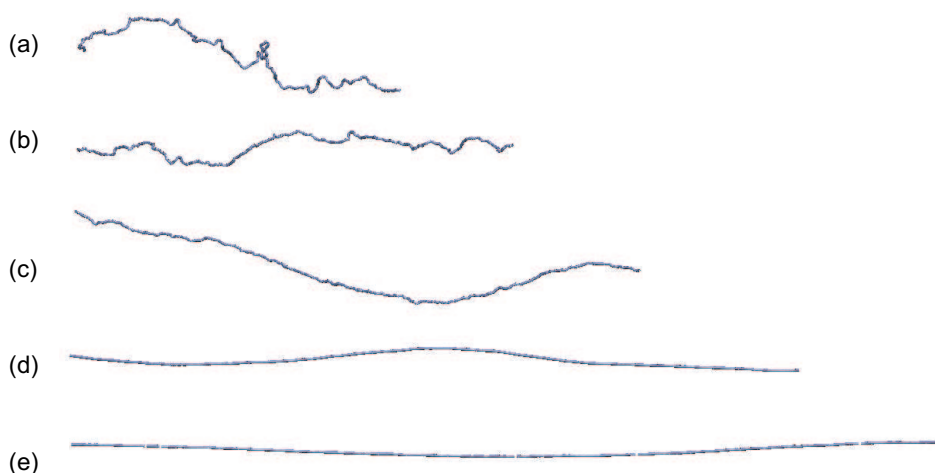
**Figure 19.** Stretching dynamics of a long alpha-helical molecule, with length of 249.5 nm, which is approximately 50 times larger than the persistence length. The plot depicts snapshots that illustrate the transition from entropic elasticity when the molecule is highly convoluted (subplots (a) and (b)) to a regime where the molecule is beginning to be stretched out entirely. The final subplots (d) and (e) correspond to the regime when energetic elasticity starts to govern the elastic behavior. The stretching force is applied using a steered MD algorithm.
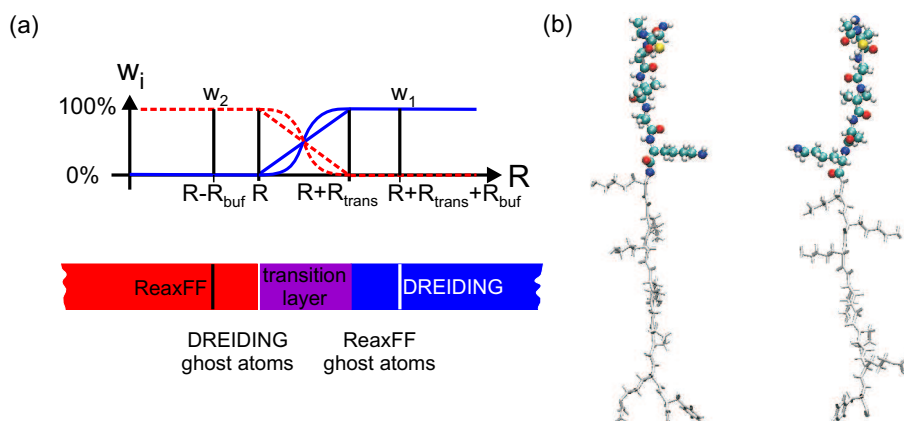


**Figure 20.** Concept of handshaking reactive and nonreactive force fields using force mixing. Subplot (a) depicts the theoretical method of smoothly transitioning from one force field to another, and subplot (b) shows two snapshots of an example calculations of a small polypeptide molecule. The upper end of the molecule is chosen to be reactive. The colored atoms are those that are included in the ReaxFF treatment, including ghost atoms and the atoms in the transition region. The size of the ghost atom region is chosen equal or larger than the cutoff radius the corresponding force field.

parameters, the width of the transition region $R_{\text{trans}}$ and the width of the ghost atom region $R_{\text{buf}}$. While the size of the transition region can be chosen arbitrarily (although ideally, the transition is made very smooth so that energy is conserved), the size of the ghost atom region must be larger than the potential cutoff region, $R_{\text{buf}} > R_{\text{cut}}$. Using a decomposition scheme, each atom is assigned to one or more force engines. This flag determines which atoms are treated by a particular force engine that is available. In addition, each atom features an array weights $w_i$ that determine how much force is included from each force engine. The sum of all weights sum up to one, $\sum w_i = 1$. After each force calculation step with all $N$ force engines, the contributions from each engine (denoted by $\bar{F}_{j,i}$ for atom $j$) is summed up, yielding the resulting force on atom $j$, $\bar{F}_j = \sum \bar{F}_{j,i} w_i$. Here we demonstrate that this combination enables large reactive regions of the system to describe the formation and breakage of bonds as needed, while allowing other regions not participating in the reaction to be treated more efficiently. We illustrate our new hybrid method in a study of stretching of small organic molecules, wave propagation studies and modeling of proton transfer in a small protein. Our results suggest that our hybrid model is a practical tool for certain applications including modeling protein dynamics. The possibility of performing such fast screening of different reaction paths may have a major impact on because it may replace existing QM/MM schemes for some cases. However, our model does not conserve energy if the reactive and nonreactive regions are updated dynamically during the simulation.

Figure 20b shows two snapshots of an example calculations of a small polypeptide molecule, obtained using the approach described above, studying the dynamics of the molecule in equilibrium, at a temperature of 300 K. The upper end of the molecule is chosen to be reactive. The colored atoms are those that are included in the ReaxFF treatment, including ghost atoms and the atoms in the transition region. In our example, we chose $R_{\text{buf}} = 10\,\text{Å}$ and $R_{\text{trans}} = 5\,\text{Å}$. The hybrid model is computationally much more efficient than a pure reactive treatment. We leave further analyses to future publications.

**5.3. *Summary and outlook.*** In this article, we have reported several stretching and unfolding studies of proteins with increasing structural complexity. The results indicate that the secondary and tertiary protein structure has significant effect on the deformation mechanics.

The most important contributions of this paper are:

- to the best of our knowledge, we have reported the first fully reactive treatment of protein molecule mechanics, enabling a coherent description of the intimate links between molecular chemistry and molecular mechanics;

- we have reported large-deformation studies of unfolding and molecular fracture of a AH protein structure, including estimates for Young's modulus as a function of strain and a prediction of its fracture stress, including an atomistic analysis of the bending stiffness of a AH protein;

- we have reported the unfolding dynamics of two proteins, 1AKG and 194L (lysozyme), which illustrates the significance of a reactive treatment in particular when covalent cross-links are present in the molecular structure, showing the significance of such models to describe their nanomechanical properties;

- we have reported development of a mesoscale representation of AH proteins;

- we have described a hybrid reactive-nonreactive model that enables us to perform computationally efficient atomistic reactive calculations.

Restrictions in time and length scales accessible to full atomistic studies indicate that coarse graining techniques (for example, bead models, as discussed in Section 5.1, see Figure 17a) are critical to enable a unified treatment of elastic contributions (for example, the competition between entropic and energetic elasticity, as shown in Figure 17b). Our mesoscale studies predict a smooth transition between these two sources of elasticity as the molecule is stretched shown in Figure 18, where the two extreme cases agree with the predictions by Equations (2) and (3). We emphasize that the bead model can only be as accurate as the input parameters from full atomistic simulation. For example, the high strain rates in MD can induce inaccuracies in the unfolding behavior, thus rendering the corresponding mesoscale model incorrect. This issue can only be addressed by developing more accurate full atomistic methods that can traverse across different time scales. In addition to tensile and bending loading, other loading conditions such as torsional loading or shear of assemblies molecules [Buehler 2006a] could be investigated. Such additional information could also help to render the mesoscale molecular model more accurate.

We further have introduced a hybrid concurrent multiscale model (Section 5.2) that combines reactive and nonreactive force fields using mixed Hamiltonians, which can be an alternative to full reactive studies. An example application of this method is provided in Figure 20.

Our studies could eventually find useful applications in several scientific disciplines. For example, a better understanding of the mechanical response of proteins to mechanical stimulation could lead to advances in the biological sciences. Other applications may be related to provide design suggestions for new biopolymers that could be designed and synthesized based on recombinant DNA technologies [Petka et al. 1998; Tirrell 2002; Langer and Tirrell 2004]. Such new strategies to synthesize materials represent exciting opportunities at the intersections of materials science, biology and chemical engineering. The hybrid reactive-nonreactive modeling scheme could find useful applications in studies and design of enzymes, as it represents an efficient alternative to QM/MM methods [Wang et al. 2001].

Finally, we emphasize that theoretical modeling approaches as discussed in this article are not intended to replace experiment, but rather work hand in hand with experimental efforts to improve our understanding of the complex mechanics of protein materials. We believe that the combination of theory, computer simulation and experiment represents a particularly promising combination to advance the science of deformation and fracture of natural and biological materials.

## Appendix A.  Mathematical formulation of the reactive mesoscale model

We use a reactive mesoscopic model describing alpha helical (AH) molecules as a collection of beads interacting according to interparticle multibody potentials (see Figure 18a). The total energy of the system is given by

$$E = E_T + E_B + E_{\text{weak}}. \tag{A.1}$$

The total energy is given by the sum over all pair-wise and three-body interactions,

$$E_I = \sum_{\text{pairs}} \phi_I(r), \qquad E_B = \sum_{\text{angles}} \phi_B(\varphi). \tag{A.2}$$

The bending energy is

$$\phi_B(\varphi) = \tfrac{1}{2} k_B (\varphi - \varphi_0)^2, \tag{A.3}$$

with $k_B$ relating to the bending stiffness of the molecule. The bending stiffness parameter is given by

$$k_B = \frac{3EI}{2r_0}.$$

The bending stiffness of a AH molecule is obtained from full atomistic simulation (see main text). The mass of each bead is determined by distributing the mass of the entire AH molecule homogeneously into all beads.

We approximate the nonlinear stress-strain behavior under tensile loading by a multilinear model. The multilinear model is a combination of four spring constants $k_T^{(i)}$, which are turned on at specific intervals of molecular stretch. A similar model has been used successfully in earlier studies of fracture [Buehler et al. 2003; Buehler and Gao 2006a], where the function $E_T$ is given by integrating $F_T(r)$ over the radial distance. The force between two particles is

$$F_T(r) = -\frac{\partial \phi_T(r)}{\partial r} = H(r_{\text{break}} - r) \begin{cases} k_T^{(1)}(r - r_0), & r_1 > r, \\ R_1 + k_T^{(2)}(r - r_1), & r_1 \leq r < r_2, \\ R_2 + k_T^{(3)}(r - r_2), & r_2 \leq r < r_3, \\ R_3 + k_T^{(4)}(r - r_3), & r_3 \leq r, \end{cases} \tag{A.4}$$

where $H(r - r_{\text{break}})$ is the Heaviside function $H(a)$, which is defined to be zero for $a < 0$, and one for $a \geq 0$. The parameters $R_1 = k_T^{(1)}(r_1 - r_0)$, $R_2 = k_T^{(2)}(r_2 - r_1)$ and $R_3 = k_T^{(3)}(r_3 - r_2)$ come from force continuity conditions. They are fitted to reproduce the force-stretch behavior obtained using the full atomistic model with the molecular formulation.

All parameters are calculated directly from full atomistic results, without empirical fitting. The entire set of parameters of the mesoscopic model is summarized in Table 4.

Since these equations are derived from atomistic simulations at relatively large strain rates, Equations (A.1)–(A.4) are only literally valid for comparable deformation rates. Under much smaller deformation rates, the parameters may change significantly.

| | |
|---|---|
| Equilibrium bead distance $r_0$ (in Å) | 5.00 |
| Critical distances $r_1$, $r_2$ and $r_3$ (in Å) | 5.90, 11.50, 13.0 |
| Tensile stiffness parameters $k_T^{(1)}$, $k_T^{(2)}$, $k_T^{(3)}$, $k_T^{(4)}$ (in kcal/mol/Å²) | 23.80, 0.56, 32.20, 54.60 |
| Bond breaking distance $r$ (in Å) | 13.35 |
| Equilibrium angle $\varphi_0$ (in degrees) | 180.00 |
| Bending stiffness parameter $k_B$ (in kcal/mol/rad²) | 3.44 |
| Mass of each mesoscale particle (in amu) | 400.00 |

**Table 4.** Summary of the parameters used in the mesoscopic molecular model, based on full atomistic modeling of alpha-helical molecules (1 kcal/mol/Å = 69.479 pN).

## Appendix A  Molecular visualization scheme

We use the Visual Molecular Dynamics (VMD) program to visualize MD simulation results [Humphrey et al. 1996]. Proteins are depicted in various ways, depending on the type of information that is to be highlighted. In the standard format, atoms are plotted as spheres, and bonds between atoms are drawn as thin lines. Note that whether an atom is bonded or not is determined based on a cutoff scheme, which may not reflect the actual treatment of atoms in the reactive potential, which features a smooth bond order-distance relationship.

In the cartoon mode, helices are drawn as cylinders, beta sheets as solid ribbons with arrows, and all other structure including coils and turns as a tube or wire-like structure. In our plots we typically do not show water molecules and only render atoms that are part of the protein.

## Acknowledgement

## References

[Aizenberg et al. 2005]  J. Aizenberg, J. C. Weaver, M. S. Thanawala, V. C. Sundar, D. E. Morse, and P. Fratzl, "Skeleton of Euplectella sp.: structural hierarchy from the nanoscale to the macroscale", *Science* **309**:5732 (2005), 275–278.

[Akkermans and Warren 2004]  R. L. C. Akkermans and P. B. Warren, "Multiscale modelling of human hair", *Philos. T. Roy. Soc. A* **362**:1821 (2004), 1783–1793.

[Alberts et al. 2002]  B. Alberts, A. Johnson, J. Lewis, M. Raff, K. Roberts, and P. Walter, *Molecular biology of the cell*, 4th ed., Garland Science, 2002.

[Anderson 1991]  T. L. Anderson, *Fracture mechanics: fundamentals and applications*, CRC Press, 1991.

[Arteca 2003]  G. A. Arteca, "Stress-induced shape transitions in polymers using a new approach to steered molecular dynamics", *Phys. Chem. Chem. Phys.* **5**:2 (2003), 407–414.

[Arteca and Li 2004]  G. A. Arteca and Z. Y. Li, "Effect of proline kinks on the mechanical unfolding of alpha-helices", *Chem. Phys. Lett.* **399**:4–6 (2004), 496–502.

[Astbury and Street 1932]  W. T. Astbury and A. Street, "X-ray studies of the structure of hair, wool and related fibres, I: general", *T. Roy. Soc. Lond. A* **230** (1932), 75–101.

[Balsera et al. 1997] M. Balsera, S. Stepaniants, S. Izrailev, Y. Oono, and K. Schulten, "Reconstructing potential energy functions from simulated force-induced unbinding processes", *Biophys. J.* **73**:3 (1997), 1281–1287.

[Brenner 1990]  D. W. Brenner, "Empirical potential for hydrocarbons for use in simulating the chemical vapor-deposition of diamond films", *Phys. Rev. B* **42**:15 (1990), 9458–9471.

[Brenner et al. 2002]  D. W. Brenner, O. A. Shenderova, J. A. Harrison, S. J. Stuart, B. Ni, and S. B. Sinnott, "A second-generation reactive empirical bond order (REBO) potential energy expression for hydrocarbons", *J. Phys. Condens. Matter* **14**:4 (2002), 783–802.

[Buehler 2006a]  M. J. Buehler, "Atomistic and continuum modeling of mechanical properties of collagen: elasticity, fracture and self-assembly", *J. Mater. Res.* **21**:8 (2006), 1947–1961.

[Buehler 2006b]  M. J. Buehler, "Large-scale hierarchical molecular modeling of nanostructured biological materials", *J. Comput. Theor. Nanoscience* **3**:5 (2006), 603–623.

[Buehler 2006c]  M. J. Buehler, "Mechanics of protein crystals: atomistic modeling of elasticity and fracture", *J. Comput. Theor. Nanoscience* **3**:5 (2006), 670–683.

[Buehler 2006d]  M. J. Buehler, "Nature designs tough collagen: explaining the nanostructure of collagen fibrils", *P. Natl. Acad. Sci. USA* **103**:33 (2006), 12285–12290.

[Buehler and Gao 2006a]  M. J. Buehler and H. Gao, "Dynamical fracture instabilities due to local hyperelasticity at crack tips", *Nature* **439**:7074 (2006), 307–310.

[Buehler and Gao 2006b]  M. J. Buehler and H. Gao, "Ultra large scale atomistic simulations of dynamic fracture", Chapter 10, pp. 427–467 in *Handbook of theoretical and computational nanotechnology*, vol. 2, edited by M. Rieth and W. Schommers, American Scientific Publishers, Stevenson Ranch, CA, 2006.

[Buehler et al. 2003]  M. J. Buehler, F. F. Abraham, and H. Gao, "Hyperelasticity governs dynamic fracture at a critical length scale", *Nature* **426**:6963 (2003), 141–146.

[Buehler et al. 2004]  M. J. Buehler, A. Hartmaier, H. Gao, M. Duchaineau, and F. F. Abraham, "Atomic plasticity: description and analysis of a one-billion atom simulation of ductile materials failure", *Comput. Methods Appl. Mech. Eng.* **193**:48–51 (2004), 5257–5282.

[Buehler et al. 2005]  M. J. Buehler, A. Hartmaier, H. Gao, M. A. Duchaineau, and F. F. Abraham, "The dynamical complexity of work-hardening: a large-scale molecular dynamics simulation", *Acta Mech. Sin.* **21**:2 (2005), 103–111.

[Buehler et al. 2006]  M. J. Buehler, A. C. T. van Duin, and W. A. Goddard, III, "Multiparadigm modeling of dynamical crack propagation in silicon using a reactive force field", *Phys. Rev. Lett.* **96**:9 (2006), 095505–095509.

[Bustamante et al. 1994]  C. Bustamante, J. F. Marko, E. D. Siggia, and S. Smith, "Entropic elasticity of lambda-phage DNA", *Science* **265**:5178 (1994), 1599–1600.

[Chenoweth et al. 2005]  K. Chenoweth, S. Cheung, A. C. T. van Duin, W. A. Goddard, III, and E. M. Kober, "Simulations on the thermal decomposition of a poly(dimethylsiloxane) polymer using the ReaxFF reactive force field", *J. Am. Chem. Soc.* **127**:19 (2005), 7192–7202.

[Cheung et al. 2005]  S. Cheung, W. Q. Deng, A. C. T. van Duin, and W. A. Goddard, III, "ReaxFF(MgH) reactive force field for magnesium hydride systems", *J. Phys. Chem. A* **109**:5 (2005), 851–859.

[Cieplak and Marszalek 2005]  M. Cieplak and P. E. Marszalek, "Mechanical unfolding of ubiquitin molecules", *J. Chem. Phys.* **123**:19 (2005), #194903.

[Cieplak et al. 2002]  M. Cieplak, T. X. Hoang, and M. O. Robbins, "Thermal folding and mechanical unfolding pathways of protein secondary structures", *Proteins* **49**:1 (2002), 104–113.

[Contera et al. 2005]  S. A. Contera, V. Lemaître, M. R. R. Planque, A. Watts, and J. F. Ryan, "Unfolding and extraction of a transmembrane alpha-helical peptide: dynamic force spectroscopy and molecular dynamics simulations", *Biophys. J.* **89**:5 (2005), 3129–3140.

[Courtney 1990]  T. H. Courtney, *Mechanical behavior of materials*, McGraw-Hill, 1990.

[Cui et al. 2002]  Q. Cui, H. Guo, and M. Karplus, "Combining ab initio and density functional theories with semiempirical methods", *J. Chem. Phys.* **117**:12 (2002), 5617–5631.

[Dao et al. 2003]  M. Dao, C. T. Lim, and S. Suresh, "Mechanics of the human red blood cell deformed by optical tweezers", *J. Mech. Phys. Solids* **51**:11–12 (2003), 2259–2280.

[Datta et al. 2005]  D. Datta, A. C. T. van Duin, and W. A. Goddard, "Extending ReaxFF to biomacromolecules", 2005. Unpublished.

[van Duin et al. 2001]  A. C. T. van Duin, S. Dasgupta, F. Lorant, and W. A. Goddard, III, "ReaxFF: a reactive force field for hydrocarbons", *J. Phys. Chem. A* **105**:41 (2001), 9396–9409.

[van Duin et al. 2003]  A. C. T. van Duin, A. Strachan, S. Stewrnan, Q. Zhang, X. Xu, and W. A. Goddard, III, "ReaxFF SiO: reactive force field for silicon and silicon oxide systems", *J. Phys. Chem. A* **107**:19 (2003), 3803–3811.

[Fainzilber et al. 1994]  M. Fainzilber, A. Hasson, R. Oren, A. L. Burlingame, D. Gordon, M. E. Spira, and E. Zlotkin, "New mollusk-specific alpha-conotoxins block aplysia neuronal acetylcholine-receptors", *Biochemistry* **33**:32 (1994), 9523–9529.

[Feig and Brooks 2004]  M. Feig and C. L. Brooks, "Recent advances in the development and application of implicit solvent models in biomolecule simulations", *Curr. Opin. Struct. Biol.* **14**:2 (2004), 217–224.

[Fudge and Gosline 2004] D. S. Fudge and J. M. Gosline, "Molecular design of the alpha-keratin composite: insights from a matrix-free model, hagfish slime threads", *P. Roy. Soc. Lond. B Bio.* **271**:1536 (2004), 291–299.

[Gao et al. 2001] M. Gao, H. Lu, and K. Schulten, "Simulated refolding of stretched titin immunoglobulin domains", *Biophys. J.* **81**:4 (2001), 2268–2277.

[Gao et al. 2002] M. Gao, H. Lu, and K. Schulten, "Unfolding of titin domains studied by molecular dynamics simulations", *J. Muscle Res. Cell M.* **23**:5–6 (2002), 513–521.

[Gouldstone et al. 2001] A. Gouldstone, K. J. V. Vliet, and S. Suresh, "Nanoindentation: simulation of defect nucleation in a crystal", *Nature* **411**:6838 (2001), 656.

[Gupta et al. 2004] H. S. Gupta, P. Messmer, P. Roschger, S. Bernstorff, K. Klaushofer, and P. Fratz, "Synchrotron diffraction study of deformation mechanisms in mineralized tendon", *Phys. Rev. Lett.* **93**:12 (2004), #158101.

[Gupta et al. 2005] H. S. Gupta, W. Wagermaier, G. A. Zickler, D. R. B. Aroush, S. S. Funari, P. Roschger, H. D. Wagner, and P. Fratzl, "Nanoscale deformation mechanisms in bone", *Nano Letters* **5**:10 (2005), 2108–2111.

[Han et al. 2005] S. S. Han, A. C. T. van Duin, W. A. Goddard, III, and H. M. Lee, "Optimization and application of lithium parameters for the reactive force field, ReaxFF", *J. Phys. Chem. A* **109**:20 (2005), 4575–4582.

[Harata and Kanai 2002] K. Harata and R. Kanai, "Crystallographic dissection of the thermal motion of protein-sugar complex", *Proteins* **48**:1 (2002), 53–62.

[Hartmaier et al. 2005] A. Hartmaier, M. J. Buehler, and H. J. Gao, "Multiscale modeling of deformation in polycrystalline thin metal films on substrates", *Adv. Eng. Mater.* **7**:3 (2005), 165–169.

[Hulmes et al. 1995] D. J. S. Hulmes, T. J. Wess, D. J. Prockop, and P. Fratzl, "Radial packing, order, and disorder in collagen fibrils", *Biophys. J.* **68**:5 (1995), 1661–1670.

[Humphrey et al. 1996] W. Humphrey, A. Dalke, and K. Schulten, "VMD: visual molecular dynamics", *J. Mol. Graphics* **14**:1 (1996), 33.

[Jager and Fratzl 2000] I. Jager and P. Fratzl, "Mineralized collagen fibrils: a mechanical model with a staggered arrangement of mineral particles", *Biophys. J.* **79**:4 (2000), 1737–1746.

[Kadau et al. 2004] K. Kadau, T. C. Germann, and P. S. Lomdahl, "Large-scale molecular-dynamics simulation of 19 billion particles", *Int. J. Mod. Phys. C* **15**:1 (2004), 193–201.

[Karplus and McCammon 2002] M. Karplus and J. A. McCammon, "Molecular dynamics simulations of biomolecules", *Nat. Struct. Biol.* **9**:9 (2002), 646–652.

[Kiss et al. 2006] B. Kiss, A. Karsai, and M. S. Z. Kellermayer, "Nanomechanical properties of desmin intermediate filaments", *J. Struct. Biol.* **155**:2 (2006), 327–339.

[Landis et al. 2002] W. J. Landis, B. L. H. Kraus, and C. A. Kirker-Head, "Vascular-mineral spatial correlation in the calcifying turkey leg tendon", *Connect. Tissue Res.* **43**:4 (2002), 595–605.

[Langer and Tirrell 2004] R. Langer and D. A. Tirrell, "Designing materials for biology and medicine", *Nature* **428**:6982 (2004), 487–492.

[Leach 2001] A. R. Leach, *Molecular modelling: principles and applications*, 2nd ed., Pearson Prentice Hall, 2001.

[Li and Arteca 2005] Z. Y. Li and G. A. Arteca, "Simulated force-induced unfolding of alpha-helices: dependence of stretching stability on primary sequence", *Phys. Chem. Chem. Phys.* **7**:9 (2005), 2018–2026.

[Lorenzo and Caffarena 2005] A. C. Lorenzo and E. R. Caffarena, "Elastic properties, Young's modulus determination and structural stability of the tropocollagen molecule: a computational study by steered molecular dynamics", *J. Biomech.* **38**:7 (2005), 1527–1533.

[Lu et al. 1998] H. Lu, B. Isralewitz, A. Krammer, V. Vogel, and K. Schulten, "Unfolding of titin immunoglobulin domains by steered molecular dynamics simulation", *Biophys. J.* **75**:2 (1998), 662–671.

[MacKerell et al. 1998] A. D. MacKerell, D. Bashford, M. Bellott, R. L. Dunbrack, J. D. Evanseck, M. J. Field, S. Fischer, J. Gao, H. Guo, and S. Ha, "All-atom empirical potential for molecular modeling and dynamics studies of proteins", *J. Phys. Chem. B* **102**:15 (1998), 3586–3616.

[Marko and Siggia 1995] J. F. Marko and E. D. Siggia, "Stretching DNA", *Macromolecules* **28**:26 (1995), 8759–8770.

[Mayo et al. 1990]  S. L. Mayo, B. D. Olafson, and W. A. Goddard, III, "Dreiding: a generic force-field for molecular simulations", *J. Phys. Chem.* **94**:26 (1990), 8897–8909.

[Mehta et al. 1999]  A. D. Mehta, M. Rief, and J. A. Spudich, "Biomechanics, one molecule at a time", *J. Biol. Chem.* **274**:21 (1999), 14517–14520.

[Nalla et al. 2003]  R. K. Nalla, J. H. Kinney, and R. O. Ritchie, "Effect of orientation on the in vitro fracture toughness of dentin: the role of toughening mechanisms", *Biomaterials* **24**:22 (2003), 3955–3968.

[Nalla et al. 2005]  R. K. Nalla, J. J. Kruzic, J. H. Kinney, and R. O. Ritchie, "Mechanistic aspects of fracture and *R*-curve behavior in human cortical bone", *Biomaterials* **26**:2 (2005), 217–231.

[Nelson et al. 1996]  M. T. Nelson, W. Humphrey, A. Gursoy, A. Dalke, L. V. Kalé, R. D. Skeel, and K. Schulten, "NAMD: a parallel, object oriented molecular dynamics program", *Int. J. High Perform. Comput. Appl.* **10**:4 (1996), 251–268.

[Nielson et al. 2005]  K. D. Nielson, A. C. T. van Duin, J. Oxgaard, W. Q. Deng, and W. A. Goddard, III, "Development of the ReaxFF reactive force field for describing transition metal catalyzed reactions, with application to the initial stages of the catalytic formation of carbon nanotubes", *J. Phys. Chem. A* **109**:3 (2005), 493–499.

[Ortiz et al. 2005]  V. Ortiz, S. O. Nielsen, M. L. Klein, and D. E. Discher, "Unfolding a linker between helical repeats", *J. Mol. Biol.* **349**:3 (2005), 638–647.

[Papadopoulos et al. 2006]  P. Papadopoulos, G. Floudas, I. Schnell, I. Lieberwirth, T. Q. Nguyen, and H. A. Klok, "Thermodynamic confinement and alpha-helix persistence length in poly (gamma-benzyl-L-glutamate)-b-poly (dimethyl siloxane)-b-poly (gamma-benzyl-L-glutamate) triblock copolymers", *Biomacromolecules* **7**:2 (2006), 618–626.

[Papamokos and Demetropoulos 2004]  G. V. Papamokos and I. N. Demetropoulos, "Biomolecular springs: low-frequency collective helical vibrations of Ace-Gly(n)-NHMe (n=3-8). A DFT study employing the PW91(XC) functional", *J. Phys. Chem. A* **108**:40 (2004), 8160–8169.

[Peterlik et al. 2006]  H. Peterlik, P. Roschger, K. Klaushofer, and P. Fratzl, "From brittle to ductile fracture of bone", *Nat. Mater.* **5**:1 (2006), 52–55.

[Petka et al. 1998]  W. A. Petka, J. L. Harden, K. P. McGrath, D. Wirtz, and D. A. Tirrell, "Reversible hydrogels from self-assembling artificial proteins", *Science* **281**:5375 (1998), 389–392.

[Phillips et al. 2005]  J. C. Phillips, R. Braun, W. Wang, J. Gumbart, E. Tajkhorshid, E. Villa, C. Chipot, R. D. Skeel, L. Kalé, and K. Schulten, "Scalable molecular dynamics with NAMD", *J. Comput. Chem.* **26**:16 (2005), 1781–1802.

[Puxkandl et al. 2002]  R. Puxkandl, I. Zizak, O. Paris, J. Keckes, W. Tesch, S. Bernstorff, P. Purslow, and P. Fratzl, "Viscoelastic properties of collagen: synchrotron radiation investigations and structural model", *Philos. T. Roy. Soc. B* **357**:1418 (2002), 191–197.

[Rappe and Goddard 1991]  A. K. Rappe and W. A. Goddard, "Charge equilibration for molecular-dynamics simulations", *J. Phys. Chem.* **95**:8 (1991), 3358–3363.

[Rief et al. 1997]  M. Rief, M. Gautel, F. Oesterhelt, J. M. Fernandez, and H. E. Gaub, "Reversible unfolding of individual titin immunoglobulin domains by AFM", *Science* **276**:5315 (1997), 1109–1112.

[Rief et al. 2000]  M. Rief, M. Gautel, and H. E. Gaub, "Unfolding forces of titin and fibronectin domains directly measured by AFM", pp. 129–141 in *Elastic filaments of the cell*, 2000.

[Ritchie et al. 2004]  R. O. Ritchie, J. J. Kruzic, C. L. Muhlstein, R. K. Nalla, and E. A. Stach, "Characteristic dimensions and the micro-mechanisms of fracture and fatigue in 'nano' and 'bio' materials", *Int. J. Fract.* **128**:1–4 (2004), 1–15.

[Root et al. 2006]  D. D. Root, V. K. Yadavalli, J. G. Forbes, and K. Wang, "Coiled-coil nanomechanics and uncoiling and unfolding of the superhelix and alpha-helices of myosin", *Biophys. J.* **90**:8 (2006), 2852–2866.

[Sasaki and Odajima 1996]  N. Sasaki and S. Odajima, "Elongation mechanism of collagen fibrils and force-strain relations of tendon at each level of structural hierarchy", *J. Biomech.* **29**:9 (1996), 1131–1136.

[Schwaiger et al. 2002]  I. Schwaiger, C. Sattler, D. R. Hostetter, and M. Rief, "The myosin coiled-coil is a truly elastic protein structure", *Nat. Mater.* **1**:4 (2002), 232–235.

[Springborg 1997]  M. Springborg, *Density-functional methods in chemistry and materials science*, Wiley research series in Theoretical Chemistry, Wiley, 1997.

[Strachan et al. 2003] A. Strachan, A. C. T. van Duin, D. Chakraborty, S. Dasgupta, and W. A. Goddard, III, "Shock waves in high-energy materials: the initial chemical events in nitramine RDX", *Phys. Rev. Lett.* **91**:9 (2003), #098301.

[Strachan et al. 2005] A. Strachan, E. M. Kober, A. C. T. van Duin, J. Oxgaard, and W. A. Goddard, III, "Thermal decomposition of RDX from reactive molecular dynamics", *J. Chem. Phys.* **122**:5 (2005), #054502.

[Strelkov et al. 2002] S. V. Strelkov, H. Herrmann, N. Geisler, T. Wedig, R. Zimbelmann, U. Aebi, and P. Burkhard, "Conserved segments 1A and 2B of the intermediate filament dimer: their atomic structures and role in filament assembly", *EMBO J.* **21**:6 (2002), 1255–1266.

[Stuart et al. 2000] S. J. Stuart, A. B. Tutein, and J. A. Harrison, "A reactive potential for hydrocarbons with intermolecular interactions", *J. Chem. Phys.* **112**:14 (2000), 6472–6486.

[Sun et al. 2001] Y. L. Sun, Z. P. Luo, and K. N. An, "Stretching short biopolymers using optical tweezers", *Biochem. Biophys. Res. Commun.* **286**:4 (2001), 826–830.

[Sun et al. 2004] Y. L. Sun, Z. P. Luo, A. Fertala, and K. N. An, "Stretching type II collagen with optical tweezers", *J. Biomech.* **37**:11 (2004), 1665–1669.

[Tersoff 1988] J. Tersoff, "Empirical interatomic potential for carbon, with applications to amorphous carbon", *Phys. Rev. Lett.* **61**:25 (1988), 2879–2882.

[Tirrell 2002] D. A. Tirrell, "Molecular engineering of protein assembly on surfaces", *Abstr. Pap. Am. Chem. S.* **224** (2002), U408–U408.

[Vaney et al. 1996] M. C. Vaney, S. Maignan, M. Riès-Kautt, and A. Ducruix, "High-resolution structure (1. 33 angstrom) of a HEW lysozyme tetragonal crystal grown in the APCF apparatus. Data and structural comparison with a crystal grown under microgravity from SpaceHab-01 mission", *Acta Crystallogr. Sect. D* **52** (1996), 505–517.

[Wang et al. 2001] W. Wang, O. Donini, C. M. Reyes, and P. A. Kollman, "Biomolecular simulations: recent developments in force fields, simulations of enzyme catalysis, protein-ligand, protein-protein, and protein-nucleic acid noncovalent interactions", *Annu. Rev. Biophys. Biom.* **30** (2001), 211–243.

[Whitesides and Wong 2006] G. M. Whitesides and A. P. Wong, "The intersection of biology and materials science", *MRS Bull.* **31**:1 (2006), 19–27.

MARKUS J. BUEHLER: mbuehler@mit.edu

*Laboratory for Atomistic and Molecular Mechanics, Department of Civil and Environmental Engineering, Massachusetts Institute of Technology, 77 Massachusetts Ave., Room 1-272, Cambridge, MA 02139, United States*

# MICROMECHANICAL PROPERTIES OF CHONDROCYTES AND CHONDRONS: RELEVANCE TO ARTICULAR CARTILAGE TISSUE ENGINEERING

GIDON OFEK AND KYRIACOS A. ATHANASIOU

Articular cartilage is a highly mechanical tissue, performing multiple functions to ensure proper joint movement. Degradation of this tissue may be due to improper loading conditions that lead to a debilitating condition known as osteoarthritis. Furthermore, it is believed that mechanical signals transmitted from the tissue to cellular levels are necessary for the production of essential extracellular matrix components responsible for cartilage viability. Examinations of the tissue on its most rudimentary level elucidate mechanical regimens related to cartilage health and disease. A fundamental unit approach has been employed to study the biomechanical properties of single cells with discrete pericellular and extracellular matrix layers. This approach enables researchers to develop definitive relationships between mechanical stimulation and changes in gene expression corresponding to regenerative or catabolic processes. The knowledge gained from these studies sheds light on the etiology of osteoarthritis and elucidate the mechanical loading regimens useful for promoting articular cartilage health. This review article discusses the micromechanical environment of the cartilage cell, the chondrocyte, and the mechanical models and experimental techniques utilized to examine its physical characteristics. This information is then related to changes in cellular behavior and its potential toward tissue engineering of articular cartilage.

## 1. Introduction

Articular cartilage is the load-bearing material lining diarthrodial joints. It is a specialized type of hyaline cartilage and a highly versatile tissue, serving multiple functions to ensure proper joint movement. Together with the synovial fluid, it provides a lubricating and wear resistant surface, facilitating nearly frictionless motion about the articulating joints of our body. In addition, articular cartilage works to resist and distribute high compressive loads from one subchondral bone to another. Due to its biomechanical nature, articular cartilage health is largely determined by a variety of mechanical factors. It is well known that mechanical forces can elicit particular changes in the viability of articular cartilage, from the cellular to tissue levels [Freeman et al. 1994; Buschmann et al. 1995; Smith et al. 1995; Chen and Sah 1998; Knight et al. 1998; Lee et al. 1998; Carver and Heath 1999; Ragan et al. 1999; Smith et al. 2000b; Smith et al. 2000a; Roberts et al. 2001; Chowdhury et al. 2003]. Mechanical stimuli can induce modulations in cartilage tissue metabolism, in either a catabolic or anabolic manner. Therefore, the goal of much current research is to elucidate specific regimens of mechanical forces that will lead to the growth and strengthening of articular cartilage.

Under conditions of improper joint loading, the signaling pathways leading to normal gene regulation may not be stimulated correctly, and articular cartilage will degenerate. It has been shown that an

abnormal mechanical environment within the tissue, created in cases of high joint impact or due to an accumulation of small repeated loading events, significantly affects cellular behavior and may result in pathological extracellular matrix (ECM) synthesis and apoptosis [Dekel and Weissman 1978; Radin et al. 1984; Ehrlich et al. 1987; Radin et al. 1991; Jeffrey et al. 1995; Kurz et al. 2001; J. Borrelli et al. 2003]. These detrimental tissue changes lead to a condition known as osteoarthritis, which afflicts millions of Americans and significantly affects the United States economy [Arthritis Foundation 2006].

This review will begin by briefly discussing the physiological and structural properties of articular cartilage and the need to pursue tissue engineering techniques in order to treat patients with osteoarthritis. If the reader is interested, a more comprehensive discussion of articular cartilage physiology can be found in several excellent reviews [Buckwalter et al. 1991; Mow and Ratcliffe 1997; Hu and Athanasiou 2003] Due to the heterogeneous nature of the tissue, it is important to look individually at articular cartilage's most fundamental units in order to develop definitive relationships between applied stimuli and changes in cellular behavior. Therefore, to formulate effective treatment methodologies for osteoarthritis, it is critical to first study articular cartilage on its most basic level, the *chondrocyte* cell, so that regulatory mechanisms within cartilage can be directly correlated with mechanical factors. Researchers may then move upwards toward the tissue level, building upon single cell research by including discrete ECM regions, to elucidate on all fronts the role of mechanical stimulation in cartilage heath and disease. As such, this review will primarily focus on the mechanical environment necessary to bring about a favorable response from the cell and the *chondron*, which is the cell within its local microenvironment, and its tissue engineering implications.

The single cell, chondron, microexplant, and tissue construct are metabolic units of increasing complexity. This review utilizes the concept of a *fundamental unit approach* to demonstrate how research conducted at each of these phases may be interrelated. The fundamental unit approach is a modular template that facilitates research and understanding of these phases, and consists of modeling, experimental validation, and stimulating the unit of interest. Information gained from this research can be used in the formulation of necessary treatment methodologies, such as tissue replacement strategies, for patients suffering from osteoarthritis.

## 2. Articular cartilage structure and tissue engineering

**2.1.** *Heterogeneous tissue properties.*  Articular cartilage tissue is nonuniform in its composition, varying in terms of matrix components, matrix organization, cellular phenotypes, and organization. It is largely composed of chondrocytes sparsely interdispersed within an intricate network of collagen fibrils, proteoglycans, lipids, and various ionic and nonionic solutes [Mow and Ratcliffe 1997]. Due to the inherent heterogeneity of articular cartilage, chondrocytes in one location may sense and respond to forces differently than cells in another location. Therefore observations of the tissue on the bulk level may not accurately reflect the intrinsic phenotypic and morphological differences existing within various subpopulations of chondrocytes in cartilage [Darling et al. 2004]. As will be further discussed in detail, chondrocytes perceive stimuli within their individual mechanical microenvironments. To begin with, an understanding of the structural properties of articular cartilage is necessary to appreciate the scope of the cellular microenvironment and grasp the heterogeneous nature of this tissue.

Articular cartilage is often considered to consist of both a solid and fluid phase. The interaction and arrangement of these various tissue components and phases provide articular cartilage with its unique functional capabilities. The primary component of articular cartilage is interstitial water that accounts for 60–85% of its wet weight. Water and various electrolytes in the tissue are denoted as the fluid phase. Collagens, particularly type II collagen, make up approximately 50%–75% of the solid phase and are responsible for the tensile characteristics of the tissue [Buckwalter et al. 1991]. Proteoglycans and other glycoproteins compose a majority of the remaining solid phase [Mow and Ratcliffe 1997], and contribute to the compressive and flow-dependent viscoelastic properties of articular cartilage [Mak 1986]. Proteoglycans are a highly specific type of glycoprotein, containing long, unbranched, negatively charged chains of glycosaminoglycans (GAGs) attached to a central link protein. Aggrecan is the most predominant proteoglycan in articular cartilage [Buckwalter et al. 1991; Mow and Ratcliffe 1997].

The spatial arrangement of collagens and proteoglycans has been shown to affect cellular metabolism [Muir 1983]. The thickness of the collagen fibers is determined by a fixed charge density created by the adjacent GAG chains [Katz et al. 1986]. The interaction of electrostatic charges from the GAGs and cations from the fluid phase contribute to the regulation of interstitial water content through a swelling pressure following the Donnan osmotic pressure law [Buschmann and Grodzinsky 1995]. The swelling generated by the resulting outward osmotic pressure is fettered by the cross-linked network of collagen and aggregan [Maroudas 1976]. When articular cartilage is compressed, fluid exits the tissue and experiences a drag via osmotic pressure. This drag enables the tissue to deform viscoelastically and act as a damper and distributor of applied forces.

Articular cartilage consists of four distinct zones: superficial, middle, deep, and calcified layers. Each layer is known to vary in matrix composition, and cellular, metabolic and mechanical properties [Aydelotte and Kuettner 1988; Aydelotte et al. 1988; Guilak et al. 1995; Wong et al. 1996; Freemont et al. 1997; Lee et al. 1998; Scott et al. 2005; Darling et al. 2006; Shieh and Athanasiou 2006; Youn et al. 2006]. Transitioning from the superficial layer to the deep layer, water content decreases and collagen fiber alignment changes from a tangential orientation to a radial direction along the tissue [Minns and Steven 1977; Buckwalter et al. 1991; Mow and Ratcliffe 1997]. The superficial layer is the outermost level of cartilage, encompassing the upper 10–20% of the tissue, and is characterized by a high tensile strength due to the tangential alignment of collagen fibrils [Verteramo and Seedhom 2004]. Chondrocytes in this region are stiffest and produce a specific superficial zone protein that aids in providing articular cartilage with its lubricating surface and prevents undesirable cell adhesion in this region [Flannery et al. 1999]. The middle layer contains more rounded chondrocytes and the greatest proteoglycan levels compared to the other layers. The deep layer is the thickest region of articular cartilage, although it contains the lowest amounts of interstitial fluid and collagen. Despite their low abundance in the deep layer, collagen fibers in this region are the greatest in diameter and function as a connection between articular cartilage and the underlying subchondral bone. The high compressive mechanical properties of this region can also be attributed to the radial orientation of these fibers [Mow and Ratcliffe 1997]. Lining the underside of the deep layer is a tidemark, conspicuously separating the region from the calcified layer below. In this final layer, chondrocytes are mostly inert and sheathed within a calcium fortified milieu [Marles et al. 1991].

With the cell as the center, distinct matrix divisions also exist concentrically within articular cartilage. Extending radially from the cell, pericellular, territorial, and interterritorial matrices each play a role in

chondrocyte maintenance and articular cartilage function. The ECM region consists of both the territorial and interterritorial matrices and is known to contain the vast majority of collagen and aggrecan proteins in cartilage tissue. The pericellular matrix (PCM) is most prominent in the middle and deep layers of the tissue and immediately surrounds the chondrocyte within a lacuna. The PCM, together with its enclosed cell, is defined as the *chondron* and is considered to be the smallest metabolic and functional unit of articular cartilage [Poole 1997]. Examinations of isolated chondrons have provided researchers with vast insight into the micromechanical environment of the chondrocyte in vivo. It has been found that the PCM is important in directly conveying biomechanical and biochemical stimuli on to the chondrocyte and will be discussed in greater detail later.

**2.2.** *Tissue engineering potential for articular cartilage.* Though primarily serving a mechanical function, articular cartilage lacks the vasculature and lymphatic system to repair itself under conditions of wear and tear or traumatic injury [Buckwalter et al. 1991; Mow and Ratcliffe 1997]. Since articular cartilage is unable to naturally restore its original structure and functionality after damage, ample research has focused toward understanding the etiology of osteoarthritis and to tissue engineer fully functional neotissue as a replacement for diseased cartilage. In cases of severe articular cartilage pathology, tissue replacement may become necessary. In the laboratory, it is now possible to engineer cartilage of clinically relevant dimensions and properties [Graff et al. 2003; Hu and Athanasiou 2006; Kang et al. 2006], and this may have profound implications for orthopedics in the near future.

Due to the inherent biomechanical nature and function of articular cartilage, the majority of tissue engineering techniques employ various mechanical stimuli as promoters of ECM synthesis and tissue growth. While external loading regimens are applied on the bulk tissue construct level, it is the chondrocyte itself which produces the proteins necessary for healthy and viable cartilage. Therefore, an understanding of chondrocyte mechanotransduction and its mechanical environment is paramount toward elucidating the ideal methodologies for stimulating cartilage tissue. As will be later discussed, forces and deformations applied onto the construct will transduce down through the chondrocyte microenvironment and can effect gene expression. Therefore, when considering a tissue engineering approach to articular cartilage, it is critical to understand how mechanical signals are interpreted by the individual cell.

While unified by a realm of exogenous stimuli, such as mechanical factors, which modulate cartilage development and growth, current tissue engineering techniques can themselves vary in their methods to coalesce isolated cells. Traditionally, tissue engineering techniques employ a degradable polymer scaffold upon which to seed a desired cell density. Since chondrocytes are already able to create cartilage ECM elements, such as the collagen and GAG types found in cartilage, they immediately come to mind as the appropriate cell type to be used in tissue engineering of articular cartilage. As the scaffold degrades, it is replaced by a natural matrix produced by the cells. Some common scaffold types include collagen [Wakitani et al. 1998], poly(DL-lactic acid) and poly(glycolic acid) [Sittinger et al. 1996], and more recently, poly(1,8-octanediol citrate) [Kang et al. 2006], with promising results.

Despite the vast potential of scaffold-based tissue engineering approaches, they do include several notable drawbacks. Whenever dealing with degradable polymers, researchers must consider issues of biodegradability, degradation products' toxicity, stress-shielding, and hindrance of cell-to-cell communication. To avoid such scaffold-related concerns, many scaffoldless approaches have been tested and utilized in the past few years. Autologous chondrocyte implantation is the most common technique of

this sort and the leading method to treat osteoarthritic patients under the age of 55. In this procedure, the defected cartilage region is cleared of debris and covered by a periosteum flap. The surgeon then injects a high density of the patient's own chondrocyte cells underneath the flap where they may develop into healthy cartilage tissue [Romeo et al. 2002; Micheli et al. 2006]. In contrast, scaffoldless procedures have also been employed to grow articular cartilage outside the body with the goal of then transplanting the neotissue into the defective region. Pellet culture [Graff et al. 2003] and aggregate culture [Horton et al. 1987; Furukawa et al. 2003] techniques have been implemented to grow articular cartilage constructs and tested under various mechanical conditions. Another scaffoldless approach, known as the self-assembling process, has recently been validated by Hu and Athanasiou [Hu and Athanasiou 2006] to produce cartilage tissue constructs with biomechanical and biochemical properties nearing those of native tissue. This novel approach, which involves seeding of primary chondrocytes at high-density over agarose wells, can be employed using various molds to create the desired shape for an articular cartilage implant.

**2.3. *Fundamental unit approach.*** Elucidating the mechanical properties of single cells and chondrons and of their behavior in response to mechanical stimuli will provide great insight into the most rudimentary level of articular cartilage. This is a necessary first step toward tissue engineering of articular cartilage and understanding the regimens of mechanical stimuli needed to elicit favorable gene responses, in terms of ECM production and cellular proliferation, from within a tissue construct. Information on how chondrocytes respond to various forces within their own microenvironment will greatly aid researchers toward developing a functional tissue replacement for deteriorated cartilage in patients suffering from osteoarthritis.

The majority of previous studies investigating chondrocyte mechanotransduction have looked at the mechanical response of an entire population of cells in their ECM. Though these experiments have been essential in furthering our knowledge of mechanotransduction and of the influence of mechanical stimuli on cellular behavior, they are subject to significant limitations. Most notably, testing cells in a bulk manner does not take into consideration variables such as individual cell shape, position, orientation, or local ECM characteristics. Cells within the same population may experience different stress-strain patterns under similar testing modalities. Therefore, the observed response may not accurately reflect a true response to the presumed applied force. Moreover, past research has strongly suggested that an individual chondrocyte responds to mechanical stimuli within its local environment, as opposed to the aggregate mechanical environment of the whole tissue [Mow et al. 1994; Guilak and Mow 2000].

To overcome such drawbacks, a fundamental unit approach can be utilized, wherein mechanical forces are applied to a single metabolic unit and the resulting changes in cellular behavior are recorded. By applying a well-defined force and recording the subsequent changes in the same unit, definitive relationships between mechanical stimuli and their intracellular effect can be developed. Therefore, the effects of the magnitude, duration, and frequency of a certain load regimen application can be examined unequivocally. This approach presents the additional advantage of uncovering the direct role of biomechanical forces as potential stimulators of tissue healing or degeneration via observation of particular changes in gene regulation related to regenerative, catabolic, or apoptotic cell behavior (Figure 1). Forces precipitating the onset of osteoarthritis may be observed and studied to further our knowledge of this degenerative
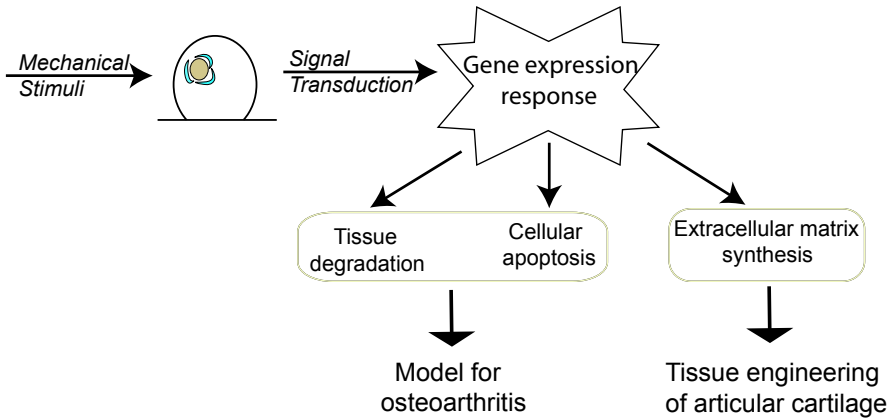
**Figure 1.** Response of a single cell to mechanical forces. Mechanical stimuli inducing tissue degradation and cellular apoptosis may be used at models for osteoarthritis. In contrast, stimuli leading to ECM synthesis should be included in any tissue engineering approach for articular cartilage.

disease. Similarly, loading regimens inducing favorable gene responses can be easily identified and utilized in further work to develop articular cartilage neotissue. Furthermore, mechanical stimuli may also be examined in conjunction with additional exogenous factors, such as growth factors or oxygen tension levels. Combinations of these factors have exhibited a synergistic effect on chondrocyte metabolism and may prove to be quite useful in tissue engineering articular cartilage [Gooch et al. 2001; Hansen et al. 2001; Jin et al. 2003; Mauck et al. 2003; Scherer et al. 2004], yet are beyond the scope of this review.

While examinations on a single cell level present several distinct advantages in tissue engineering, they are not without their own caveats. The response of individual cells seeded on a dish can potentially be quite different from that of cells interdispersed within an extracellular matrix or polymer scaffold. In these situations, which are more related to the chondrocyte's environment in vivo, mechanical stimuli are not directly applied onto the cell but rather are a result of a secondary response, such as gel compression or shear due to induced fluid flow. Therefore, the methods used to stimulate and mechanically test individual cells, which will be discussed in detail later, can never fully reproduce the true mechanical environment within articular cartilage. It is also known that cells within articular cartilage are in constant communication with each other and these molecular signals can also affect chondrocyte behavior and gene response [D'Andrea and Vittur 1996; D'Andrea et al. 1998; D'Andrea et al. 2000]. However, it should be noted that single cell research is simply the first step in a modular approach to tissue engineering of articular cartilage. The research performed with individual cells can provide great insight into the mechanical environment necessary to elicit favorable cellular responses, which can then be translated upwards toward the tissue level. Findings which elucidate loading parameters favorable to the individual cell can be utilized in subsequent phases, which will eventually involve cells embedded within a matrix. This knowledge may include the ideal type of loading regimen (hydrostatic pressure, direct compression, shear, and so on) and their corresponding force levels, applied to the tissue construct, which will bring about the production of essential matrix components from the cells.
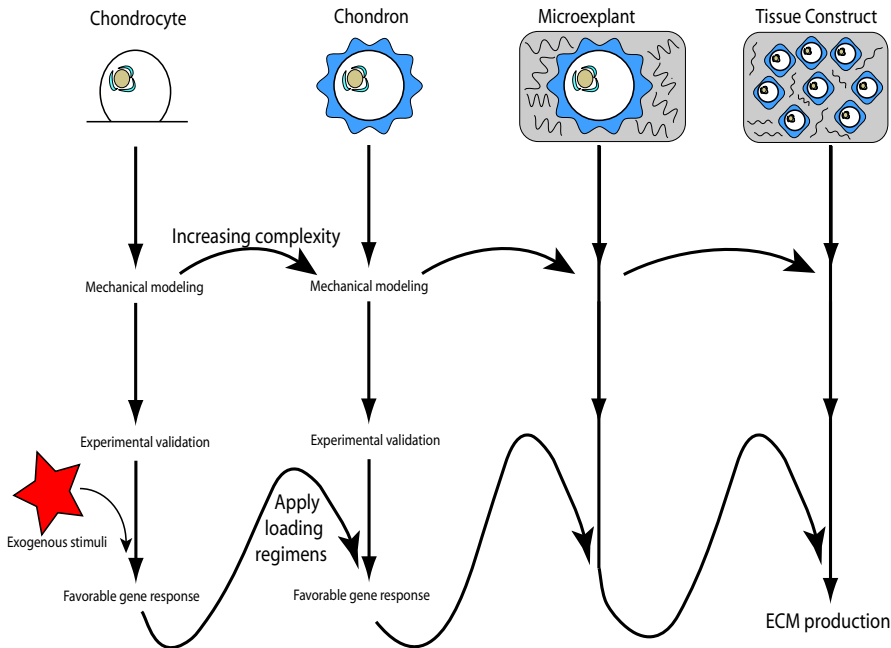
**Figure 2.** Functional unit approach. Research with a single cell will provide an excellent starting point for subsequent research of the chondron, microexplant, and cartilage tissue. Each phase consists of three steps which examine the biomechanical properties of individual units within articular cartilage. With each added level of complexity, researchers gain invaluable insight toward understanding the effects of mechanical forces on cellular behavior. This knowledge may be used to elucidate regimens of mechanical stimulation necessary toward tissue engineering articular cartilage.

The fundamental unit approach to tissue engineering of articular cartilage consists of four interrelated phases: single cells, single chondrons, microexplants, and tissue constructs, each of which thoroughly examines mechanical behavior through increasingly complex models and uses a series of steps that are translatable from one phase to the next. Each phase contains three main steps. Researchers first need to develop mathematical models for the properties and characteristics of each unit. These models then need to be validated through direct experimental techniques. Finally, various combinations of the previously described exogenous factors can be applied to the single unit in order to determine ideal stimulation levels to produce a well-developed neotissue (Figure 2). Moving stepwise through each phase, researchers could adapt this knowledge to account for the additional PCM and ECM regions to reach desired levels for gene expression. Advanced mechanical modeling will enable researchers to correlate the applied stresses or strains back down to the cellular level for each phase. Multiscale models have recently been developed to account for the intrinsic matrix variation and cellular spatial arrangement within articular cartilage. These models can be utilized to predict the local mechanical environment of chondrocytes under various loading conditions [Guilak and Mow 2000; Breuls et al. 2002; Wang et al. 2002].

Moreover, models used to examine the properties of individual cells can be translated to the tissue level by maintaining the same underlying physical principles and assumptions governing cellular properties.

With each added level of complexity, the mechanical model for chondrocytes will not change, enabling researchers to translate these properties to different spatial scales. Therefore, those mechanical loading regimens which elicit the upregulation of ECM genes can be applied and tailored to each subsequent phase in the approach, in order to work toward the greatest ECM production due to stimulation at the tissue level. The fundamental unit approach provides researchers with an indispensable tool for translating the effect of mechanical forces back down to the cellular level and for developing strong and healthy cartilage tissue in vitro.

## 3. Cellular microenvironment

To accurately model the mechanical characteristics of single cells and chondrons, an appreciation of the cellular microenvironment is necessary. This is an essential component of the first step of the fundamental unit approach and will enable researchers to develop appropriate mechanical models of increasing complexity describing each matrix layer surrounding the cell, as well as the cell itself. All components within the immediate surroundings of the chondrocyte can potentially act as force transducers onto the cell and affect cellular transcriptional changes. Mechanical forces applied to cartilage tissue are conveyed down to the subcellular levels via linkages between the ECM, PCM, cytoskeleton, and nuclear lamina. The cellular microenvironment consists of the latter three connections, which serve as the principal mechanical components of the chondron.

**3.1. *PCM composition and function.*** The chondron, that is, the chondrocyte together with its PCM, has been studied for years and much progress has been made to establish its structure. The PCM is known to contain collagen types II, VI, and IX [Poole et al. 1988a; Poole et al. 1988b], and significant concentrations of decorin [Poole et al. 1996], hyaluronan [Goldberg and Toole 1984], and sulphated glycosaminoglycans [Poole et al. 1990]. Of the aforementioned proteins, type VI collagen is considered a key molecular marker of chondron microanatomy [Poole et al. 1988a; Poole et al. 1992] and is essential in maintaining the microenvironment of the cell. The glycoprotein fibronectin is also localized within the pericellular region in adult articular cartilage [Poole et al. 1990] and has been shown to interact directly with type VI collagen to create a scaffold for the assembly of other essential PCM proteins [Chang et al. 1997].

The biochemical and biomechanical contributions of the PCM to the chondrocyte microenvironment have also been studied. In particular, it is known that the PCM surrounding the chondrocyte organizes and constructs collagen fibrils [Poole 1997] regulates cellular osmolarity [Hing et al. 2002] and modulates growth factor interactions with the enclosed cell [Ruoslahti and Yamaguchi 1991]. The mechanical properties of the PCM are known to differ from the larger territorial and interterritorial matrices inside the cartilage tissue and are approximately 10-fold greater in stiffness than the enclosed chondrocyte [Guilak et al. 1999; Guilak and Mow 2000; Alexopoulos et al. 2003; Alexopoulos et al. 2005b; Alexopoulos et al. 2005a]. In this manner, the PCM acts as a biomechanical buffer of stresses applied onto the chondrocyte.

Considering these biochemical and biomechanical functional roles, it is no surprise that the PCM has received special attention in tissue engineering of articular cartilage and research toward maintaining a healthy, well-developed ECM [Larson et al. 2002; Kelly et al. 2004; Graff et al. 2003; Fraser et al. 2006].

**3.2.** *Cytoskeleton.* The cytoskeleton provides a framework for cellular structure and plays a key role in the mechanical characteristics of the cell. It is primarily composed of three main structural proteins: microtubules, microfilaments, and intermediate filaments [Becker et al. 2003]. Understanding the properties and behavioral changes of cytoskeletal components is important for discerning the mechanobiology of individual chondrocytes.

**3.2.1.** *Cytoskeletal components.* Microtubules extend over the entire cytoplasm of the cell, forming a scaffold upon which other cytoskeletal elements can branch out [Langelier et al. 2000]. Due to their omnipresence, microtubules function to support cellular shape and the movement of organelles. They are also the largest fibers of the cytoskeleton and consist of hollow cylindrical tubes of the globular protein tubulin [Becker et al. 2003].

Intermediate filaments span the entirety of the cell and serve primarily to mechanically link the nuclear lamina with integrin receptors on the cell surface [Maniotis et al. 1997]. They are considered the most stable of cytoskeletal elements, comprised of protofilaments or fibrous proteins. Intermediate filaments are also involved in providing additional support in maintaining cell shape and structure [Becker et al. 2003].

Microfilaments, which are the smallest of cytoskeletal elements and are composed of two threaded polymer chains of $F$-actin, are involved primarily in cell motility [Becker et al. 2003]. These proteins are located cortically, with many focal adhesion points along the cell membrane. In addition, microfilaments are important in resisting cell deformation due to applied mechanical forces, particularly shear stresses [Janmey et al. 1991].

**3.2.2.** *Tensegrity model.* The organization of the cytoskeleton has been described using a tensegrity model [Wang et al. 1993; Ingber 1997; Chen and Ingber 1999; Volokh 2003]. This approach attempts to explain cellular structure and behavior by modeling the cytoskeleton as an interwoven mesh of discrete compressive and tensile elements in a three-dimensional configuration. Applying the tensegrity model to the cytoskeleton, the microtubules serve as struts which resist compression and which can reorient their position due to prestresses produced by the contractility of both microfilaments and intermediate filaments. The various mesh elements can be anchored to each other or the ECM. Applied stresses are distributed and transmitted through this lattice, depending on the preferred directionality of the mechanical coupling between elements [Chen and Ingber 1999].

**3.2.3.** *Response to mechanical forces.* It is believed that the cytoskeleton plays a direct role in mechanotransduction within the cell [Wang et al. 1993; Ingber 1997; Wang and Stamenovic 2000]. The structure and organization of cytoskeletal proteins has been shown to have a strong influence in force transmission onto the nucleus [Wang et al. 1993] and the mechanical properties of the chondrocyte as a whole [Trickey et al. 2004; Leipzig et al. 2006]. It has further been reported that the cytoskeleton remodels and thickens in response to applied mechanical loads [Durrant et al. 1999; Jortikka et al. 2000; Langelier et al. 2000], suggesting that these organizational or conformational changes may effect mechanical signal transduction within the cell, and thereby alter the regulation of essential ECM proteins [Jortikka et al. 2000].

**3.3.** *Nucleus.* The mechanical properties of the chondrocyte's nucleus are also of great interest. The chondrocyte nucleus has been described as a viscoelastic structure [Guilak et al. 2000], containing both solid and fluid elements. It is known to be considerably stiffer than the cell itself, potentially indicating a

unique nuclear function to mediate mechanical forces with the enclosed genomic DNA. Moreover, it has been shown that the nucleus will respond, in terms of its physical dimensions and volumetric properties, to an induced strain applied on the cartilage tissue level [Guilak 1995], and that these changes correlate with the synthesis of certain ECM proteins [Buschmann et al. 1996].

The nucleus is supported by a filamentous meshwork known as the nuclear lamina, positioned underneath the nuclear envelope. This lamina provides a framework for nuclear structure and serves as an intermediary between the cytoskeletal network and chromatin [Aebi et al. 1986]. Hence, deformation of the nucleus is often seen as the most direct transducer of cellular mechanotransduction. Alterations in the structural characteristics of the nucleus can cause changes in chromosome alignment via the lamina network, affecting the accessibility of genomic sequences to various transcriptional factors or other molecular signals.

## 4. Single cell approach

While studies of cartilage mechanobiology can quantify stress and strain at the bulk tissue level, few studies have attempted to quantify the local mechanical environment around the cell. Doing so would help to identify levels of mechanical stimuli at the cellular level relevant to cartilage health and disease [Stockwell 1987]. By applying different mechanical models and making the necessary geometric and physical assumptions, researchers can describe with growing accuracy the mechanical characteristics of single cells. This first phase of the fundamental unit approach consists of mathematical modeling, validating these models through direct experimentation, and determining appropriate mechanical loading regimens to elicit favorable gene responses on the single cell level.

**4.1.** *Cellular mathematical modeling.* Three models, of increasing complexity, have been used in recent literature to determine the mechanical properties of individual chondrocytes: 1) punch model, 2) viscoelastic model, and 3) linear biphasic model. While all of the models arrive at different constitutive relations between stress and strain within the continuum, all have been developed using basic physical principles and can accurately predict the equilibrium deformation of a cell due to an applied force. The various models serve as a foundation for later mathematical models describing more complex situations such as those with the chondron or tissue microexplants.

**4.1.1.** *Punch model.* The punch model is one of the simplest in single cell mechanics, treating the cell as a linearly elastic, homogeneous, isotropic, and incompressible half-space. Although the punch model does not account for strain- or time-dependent responses by the cell, it is useful in ascertaining the elastic modulus of stiffer, anchorage-dependent cells, namely chondrocytes. It has been applied in both the testing modalities of cell indentation and micropipette aspiration to determine the mechanical properties of single cells.

The solution to indentation experiments can be obtained by solving Cauchy's equations of motion under conditions of axial symmetry. Neglecting inertial forces, the equations governing stress distributions

reduce to

$$\frac{d\sigma_{rr}}{dr} + \frac{d\sigma_{rz}}{dr} + \frac{1}{r}(\sigma_{rr} - \sigma_{\theta\theta}) = 0, \tag{1}$$

$$\frac{d\sigma_{rz}}{dr} + \frac{d\sigma_{zz}}{dz} + \frac{\sigma_{rz}}{r} = 0. \tag{2}$$

Then by representing the stress components by a single function and applying the method of Hankel transforms, a relationship between applied force and Young's modulus can be derived for a given indenter displacement [Harding and N. 1944; Tran-Cong 1997]. There are three common indenter shapes that can be used to prod the cell: conical, spherical, and flat-ended cylindrical. For the rigid conical punch, the solution for Young's modulus is

$$E = \frac{2P(1 - \upsilon^2)}{\pi \varepsilon a}, \tag{3}$$

where $P$ is the applied force, $\upsilon$ is the Poisson's ratio of the cell, $\varepsilon$ is the indentation depth, and $a$ is the indenter radius at the cell's surface [Harding and N. 1944]. For a rigid spherical indenter, the Young's modulus is shown to be

$$E = \frac{3P(1 - \upsilon^2)}{4R^{1/2}\varepsilon^{3/2}}, \tag{4}$$

where $R$ is the radius of the indenting sphere [Harding and N. 1944]. The last case of a cylindrical end is the most common among indentation experiments. In this situation, the cell's Young's modulus is

$$E = \frac{P(1 - \upsilon^2)}{2\varepsilon a}. \tag{5}$$

The punch model solution under the experimental modality of micropipette aspiration has been previously described by Theret et al. [1988], and later compared to more complex continuum mechanics models [Jones et al. 1999; Haider and Guilak 2002; Youn et al. 2006]. This model describes the Young's modulus of the cell as

$$E = \frac{3a\Delta P}{2\pi L}\phi_p(\eta), \tag{6}$$

where $\Delta P$ is the applied external suction pressure, $a$ is the inner radius of the micropipette, $L$ is the distance the cell is aspirated in the micropipette, and $\phi_p(\eta)$ is a function of the inner and outer radii of the micropipette.

**4.1.2.** *Viscoelastic model.* The viscoelastic model accurately depicts the behavioral response of chondrocyte cells to an applied stress or strain, by describing the cell as containing both fluid-like and solid-like structural elements. The most common viscoelastic model for the chondrocyte is the standard linear solid (SLS), where the cell is represented using a circuit analog of springs and dashpots. The springs are strain-dependent elements, whereas the dashpots are varying according to strain rate. In the SLS model, the spring is in series with an element consisting of a spring and dashpot in parallel. Using this one-dimensional analog, the constitutive equation describing the stress and stress relationship is written

$$(E_1 + E_2)\sigma + \eta\frac{d\sigma}{dt} = E_1 E_2 \varepsilon + E_1 \eta \frac{d\varepsilon}{dt}, \tag{7}$$

where $E_1$ and $E_2$ are the elastic constants for the two springs, $\eta$ is the coefficient of viscosity for the fluid element, and $\sigma$ and $\varepsilon$ represent the stress and strain within the system, respectively [Ozkaya and Nordin c1999].

By including characteristics of both viscous fluids and elastic solids, this model can predict the cellular creep response to an applied constant stress and stress-relaxation response to a step strain. The SLS model has been used to describe chondrocyte behavior in many testing modalities, including cell indentation, unconfined compression, and micropipette aspiration. The indentation solution was first developed by Ting [1966] to describe the behavior of a viscoelastic half-space. A more recent creep indentation solution was developed by Cheng et al. [2000] and used by Koay et al. [2003] to test the material properties of single chondrocytes. The SLS model has also been applied to micropipette aspiration experiments using a solution originally developed by Sato et al. [1990] and to unconfined compression creep tests on single cells using a relationship described by Leipzig and Athanasiou [2005]. This model allows researchers to elucidate three mechanical parameters describing the individual chondrocyte: instantaneous modulus ($E_0$), relaxed modulus ($E_\infty$), and apparent viscosity ($\mu$) of the continuum [Koay et al. 2003].

**4.1.3.** *Linear biphasic model.* Developed by Mow et al. [1980], the biphasic model describes a material as having both a fluid and solid phase. Though initially difficult to conceive, this theoretical model treats each spatial point within the continuum as a mixture of both a liquid and a solid. To reduce the relations of conservation of mass and momentum describing this continuum to workable equations, several assumptions need to be made. The solid matrix is assumed to be linearly elastic, isotropic, nondissipative, and incompressible, and the fluid phase is inviscid and also incompressible. Additionally, the fluid is assumed to flow through the porous solid medium, creating a frictional drag force which accounts for the time-dependent behavior of the continuum. These assumptions enable the following constitutive relationships to be made for the solid matrix and fluid components:

$$T^s = -\phi^s pI + \lambda_s eI + 2\mu_s E,$$
$$T^f = -\phi^f pI,$$

where $T^s$ and $T^f$ are the stress tensors for the solid and fluid phases respectively, $\phi$ denotes the volume fraction for each phase, and $p$ is the hydrostatic pressure within the medium. Further denoted for the solid matrix, $E$ is the infinitesimal strain tensor and $e$ is its volumetric change, and $\lambda$ and $\mu$ are the Lamé constants [Mak et al. 1987].

Applied to single cells, this model correctly depicts the interaction of both fluid and solid behavioral components inside the confines of the cell membrane. Solid elements, such as cytoskeletal proteins, the nucleus, and organelles create a porous continuum for the free flowing cytoplasmic fluid. Through cell indentation [Shin and Athanasiou 1999], unconfined compression [Leipzig and Athanasiou 2005], and micropipette aspiration [Trickey et al. 2006] experimental techniques, the biphasic model has been used to extract the following three intrinsic mechanical properties of the material's solid phase: the aggregate modulus ($H_A$), permeability ($k$) and Poisson's ratio ($\upsilon_s$). In addition, more complex versions of the biphasic model have recently been developed to predict cellular behavior within articular cartilage tissue [Wu et al. 1999; Guilak and Mow 2000].

**4.2.** *Experimental validation.* Several experimental modalities have been used on single chondrocytes in recent years. Applying the three mechanical models described in the first step of the single cell
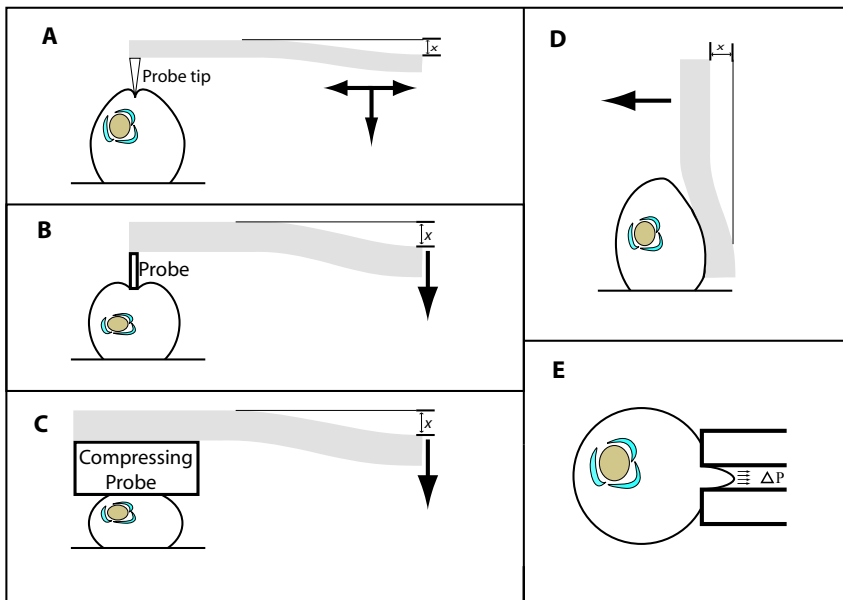
**Figure 3.** Experimental modalities for mechanically testing single chondrocytes. Techniques of (A) atomic force microscopy, (B) cytoindentation, (C) unconfined compression, and (D) cytodetachment utilize the anchorage-dependent characteristics of chondrocytes to obtain relevant mechanical properties. Each of these four techniques applies a controlled force or displacement to the cell through a probe attached to a cantilever. The probe deflection $x$ due to the cell's reactive force is as shown. In contrast, (E) micropipette aspiration employs a micropipette to apply a controlled suction pressure $\Delta P$ on the cell, and the resulting deformation is recorded.

approach, researchers have obtained cellular characteristics through either stress- or strain-controlled experiments. Major advancements in high precision systems have made it possible to apply forces or deformations on a scale relevant to that of a single cell. While not an all-inclusive list, several of the more prominent single cell experimental techniques include:

- atomic force microscopy
- cytoindentation
- cytodetachment
- unconfined compression
- micropipette aspiration (Figure 3).

The first four methods take advantage of the anchorage-dependent characteristics of chondrocytes to elucidate salient mechanical properties, while micropipette aspiration tests generally treat the cells as free-floating within a fluid medium. A summary of the salient mechanical properties obtained through the aforementioned experimental techniques is delineated in 1.

**4.2.1.** *Atomic force microscopy.* Atomic force microscopy (AFM) has been used to provide researchers with a high-resolution topographic description of variations along the cell surface. With accuracy on the order of picometers, AFM is a popular technique to obtain a detailed spatial map regarding local pressure points on the cell. As an example, Bader et al. [2002] used AFM to examine the nonlinear force–displacement response of single chondrocytes at various positions on the cell surface. Their results showed that the center of the cell was most resistant to an applied indentation. Therefore, AFM can be quite advantageous in studying heterogeneous materials, such as chondrocytes and their associated matrix, where highly localized differences exist.

Current AFM techniques generally consist of a pyramidal-shaped probe, with a diameter on the order of nanometers, attached to cantilever beam indenting the cell. The minute contact area of the probe and the cell provides AFM its high local precision. A piezoelectric motor displaces the probe toward the cell and force levels upon indentation are measured using Hooke's law, $F = kx$, based on the deflection, $x$, and stiffness, $k$, of the cantilever beam. Controlled feed back loops are used to maintain either desired constant force or displacement levels. Force and displacement data, over time, can then be fitted to elastic, viscoelastic, or biphasic models to acquire specific material properties.

A study by Darling et al. [2006] examined the viscoelastic nature of porcine articular chondrocytes from both superficial and middle/deep zones using AFM. The authors derived a viscoelastic solution for the punch problem with a spherical indenter (see Equation (4)). Applying a ramp velocity of 6.25 $\mu$m/s to reach a target force of 2.5 nN, held for 60 seconds at the center of the cell, the stress-relaxation experiments yielded relevant mechanical properties. It was found that superficial zone chondrocytes were stiffer than middle/deep cells in terms of instantaneous moduli (0.55 kPa versus 0.29 kPa) and relaxed moduli (0.31 kPa versus 0.09 kPa), and had a greater apparent viscosity (1.15 kPa-s versus 0.61 kPa-s).

Ng et al. [2007] recently utilized AFM to investigate chondrocyte viscoelastic properties with its developing PCM. Individual chondrocytes, with and without their associated matrix, were placed in custom-made pyramidal wells in preparation for testing. This provides the significant advantage of testing individual cells or chondrons without requiring them to be adherent on a substrate. Accurate spatial maps were obtained and finite element and Hertzian modeling was used to obtain biomechanical properties. In addition, a hysteresis upon unloading the probe was also observed, confirming previous findings regarding the time-dependent behavior of chondrocyte cells.

**4.2.2.** *Cytoindentation.* One increasingly popular technique to study the mechanical properties of single cells is cytoindentation. This recently developed procedure investigates a cell's ability to withstand controlled indentations by a flat-ended miniature borosilicate glass probe 5 $\mu$m in diameter, which is attached to a much larger cantilever beam. Cytoindentation utilizes similar cantilever principles as in AFM to determine the applied force based upon the deflection of the beam. A force transducing system is then employed to measure the cell's reactive force, on the order a single nanonewton, for a given displacement of the probe. The earliest model of the cytoindenter was developed by Shin and Athanasiou [1999] to study the biomechanical properties of individual MG63 osteosarcoma cells. In this version of the device, the deflection of the cantilever was measured by a dual photodiode system, enhanced by light microscopy. This system monitors the displacement of the end of the cantilever beam as a function of the voltage difference between the two photodiodes and is designated as the displacement on the cell. A piezoelectric motor applied a controlled ramp displacement with 0.275 $\mu$m increments to a 2.0 $\mu$m final

depth and a linear biphasic finite element model was used to determine cellular characteristics based upon recorded force measurements. The results showed that the cells had a permeability of $1.18 \times 10^{-10}$ m$^4$N$^{-1}$s$^{-1}$, which is strikingly greater than that of articular cartilage [Ateshian et al. 1997]. Additionally, the cells had an aggregate modulus of 2.05 kPa, shear modulus of 0.41 kPa, and Poisson's ratio of 0.37.

Recently, Koay et al. [2003] modified the cytoindenter setup to enable a laser micrometer to record the displacement at the end of the cantilever. Using a closed loop algorithm, the authors applied creep tests on single chondrocytes at a test load of 50 nN for either 15 or 20 seconds. Both punch and viscoelastic continuum models were used to determine the mechanical properties of the chondrocytes. The punch model (see Equation (5)) yielded an average Young's modulus of 1.10 kPa. The viscoelastic model resulted in an instantaneous modulus of 8 kPa, relaxed modulus of 1.01 kPa, and apparent viscosity of 1.5 kPa-s for the chondrocyte.

**4.2.3.** *Cytodetachment.* The cytodetacher measures the adhesive properties of cells attached to various substrata and also can be used to examine the response in cellular behavior to an applied shearing force [Athanasiou et al. 1999]. In this device, a piezoelectric translator drives a small diameter carbon filament, attached to a larger glass cantilever, parallel to the cell substratum. Similar to experimentation with the cytoindenter, cantilever beam theory is utilized to calculate the reactive forced based upon the deflection of the beam recorded by dual photodiodes. The first study employing the cytodetacher examined the force necessary to detach articular chondrocytes after seeding for 2 hours on untreated glass, bovine serum albumin-coated glass, and fibronectin coated glass. It was observed that the quantified adhesiveness of the cells on fibronectin (72.6 nN) were significantly greater than both the bovine serum albumin (20.3 nN) and untreated glass (38.9 nN) experimental groups [Athanasiou et al. 1999]. Follow-up studies further modified the cytodetacher and examined the temporal characteristics of chondrocyte adhesive properties. It was observed that cellular adhesion strength increased significantly with seeding time and could be attributed to a spreading of the actin cytoskeleton [Hoben et al. 2002; Huang et al. 2003]. Quantifying cellular adhesion strength will prove to be quite useful when examining cell-matrix interfaces in more complex situations in subsequent phases of the fundamental unit approach.

**4.2.4.** *Unconfined compression.* Additional simple modifications of the cytoindenter and cytodetacher have made it possible to examine the effects of unconfined compression on single chondrocytes. This testing modality has been extensively utilized to study both the material properties and mechanical behavior of chondrocytes [Leipzig and Athanasiou 2005; Leipzig et al. 2006; Shieh and Athanasiou 2006; Shieh et al. 2006]. In order to adapt the mechanical models to extract properties via this experimental technique, a suitable geometry for the chondrocyte was identified to accurately depict the anchorage-dependent properties and structure of the cell. Using vertical scanning interferometry, Scott et al. [2005] determined that a disc-shape would be an appropriate model for the cell, and Leipzig and Athanasiou [2005] used this shape to develop unconfined creep compression solutions for elastic, standard linear solid, and linear biphasic mechanical models. Using the cytoindenter device, the original 5 $\mu$m diameter indenter was replaced with a wider 50.8 $\mu$m diameter tungsten probe to apply constant loads of 75 nN for 45 seconds onto the chondrocyte. It was observed that viscoelastic model best fit the creep behavior of the individual cell, most notably in the early response phase to the applied force. Leipzig and Athanasiou [2005] also determined the elastic modulus for chondrocyte to be 2.55 kPa. Curvefitting the data to the viscoelastic model resulted in an instantaneous modulus of 2.47 kPa, relaxed modulus of 1.48 kPa, and

apparent viscosity of 1.92 kPa-s. Finally the biphasic fit yielded an aggregate modulus of 2.58 kPa, cell permeability of $2.57 \times 10^{-12}$ m$^4$N$^{-1}$s$^{-1}$ and Poisson's ratio of 0.069.

Shieh and Athanasiou [2006] expanded unconfined compression experiments to look at zonal variations and attachment times in chondrocyte viscoelastic mechanical properties. Similar to later findings by Darling et al. [2006], it was determined that superficial zone cells were significantly stiffer than those from the middle/deep region in terms of instantaneous moduli (1.59 kPa versus 0.69 kPa), relaxed moduli (1.20 kPa versus 0.49 kPa), and apparent viscosity (6.32 kPa-s versus 0.18 kPa-s) after 18 hours of seeding. Similar trends were also observed in the experimental group given three hours to attach.

Shieh et al. [2006] also modified the original cytodetacher setup to study the response of single chondrocytes to various levels of strain under unconfined compression. By placing seeded chondrocytes perpendicular to the advancing probe, the authors were able to apply specific deformations onto the individual cell for 30 seconds and to record the subsequent cellular recovery behavior through videocapture. Quite interestingly, the cells exhibited a change in their response around 25–30% strain levels. This critical point in chondrocyte behavior may have vast implications toward determining threshold levels for eliciting particular biochemical responses from the cell in terms of tissue engineering articular cartilage. Moreover, this yield strain may be analogous to an intrinsic threshold where bulk tissue is damaged and chondrocytes no longer experience their normal in vivo mechanical environment.

**4.2.5.** *Micropipette aspiration.* One of the earlier methods to measure the mechanical characteristics of individual cells is through micropipette aspiration. In this technique, a miniature pipette applies a negative suction pressure onto the surface of the cell, thereby deforming its membrane inward through the pipette. By recording this event, researchers are able to calculate salient mechanical properties of the cell based upon the amount of membrane deformation, the required suction pressure levels, and the geometric relations pertaining to the shape of the pipette. Similar to the cytodetacher, this technique can also be used to quantify the mechanical adhesiveness of a cell attached to a particular substratum.

Micropipette aspiration has frequently been used to determine the mechanical properties of chondrocytes harvested from both normal and osteoarthritic articular cartilage. Jones et al. [1999] first used this approach to compare cellular mechanical characteristics, such as Young's modulus and volumetric properties, from both healthy and diseased tissue. They applied maximum pressures between 0.05 and 1 kPa through a micropipette with an inner diameter of approximately 5 $\mu$m. By modeling the cell as a homogeneous elastic half-space (see Equation (6)), they determined that no differences existed between the Young's modulus of normal and osteoarthritic chondrocytes (0.65 kPa versus 0.67 kPa). However, significant differences were observed in cell volume changes immediately and 600 seconds after complete aspiration of the cells into the micropipette. Normal chondrocytes only exhibited an 11% volume change, while osteoarthritic cells lost 20% of their volume. A similar study by Trickey et al. [2000] applied the standard linear solid model to micropipette experiments on normal and osteoarthritic chondrocytes. Their results showed that cells from diseased cartilage tissue were stiffer and more viscous than healthy cells, with regards to instantaneous moduli (0.63 kPa versus 0.41 kPa), relaxed moduli (0.33 kPa versus 0.24 kPa), and apparent viscosity (5.8 kPa-s versus 3.0 kPa-s). Trickey et al. [2006] recently applied a biphasic model to compare the recovery behavior of chondrocytes from the two sources. While there were no significant differences between the Poisson's ratio of normal and osteoarthritic cells (0.38 versus

0.36), osteoarthritic chondrocytes did exhibit a greater characteristic recovery time upon release of the suction pressure.

**4.3.** *Effects of mechanical stimuli on single cells.* The last step in the single cell approach is to determine regimens of mechanical stimulation that elicit favorable gene responses. Using the knowledge attained through modeling and experimental validation, researchers can tailor the applied stimuli to the individual cell. Leipzig and Athanasiou [2006] and Shieh and Athanasiou [2007] have most recently used the technique of single cell reverse transcriptase polymerase chain reaction (scRT-PCR) to qualify gene expression changes due to direct mechanical stimulation. scRT-PCR has recently been validated as a highly sensitive and effective means to detect alterations in gene regulation within a single cell [Eleswarapu et al. 2007]. Briefly, their experimental set-up involved using the previously described unconfined compression device to apply particular loading regimens upon adherent chondrocytes. Then through a custom designed micropipette aspirator, the same cell was removed from its substrate and placed into a lysis buffer in order to disrupt the cell membrane. Following protocols essentially similar to that of traditional RT-PCR, the RNA for each individual cell was isolated and reverse transcribed into cDNA. Specific primers and probes for DNA sequences of interest were optimized in conjunction with real-time PCR to measure relative gene expression levels.

Shieh and Athanasiou [2007] examined the effects of static, intermittent, and dynamic compression cycles on the gene expression levels for type II collagen, aggrecan, tissue inhibitor of metalloproteinase-1 (TIMP-1), and matrix metalloproteinase-1 (MMP-1) on individual chondrocytes. Both type II collagen and aggrecan genes are considered related to regenerative pathways for articular cartilage. In contrast, TIMP-1 and MMP-1 are catabolic genes, known to be involved in matrix degeneration. A housekeeping gene of GAPDH was used to identify any variability between samples. It was found that static compression of 50 and 100 nN downregulated type II collagen and aggrecan, while dynamic loading at the same force levels significantly alleviated these negative effects. Leipzig and Athanasiou [2006] also looked at the effects of mechanical stimulation on chondrocyte gene expression. Adding an additional complication, the authors examined 25 nN, 50 nN, and 100 nN static loading in the presence of known growth factors, TGF-$\beta$1 and IGF-1. It was observed that increased static loading significantly decreased type II collagen and aggrecan levels, and increased TIMP-1 abundance. Furthermore, the addition of soluble growth factors provided a form of mechanoprotection against the detrimental effects of static loading. Taken together, these results clearly demonstrate that it is possible to measure gene expression on the single cell level, providing credence to future experiments on the chondron level. Moreover, these findings correlate very well with tissue engineering studies involving large number of chondrocytes in dynamically loaded matrices, with and without the addition of growth factors [Mauck et al. 2003; Kisiday et al. 2004; Ng et al. 2006]. Research on the single cell level may therefore prove to be useful toward identifying the ideal frequency of these dynamic loads applied to the tissue construct, and their associated magnitudes.

## 5. Single chondron approach

After studying the biomechanical properties and behavior of single cells, the next logical progression within the fundamental approach is to look at single chondrons. Examinations of the characteristics of the chondron include cell-matrix interactions and the three-dimensional configuration of the chondrocyte

embedded in articular cartilage tissue. The information gained from experiments with single chondrons sheds light on how the tissue functions and responds in its mechanical environment, and contributes to the overall goal of generating a tissue that more closely mimics the properties of native cartilage. By including the PCM in these experiments, researchers gain a physiologically relevant model of chondrocyte behavior and structure in vitro, while maintaining all the previously mentioned advantages as in the single cell approach. To date, little research has been completed to directly correlate the effect of mechanical stimuli and gene expression on single chondrons. However, the potential for this research is extensive, and significant strides have already been made in chondron mathematical modeling and experimental techniques.

**5.1.** *Chondron mathematical modeling.* To accurately depict the mechanical effect of the PCM on chondrocyte behavior, mathematical models for the chondron need to include a cell-matrix interface to describe the bilayered nature of this continuum. There are currently two main models used in the mechanical testing of single chondrons: 1) the layered half-space model, and 2) the multiscale biphasic model. Modeling the interface of the cell and its immediate surroundings presents several significant advantages in articular cartilage micromechanics. First, researchers can accurately portray the role of the PCM as an immediate transducer of mechanical forces onto the enclosed chondrocyte. Second, peak stress and flow conditions around the cell may be predicted. Third, the micromechanical environment of the cell can be directly linked to cellular metabolic and structural changes to further understand chondron mechanobiology.

**5.1.1.** *Layered half-space model.* The layered elastic half-space model is an extension of the previously described punch problem, including an elastic layer lining the elastic half space. The outer layer (corresponding to the PCM) is assumed to be infinite, isotropic, and homogeneous. Similarly, the enclosed region, corresponding to the chondrocyte, is treated as an isotropic, homogeneous, and semiinfinite half-space. Each layer is assumed to be a linearly elastic solid, with different Lamé elastic constants, and both layers are in perfect contact with each other [Dhaliwal 1970]. Solutions have been developed for the stress distribution within a bilayered material undergoing static deformation by a flat-ended rigid circular indenter [Dhaliwal 1970; Schwarzer 2000] or by a given force application [Horton et al. 1987]. These solutions can be potentially applied to the indentation problem of individual chondrons, although presenting practical experimental hurdles. Kumar and Hiremath [1982] have solved the punch problem for an annular shaped indenter and Alexopoulos et al. [2003] have extended this solution in order to determine the mechanical characteristics of single chondrons using micropipette aspiration.

**5.1.2.** *Multiscale biphasic model.* The multiscale biphasic model utilizes a finite element approach to elucidate the mechanical characteristics of the individual matrix layers extending radially outward from the chondrocyte. This approach considers cell-PCM and PCM-ECM interactions within articular cartilage and has been employed to determine the mechanical properties of the chondrocyte's PCM. Bachrach et al. [1995] originally described the cell-matrix interface within soft biological tissues under confined compression conditions. Later, Wu and Herzog [2000] developed a model to determine the effect of time and position under unconfined loading conditions in the local mechanical environment of the chondrocytes embedded within the articular cartilage matrix. A further advancement of this approach was the inclusion of distinct matrix layers surrounding the cell, particularly pertaining to the PCM and ECM, into a biphasic finite element model by Guilak and Mow [2000]. Each level, including the cell, is assumed

to be a biphasic material with continuous boundary conditions at each interface. Most recently, a radial biphasic model has been developed by Haider [2004] to describe the transmission of mechanical forces throughout the chondron.

**5.2.** *Experimental validation.* Due to practical limitations, the majority of single chondron mechanical experiments have utilized the technique of micropipette aspiration. This is in large part due to the non-adhesive properties of the PCM, thus making it difficult to apply a constant load without the chondron slipping away. Micropipette aspiration has been extensively used to elucidate the osteoarthritic and zonal differences in chondrocyte biomechanical characteristics and its associated PCM [Alexopoulos et al. 2003; Alexopoulos et al. 2005b; Guilak et al. 2005]. Alexopoulos et al. [2003] developed an analytical solution for the layered half-space model for chondron micropipette aspiration. This was the first reported study to directly measure PCM mechanical properties of single chondrons. The authors compared their newly developed layered half-space model to elastic half-space and shell models for the PCM and chondron, respectively. Single chondrons were isolated mechanically from the superficial and middle/deep zones of both healthy and osteoarthritic human articular cartilage tissue. The layered half-space model yielded Young's moduli of 68.9 kPa and 39.1 kPa for normal and osteoarthritic chondrons, respectively, from the superficial zone, and 62.0 kPa and 43.9 kPa, respectively, from the middle/deep zone. Alexopoulos et al. [2005b] later applied a biphasic model to similar single chondron micropipette aspiration experiments and found that osteoarthritic PCM was less stiff and more permeable than normal PCM. These results bolster the observation that PCM, in addition to ECM, degrades in terms of its mechanical integrity upon the onset of osteoarthritis. The layered half-space model was again used by Guilak et al. [2005] to study the zonal variations in chondron mechanical properties within canine articular cartilage. Confirming previous observations, there was little difference in the Young's modulus of the PCM between superficial and middle/deep zones (24.0 kPa versus 23.2 kPa). The aforementioned results for PCM mechanical properties are outlined in Table 1.

## 6. Conclusions

The fundamental unit approach provides several advantages toward elucidating and effecting tissue engineering of articular cartilage. The ability to develop definitive relationships between mechanical stimulation and cellular behavior will enable researchers to define appropriate loading regimens that are favorable to the cell as it develops within a tissue engineered construct. Conversely, an understanding of the mechanical forces pertaining to degenerative processes, that is, osteoarthritis, may allow researchers to devise intervention regimens and other possible treatment modalities. Advanced mechanical modeling enables researchers to correlate mechanical forces between layers and has progressed substantially in recent years. As previously described, the punch model for single cells can be related to the layered half-space model for chondrons and the biphasic model can be adapted to account for discrete matrix layers. Mechanical models on the cellular level can be scaled up to the tissue level by maintaining the same governing principles of chondrocyte behavior and physical properties. Loading regimens can then be translated between phases until one eventually determines an ideal regimen on the tissue construct level which will elicit the production of necessary ECM proteins.

Of further special interest is the possibility of using one of the previously described tissue engineering approaches, particularly on the scale of a single chondron, as a model for articular cartilage development.

| Tissue source | Experimental technique | Mechanical model | Material properties |
|---|---|---|---|
| Porcine femoral joints [Darling et al. 2006] | AFM | Viscoelastic | $E_o = 0.55\,\text{kPa}$, $E_\infty = 0.31\,\text{kPa}$, $\mu = 1.15\,\text{kPa-s}$ [++] |
| | | | $E_o = 0.29\,\text{kPa}$, $E_\infty = 0.17\,\text{kPa}$, $\mu = 0.41\,\text{kPa-s}$ |
| | Micropipette aspiration | Viscoelastic | $E_o = 0.45\,\text{kPa}$, $E_\infty = 0.14\,\text{kPa}$, $\mu = 2.570\,\text{kPa-s}$ |
| Bovine metatarsal joints | Cytoindentation [Koay et al. 2003] | Elastic | $E_Y = 1.10\,\text{kPa}$ |
| | | Viscoelastic | $E_o = 8.00\,\text{kPa}$, $E_\infty = 1.09\,\text{kPa}$, $\mu = 1.50\,\text{kPa-s}$ |
| Bovine metatarsal joints | Unconfined compression [Leipzig and Athanasiou 2005] | Elastic | $E_Y = 2.55\,\text{kPa}$ |
| | | Viscoelastic | $E_o = 2.47\,\text{kPa}$, $E_\infty = 1.48\,\text{kPa}$, $\mu = 1.92\,\text{kPa-s}$ |
| | | Biphasic | $H_A = 2.58\,\text{kPa}$, $k = 2.57 \times 10^{-12}\,\text{m}^4\text{N}^{-1}\text{s}^{-1}$, $\upsilon_s = 0.069$ |
| Bovine metatarsal joints | Unconfined compression [Shieh and Athanasiou 2006] | Viscoelastic | $E_o = 1.59\,\text{kPa}$, $E_\infty = 1.20\,\text{kPa}$, $\mu = 6.32\,\text{kPa-s}$ [++] |
| | | | $E_o = 0.69\,\text{kPa}$, $E_\infty = 0.49\,\text{kPa}$, $\mu = 3.18\,\text{kPa-s}$ |
| Canine femoral articular cartilage [Guilak et al. 2005] | Micropipette aspiration | Layered half-space | $E_Y = 24.0\,\text{kPa}$ [##++] |
| | | | $E_Y = 23.2\,\text{kPa}$ [##] |
| Healthy human articular cartilage | Micropipette aspiration | Punch [Jones et al. 1999] | $E_Y = 0.65\,\text{kPa}$ |
| | | Viscoelastic [Trickey et al. 2000] | $E_o = 0.41\,\text{kPa}$, $E_\infty = 0.24\,\text{kPa}$, $\mu = 3.0\,\text{kPa-s}$ |
| | | Biphasic [Trickey et al. 2006] | $\upsilon_s = 0.38$ |
| | | Layered half-space [Alexopoulos et al. 2003] | $E_Y = 68.9\,\text{kPa}$ [##++] |
| | | | $E_Y = 62.0\,\text{kPa}$ [##] |
| | | Multiscale biphasic [Alexopoulos et al. 2005b] | $E_Y = 39.7\,\text{kPa}$, $k = 4.71 \times 10^{-17}\,\text{m}^4\text{N}^{-1}\text{s}^{-1}$ [##++] |
| | | | $E_Y = 36.8\,\text{kPa}$, $k = 3.69 \times 10^{-17}\,\text{m}^4\text{N}^{-1}\text{s}^{-1}$ [##] |
| Osteoarthritic human articular cartilage | Micropipette aspiration | Punch [Jones et al. 1999] | $E_Y = 0.67\,\text{kPa}$ |
| | | Viscoelastic [Trickey et al. 2000] | $E_o = 0.63\,\text{kPa}$, $E_\infty = 0.33\,\text{kPa}$, $\mu = 5.80\,\text{kPa-s}$ |
| | | Biphasic [Trickey et al. 2006] | $\upsilon_s = 0.38$ |
| | | Layered half-space [Alexopoulos et al. 2003] | $E_Y = 39.1\,\text{kPa}$ [##++] |
| | | | $E_Y = 43.9\,\text{kPa}$ [##] |
| | | Multiscale biphasic [Alexopoulos et al. 2005b] | $E_Y = 20.8\,\text{kPa}$, $k = 10.46 \times 10^{-17}\,\text{m}^4\text{N}^{-1}\text{s}^{-1}$ [##++] |
| | | | $E_Y = 24.4\,\text{kPa}$, $k = 9.91 \times 10^{-17}\,\text{m}^4\text{N}^{-1}\text{s}^{-1}$ [##] |

**Table 1.** Overview of published mechanical properties for the individual chondrocyte and its associated PCM. All material properties are for chondrocytes isolated from the middle/deep region of articular cartilage unless otherwise denoted. Legend: ++ Superficial zone characteristics; ## PCM mechanical parameters.

On this level, researchers can elucidate the role of the pericellular and territorial matrices in the formation of strong and healthy cartilage tissue. Research in this field may enable investigators to answer several pertinent questions regarding articular cartilage development:

1) How does the expansion of the PCM affect the growth of other ECM regions?

2) Do the thresholds for ideal cartilage mechanical stimulation change as the PCM creates a more robust mechanical buffer around the chondrocyte?

3) How do these local matrix changes facilitate or modulate the passage of cytokines and growth factors among the cells in the construct?

While ample research has already been performed on single chondrocytes, there are several areas for future studies aside from the mechanical aspects described in this review. Additional combinations of various exogenous factors, including oxygen tension levels and growth factors, may be used in conjunction with mechanical stimulation to optimize the biochemical response of individual cells. It would also be of great interest to examine the temporal effects of gene expression after mechanical stimulation. This knowledge could potentially provide researchers with a working time frame for eliciting particular cellular responses. For instance, after a certain time point, changes in gene expression may return to baseline values or remain permanently changed. Lastly, deformations on the cellular and nuclear level can be directly linked to changes in gene expression to further our understanding of chondrocyte mechanobiology.

Mechanical testing of single chondrons can be seen as a logical next step after single cell experiments. Many single chondrocyte experiments require seeding the cells onto a substrate, which does not account for their three-dimensional configuration in vivo and may alter cytoskeletal structure and cellular organization. Studying single cells with their associated matrix allows researchers to observe changes in cellular behavior more indicative of an in vivo response. However, as yet, micropipette aspiration is the only technique used to directly measure the mechanical properties of single chondrons. Despite the ability of micropipette aspiration to quantify cellular and PCM properties, it cannot be used to apply compressive forces or controlled deformations on single chondrons. This can be seen as a significant drawback, as it prevents researchers from performing conventional stress relaxation experiments. Furthermore, the types of forces normally experienced by chondrocytes in vivo, namely compressive, shear, or hydrostatic forces, cannot be achieved using micropipette aspiration alone. This leaves the window wide open for new techniques to be developed, which may be used to directly stimulate individual chondrons and measure their gene expression response.

As previously described, Ng et al. [2007] recently fabricated microwells that are capable of holding chondrons in place during AFM experimentation, thereby providing a potentially significant experimental modality to be used on single chondrons. In addition, other techniques may employ a type of matrix glue to attach the chondrons onto a given substrate prior to mechanical testing. Coverslips coated with monoclonal antibodies specific to PCM proteins can be used to immobilize chondrons for direct compression experiments. Similarly, micropipette aspiration also may be employed to apply a small tare load to hold the chondrons in position while a probe compresses the sample on the other end. In short, the potentials for chondron mechanical testing and stimulation are vast, with profound implications in articular cartilage micromechanics. Future experiments will need to examine the possibilities of various new approaches and study the threshold levels necessary to elicit positive responses from single chondrons.

Then following the fundamental unit approach, researchers can work upwards toward the overarching goal of tissue engineering articular cartilage.

# References

[Aebi et al. 1986] U. Aebi, J. Cohn, L. Buhle, and L. Gerace, "The nuclear lamina is a meshwork of intermediate-type filaments", *Nature* **323**:6088 (1986), 560–564.

[Alexopoulos et al. 2003] L. G. Alexopoulos, M. A. Haider, T. P. Vail, and F. Guilak, "Alterations in the mechanical properties of the human chondrocyte pericellular matrix with osteoarthritis", *J. Biomech. Eng. (Trans. ASME)* **125**:3 (2003), 323–333.

[Alexopoulos et al. 2005a] L. G. Alexopoulos, L. A. Setton, and F. Guilak, "The biomechanical role of the chondrocyte pericellular matrix in articular cartilage", *Acta Biomater.* **1**:3 (2005), 317–325.

[Alexopoulos et al. 2005b] L. G. Alexopoulos, G. M. Williams, M. L. Upton, L. A. Setton, and F. Guilak, "Osteoarthritic changes in the biphasic mechanical properties of the chondrocyte pericellular matrix in articular cartilage", *J. Biomech.* **38**:3 (2005), 509–517.

[Arthritis Foundation 2006] "Disease Center: Osteoarthritis", 2006, Available at www.arthritis.org.

[Ateshian et al. 1997] G. A. Ateshian, W. H. Warden, J. J. Kim, R. P. Grelsamer, and V. C. Mow, "Finite deformation biphasic material properties of bovine articular cartilage from confined compression experiments", *J. Biomech.* **30**:11-12 (1997), 1157–1164.

[Athanasiou et al. 1999] K. A. Athanasiou, B. S. Thoma, D. R. Lanctot, D. Shin, C. M. Agrawal, and R. G. LeBaron, "Development of the cytodetachment technique to quantify mechanical adhesiveness of the single cell", *Biomaterials* **20**:23–24 (1999), 2405–2415.

[Aydelotte and Kuettner 1988] M. B. Aydelotte and K. E. Kuettner, "Differences between sub-populations of cultured bovine articular chondrocytes. I. Morphology and cartilage matrix production", *Connect. Tissue Res.* **18**:3 (1988), 205–22.

[Aydelotte et al. 1988] M. B. Aydelotte, R. R. Greenhill, and K. E. Kuettner, "Differences between sub-populations of cultured bovine articular chondrocytes. II. Proteoglycan metabolism", *Connect. Tissue Res.* **18**:3 (1988), 223–34.

[Bachrach et al. 1995] N. M. Bachrach, W. B. Valhmu, E. Stazzone, A. Ratcliffe, W. M. Lai, and V. C. Mow, "Changes in proteoglycan synthesis of chondrocytes in articular cartilage are associated with the time-dependent changes in their mechanical environment", *J. Biomech.* **28**:12 (1995), 1561–1569.

[Bader et al. 2002] D. L. Bader, T. Ohashi, M. M. Knight, D. A. Lee, and M. Sato, "Deformation properties of articular chondrocytes: a critique of three separate techniques", *Biorheology* **39**:1-2 (2002), 69–78.

[Becker et al. 2003] W. M. Becker, L. J. Kleinsmith, and J. Hardin, *The world of the cell*, 5th ed., Benjamin/Cummings, San Francisco, 2003.

[Breuls et al. 2002] R. G. Breuls, B. G. Sengers, C. W. Oomens, C. V. Bouten, and F. P. Baaijens, "Predicting local cell deformations in engineered tissue constructs: a multilevel finite element approach", *J. Biomech. Eng. (Trans. ASME)* **124**:2 (2002), 198–207.

[Buckwalter et al. 1991] J. A. Buckwalter, E. B. Hunziker, L. C. Rosenberg, R. Coutts, M. Adams, and D. Eyre, "Articular cartilage: composition and structure", pp. 405–425 in *Injury and repair of the muscoloskeletal soft tissue*, edited by S. L. Woo and J. A. Buckwalter, Park Ridge, 1991.

[Buschmann and Grodzinsky 1995] M. D. Buschmann and A. J. Grodzinsky, "A molecular model of proteoglycan-associated electrostatic forces in cartilage mechanics", *J. Biomech. Eng. (Trans. ASME)* **117**:2 (1995), 179–92.

[Buschmann et al. 1995] M. Buschmann, Y. A. Gluzband, and E. B. Grodzinsky, A. J.and Hunziker, "Mechanical compression modulates matrix biosynthesis in chondrocyte/agarose culture", *J. Cell Sci.* **108**:4 (1995), 1497–1508.

[Buschmann et al. 1996] M. D. Buschmann, E. B. Hunziker, Y. J. Kim, and A. J. Grodzinsky, "Altered aggrecan synthesis correlates with cell and nucleus structure in statically compressed cartilage", *J. Cell Sci.* **109**:2 (1996), 499–508.

[Carver and Heath 1999] S. E. Carver and C. A. Heath, "Increasing extracellular matrix production in regenerating cartilage with intermittent physiological pressure", *Biotechnol. Bioeng.* **62**:2 (1999), 166–174.

[Chang et al. 1997] J. Chang, H. Nakajima, and C. A. Poole, "Structural colocalisation of type VI collagen and fibronectin in agarose cultured chondrocytes and isolated chondrons extracted from adult canine tibial cartilage", *J. Anat.* **190**:4 (1997), 523–532.

[Chen and Ingber 1999] C. S. Chen and D. E. Ingber, "Tensegrity and mechanoregulation: from skeleton to cytoskeleton", *Osteoarthr. Cartilage* **7**:1 (1999), 81–94.

[Chen and Sah 1998] A. C. Chen and R. L. Sah, "Effect of static compression on proteoglycan biosynthesis by chondrocytes transplanted to articular cartilage in vitro", *J. Orthopaed. Res.* **16**:5 (1998), 542–550.

[Cheng et al. 2000] L. Cheng, X. Xia, W. Yu, L. E. Scriven, and W. W. Gerberich, "Flat-punch indentation of viscoelastic material", *J. Polym. Sci. Pol. Phys.* **38**:1 (2000), 10–22.

[Chowdhury et al. 2003] T. Chowdhury, D. L. Bader, J. C. Shelton, and D. A. Lee, "Temporal regulation of chondrocyte metabolism in agarose constructs subjected to dynamic compression", *Arch. Biochem. Biophys.* **417**:1 (2003), 105–111.

[D'Andrea and Vittur 1996] P. D'Andrea and F. Vittur, "Gap junctions mediate intercellular calcium signalling in cultured articular chondrocytes", *Cell Calcium* **20**:5 (1996), 389–397.

[D'Andrea et al. 1998] P. D'Andrea, A. Calabrese, and M. Grandolfo, "Intercellular calcium signalling between chondrocytes and synovial cells in co-culture", *Biochem. J.* **329**:Pt 3 (1998), 681–687.

[D'Andrea et al. 2000] P. D'Andrea, A. Calabrese, I. Capozzi, M. Grandolfo, R. Tonon, and F. Vittur, "Intercellular Ca2+ waves in mechanically stimulated articular chondrocytes", *Biorheology* **37**:1–2 (2000), 75–83.

[Darling et al. 2004] E. M. Darling, J. C. Hu, and K. A. Athanasiou, "Zonal and topographical differences in articular cartilage gene expression", *J. Orthopaed. Res.* **22**:6 (2004), 1182–1187.

[Darling et al. 2006] E. M. Darling, S. Zauscher, and F. Guilak, "Viscoelastic properties of zonal articular chondrocytes measured by atomic force microscopy", *Osteoarthr. Cartilage* **14**:6 (2006), 571–579.

[Dekel and Weissman 1978] S. Dekel and S. L. Weissman, "Joint changes after overuse and peak overloading of rabbit knees in vivo", *Acta Orthop. Scand.* **49**:6 (1978), 519–528.

[Dhaliwal 1970] R. S. Dhaliwal, "Punch problem for an elastic layer overlying an elastic foundation", *Int. J. Eng. Sci.* **8**:4 (1970), 273–288.

[Durrant et al. 1999] L. A. Durrant, C. W. Archer, M. Benjamin, and J. R. Ralphs, "Organisation of the chondrocyte cytoskeleton and its response to changing mechanical conditions in organ culture", *J. Anat.* **194**:3 (1999), 343–353.

[Ehrlich et al. 1987] M. G. Ehrlich, A. L. Armstrong, B. V. Treadwell, and H. J. Mankin, "The role of proteases in the pathogenesis of osteoarthritis", *J. Rheumatol.* **14** (1987), 30–2.

[Eleswarapu et al. 2007] S. V. Eleswarapu, N. D. Leipzig, and K. A. Athanasiou, "Gene expression of single articular chondrocytes", *Cell Tissue Res.* **327**:1 (2007), 43–54.

[Flannery et al. 1999] C. R. Flannery, C. E. Hughes, B. L. Schumacher, D. Tudor, M. B. Aydelotte, K. E. Kuettner, and B. Caterson, "Articular cartilage superficial zone protein (SZP) is homologous to megakaryocyte stimulating factor precursor and is a multifunctional proteoglycan with potential growth-promoting, cytoprotective, and lubricating properties in cartilage metabolism", *Biochem. Biophys. Res. Commun.* **254**:3 (1999), 535–541.

[Fraser et al. 2006] S. A. Fraser, A. Crawford, A. Frazer, S. Dickinson, A. P. Hollander, I. M. Brook, and P. V. Hatton, "Localization of type VI collagen in tissue-engineered cartilage on polymer scaffolds", *Tissue Eng.* **12**:3 (2006), 569–577.

[Freeman et al. 1994] P. M. Freeman, R. N. Natarajan, J. H. Kimura, and T. P. Andriacchi, "Chondrocyte cells respond mechanically to compressive loads", *J. Orthopaed. Res.* **12**:3 (1994), 311–320.

[Freemont et al. 1997] A. J. Freemont, V. Hampson, R. Tilman, P. Goupille, Y. Taiwo, and J. A. Hoyland, "Gene expression of matrix metalloproteinases 1, 3, and 9 by chondrocytes in osteoarthritic human knee articular cartilage is zone and grade specific", *Ann. Rheum. Dis.* **56**:9 (1997), 542–548.

[Furukawa et al. 2003] K. S. Furukawa, H. Suenaga, K. Toita, A. Numata, J. Tanaka, T. Ushida, Y. Sakai, and T. Tateishi, "Rapid and large-scale formation of chondrocyte aggregates by rotational culture", *Cell Transplant.* **12**:5 (2003), 475–479.

[Goldberg and Toole 1984] R. L. Goldberg and B. P. Toole, "Pericellular coat of chick embryo chondrocytes: structural role of hyaluronate", *J. Cell Biol.* **99**:6 (1984), 2114–2122.

[Gooch et al. 2001] K. J. Gooch, T. Blunk, D. L. Courter, A. L. Sieminski, P. M. Bursac, G. Vunjak-Novakovic, and L. E. Freed, "IGF-I and mechanical environment interact to modulate engineered cartilage development", *Biochem. Biophys. Res. Commun.* **286**:5 (2001), 909–915.

[Graff et al. 2003] R. D. Graff, S. S. Kelley, and G. M. Lee, "Role of pericellular matrix in development of a mechanically functional neocartilage", *Biotechnol. Bioeng.* **82**:4 (2003), 457–464.

[Guilak 1995] F. Guilak, "Compression-induced changes in the shape and volume of the chondrocyte nucleus", *J. Biomech.* **28**:12 (1995), 1529–1541.

[Guilak and Mow 2000] F. Guilak and V. C. Mow, "The mechanical environment of the chondrocyte: a biphasic finite element model of cell-matrix interactions in articular cartilage", *J. Biomech.* **33**:12 (2000), 1663–1673.

[Guilak et al. 1995] F. Guilak, A. Ratcliffe, and V. C. Mow, "Chondrocyte deformation and local tissue strain in articular cartilage: a confocal microscopy study", *J. Orthopaed. Res.* **13**:3 (1995), 410–421.

[Guilak et al. 1999] F. Guilak, W. R. Jones, H. P. Ting-Beall, and G. M. Lee, "The deformation behavior and mechanical properties of chondrocytes in articular cartilage", *Osteoarthr. Cartilage* **7**:1 (1999), 59–70.

[Guilak et al. 2000] F. Guilak, J. R. Tedrow, and R. Burgkart, "Viscoelastic properties of the cell nucleus", *Biochem. Biophys. Res. Commun.* **269**:3 (2000), 781–786.

[Guilak et al. 2005] F. Guilak, L. G. Alexopoulos, M. A. Haider, H. P. Ting-Beall, and L. A. Setton, "Zonal uniformity in mechanical properties of the chondrocyte pericellular matrix: micropipette aspiration of canine chondrons isolated by cartilage homogenization", *Ann. Biomed. Eng.* **33**:10 (2005), 1312–1318.

[Haider 2004] M. A. Haider, "A radial biphasic model for local cell-matrix mechanics in articular cartilage", *SIAM J. Appl. Math.* **64**:5 (2004), 1588–1608.

[Haider and Guilak 2002] M. A. Haider and F. Guilak, "An axisymmetric boundary integral model for assessing elastic cell properties in the micropipette aspiration contact problem", *J. Biomech. Eng. (Trans. ASME)* **124**:5 (2002), 586–595.

[Hansen et al. 2001] U. Hansen, M. Schunke, C. Domm, N. Ioannidis, J. Hassenpflug, T. Gehrke, and B. Kurz, "Combination of reduced oxygen tension and intermittent hydrostatic pressure: a useful tool in articular cartilage tissue engineering", *J. Biomech.* **34**:7 (2001), 941–949.

[Harding and N. 1944] J. W. Harding and S. I. N., "The elastic stresses produced by the indentation of the plane surface of a semi-infinite elastic solid by a rigid punch", pp. 16–26 in *P. Camb. Philos. Soc.*, 1944.

[Hing et al. 2002] W. A. Hing, A. F. Sherwin, J. M. Ross, and C. A. Poole, "The influence of the pericellular microenvironment on the chondrocyte response to osmotic challenge", *Osteoarthr. Cartilage* **10**:4 (2002), 297–307.

[Hoben et al. 2002] G. Hoben, W. Huang, B. S. Thoma, R. G. LeBaron, and K. A. Athanasiou, "Quantification of varying adhesion levels in chondrocytes using the cytodetacher", *Ann. Biomed. Eng.* **30**:5 (2002), 703–712.

[Horton et al. 1987] W. A. Horton, M. A. Machado, J. W. Chou, and D. Campbell, "Achondrogenesis type II, abnormalities of extracellular matrix", *Pediatr. Res.* **22**:3 (1987), 324–9.

[Hu and Athanasiou 2003] J. C. Hu and K. A. Athanasiou, "Structure and function of articular cartilage", pp. 73–98 in *Handbook of histology methods for bone and cartilage*, edited by Y. H. An and K. L. Martin, Humana Press, Totowa, NJ, 2003.

[Hu and Athanasiou 2006] J. C. Hu and K. A. Athanasiou, "A self-assembling process in articular cartilage tissue engineering", *Tissue Eng.* **12**:4 (2006), 969–979.

[Huang et al. 2003] W. Huang, B. Anvari, J. H. Torres, R. G. LeBaron, and K. A. Athanasiou, "Temporal effects of cell adhesion on mechanical characteristics of the single chondrocyte", *J. Orthopaed. Res.* **21**:1 (2003), 88–95.

[Ingber 1997] D. E. Ingber, "Tensegrity: the architectural basis of cellular mechanotransduction", *Annu. Rev. Physiol.* **59** (1997), 575–599.

[J. Borrelli et al. 2003] J. J. Borrelli, K. Tinsley, W. M. Ricci, M. Burns, I. E. Karl, and R. Hotchkiss, "Induction of chondrocyte apoptosis following impact load", *J. Orthop. Trauma* **17**:9 (2003), 635–641.

[Janmey et al. 1991] P. A. Janmey, U. Euteneuer, P. Traub, and M. Schliwa, "Viscoelastic properties of vimentin compared with other filamentous biopolymer networks", *J. Cell Biol.* **113**:1 (1991), 155–160.

[Jeffrey et al. 1995] J. E. Jeffrey, D. W. Gregory, and R. M. Aspden, "Matrix damage and chondrocyte viability following a single impact load on articular cartilage", *Arch. Biochem. Biophys.* **322**:1 (1995), 87–96.

[Jin et al. 2003] M. Jin, G. R. Emkey, P. Siparsky, S. B. Trippel, and A. J. Grodzinsky, "Combined effects of dynamic tissue shear deformation and insulin-like growth factor I on chondrocyte biosynthesis in cartilage explants", *Arch. Biochem. Biophys.* **414**:2 (2003), 223–231.

[Jones et al. 1999] W. R. Jones, H. P. Ting-Beall, G. M. Lee, S. S. Kelley, R. M. Hochmuth, and F. Guilak, "Alterations in the Young's modulus and volumetric properties of chondrocytes isolated from normal and osteoarthritic human cartilage", *J. Biomech.* **32**:2 (1999), 119–127.

[Jortikka et al. 2000] M. O. Jortikka, J. J. Parkkinen, R. I. Inkinen, J. Karner, H. T. Jarvelainen, L. O. Nelimarkka, M. I. Tammi, and M. J. Lammi, "The role of microtubules in the regulation of proteoglycan synthesis in chondrocytes under hydrostatic pressure", *Arch. Biochem. Biophys.* **374**:2 (2000), 172–80.

[Kang et al. 2006] Y. Kang, J. Yang, S. Khan, L. Anissian, and G. A. Ameer, "A new biodegradable polyester elastomer for cartilage tissue engineering", *J. Biomed. Mater. Res. A* **77A**:2 (2006), 331–339.

[Katz et al. 1986] E. P. Katz, E. J. Wachtel, and A. Maroudas, "Extrafibrillar proteoglycans osmotically regulate the molecular packing of collagen in cartilage", *Biochim. Biophys. Acta* **882**:1 (1986), 136–139.

[Kelly et al. 2004] T. A. Kelly, C. C. Wang, R. L. Mauck, G. A. Ateshian, and C. T. Hung, "Role of cell-associated matrix in the development of free-swelling and dynamically loaded chondrocyte-seeded agarose gels", *Biorheology* **41**:3–4 (2004), 223–237.

[Kisiday et al. 2004] J. D. Kisiday, M. Jin, M. A. DiMicco, B. Kurz, and A. J. Grodzinsky, "Effects of dynamic compressive loading on chondrocyte biosynthesis in self-assembling peptide scaffolds", *J. Biomech.* **37**:5 (2004), 595–604.

[Knight et al. 1998] M. M. Knight, S. A. Ghori, D. A. Lee, and D. L. Bader, "Measurement of the deformation of isolated chondrocytes in agarose subjected to cyclic compression", *Med. Eng. Phys.* **20**:9 (1998), 684–688.

[Koay et al. 2003] E. J. Koay, A. C. Shieh, and K. A. Athanasiou, "Creep indentation of single cells", *J. Biomech. Eng. (Trans. ASME)* **125**:3 (2003), 334–341.

[Kumar and Hiremath 1982] M. Kumar and K. U. Hiremath, "Annular punch problem for an elastic layer overlying an elastic foundation", *Indian J. Pure Appl. Math.* **13**:5 (1982), 573–580.

[Kurz et al. 2001] B. Kurz, M. Jin, P. Patwari, D. M. Cheng, M. W. Lark, and A. J. Grodzinsky, "Biosynthetic response and mechanical properties of articular cartilage after injurious compression", *J. Orthopaed. Res.* **19**:6 (2001), 1140–1146.

[Langelier et al. 2000] E. Langelier, R. Suetterlin, C. D. Hoemann, U. Aebi, and M. D. Buschmann, "The chondrocyte cytoskeleton in mature articular cartilage: structure and distribution of actin, tubulin, and vimentin filaments", *J. Histochem. Cytochem.* **48**:10 (2000), 1307–1320.

[Larson et al. 2002] C. M. Larson, S. S. Kelley, A. D. Blackwood, A. J. Banes, and G. M. Lee, "Retention of the native chondrocyte pericellular matrix results in significantly improved matrix production", *Matrix Biol.* **21**:4 (2002), 349–359.

[Lee et al. 1998] D. Lee, T. Noguchi, M. M. Knight, L. O'Donnell, G. Bentley, and D. L. Bader, "Response of chondrocyte subpopulations cultured within unloaded and loaded agarose", *J. Orthopaed. Res.* **16**:6 (1998), 726–733.

[Leipzig and Athanasiou 2005] N. D. Leipzig and K. A. Athanasiou, "Unconfined creep compression of chondrocytes", *J. Biomech.* **38**:1 (2005), 77–85.

[Leipzig and Athanasiou 2006] N. D. Leipzig and K. A. Athanasiou, "Static compression alters the gene expression of single cells", 2006. submitted to *Science*.

[Leipzig et al. 2006] N. D. Leipzig, S. V. Eleswarapu, and K. A. Athanasiou, "The effects of TGF-beta1 and IGF-I on the biomechanics and cytoskeleton of single chondrocytes", *Osteoarthr. Cartilage* **14**:12 (2006), 1227–1236.

[Mak 1986] A. F. Mak, "The apparent viscoelastic behavior of articular cartilage–the contributions from the intrinsic matrix viscoelasticity and interstitial fluid flows", *J. Biomech. Eng. (Trans. ASME)* **108**:2 (1986), 123–30.

[Mak et al. 1987] A. F. Mak, W. M. Lai, and V. C. Mow, "Biphasic indentation of articular cartilage. I. Theoretical analysis", *J. Biomech.* **20**:7 (1987), 703–714.

[Maniotis et al. 1997] A. J. Maniotis, C. S. Chen, and D. E. Ingber, "Demonstration of mechanical connections between integrins, cytoskeletal filaments, and nucleoplasm that stabilize nuclear structure", *P. Natl. Acad. Sci. USA* **94**:3 (1997), 849–854.

[Marles et al. 1991] P. J. Marles, J. A. Hoyland, R. Parkinson, and A. J. Freemont, "Demonstration of variation in chondrocyte activity in different zones of articular cartilage: an assessment of the value of in-situ hybridization", *Int. J. Exp. Pathol.* **72**:2 (1991), 171–82.

[Maroudas 1976] A. I. Maroudas, "Balance between swelling pressure and collagen tension in normal and degenerate cartilage", *Nature* **260**:5554 (1976), 808–809.

[Mauck et al. 2003] R. L. Mauck, S. B. Nicoll, S. L. Seyhan, G. A. Ateshian, and C. T. Hung, "Synergistic action of growth factors and dynamic loading for articular cartilage tissue engineering", *Tissue Eng.* **9**:4 (2003), 597–611.

[Micheli et al. 2006] L. J. Micheli, J. B. Moseley, A. F. Anderson, J. E. Browne, C. Erggelet, R. Arciero, F. H. Fu, and B. R. Mandelbaum, "Articular cartilage defects of the distal femur in children and adolescents: treatment with autologous chondrocyte implantation", *J. Pediatr. Orthop.* **26**:4 (2006), 455–60.

[Minns and Steven 1977] R. J. Minns and F. S. Steven, "The collagen fibril organization in human articular cartilage", *J. Anat.* **123**:Pt 2 (1977), 437–457.

[Mow and Ratcliffe 1997] V. C. Mow and A. Ratcliffe, "Structure and function of articular cartilage and meniscus", pp. 113–177 in *Basic orthopaedic biomechanics*, edited by V. C. Mow and W. C. Hayes, Lippincott-Raven, Philadelphia, 1997.

[Mow et al. 1980] V. C. Mow, S. C. Kuei, W. M. Lai, and C. G. Armstrong, "Biphasic creep and stress relaxation of articular cartilage in compression? Theory and experiments", *J. Biomech. Eng. (Trans. ASME)* **102**:1 (1980), 73–84.

[Mow et al. 1994] V. C. Mow, N. M. Bachrach, L. A. Setton, and F. Guilak, "Stress, strain, pressure and flow fields in articular cartilage and chondrocytes", pp. 345–379 in *Cell mechanics and cellular engineering*, Springer, New York, 1994.

[Muir 1983] H. Muir, "Proteoglycans as organizers of the intercellular matrix", *Biochem. Soc. Trans.* **11**:6 (1983), 613–22.

[Ng et al. 2006] K. W. Ng, R. L. Mauck, L. Y. Statman, E. Y. Lin, G. A. Ateshian, and C. T. Hung, "Dynamic deformational loading results in selective application of mechanical stimulation in a layered, tissue-engineered cartilage construct", *Biorheology* **43**:3–4 (2006), 497–507.

[Ng et al. 2007] L. Ng, H. H. Hung, A. Sprunt, S. Chubinskaya, C. Ortiz, and A. Grodzinsky, "Nanomechanical properties of individual chondrocytes and their developing growth factor-stimulated pericellular matrix", *J. Biomech.* **40**:5 (2007), 1011–1023.

[Ozkaya and Nordin c1999] N. Ozkaya and M. Nordin, *Fundamentals of biomechanics: equilibrium, motion, and deformation*, 2nd ed., edited by D. L. Leger, Springer, New York, c1999.

[Poole 1997] C. A. Poole, "Articular cartilage chondrons: form, function and failure", *J. Anat.* **191**:1 (1997), 1–13.

[Poole et al. 1988a] C. A. Poole, S. Ayad, and J. R. Schofield, "Chondrons from articular cartilage. I. Immunolocalization of type VI collagen in the pericellular capsule of isolated canine tibial chondrons", *J. Cell Sci.* **90**:4 (1988), 635–643.

[Poole et al. 1988b] C. A. Poole, S. F. Wotton, and V. C. Duance, "Localization of type IX collagen in chondrons isolated from porcine articular cartilage and rat chondrosarcoma", *Histochem. J.* **20**:10 (1988), 567–574.

[Poole et al. 1990] C. A. Poole, T. Honda, S. J. Skinner, J. R. Schofield, K. F. Hyde, and H. Shinkai, "Chondrons from articular cartilage. II. Analysis of the glycosaminoglycans in the cellular microenvironment of isolated canine chondrons", *Connect. Tissue Res.* **24**:3–4 (1990), 319–30.

[Poole et al. 1992] C. A. Poole, S. Ayad, and R. T. Gilbert, "Chondrons from articular cartilage. V. Immunohistochemical evaluation of type VI collagen organisation in isolated chondrons by light, confocal and electron microscopy", *J. Cell Sci.* **103**:4 (1992), 1101–1110.

[Poole et al. 1996] A. R. Poole, L. C. Rosenberg, A. Reiner, M. Ionescu, E. Bogoch, and P. J. Roughley, "Contents and distributions of the proteoglycans decorin and biglycan in normal and osteoarthritic human articular cartilage", *J. Orthopaed. Res.* **14**:5 (1996), 681–689.

[Radin et al. 1984] E. L. Radin, R. B. Martin, D. B. Burr, B. Caterson, R. D. Boyd, and C. Goodwin, "Effects of mechanical loading on the tissues of the rabbit knee", *J. Orthopaed. Res.* **2**:3 (1984), 221–234.

[Radin et al. 1991]  E. L. Radin, D. B. Burr, B. Caterson, D. Fyhrie, T. D. Brown, and R. D. Boyd, "Mechanical determinants of osteoarthrosis", *Semin. Arthritis. Rheu.* **21**:3 Suppl 2 (1991), 12–21.

[Ragan et al. 1999]  P. Ragan, A. M. Badger, M. Cook, V. I. Chin, M. Gowen, A. J. Grodzinsky, and M. W. Lark, "Down-regulation of chondrocyte aggrecan and type-II collagen gene expression correlates with increases in static compression magnitude and duration", *J. Orthopaed. Res.* **17**:6 (1999), 836–842.

[Roberts et al. 2001]  S. R. Roberts, M. M. Knight, D. A. Lee, and D. L. Bader, "Mechanical compression influences intracellular Ca2+ signaling in chondrocytes seeded in agarose constructs", *J. Appl. Physiol.* **90**:4 (2001), 1385–1391.

[Romeo et al. 2002]  A. A. Romeo, B. J. Cole, A. D. Mazzocca, J. A. Fox, K. B. Freeman, and E. Joy, "Autologous chondrocyte repair of an articular defect in the humeral head", *Arthroscopy* **18**:8 (2002), 925–929.

[Ruoslahti and Yamaguchi 1991]  E. Ruoslahti and Y. Yamaguchi, "Proteoglycans as modulators of growth factor activities", *Cell* **64**:5 (1991), 867–869.

[Sato et al. 1990]  M. Sato, D. P. Theret, L. T. Wheeler, N. Ohshima, and R. M. Nerem, "Application of the micropipette technique to the measurement of cultured porcine aortic endothelial cell viscoelastic properties", *J. Biomech. Eng. (Trans. ASME)* **112**:3 (1990), 263–8.

[Scherer et al. 2004]  K. Scherer, M. Schunke, R. Sellckau, J. Hassenpflug, and B. Kurz, "The influence of oxygen and hydro-static pressure on articular chondrocytes and adherent bone marrow cells in vitro", *Biorheology* **41**:3–4 (2004), 323–333.

[Schwarzer 2000]  N. Schwarzer, "Arbitrary load distribution on a layered half space", *J. Tribol. (Trans. ASME)* **122**:4 (2000), 672–681.

[Scott et al. 2005]  C. C. Scott, A. Luttge, and K. A. Athanasiou, "Development and validation of vertical scanning interferom-etry as a novel method for acquiring chondrocyte geometry", *J. Biomed. Mater. Res. A* **72A**:1 (2005), 83–90.

[Shieh and Athanasiou 2006]  A. C. Shieh and K. A. Athanasiou, "Biomechanics of single zonal chondrocytes", *J. Biomech.* **39**:9 (2006), 1595–1602.

[Shieh and Athanasiou 2007]  A. C. Shieh and K. A. Athanasiou, "Dynamic compression of single cells", *Osteoarthr. Cartilage* **15**:3 (2007), 328–334.

[Shieh et al. 2006]  A. C. Shieh, E. J. Koay, and K. A. Athanasiou, "Strain-dependent recovery behavior of single chondrocytes", *Biomech. Model. Mechanobiol.* **5**:2–3 (2006), 172–179.

[Shin and Athanasiou 1999]  D. Shin and K. Athanasiou, "Cytoindentation for obtaining cell biomechanical properties", *J. Orthopaed. Res.* **17**:6 (1999), 880–890.

[Sittinger et al. 1996]  M. Sittinger, D. Reitzel, M. Dauner, H. Hierlemann, C. Hammer, E. Kastenbauer, H. Planck, G. R. Burmester, and J. Bujia, "Resorbable polyesters in cartilage engineering: affinity and biocompatibility of polymer fiber struc-tures to chondrocytes", *J. Biomed. Mater. Res.* **33**:2 (1996), 57–63.

[Smith et al. 1995]  R. Smith, B. S. Donlon, M. K. Gupta, M. Mohtai, P. Das, D. R. Carter, J. Cooke, G. Gibbons, N. Hutchin-son, and D. J. Schurman, "Effects of fluid-induced shear on articular chondrocyte morphology and metabolism in vitro", *J. Orthopaed. Res.* **13**:6 (1995), 824–831.

[Smith et al. 2000a]  R. L. Smith, J. Lin, M. C. D. Trindade, J. Shida, G. Kajiyama, T. Vu, A. R. Hoffman, M. C. H. Meulen, S. B. Goodman, D. J. Schurman, and D. R. Carter, "Time-dependent effects of intermittent hydrostatic pressure on articular chondrocyte type II collagen and aggrecan mRNA expression", *J. Rehabil. Res. Dev.* **37**:2 (2000), 153–162.

[Smith et al. 2000b]  R. L. Smith, M. C. D. Trindade, T. Ikenoue, M. Mohtai, P. Das, D. R. Carter, S. B. Goodman, and D. J. Schurman, "Effects of shear stress on articular chondrocyte metabolism", *Biorheology* **37**:1–2 (2000), 95–107.

[Stockwell 1987]  R. A. Stockwell, *Structure and function of the chondrocyte under mechanical stress*, edited by H. J. Helminen et al., Wright and Sons, Bristol, 1987.

[Theret et al. 1988]  D. P. Theret, M. J. Levesque, M. Sato, R. M. Nerem, and L. T. Wheeler, "The application of a homogeneous half-space model in the analysis of endothelial cell micropipette measurements", *J. Biomech. Eng. (Trans. ASME)* **110**:3 (1988), 190–9.

[Ting 1966]  T. C. T. Ting, "The contact stresses between a rigid indenter and a viscoelastic half space", *J. Appl. Mech. (Trans. ASME)* **33** (1966), 845–854.

[Tran-Cong 1997] T. Tran-Cong, "On the solutions of Boussinesq, Love, and Reissner and Wennagel for axisymmetric elastic deformations", *Q. J. Mech. Appl. Math.* **50**:2 (1997), 195–210.

[Trickey et al. 2000] W. R. Trickey, G. M. Lee, and F. Guilak, "Viscoelastic properties of chondrocytes from normal and osteoarthritic human cartilage", *J. Orthopaed. Res.* **18**:6 (2000), 891–898.

[Trickey et al. 2004] W. R. Trickey, T. P. Vail, and F. Guilak, "The role of the cytoskeleton in the viscoelastic properties of human articular chondrocytes", *J. Orthopaed. Res.* **22**:1 (2004), 131–139.

[Trickey et al. 2006] W. R. Trickey, F. P. Baaijens, T. A. Laursen, L. G. Alexopoulos, and F. Guilak, "Determination of the Poisson's ratio of the cell: recovery properties of chondrocytes after release from complete micropipette aspiration", *J. Biomech.* **39**:1 (2006), 78–87.

[Verteramo and Seedhom 2004] A. Verteramo and B. B. Seedhom, "Zonal and directional variations in tensile properties of bovine articular cartilage with special reference to strain rate variation", *Biorheology* **41**:3–4 (2004), 203–213.

[Volokh 2003] K. Y. Volokh, "Cytoskeletal architecture and mechanical behavior of living cells", *Biorheology* **40**:1–3 (2003), 213–220.

[Wakitani et al. 1998] S. Wakitani, T. Goto, R. G. Young, J. M. Mansour, V. M. Goldberg, and A. I. Caplan, "Repair of large full-thickness articular cartilage defects with allograft articular chondrocytes embedded in a collagen gel", *Tissue Eng.* **4**:4 (1998), 429–444.

[Wang and Stamenovic 2000] N. Wang and D. Stamenovic, "Contribution of intermediate filaments to cell stiffness, stiffening, and growth", *Am. J. Physiol. Cell Physiol.* **279**:1 (2000), C188–C194.

[Wang et al. 1993] N. Wang, J. P. Butler, and D. E. Ingber, "Mechanotransduction across the cell surface and through the cytoskeleton", *Science* **260**:5111 (1993), 1124–1127.

[Wang et al. 2002] C. C. Wang, X. E. Guo, D. Sun, V. C. Mow, G. A. Ateshian, and C. T. Hung, "The functional environment of chondrocytes within cartilage subjected to compressive loading: a theoretical and experimental approach", *Biorheology* **39**:1–2 (2002), 11–25.

[Wong et al. 1996] M. Wong, P. Wuethrich, P. Eggli, and E. Hunziker, "Zone-specific cell biosynthetic activity in mature bovine articular cartilage: a new method using confocal microscopic stereology and quantitative autoradiography", *J. Orthopaed. Res.* **14**:3 (1996), 424–432.

[Wu and Herzog 2000] J. Z. Wu and W. Herzog, "Finite element simulation of location- and time-dependent mechanical behavior of chondrocytes in unconfined compression tests", *Ann. Biomed. Eng.* **28**:3 (2000), 318–330.

[Wu et al. 1999] J. Z. Wu, W. Herzog, and M. Epstein, "Modelling of location- and time-dependent deformation of chondrocytes during cartilage loading", *J. Biomech.* **32**:6 (1999), 563–572.

[Youn et al. 2006] I. Youn, J. B. Choi, L. Cao, L. A. Setton, and F. Guilak, "Zonal variations in the three-dimensional morphology of the chondron measured in situ using confocal microscopy", *Osteoarthr. Cartilage* **14**:9 (2006), 889–897.

GIDON OFEK: ofek@rice.edu
*Department of Bioengineering, Rice University, P.O. Box 1892, Houston, TX 77251-1892, United States*

KYRIACOS A. ATHANASIOU: athanasiou@rice.edu
*Department of Bioengineering, Rice University, P.O. Box 1892, Houston, TX 77251-1892, United States*

# ASSESSMENT OF THE MECHANICAL PROPERTIES OF THE NUCLEUS INSIDE A SPHERICAL ENDOTHELIAL CELL BASED ON MICROTENSILE TESTING

SHINJI DEGUCHI, MASAYUKI YANO, KEN HASHIMOTO,
HIROYUKI FUKAMACHI, SEIICHI WASHIO AND KATSUHIKO TSUJIOKA

The effect of extracellular forces on the nucleus deformation is an important research issue for better understanding of the intracellular force transmission mechanism. Approaches to this issue employing a microtensile test of single cells are helpful because the test enables one to give a well-controlled load onto the specimen with wide force and strain ranges. In the present study, tensile tests of single cells having a spherical shape are conducted by using a microtensile test system with a feedback control of displacement rate. Deformations of the nucleus inside the cell during the cell stretch and subsequent creep recovery after unloading are then quantified based on an image analysis. In order to characterize the creep recovery behaviors of the cell and its nucleus, one-dimensional analytical viscoelastic models and a power-law function are fitted to the creep recovery data. In addition, systematic finite element analyses are performed to estimate the intracellular stress distribution and elastic modulus of the cell and nucleus assumed to be continuum materials. These results indicate that the mechanical behaviors of the nucleus within a cell under stretching and unloading are similar to those under compression loadings previously reported.

## 1. Introduction

Mechanical forces inherent in the living body are known to regulate physiology and pathogenesis of diseases in addition to chemical factors such as hormones [Davies 1995]. For example, fluid shear stress due to blood flow affects endothelial cells that line the blood vessel and induces antiatherosclerotic functions. In cells, mechanical forces are somehow converted into changes in gene expression leading to such biochemical responses. However, the mechanism by which cells sense forces is still unclear and has been gaining increasing attention from researchers. This is partly because, from a mechanical viewpoint, it remains elusive how externally applied forces are transmitted to intracellular force-sensors including the nucleus that encloses genes [Davies 1995; Janmey 1998; Ingber 2003].

To understand the physical pathway of intracellular force transmission, mechanical behaviors of individual cells [Dong et al. 1991; Karcher et al. 2003; Hashimoto et al. 2004; Desprat et al. 2005; Fernandez et al. 2006; Kasza et al. 2007] and subcellular structural components such as cytoskeletal filaments [Deguchi et al. 2006] and the nucleus [Caille et al. 1998; 2002; Guilak et al. 2000; Dahl et al. 2004; 2005; Tseng et al. 2004; Deguchi et al. 2005a; Rowat et al. 2005; 2006; Vaziri et al. 2006] have been investigated. The cytoskeletal filaments are thin protein fibers used for support of intracellular

force, cell movement, material transfer within the cell, and so forth. To this end, many experimental approaches that enable to measure the mechanical properties of micron-size biological specimens have ever been developed. In the following two paragraphs, we briefly review such micro and nanomechanical testing techniques: pipette aspiration, atomic force microscopy (AFM) indentation, optical tweezers, and micromechanical test using a pair of microcantilevers.

The pipette aspiration technique uses a small glass tube to aspirate a part of a biological specimen by applying negative pressures inside the tube. The relation between the negative pressures and resultant aspirated lengths of the specimen can give an estimate of the stiffness. This technique was applied to floating cells [Sato et al. 1990] and nuclei isolated from cells [Guilak et al. 2000; Dahl et al. 2004; Deguchi et al. 2005a].

In contrast, the AFM pushes a local part of a biological specimen by using an accurately displaced flexible microcantilever whose stiffness is known in advance. Detection of the cantilever's deflection by the use of an optical technique yields the relation between the indentation lengths and forces loaded onto the specimen surface, giving the stiffness of the specimen. This technique was applied to adherent cells [Haga et al. 2000; Sato et al. 2000] or isolated nuclei [Vaziri et al. 2006]. Employment of analytical [Sato et al. 1990; Haider and Guilak 2000] or computational models [Vaziri et al. 2006] in interpretations of these experimental results can provide more accurate estimations of the mechanical properties. The optical tweezers, introduced by Ashkin et al. [1986], enable a noncontact trapping as well as a manipulation of a specimen by laser radiation pressure. This technique was used to stretch a single cell, by moving trapped beads that attach to the cell, to evaluate mechanical properties [Mills et al. 2004]. A constraint of its low trapping stiffness, however, restricts the maximum generative force to an approximately piconewton order of magnitude.

In the micromechanical test using a pair of microcantilevers, a biological specimen is pulled apart by using a pair of thin needles or microplates [Kishino and Yanagida 1988; Miyazaki et al. 2000; Nagayama et al. 2006; 2007; Deguchi et al. 2006; Desprat et al. 2005], or compressed by microplates [Caille et al. 2002]. By measuring the deflection of the needle or microplate whose stiffness is known in advance, loading-deformation relationship of the specimen can be obtained. Accordingly, the microtensile or compression test is similar to the AFM, but the former is performed in a projected horizontal plane to observe the specimen deformation during the testing. The test can give a large strain, which is different from the pipette aspiration and conventional AFM that can only investigate the effect of a local loading. Hence, this test done in a projected horizontal plane is very useful for evaluation of the mechanical properties at the scale of the whole cell and biological filamentous structure. Also, in contrast to the above-mentioned narrow force range of the optical tweezers, design adjustment of the needle or microplate shape and size enables a force measurement with a wide range from subpiconewton [Kishino and Yanagida 1988] to micronewton [Miyazaki et al. 2000]. Therefore, the technique is more applicable, from the standpoints of strain and force ranges, to a variety of mechanical tests of biological specimen.

We previously developed a microtensile test system using such thin needles with a feedback control [Deguchi et al. 2005b]. The feedback control utilizes a servo system to give an arbitrary magnitude of strain or load as well as a strain rate onto a biological specimen. The system was used for single stress fibers, one of the cytoskeletal filaments, isolated form cells [Deguchi et al. 2006].

In the present study, the system is applied to a single cell, which is larger than the stress fiber in size and probably in force magnitude required for stretching. Deformation behaviors of one of the

principal subcellular structural components, the nucleus, are the subject of much debate. Furthermore, to investigate viscoelastic behaviors of the nucleus and cell, a creep recovery of those materials after unloading was observed.

## 2. Method

**2.1.** *Cell preparation.* Bovine aortic endothelial cells were cultured in the modified version of Dulbecco's Eagle medium supplemented with 10% fetal bovine serum and 1% each of penicillin and streptomycin. The cells were used at passages 4 and 5 for experiments. Immediately before experiments the cells were rinsed with phosphate buffered saline and treated with trypsin that inhibits cell adhesion. The cells detached from the dish surface were then seeded on a suspension dish containing the culture medium and used for experiments.

**2.2.** *Tensile test system.* Microtensile tests of the individual cells are conducted by using a tensile test system, which we had developed before [Deguchi et al. 2005b] and partially improved for the present study. Briefly, the system was developed on an inverted-microscope (IX-71, Olympus) equipped with two micromanipulators (Narishige) and a CCD camera (Sony) hooked up to an image processor (C3160, Hamamatsu). A floating cell, having a round shape, is captured with a pair of cantilevers displaced by using the micromanipulators as shown in Figure 1. The cantilever, which consists of a carbon fiber and a glass rod, is handmade: a thin carbon fiber having a diameter of 8 $\mu$m is attached, with an epoxy adhesive, to the tip of a glass rod having a 1 mm diameter so as to have an appropriate length described below. We prepare two types of the cantilevers by adjusting the carbon fiber length: deflectable and nondeflectable; see Figure 1. For the deflectable cantilever, the length of the carbon fiber located at the tip of a glass rod
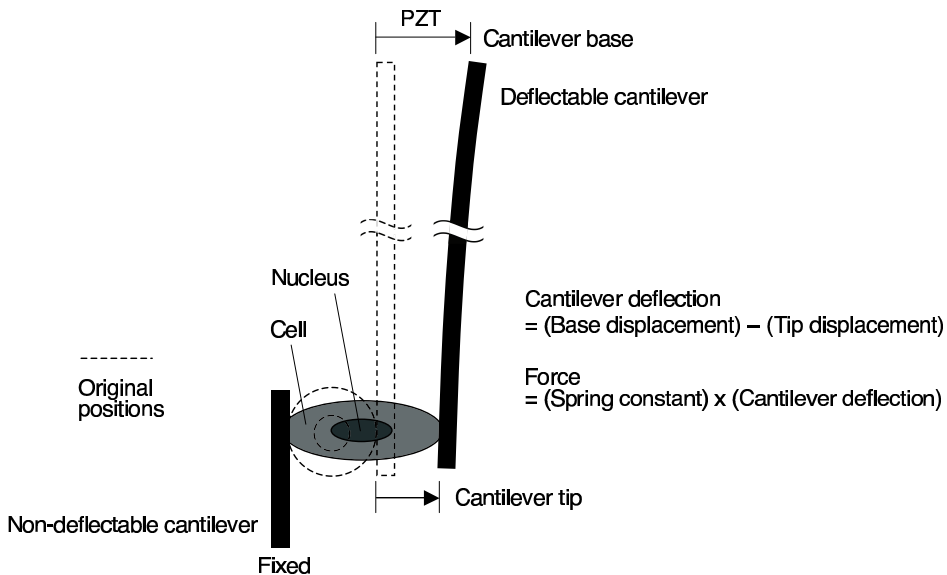


**Figure 1.** Schematic diagram of the tensile test of a single cell. The cantilever and the cell are not depicted in precise relative scale, and the cantilever deflection is exaggerated.

is set to be ~2–3 mm. This is so thin that the deflectable cantilever is easily bent. The spring constant for bending of the cantilever is determined by a cross-calibration method [Kishino and Yanagida 1988]. For the nondeflectable cantilever, the carbon fiber is set to have an ~100 $\mu$m length. This is so short that the nondeflectable cantilever has a relatively large value of the spring constant and therefore does not bend against a force that appears in this experiment, approximately less than 10 $\mu$N.

In a tensile test a captured cell is stretched by displacing a base part of the deflectable cantilever, while keeping the nondeflectable cantilever unchanged; see Figure 1. The displacement of the deflectable cantilever base is made by a piezoelectric actuator (PZT, NEC Tokin) that is connected to the cantilever base and is driven by a PZT driver controlled by a computer; see Figure 2. A strain-gauge is attached to a surface of the PZT. An extension of the PZT yields a change in the resistance of the strain-gauge, which is detected by a bridge circuit. Thus, we can obtain the displacement of the base part of the deflectable cantilever from the strain-gauge system as shown in Figure 2. Meanwhile, the displacement of the cantilever tip is obtained by the image processor as follows. The cell and the cantilevers are observed during tests by the CCD camera under a halogen light illumination. The image taken by the camera is displayed on a monitor and is also sent to the image processor. The carbon fiber on the tip of the cantilever shuts out a part of the halogen light used to observe the cell. Then, the position of the cantilever tip can be tracked by a binary image processing. The electric outputs, corresponding to the cantilever tip and base displacements, are sent to the computer. Values of the deflection of the cantilever are then obtained by subtracting the tip displacement from the base displacement on a program written in LabVIEW (National Instruments). The tensile force required for stretching the cell is obtained by multiplying the deflection of the cantilever by its spring constant. We can thus obtain the force-displacement relationship of the cell because the displacement of the tip of the deflectable cantilever is equal to that of the stretched cell.

Force-displacement relationship of living tissues is in part affected by strain rate in the mechanical test [Fung 1993]. Although the effect of strain rate on tensile properties is not touched upon in the present study, the experimental setup is expected to have a strain rate control capability in view of a future investigation of the strain rate effect. The tensile test system used in this study adopts a servo control to realize a constant strain rate with a PID controller [Deguchi et al. 2005b]. Prior to the experiment, a desired path for the cantilever tip movement as a function of time is determined and put into the program. Here, a straight line having a constant slope of 1 $\mu$m/s is chosen for the desired path. The displacement of the base part of the cantilever, which is the only portion allowed to be directly manipulated by the use of the actuator PZT, is controlled to make the cantilever tip follow the desired path by giving an appropriate input to the PZT driver; see Figure 2. The appropriate input is obtained from the PID controller written in the program, whose optimum gain is determined based on stability according to a calibration conducted
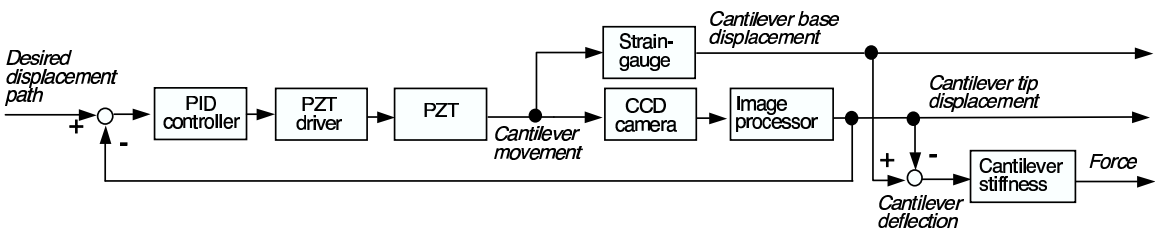


**Figure 2.** Circuit diagram of the servo system for displacement rate control.

before experiments. Accordingly, the tensile test system enables microtensile tests with an arbitrary strain rate even if the mechanical response of the biological specimen is unknown. This control system is also applicable to a constant loading test for investigating viscoelastic creep behaviors, as reported by other researchers using a similar system [Desprat et al. 2005].

**2.3.** *Tensile test.* Tensile tests of the cells were performed at room temperature (20° C). Before experiments, the tip of the cantilevers was thinly coated with a polyurethane adhesive [Shue and Brozovich 1999; Smith et al. 2000; Nagayama et al. 2006] by using another cantilever having a mass of the adhesive at its tip. The suspension dish containing the floating cells was then mounted on the stage of the microscope. A single cell located at the bottom of the dish was touched at each side by the cantilevers. The targeted cell was held in place for 3 min to strengthen the adhesion between the cell and cantilever. The cell was then lifted up from the bottom carefully. The program is then executed to start a tensile test of the cell. Time course changes in the electric outputs during the tensile test were recorded on the computer and synchronized with video images taken by the camera.

**2.4.** *Image analysis.* The nucleus displacement during the experiment was investigated by image analyses using software (IMAQ, National Instruments). Brightness of each picture element along a survey line was examined. The survey line was selected to cover the whole cell and cantilevers in the direction of the stretch. Positions of the cantilevers and the boundary between the cytoplasm and the nucleoplasm correspond to local minimum brightness points. This allowed us to track the movements of those points.

**2.5.** *Finite element analysis.* A computational cell model was developed in the finite element software (ANSYS) run on a personal computer. Only two separate regions, the cytoplasm and nucleus, were taken into account in the cell model. Here, the cytoplasm and nucleus are both assumed to be continuous, homogeneous, isotropic and hyperelastic materials. Caille et al. [2002] proposed that endothelial cells can be represented as a neoHookean material. They expressed the strain energy function by two parameters, the elastic modulus and Poisson's ratio. We used this model in the finite element analysis of the tensile test. We assumed both the cytoplasm and nucleus are almost incompressible, with Poisson's ratio of 0.48 [Vaziri et al. 2006]. The entire cell and nucleus were both modeled as concentric spheres, with diameters of 21 $\mu$m and 10 $\mu$m, respectively. To model the fixed cantilever, a part of the left edge of the cytoplasm is fixed in position, while tensile stress is given to a part of the right edge of the cytoplasm. The volume of the fixed or freely moving parts of the cytoplasm is determined from the distance of 17 $\mu$m between the cantilevers. Systematic finite element simulations are performed to determine the elastic modulus of the cytoplasm $E_c$ and the nucleus $E_n$ that best fits to experimental data on the cell and nucleus deformations.

## 3. Results

**3.1.** *Tensile properties of the whole cell.* Single cells were stretched at a constant rate of 1 $\mu$m/s by using the feedback control system. A typical example of the test showed that the cell and its nucleus that had round shapes originally were both elongated during the movement of the deflectable cantilever; see Figure 3. We will particularly discuss the nucleus behavior obtained in this example. The cell detached from the right cantilever at 9.5 s after the initiation of the stretch. The detachment occurs at one end of the cell where the adhesion force is probably weaker. The cell shrank soon after the detachment and gradually returned to its original round shape. The electric outputs that represent cantilever displacements indicated
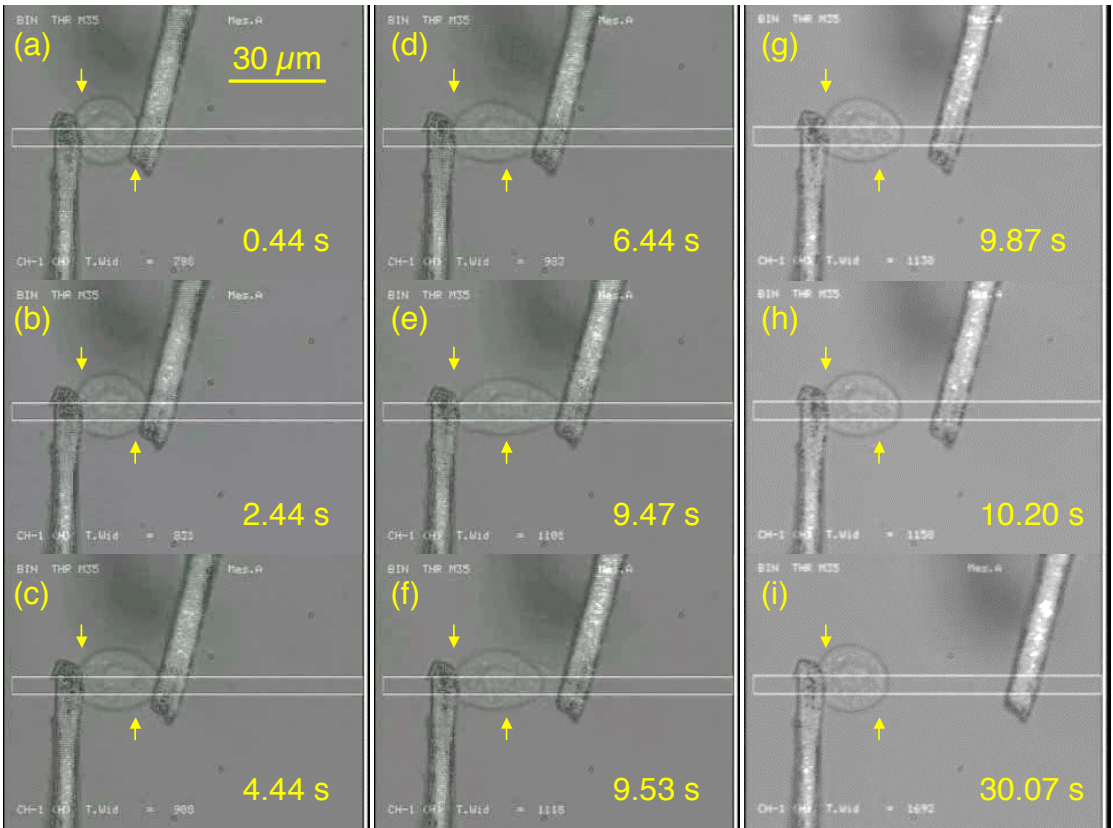
**Figure 3.** Sequential images of the tensile test and creep recovery after cell unloading. Arrows locate original positions of the inner edges of the cantilevers. White marks originally on the monitor; yellow ones added for clarification. Area within white lines shows where cantilever tip displacement is tracked by binary image processing. Time elapsed given in the lower right of each panel.

that the cantilever tip was displaced at a constant rate of $1\,\mu$m/s until the detachment occurred, while the base part showed larger displacements as shown in Figure 4. The constant rise in the cantilever tip displacement, which also corresponds to a constant rise in cell displacement in the longitudinal direction because the left cantilever is fixed, is realized by the feedback control. The difference of the tip and base displacements represents deflection of the right cantilever in bending. The deflection multiplied by the spring constant of $0.14\,$N/m yields the tensile loading onto the cell; see Figure 5. The tensile loading increased as the stretch proceeded. Here, stretching stain is defined as the ratio of the displacement to the initial longitudinal length of the cell. The initial longitudinal length of the cell is defined to be the original distance between the inner edges of the cantilevers of $17.1\,\mu$m. A representative cross-sectional area of the cell is defined as $\pi(D/2)^2$, where $D=21.1\,\mu$m is the initial lateral diameter of the cell. The original distance between the cantilevers and the initial lateral diameter of the cell were both obtained by an image analysis described in Section 3.2. Stress is defined as the tensile load divided by the above-described
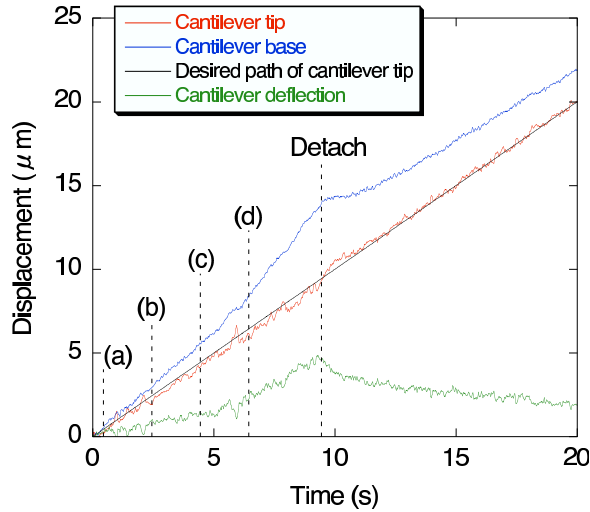
**Figure 4.** Time course of displacements of deflectable cantilever and its resultant deflection. Moments given by (a)–(d) correspond to those in Figure 3. Regression curve is obtained by the least squares method.
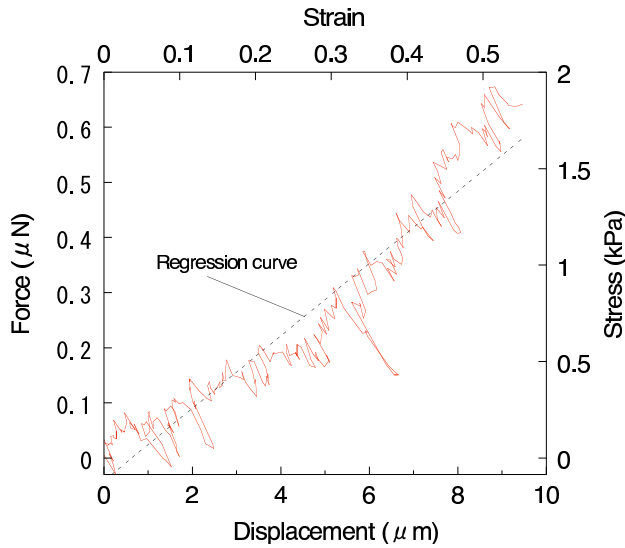


**Figure 5.** Force-displacement curve of the cell. Right ordinate and upper abscissa show stress and strain, respectively.

representative cross-sectional area calculated using the initial diameter. The ordinate and abscissa of the force-displacement relation are then converted to stress and strain, respectively; see Figure 5. The linear curve obtained by least squares regression to the stress-strain plot provides an estimate of the longitudinal elastic modulus of the cell; for the case of Figure 5 it is 3.2 kPa. The tensile tests were done for 6 cells. The elastic modulus defined above was $2.6 \pm 0.7$ kPa.
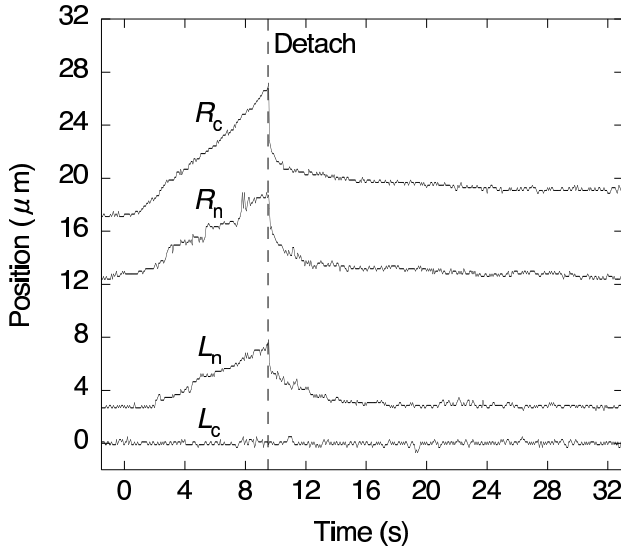
**Figure 6.** Changes in positions investigated in the image analysis. $R_c$, $L_c$ are inner edges of the right/left cantilever, respectively, and $R_n$, $L_n$ are right/left edges of nucleus.

**3.2.** *Image analysis of the cell and nucleus behaviors.* After being detached from the cantilever, the cell gradually deformed owing to viscoelasticity; see Figure 3 for $t > 9.5$. The time course of the deformation during the shrinkage was examined by the image analysis because the electric outputs representing the cantilever positions do not make sense after the detachment; see Figure 4. The image analysis and the subsequent analysis on viscoelasticity were done for the one typical case shown in Figures 3–5. The image analysis result showed that both the cell and the nucleus exhibited shrinkages after detachment and then gradually returned to their original shapes. The right edge of the cell, where the detachment occurred, approached a value different from its original position because the right cantilever originally hid the right part of the cell of length $\sim 1.9\,\mu$m.

**3.3.** *Viscoelastic properties.* From the time course displacements of the cell and nucleus edges obtained in the image analysis shown in Figure 6 the changes in the longitudinal lengths of the cell and nucleus themselves were obtained as shown in Figure 7. After being detached, both the cell and nucleus shrank to their original shapes. In order to study the viscoelastic behaviors we employ the Kelvin or standard linear model, or a power-law function.

The Kelvin model consists of a spring and a dashpot in series, that is, the Maxwell chain, that is placed with a single spring in parallel. The relation between force $F$ and its loading point displacement ($u$) is represented as [Fung 1993]:

$$F + \tau_\varepsilon \dot{F} = E(u + \tau_\sigma \dot{u}), \tag{1}$$

where $E$, $\tau_\varepsilon$, and $\tau_\sigma$ are constants. It is assumed that the cell is stretched quasistatically at time $t < 0$ and is detached at $t > 0$, which gives

$$u(0^-) = F(0)/E, \qquad t = 0^-, \tag{2}$$

$$F(t) = 0, \qquad t > 0. \tag{3}$$
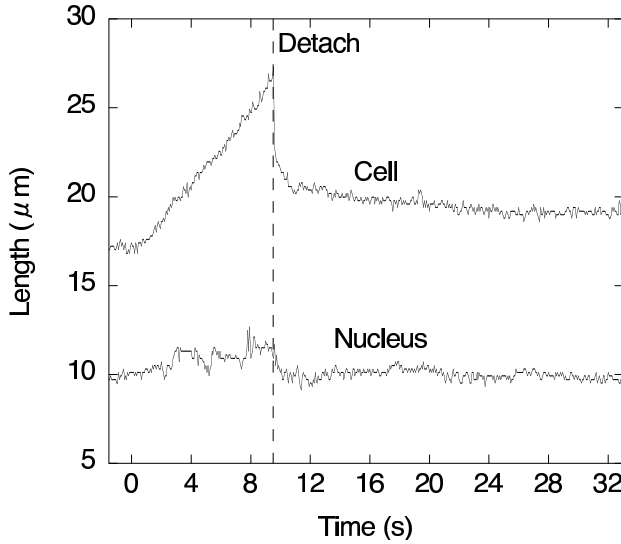
**Figure 7.** Changes in longitudinal lengths of cell and nucleus during cell stretch.

Integration of Equation (1) considering Equation (3) yields

$$u(t) = u(0^-)\frac{\tau_\varepsilon}{\tau_\sigma}e^{-t/\tau_\sigma}, \quad t \geq 0. \tag{4}$$

Here we assess mechanical properties of the nucleus under an assumption that the time course change in the nuclear deformation shown in Figure 8 is caused by the mechanical properties of the nucleus itself and is independent of the surrounding cytoplasm's influence. Performing a linear fit to the length change before detachment as shown in Figure 7, Equation (2) yields $u(0^-) = 9.6\,\mu$m for the cell and $u(0^-) = 1.6\,\mu$m for the nucleus. These values are then substituted in Equation (4). Assuming $\tau_\varepsilon$ and $\tau_\sigma$ are separated by a 0.1 s interval, Equation (4) is fitted to the creep recovery data after the unloading of the cell and nucleus to characterize fundamental viscoelasticity of the biomaterials as shown in Figure 8 [Guilak et al. 2000; Vaziri et al. 2006; Nagayama et al. 2007]. A combination of $\tau_\varepsilon = 0.2$ s and $\tau_\sigma = 0.2$ s is best fitted to the nucleus data, suggesting that the nucleus behaved like the Voigt solid instead of the standard linear solid [Fung 1993]. A single combination of $\tau_\varepsilon$ and $\tau_\sigma$ is not well fitted to the cell data; therefore, two different combinations are analyzed for the earlier and later parts of the data. The right side of Equation (3) plus a value of 1 with a combination of $\tau_\varepsilon = 0.3$ s and $\tau_\sigma = 1.2$ s represents the best fit to the former part of the cell data. A combination of $\tau_\varepsilon = 2.1$ s and $\tau_\sigma = 8.0$ s is the best fit to the latter part of the cell data.

This result suggests that a single use of the Kelvin model might be insufficient for modeling a cell viscoelastic behavior in such a large strain case. The following power-law function is then fitted to the cell creep curve:

$$u(t) = u(0^-)(1 - kt^a), \quad \text{for } t \geq 0, \tag{5}$$

where $k$ and $a$ are constants. A combination of $k = 0.79\,\mu$m/s$^{0.071}$ and $a = 0.071$ is the best fit to the curve that was shown in Figure 8, suggesting that a power-law may be an intrinsic feature of cell mechanics [Desprat et al. 2005; Fernandez et al. 2006].
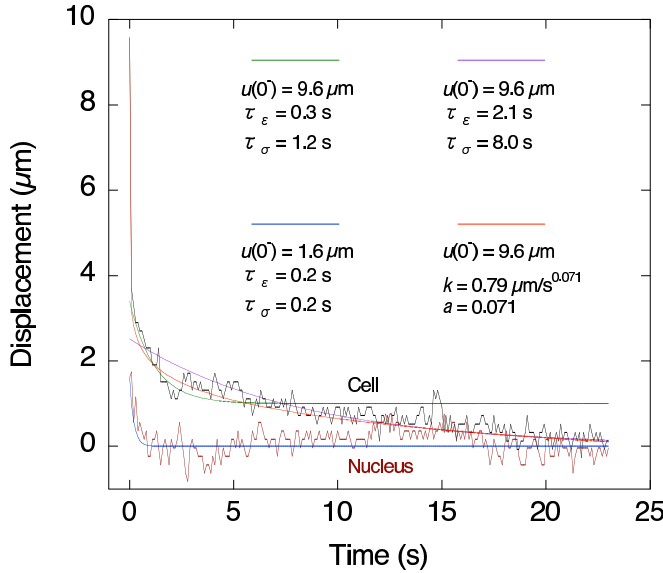
**Figure 8.** Viscoelastic model fit to displacements of cell and nucleus in creep recovery.

**3.4.** *Analytical estimation of tensile properties of the nucleus.* Force-displacement relation of the nucleus was roughly estimated under an assumption that the force detected by the cantilever was loaded onto the nucleus in the longitudinal stretching direction; see Figure 9. This assumption is similar to the one in a previous study [Maniotis et al. 1997] and is made to obtain a crude estimation, but its effectiveness is tested by finite element method in the following section. Similarly to the case of the cell (Figure 5), strain of the nucleus is defined as the ratio of the displacement to its initial length in the longitudinal direction, which is $9.95 \, \mu$m. Stress in the nucleus is defined as the force divided by a representative cross-sectional area, given by $A = \pi (D_{\text{lateral}}/2)^2 = \pi (9.95/2)^2$. The right ordinate and the upper abscissa of the force-displacement relation are also represented by the stress and the strain, respectively; see Figure 9. The slope of a linear curve obtained by least squares method for the stress-strain curve provides an estimate of an elastic modulus of $28.2 \, \text{kPa}$. For comparison, the regression curve of the force-displacement relation of the cell is shown for the left ordinate and the lower abscissa. In addition, the regression curve of the stress-strain relation of the cell is shown for the right ordinate and the upper abscissa.

**3.5.** *Further estimation of the cell and nucleus elastic modulus by finite element analysis.* Systematic finite element simulations were performed to further estimate the elastic modulus of the cytoplasm $E_c$ and the nucleus $E_n$. The longitudinal displacements (in the $x$-direction in Figure 10b) of the cell $D_c$ and the nucleus $D_n$ were computed taking various parameter values of $E_c$ and $E_n$ at $0.2 \, \text{kPa}$ and $2 \, \text{kPa}$ intervals, respectively; see Figure 11. $D_c$ was calculated from the changes in the distance between cantilevers in the $x$-direction. The experimental data just before the detachment shows that tensile loading was $0.58 \, \mu$N (Figure 5), $D_c = 9.6 \, \mu$m and $D_n = 1.6 \, \mu$m (Figure 7). The tensile stress, given by tensile loading of $0.58 \, \mu$N divided by cross-sectional area at the interface between the cell model and the right cantilever $38\pi \, \mu\text{m}^2$, was given to the right edge of the computational cell model; see Figure 10. The parameter
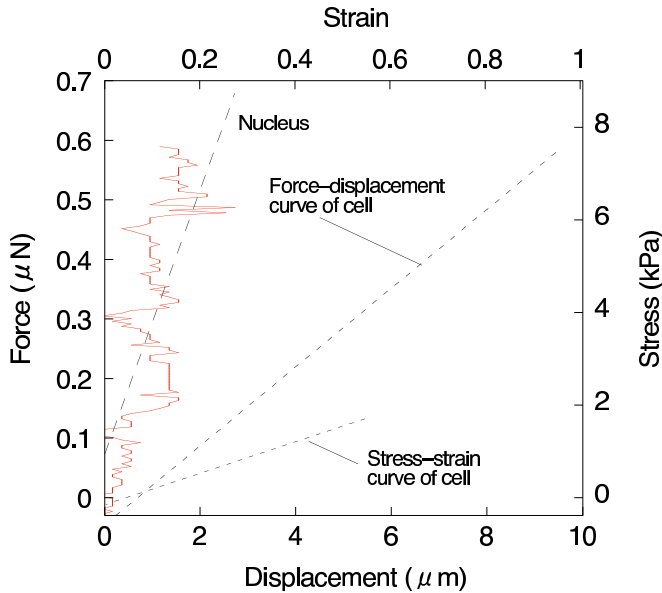
**Figure 9.** Force-displacement curve of the nucleus. Right ordinate and upper abscissa show stress and strain, respectively. For comparison, regression curve of force-displacement relation of cell is shown for left ordinate and lower abscissa. Regression curve of stress-strain relation of cell is shown for right ordinate and upper abscissa.

combination of $E_c$ and $E_n$, which results in $D_c = 9.6\,\mu\mathrm{m}$ and $D_n = 1.6\,\mu\mathrm{m}$, was analyzed. The result shows that a combination of $E_c = 3.7\,\mathrm{kPa}$ and $E_n = 32\,\mathrm{kPa}$ represents the best fit; see Figure 11.

## 4. Discussion

The most significant data obtained in this study is the behavior of the nucleus under unidirectional cell stretching and creep recovery after unloading (Figures 8–11). The tensile properties of the nucleus were first assessed under a rough assumption (Figure 9) that the force detected by the cantilever deflection was loaded onto the nucleus in the longitudinal direction. The estimated elastic modulus was 28.2 kPa, which is 8.8 times stiffer than that of the cell at $\sim 3.2\,\mathrm{kPa}$. This value is comparable in magnitude to the result reported by Maniotis et al. [1997], in which nuclei within adherent cells have a rigidity of 9 times stiffer than that of the cytoplasm when a local part of the cell membrane is pulled by using a thin glass needle. Caille et al. [2002] also reported the similar ratio of 10 times. Our result showed a good agreement with the previous studies even in the stretch of the whole portion of a cell.

The elastic modulus is further investigated by finite element analyses of the tensile test (Figures 10 and 11). The effective stress distribution (Figure 10b) shows that there is a distinct stress gradient along the lateral direction vertical to the stretch. This lateral stress gradient is in part caused by a lateral compression of the nucleus by the surrounding cytoplasm. This result indicates that the assumption done in the rough estimation, that is, only force detected by the cantilever deflection is loaded onto the nucleus, may lead to underestimate the elastic modulus of the nucleus. A parametric study employing a spherical cell shape model yielded a larger value of 32 kPa compared with 28.2 kPa that was obtained in

(a)                                        (b)
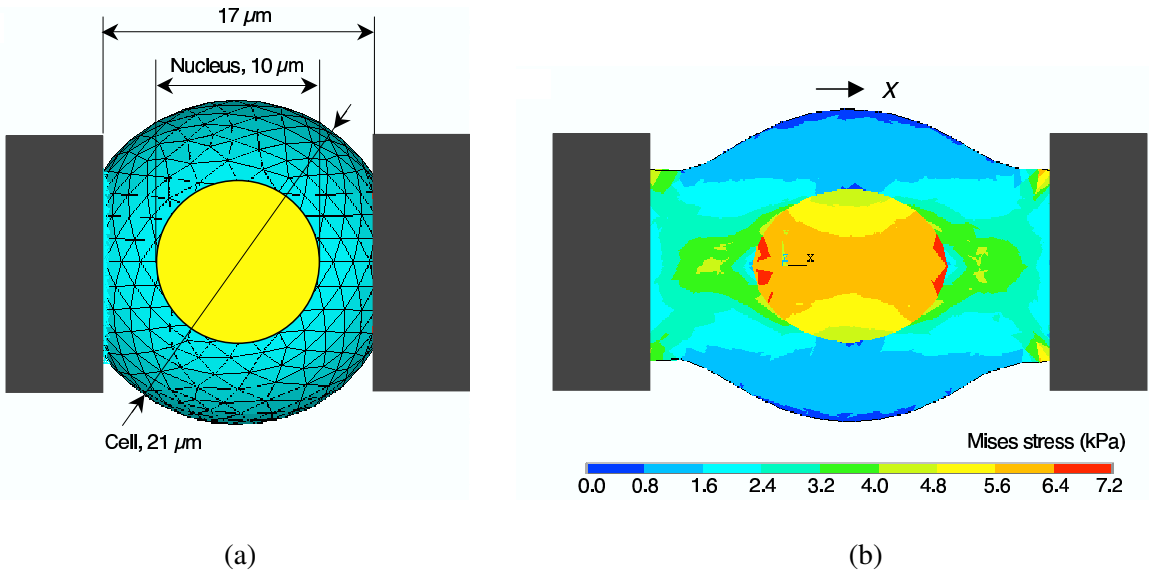
**Figure 10.** Finite element simulation of tensile test. (a) Model geometry: the cantilevers as a rigid wall. Cell meshes represent those viewed from outside, and nucleus geometry inside cell is superimposed on top. (b) Effective (von Mises) stress field in center section at a cytoplasm and nucleus elastic moduli $E_c = 3.6$ kPa, $E_n = 34$ kPa, respectively.
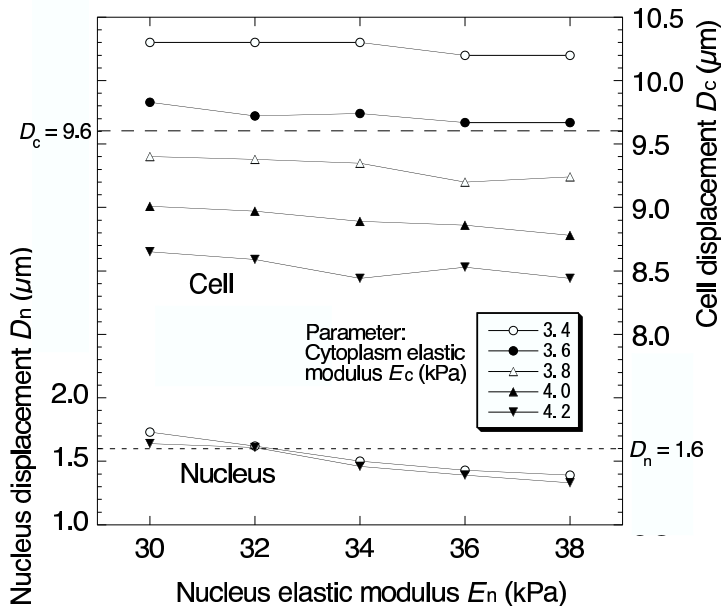


**Figure 11.** Computational results of the effect of two parameters, cytoplasm and nucleus elastic moduli $E_c$ and $E_n$, on longitudinal displacements of cell $D_c$ and nucleus $D_n$.

the simple analysis. A larger elastic modulus estimation of the cytoplasm 3.7 kPa was also obtained in the finite element analysis compared with 3.2 kPa obtained in the analytical estimation. This is caused by that stress was determined, in the rough estimation, from the initial cross-sectional area that is actually reduced gradually as stretch proceeds. Thus, computational continuum mechanics approaches can give an accurate assessment, from a macroscopic view, of the mechanical properties of cell and nucleus, rather than a simple analytical approach. Cells actually have an inhomogeneous structure composed of cytoskeletal networks and membrane-bound organelles. More accurate intracellular force transmission taking the inhomogeneous cell structure into account will be the subject of future investigation [Deguchi et al. 2005c].

The viscoelastic properties of the nucleus in the creep recovery process were assessed under the assumption that the time course change in the nuclear deformation is caused by the mechanical properties of the nucleus and is independent of an influence due to the surrounding cytoplasm. The numerical approach to the viscoelastic behaviors taking the spherical geometry into account will be an issue in the future investigation. Our result indicated that the nucleus behaved like the Voigt solid, whereas the whole cell behaved as a power-law viscoelastic material; see Figure 8. Specifically, the cell exhibited a rapid and large drop in the stretching strain immediately after the detachment and then gradually returned to its original shape. Such a gradual decrease after the detachment was not observed in the nucleus. This is consistent with the observation by Caille et al. [2002] that isolated endothelial nuclei returned elastically to their original morphology when compressing load was removed.

In contrast, Guilak et al. [2000] reported that the nuclei isolated from chondrocytes were nearly as viscous as the cytoplasm using the pipette aspiration technique. In addition, recently increasing knowledge of the mechanical properties of individual nucleus components [Dahl et al. 2004; 2005; Rowat et al. 2005; 2006] suggests nonlinear behaviors of the nucleus. Although the difference between the results is unclear, it may be due to differences in the specimen and experimental condition, for example, the loaded range applied to investigate the viscoelasticity.

The microtensile test requires a quite difficult technique (for example, to capture a small cell by using a pair of cantilevers carefully like chopsticks) compared with a well-developed system of AFM or other mechanical testing approaches [Wang et al. 1993; Karcher et al. 2003; Tseng et al. 2004] that are readily available. This may restrict the use of the microtensile test. Despite the issue, the microtensile test can elucidate nucleus responses within the cytoplasm in a well-controlled tensed state and in an unloaded state, while measuring the force required for stretching. The order of magnitude of the force in the present study was $0.1–1\,\mu N$, which is larger than optical tweezers can realize, that is, $\sim 10\,pN$ [Mills et al. 2004].

Previous microtensile tests using thin cantilevers revealed that single actin filaments and the actin-bundled stress fibers require a tensile force of piconewton order [Kishino and Yanagida 1988] and nanonewton order [Deguchi et al. 2006], respectively, to be stretched. It is thus possible for the microtensile test to do such a wide force range measurement by adjusting the spring constant of the force-detection cantilever including a microplate used in [Caille et al. 2002]. In addition, the microtensile test enables evaluation of the mechanical properties at a whole cell level with a large strain range, whereas the AFM or other methods can give a limited strain to a local part of a targeted cell.

## 5. Conclusion

Deformation behaviors of the nucleus during creep recovery after unloading show that the nucleus behaved like the Voigt solid, whereas the whole cell showed a power-law behavior. In addition, under a crude assumption that the tensile force loaded onto the cell is concentrated entirely onto the nucleus, tensile properties of the nucleus are compared with those of the cell. Also, systematic finite element analysis was conducted to make another estimation of elastic modulus of the cell and nucleus. These results indicate that the nucleus is stiffer and more elastic compared with the whole cell subjected to unidirectional stretching and unloading, thereby demonstrating inhomogeneous stiffness and viscoelasticity within a single cell.

## Acknowledgements

## References

[Ashkin et al. 1986]  A. Ashkin, J. M. Dziedzic, J. E. Bjorkholm, and S. Chu, "Observation of a single-beam gradient force optical trap for dielectric particles", *Opt. Lett.* **11**:5 (1986), 288–290.

[Caille et al. 1998]  N. Caille, Y. Tardy, and J. J. Meister, "Assessment of strain field in endothelial cells subjected to uniaxial deformation of their substrate", *Ann. Biomed. Eng.* **26**:3 (1998), 409–416.

[Caille et al. 2002]  N. Caille, O. Thoumine, Y. Tardy, and J. J. Meister, "Contribution of the nucleus to the mechanical properties of endothelial cells", *J. Biomech.* **35**:2 (2002), 177–187.

[Dahl et al. 2004]  K. N. Dahl, S. M. Kahn, K. L. Wilson, and D. E. Discher, "The nuclear envelope lamina network has elasticity and a compressibility limit suggestive of a molecular shock absorber", *J. Cell Sci.* **117** (2004), 4779–4786.

[Dahl et al. 2005]  K. N. Dahl, A. J. Engler, J. D. Pajerowski, and D. E. Discher, "Power-law rheology of isolated nuclei with deformation mapping of nuclear substructures", *Biophys. J.* **89** (2005), 2855–2864.

[Davies 1995]  P. F. Davies, "Flow-mediated endothelial mechanotransduction", *Physiol. Rev.* **75**:3 (1995), 519–560.

[Deguchi et al. 2005a]  S. Deguchi, K. Maeda, T. Ohashi, and M. Sato, "Flow-induced hardening of endothelial nucleus as an intracellular stress-bearing organelle", *J. Biomech.* **38**:9 (2005), 1751–1759.

[Deguchi et al. 2005b]  S. Deguchi, K. Ohashi, and M. Sato, "Newly designed tensile test system for in vitro measurement of mechanical properties of cytoskeletal filaments", *JSME Int. J. C Mech. Syst. Mach. Elem. Manuf.* **48** (2005), 396–402.

[Deguchi et al. 2005c]  S. Deguchi, T. Ohashi, and M. Sato, "Intracellular stress transmission through actin stress fiber network in adherent vascular cells", *Mol. Cell. Biomech.* **2**:4 (2005), 205–216.

[Deguchi et al. 2006]  S. Deguchi, T. Ohashi, and M. Sato, "Tensile properties of single stress fibers isolated from cultured vascular smooth muscle cells", *J. Biomech.* **39**:14 (2006), 2603–2610.

[Desprat et al. 2005]  N. Desprat, A. Richert, J. Simeon, and A. Asnacios, "Creep function of a single living cell", *Biophys. J.* **88** (2005), 2224–2233.

[Dong et al. 1991]  C. Dong, R. Skalak, and K. L. P. Sung, "Cytoplasmic rheology of passive neutrophils", *Biorheology* **28** (1991), 557–567.

[Fernandez et al. 2006]  P. Fernandez, P. A. Pullarkat, and A. Ott, "A master relation defines the nonlinear viscoelasticity of single fibroblasts", *Biophys. J.* **90** (2006), 3796–3805.

[Fung 1993]  Y. C. Fung, *Biomechanics: mechanical properties of living tissues*, Springer, New York, 1993.

[Guilak et al. 2000]  F. Guilak, J. R. Tedrow, and R. Burgkart, "Viscoelastic properties of the cell nucleus", *Biochem. Biophys. Res. Commun.* **269**:3 (2000), 781–786.

[Haga et al. 2000]  H. Haga, S. Sasaki, K. Kawabata, E. Ito, T. Ushiki, and T. Sambongi, "Elasticity mapping of living fibroblasts by AFM and immunofluorescence observation of cytoskeleton", *Ultramicroscopy* **82**:1-4 (2000), 253–258.

[Haider and Guilak 2000]  M. A. Haider and F. Guilak, "An axisymmetric boundary integral model for incompressible linear viscoelasticity: application to the micropipette aspiration contact problem", *J. Biomech. Eng. (Trans. ASME)* **122**:3 (2000), 236–244.

[Hashimoto et al. 2004]  K. Hashimoto, N. Kataoka, E. Nakamura, H. Asahara, Y. Ogasawara, K. Tsujioka, and F. Kajiya, "Direct observation and quantitative analysis of spatiotemporal dynamics of individual living monocytes during transendothelial migration", *Atherosclerosis* **177**:1 (2004), 19–27.

[Ingber 2003]  D. E. Ingber, "Tensegrity, I: Cell structure and hierarchical systems biology", *J. Cell Sci.* **116**:7 (2003), 1157–1173.

[Janmey 1998]  P. A. Janmey, "The cytoskeleton and cell signaling: component localization and mechanical coupling", *Physiol. Rev.* **78**:3 (1998), 763–781.

[Karcher et al. 2003]  H. Karcher, J. Lammerding, H. Huang, R. T. Lee, R. D. Kamm, and M. R. Kaazempur-Mofrad, "A three-dimensional viscoelastic model for cell deformation with experimental verification", *Biophys. J.* **85** (2003), 3336–3349.

[Kasza et al. 2007]  K. E. Kasza, A. C. Rowat, J. Liu, T. E. Angelini, C. P. Brangwynne, G. H. Koenderink, and D. A. Weitz, "The cell as a material", *Curr. Opin. Cell Biol.* **19**:1 (2007), 101–107.

[Kishino and Yanagida 1988]  A. Kishino and T. Yanagida, "Force measurements by micromanipulation of a single actin filament by glass needles", *Nature* **334**:6177 (1988), 74–76.

[Maniotis et al. 1997]  A. J. Maniotis, C. S. Chen, and D. E. Ingber, "Demonstration of mechanical connections between integrins, cytoskeletal filaments, and nucleoplasm that stabilize nuclear structure", *P. Natl. Acad. Sci. USA* **94** (1997), 849–854.

[Mills et al. 2004]  J. P. Mills, L. Qie, M. Dao, C. T. Lim, and S. Suresh, "Nonlinear elastic and viscoelastic deformation of the human red blood cell with optical tweezers", *Mol. Cell. Biomech.* **1**:3 (2004), 169–180.

[Miyazaki et al. 2000]  H. Miyazaki, Y. Hasegawa, and K. Hayashi, "A newly designed tensile tester for cells and its application to fibroblasts", *J. Biomech.* **33**:1 (2000), 97–104.

[Nagayama et al. 2006]  K. Nagayama, Y. Nagano, M. Sato, and T. Matsumoto, "Effect of actin filament distribution on tensile properties of smooth muscle cells obtained from rat thoracic aortas", *J. Biomech.* **39**:2 (2006), 293–301.

[Nagayama et al. 2007]  K. Nagayama, S. Yanagihara, and T. Matsumoto, "A novel micro tensile tester with feed-back control for viscoelastic analysis of single isolated smooth muscle cell", *Med. Eng. Phys.* **29**:5 (2007), 620–628.

[Rowat et al. 2005]  A. C. Rowat, L. J. Foster, M. M. Nielsen, M. Weiss, and J. H. Ipsen, "Characterization of the elastic properties of the nuclear envelope", *J. Roy. Soc. Interface* **2**:2 (2005), 63–69.

[Rowat et al. 2006]  A. C. Rowat, J. Lammerding, and J. H. Ipsen, "Mechanical properties of the cell nucleus and the effect of emerin deficiency", *Biophys. J.* **91** (2006), 4649–4664.

[Sato et al. 1990]  M. Sato, D. P. Theret, L. T. Wheeler, N. Ohshima, and R. M. Nerem, "Application of the micropipette technique to the measurement of cultured porcine aortic endothelial cell viscoelastic properties", *J. Biomech. Eng. (Trans. ASME)* **112** (1990), 263–268.

[Sato et al. 2000]  M. Sato, K. Nagayama, N. Kataoka, M. Sasaki, and K. Hane, "Local mechanical properties measured by atomic force microscopy for cultured bovine endothelial cells exposed to shear stress", *J. Biomech.* **33**:1 (2000), 127–135.

[Shue and Brozovich 1999]  G. H. Shue and F. V. Brozovich, "The frequency response of smooth muscle stiffness during $Ca^{2+}$-activated contraction", *Biophys. J.* **76**:5 (1999), 2361–2369.

[Smith et al. 2000]  P. G. Smith, C. Roy, S. Fisher, Q. Huang, and F. V. Brozovich, "Cellular responses to mechanical stress: selected contribution: mechanical strain increases force production and calcium sensitivity in cultured airway smooth muscle cells", *J. Appl. Physiol.* **89**:5 (2000), 2092–2098.

[Tseng et al. 2004] Y. Tseng, J. S. Lee, T. P. Kole, I. Jiang, and D. Wirtz, "Micro-organization and viscoelasticity of the interphase nucleus revealed by particle nanotracking", *J. Cell Sci.* **117**:10 (2004), 2159–2167.

[Vaziri et al. 2006] A. Vaziri, H. Lee, and M. R. Kaazempur Mofrad, "Deformation of the cell nucleus under indentation: mechanics and mechanisms", *J. Mater. Res.* **21** (2006), 2126–2135.

[Wang et al. 1993] N. Wang, J. P. Butler, and D. E. Ingber, "Mechanotransduction across the cell surface and through the cytoskeleton", *Science* **260** (1993), 1124–1127.

SHINJI DEGUCHI: deguchi@mech.okayama-u.ac.jp
*Graduate School of Natural Science and Technology, Okayama University, Tsushima-naka 3-1-1, Okayama 700-8530, Japan*

MASAYUKI YANO: *Graduate School of Natural Science and Technology, Okayama University, Tsushima-naka 3-1-1, Okayama 700-8530, Japan*

KEN HASHIMOTO: khashimo@med.kawasaki-m.ac.jp
*Department of Physiology, Kawasaki Medical School, 577 Matsushima, Kurashiki, Okayama 701-0192, Japan*

HIROYUKI FUKAMACHI: hiroyuki@keilab.mech.okayama-u.ac.jp
*Graduate School of Natural Science and Technology, Okayama University, Tsushima-naka 3-1-1, Okayama 700-8530, Japan*

SEIICHI WASHIO: washio_s@mech.okayama-u.ac.jp
*Graduate School of Natural Science and Technology, Okayama University, Tsushima-naka 3-1-1, Okayama 700-8530, Japan*

KATSUHIKO TSUJIOKA: tsujioka@med.kawasaki-m.ac.jp
*Department of Physiology, Kawasaki Medical School, 577 Matsushima, Kurashiki, Okayama 701-0192, Japan*

# MICROSCALE HYDROGELS FOR MEDICINE AND BIOLOGY: SYNTHESIS, CHARACTERISTICS AND APPLICATIONS

CHRISTOPHER RIVEST, DAVID W. G. MORRISON, BIN NI, JAMIE RUBIN,
VIKRAMADITYA YADAV, ALBORZ MAHDAVI, JEFFREY M. KARP AND ALI KHADEMHOSSEINI

Microscale hydrogels with dimensions of $200\,\mu$m or less are powerful tools for various biomedical applications such as tissue engineering, drug delivery, and biosensors, due to their size, biocompatibility, and their controllable biological, chemical, and mechanical properties. In this review, we provide a broad overview of the approaches used to synthesize and characterize microgels, as well as their applications. We discuss the various methods used to fabricate microgels, such as emulsification, micromolding, microfluidics, and photolithography. Furthermore, we discuss the effects of porosity and crosslinking density on the mechanical and biological properties of hydrogels. In addition, we give specific examples of the use of hydrogels, such as scaffolds and cell encapsulation for tissue engineering, controlled release materials for drug delivery, and environmentally sensitive sensors for microdevices. Finally, we will discuss the future applications of this technology.

## 1. Introduction

Hydrogels are crosslinked hydrophilic polymers that swell greatly in water. Hydrogels can be synthesized from a wide range of natural or synthetic polymers [Peppas et al. 2006]. Examples of common natural hydrogels include fibrin, hyaluronic acid (HA), agarose, and alginate. Similarly, common synthetic polymers that can be crosslinked to form hydrogels include poly(ethylene glycol) (PEG), poly(vinyl alcohol) (PVA), and polystyrene. Since the chemical and mechanical properties of hydrogels can be engineered, they are well suited to address problems in medicine and biology. For example, each year thousands of people die from organ failure due to shortages of transplantable organs; hydrogels can potentially be used to engineer tissue constructs. To minimize the toxic effects of high drug doses, it is often desirable to deliver drugs in a controllable manner: this too can be achieved with hydrogels synthesized with controlled porosity and crosslinking density.

Despite their widespread potential, macroscale hydrogels have a number of limitations for medical and biological applications. In tissue engineering, for example, hydrogel scaffolds may cause cell necrosis due to diffusion limitations, even though these artificial scaffolds closely mimic the chemical and mechanical properties of natural extracellular matrix (ECM). In large hydrogels it is difficult to control the three-dimensional (3D) architecture and cell-cell interactions, which makes it difficult to replicate the complexity of real tissues. Microscale hydrogels, in contrast, have no such limitations. For example, by using hydrogels of controlled sizes and shapes [Yeh et al. 2006], it is possible to minimize diffusion limitations while fabricating tissues with complex microvasculature and microarchitecture [Sefton and

|  | (+) | (−) |
|---|---|---|
| *Micromolding* | Controlled shape and size | Batch process |
| *Photolithography* | Controlled shape and size | Batch process |
|  |  | Cell toxic photoinitiator |
| *Microfluidics* | Homogeneous, continuous | Nonscalable |
| *Emulsification* | Easily scalable | Limited to spherical shapes |

**Table 1.** Advantages and disadvantages of microgel fabrication methods.

McGuigan 2006]. The use of microscale hydrogels is also useful for drug delivery applications, since the size and shape of the delivery vehicle can be used to control the rate of release and to target delivery to specific locations in the body.

This review presents a broad summary of the science and applications of microscale hydrogels. It discusses various methods for fabricating microgels, and introduces techniques for characterizing and engineering the mechanical and chemical properties of microgels. We also demonstrate the application of engineered microgels to tissue engineering, diagnostics, microdevices, and drug delivery.

## 2. Synthesis and fabrication of microgels

Microgels can be manufactured by a variety of techniques, including micromolding, emulsification, microfluidic drop formation, and photolithography (see Figure 1 and Table 1). A combination of manufacturing method, hydrogel precursor, and crosslinking agent determine the eventual mechanical, physical, and chemical characteristics of a hydrogel. All of the manufacturing methods outlined in Figure 1 can be used with a wide range of hydrogel precursors as well as crosslinking agents.
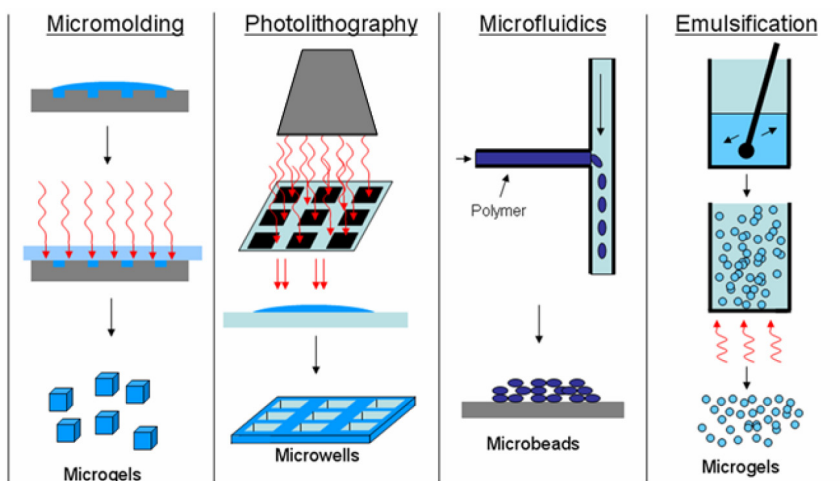


**Figure 1.** Methods of fabricating microgels.
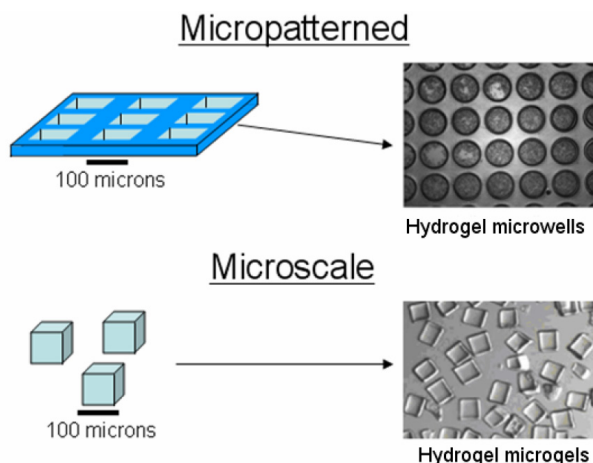
**Figure 2.** Microscale versus micropatterned hydrogels.

In this review we distinguish between microscale and microfeatured hydrogels. We define microscale hydrogels (microgels) as hydrogels with dimensions of $\approx 200\,\mu$m or less, and define microfeatured hydrogels as hydrogels that have been patterned with microscale features (see Figure 2). In this section we will discuss a few methods of manufacturing both microscale and microfeatured hydrogels.

*Emulsification.* Emulsification is the most common method used to manufacture microgels. The emulsification process typically uses a two-phase system by mixing two dissimilar substances such as a hydrophilic hydrogel precursor solution and a hydrophobic phase. Mechanical shearing forces the aqueous hydrogel prepolymer to emulsify in the hydrophobic phase (such as oil) and form a suspension of hydrogel microbeads. Varying the fluid viscosity and shear rate controls the size of the resulting microbeads. The prepolymer microbeads can then be crosslinked by a variety of methods such as heat or light.

Emulsification is used in drug delivery for fabrication of alginate microgels for insulin delivery [Reis et al. 2006], as well as for gene therapy [Alexakis et al. 1995]. Emulsification can also be used to encapsulate cells within microgels for bioreactor and immunoisolation applications [Dang and Zandstra 2005].

*Photolithography.* A common method to fabricate microgels of controlled sizes and shapes is photolithography. In photolithography, a hydrogel precursor is mixed with a photoinitiator which, when exposed to ultraviolet (UV) light, catalyzes the crosslinking reaction.

In one method, a thin film of hydrogel precursor and photoinitiator is placed underneath a photomask containing opaque patterns. The photomask is then exposed to UV light. The light reaches the underlying hydrogel precursor solution through the transparent regions of the photomask, causing the microgels to crosslink in those regions. This technique can be used to create microgels of various sizes and shapes based on the features on the mask. Photolithographic patterning of photocrosslinkable hydrogels can also be used to localize cells and generate cell-laden microstructures. For example, HepG2 cell-laden microstructures have been fabricated by encapsulating cells within crosslinkable PEG hydrogel [Liu and Bhatia 2002]. It is also possible to use this approach to generate more complex structures by combining multiple cell types into 3D structures [Koh et al. 2003]. Additionally, photolithography can create

functional components within microfluidic channels. For example, Beebe et al. [2000] manufactured microvalves by photopolymerizing hydrogels directly inside microchannels. These valves can be engineered from environmentally sensitive hydrogels, so that only specific stimuli will actuate them.

Despite the merits of photolithography for various applications, it has a number of limitations. For example, currently established photolithographic processes only produce output in batches. Recently, however, Dendukuri et al. [2006] adapted microgel photolithography into a continuous flow process. In this method, a photopolymerizable polymer is flowed through a microfluidic channel and subsequently exposed to UV light through a photomask to form microgels of specific sizes and shapes.

*Micromolding.* Micromolding is a useful technique for forming microgels and micropatterned hydrogels. Most micromolding techniques utilize a micropatterned master to mold replicas for repeated fabrication. The shape of the mold determines the shape of the resulting structures. It is now possible to fabricate microstructures as smaller than 1 $\mu$m. To fabricate microscale or microfeatured hydrogels, a hydrogel precursor is molded on the master, which is made from materials such as glass, PDMS, or silicon.

Micromolding of cell-laden hydrogels have been used to fabricate shape- and size-controlled tissue pieces that may be useful for tissue engineering [Khademhosseini et al. 2006a; 2006b; 2006c]. In these experiments, micromolded HA microwells were formed and used as docking regions for cell patterning and microarrays. The cells trapped inside the wells not only remained viable but could also be retrieved. The authors demonstrated that cell-laden microscale HA structures could be molded for incorporation into microdevices and biosensors. Fukuda et al. [2006] adopted micromolding techniques to create hydrogel microarrays and cocultures. By micromolding chitosan, they showed that various low shear-stress surface patterns could be created for the entrapment and organization of cells. Yeh et al. [2006] demonstrated the possibility of using photocrosslinkable polymers and micromolding to form stem cell seeded microgel tissue building blocks.

*Microfluidics and droplet formation.* Microfluidic techniques have been widely explored for their ability to form a variety of microgel constructs. Droplet formation within microfluidic channels can be used to fabricate highly homogeneous microgels. In one droplet-formation technology, a solution of prepolymer precursor is diverted into a larger microfluidic channel filled with a flowing solution containing the crosslinking agent [Nisisako et al. 2002]. The shear forces of the flow in the larger channel detach individual droplets of prepolymer solution, causing them to solidify into microgel constructs. The constructs are geometrically dependent on the flow rate and respective concentrations of the two microfluidic streams being mixed (see Figure 1). Other techniques utilize a microfluidic flow focusing device (MFFD) to generate reproducibly sized hydrogel spheres as small as 20 $\mu$m [Xu et al. 2005]. In addition to microfluidic channels, a number of authors have explored methods of forming droplets at the air-solution interface. For example, microneedles that are filled with a prepolymer solution can be induced to form picoliter droplets at a rate of hundreds of hertz, due to piezoelectrically induced pressure waves [Demerci et al. 2003].

Microfluidic approaches can also create macroscale hydrogels with unique spatial properties, such as concentration of density gradients. For example, hydrogels can be synthesized with spatially regulated patterning of adhesive or signaling molecules, or with an elasticity that varies from region to region. Such gels could be used for studying biological systems, directing stem cell differentiation, spatially or time-regulated drug delivery, or cell migration direction for tissue engineering [Burdick et al. 2004].

## 3. Mechanical properties of microscale hydrogels

Tissue engineering and biomedical needs call for fine control of the mechanical properties of hydrogels. For example, it might be necessary to develop a hydrogel tissue scaffold of varying mechanical rigidity or porosity. Alternatively, it may be desirable to create a hydrogel with nonuniform crosslinking for more effective drug delivery. The mechanical property of hydrogels is a function of many parameters such as the type of hydrogel, concentration, and crosslinking density. In this section we analyze the theoretical and experimental aspects of some of these parameters and examine their effect on the mechanical properties of hydrogels.

*Crosslinking and porosity.* A synthesized hydrogel has three main properties: the swollen-state polymer fraction $v_{2,s}$, the size $\xi$ of the polymer mesh, and the average molecular weight $\overline{M}_c$ of an intercrosslinked section of polymer chain [Peppas and Khare 1993]. The latter is the most important factor in hydrogel formation and governs how much a particular hydrogel solution is crosslinked. This in turn can drastically affect mechanical and chemical performance characteristics [Anseth et al. 1995]. To determine $\overline{M}_c$, the Flory–Rehner theory can be used for hydrogels prepared in a nonionic aqueous solvent. The theory states that

$$\frac{1}{\overline{M}_c} = \frac{2}{\overline{M}_n} - \frac{(\bar{v}/V_1)\left(\ln(1 - v_{2,s}) + v_{2,s} + \chi_1 v_{2,s}^2\right)}{v_{2,r}\left(\left(\frac{v_{2,s}}{v_{2,r}}\right)^{1/3} - \frac{v_{2,s}}{2v_{2,r}}\right)},$$

where $\bar{v}$ is the specific polymer volume, $v_{2,r}$ is the relaxed state polymer volume fraction, and $V_1$ is the molar water volume [Langer and Peppas 2003]. The Flory–Rehner theory for hydrogels dissolved in ionic aqueous solvents is more complex; it predicts the equations

$$\frac{V_1}{4IM_r}\left(\frac{v_{2,s}^2}{v}\right)\left(\frac{K_a}{10^{-\mathrm{pH}} - K_a}\right)^2$$
$$= \left(\ln(1 - v_{2,s}) + v_{2,s} + \chi_1 v_{2,s}^2\right) + \frac{V_1}{v\overline{M}_c}\left(1 - \frac{2\overline{M}_c}{\overline{M}_n}\right)v_{2,r}\left(\left(\frac{v_{2,s}}{v_{2,r}}\right)^{1/3} - \frac{v_{2,s}}{2v_{2,r}}\right),$$

$$\frac{V_1}{4IM_r}\left(\frac{v_{2,s}^2}{v}\right)\left(\frac{K_b}{10^{\mathrm{pH}-14} - K_a}\right)^2$$
$$= \left(\ln(1 - v_{2,s}) + v_{2,s} + \chi_1 v_{2,s}^2\right) + \frac{V_1}{v\overline{M}_c}\left(1 - \frac{2\overline{M}_c}{\overline{M}_n}\right)v_{2,r}\left(\left(\frac{v_{2,s}}{v_{2,r}}\right)^{1/3} - \frac{v_{2,s}}{2v_{2,r}}\right),$$

where $K_a$ and $K_b$ are the acid and base dissociation constants, $I$ is the ionic strength, and $M_r$ is the repeating unit molecular weight [Peppas et al. 2006]. This theory enables custom design of hydrogels and microhydrogels to satisfy particular mechanical and chemical characteristics.

Spacing between macromolecular chains is another important characteristic of hydrogels. These spaces are called *pores*. Hydrogels are generally categorized into three porosity categories: (i) nonporous, (ii) microporous, and (iii) macroporous. The polymeric mesh, or pore size of a particular hydrogel, can be calculated using the following equation:

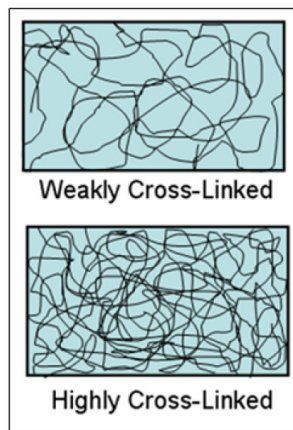$$\xi = v_{2,s}^{-1/3}\left(\frac{2C_n\overline{M}_c}{M_r}\right)^{1/2} l,$$

**Figure 3.** Highly crosslinked hydrogels and weakly crosslinked hydrogels.

where $C_n$ is the Flory characteristic ratio and $l$ is the length of the polymer backbone bond [Peppas et al. 2006].

By altering such factors as the pore size or the molecular weight between crosslinks (see Figure 3), it is possible to tailor individual hydrogel constructs to exhibit particular thermal, diffusive, or mechanical properties.

*Mechanical performance.* Hydrogels' adaptable mechanical properties makes them especially useful for drug delivery and tissue engineering. For example, mechanical forces are known to affect cell viability, gene expression, and stem cell differentiation pathways [Engler et al. 2006]. Because human tissues are highly organized structures, any engineered tissue will need to have the same degree of mechanical and physical complexity. Thus, by utilizing hydrogels of varying mechanical properties, it may be possible to mimic natural tissue.

Mechanically, hydrogels are remarkably similar to both human tissue as well as natural rubbers. Hydrogels generally exhibit excellent elastic characteristics: when loaded to deformations of 20% or less, they typically rebound instantaneously [Peppas et al. 2006]. Thus, rubber elasticity theory effectively characterizes the deformation of hydrogels. The rubber elasticity theory for solvent-based hydrogels is given as

$$\tau = \frac{\rho RT}{\overline{M}_c}\left(1 - \frac{2\overline{M}_c}{\overline{M}_n}\right)\left(\alpha - \frac{1}{\alpha^2}\right)\left(\frac{v_{2,s}}{v_{2,r}}\right)^{1/3},$$

where $\tau$ is the stress applied to the polymer sample, $T$ is the absolute experimental temperature, $\rho$ is the density of the polymer, $R$ is the universal gas constant, and $\overline{M}_c$ is the molecular weight between crosslinks [Peppas 1997].

Much work has been done to characterize mechanical characteristics of hydrogels [Anseth et al. 1995] and to determine how to synthesize a gel with desired mechanical properties [Cohen et al. 1992; Davis 1989; Greenberg 1980; Moussaid et al. 1994]. The innumerable possible combinations of composite hydrogels have inspired new techniques for high-throughput mechanical testing of polymers. In one example, over 1700 photopolymerizable materials were tested in only a few days by using an automated

nanomechanical screening system [Tweedie et al. 2005]. Using nanoindentation, an entire library of nanoliter samples placed on a glass slide was quickly tested for mechanical characteristics such as elastic modulus $E$, hardness $H$, and $P$-$h$ load-displacement hysteretic curves.

## 4. Tissue engineering

Tissue engineering is "an interdisciplinary field that applies the principles of engineering and life sciences towards the development of biological substitutes that restore, maintain, or improve tissue function or entire organs" [Langer and Vacanti 1993]. Since hydrogels are made mostly of water and natural (or synthetic biocompatible) polymers, they are often biologically compatible [Bruck 1973]. Accordingly, most hydrogels exhibit good compatibility when seeded with cells or when implanted *in vivo*.

The use of microscale hydrogels (such as microrods or microbeads), as well as microfeatured hydrogels (such as microchannels or microvasculature), has been useful in various tissue engineering applications. In the following sections we will highlight a few examples of hydrogels in tissue engineering research.

*Microscale scaffolds.* Cells require a suitable growth environment and a biomimetic 3D architecture in order to form tissues [Nguyen 2002; Peppas et al. 2006]. One method of constructing tissues from cells is by spatially orienting the cells in a desired 3D geometry with a hydrogel scaffold. Hydrogel scaffolds provide cells with environmental conditions favorable for growth by allowing nutrient transport and oxygen diffusion. Additionally, they offer temporary mechanical support for cells, until the cells can deposit their own ECM molecules. Many hydrogel materials are also biologically degradable. Consequently, as cells proliferate within the scaffold and form tissues, the scaffold itself breaks down, leaving transplantable tissues containing only natural cellular components.

Scaffold-based tissues may be built either from the top down, or from the bottom up. In the former, macroscale hydrogels are micropatterned to enable nutrient perfusion and cell adhesion. The bottom-up approach, in contrast, uses cell-laden microgels or tissue aggregates that can be combined to form larger, tissue-like constructs.

In one top-down example, a vessel was loaded with PMMA microspheres and then filled with the hydrogel precursor [Stachowiak et al. 2005]. Upon crosslinking the hydrogel, the PMMA microspheres were dissolved to create a microporous hydrogel scaffold. The resulting scaffold was then seeded with cells (see Figure 4).

Sefton and McGuigan [2006], in contrast, used a bottom-up approach: a packed bed of microgels facilitated the development of a perfusable tissue-like construct. Submillimeter hydrogel rods were seeded with endothelial cells (ECs) and then packed within a larger tube that was perfused with blood. The microscale gel rods merged to form a tissue-like construct with vascularization, due to the interstitial spaces between the microrods (see Figure 5).

Another bottom-up method due to Yeh et al. [2006] showed the potential use of HA or PEG microgel blocks as building blocks for tissues. Using photopolymerized micromolding, cell-laden microgels were fabricated with various shapes and sizes. These gels could be subsequently assembled to form complex 3D structures.
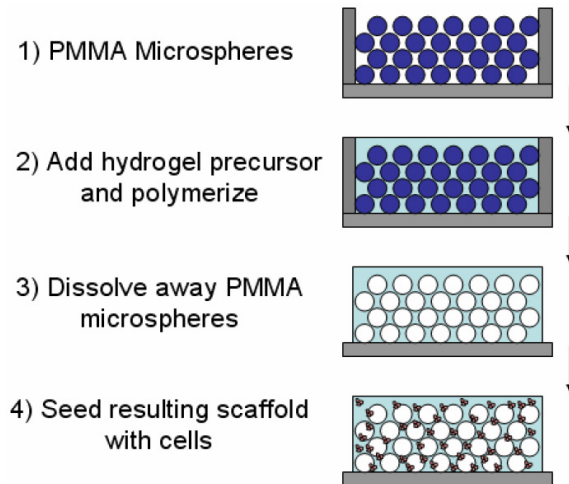
**Figure 4.** Tissue scaffold formation via microsphere dissolution.
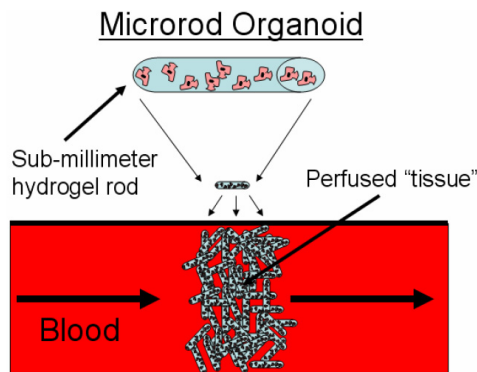


**Figure 5.** Packed bed of hydrogel microrods form a tissue-like organoid.

*Microvasculature.* One of the most difficult problems in tissue engineering is vascularization. Many attempts have been made to engineer microvasculature within tissue engineering constructs [Borenstein et al. 2002; Kaihara et al. 2000]. Although initial work was performed using nonbiodegradable PDMS and silicon, recent research has demonstrated that it is possible to create biomimetic capillary channels using micromolded biodegradable poly(glycerol-sebacate) (PGS). In this technique, hydrophilic PGS was molded onto microfabricated silicon. Multiple layers of micropatterned PGS were then stacked on one another and subsequently bonded. The resulting 3D tissue-like construct contains biomimetically sized vasculature. Eventually, this may enable the construction of perfusable engineered tissues.

Recently, Cabodi et al. [2005] demonstrated the feasibility of using sealable calcium alginate hydrogel microfluidic channels. The authors fabricated sealed microfluidic pathways (as small as $25\,\mu$m by $25\,\mu$m) within micromolded calcium alginate hydrogels. These hydrogel-based microchannels also have significant potential for generating microvasculature-like tissue structures.
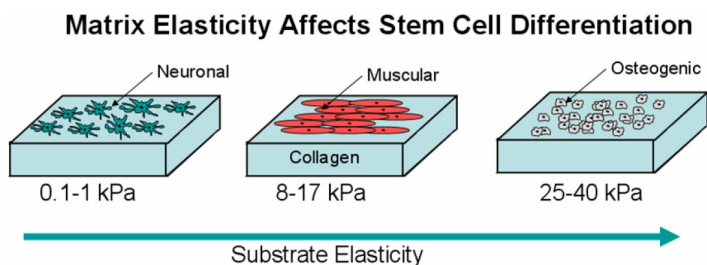
**Figure 6.** The mechanical properties of hydrogels induce directed stem cell differentiation.

***Regulation of stem cell fate.*** Embryonic stem (ES) cells are a potential source of transplantable tissues because they can both renew themselves, and differentiate into a number of desirable cell types, such as hepatocytes, pancreatic cells, cardiomyocytes, otsteoblasts, endothelial cells, and neural cells. Currently, however, it is difficult to induce ES cell differentiation uniformly in a scalable process. The challenge is that ES cells proliferate and differentiate in response to a large number of microenvironmental factors, such as soluble growth factors, matrix components, forces, and cell-cell interactions. Interactions among these various factors play different roles in affecting the resulting cell lineage at different stages of development in a highly regulated manner.

Microscale hydrogels offer a possible means of finely controlling the microenvironment of differentiating ES cells. Nonadhesive microwells fabricated from photocrosslinkable PEG have been used as part of a template-based approach for reproducible generation of uniform microtissues [Khademhosseini et al. 2006a; 2006b; 2006c]. Formation of cell aggregates called embryoid bodies (EBs) was initiated by seeding cells within photopolymerized PEG microwells. EBs could then be harvested for further differentiation of the cells. In addition, aggregates of various cell types, shapes and sizes have been manipulated by simply altering the geometry of the PEG microwells.

In addition, Dang et al. [2004] demonstrated that the microencapsulation of stem cells within hydrogels can help produce tissue progenitor cells at scalable rates. In these applications, cells encapsulated within microscale hydrogels can be separated from each other to prevent aggregation, thus enabling large-scale production of EB-derived cells.

Another recent study showed that the mechanical characteristics of the growth substrate can drastically affect stem cell differentiation [Engler et al. 2006]. Depending on the concentration of the polymer and the nature of the crosslinks, gels were manufactured with elasticities between 0.1 kPa and 40 kPa thus simulating the range of elasticities found in human tissues. In general, brain tissues exhibit an elasticity between 0.1 kPa and 1 kPa, muscle tissues are around 10 kPa, and collagenous bone is around 100 kPa. It was demonstrated that the stem cells seeded onto various substrates differentiated with great regularity into the tissue precursor mechanically similar to the underlying substrate. In these experiments, mesenchymal stem cells (MSCs) that were seeded onto soft hydrogels (0.1–1 kPa) tended to develop into neuronal precursors, while MSCs that were seeded onto stiffer gels (8–17 kPa) differentiated into muscular precursors. At the high end of the range of substrate stiffness (25–50 kPa), the MSCs tended to differentiate into collagenous bone-like tissues precursors (see Figure 6) [Engler et al. 2006].

A similar study gave insight into oncogenic stem cells differentiation by demonstrating how the mechanical properties of a 3D hydrogel matrix affects tumor cell migration speed [Zaman et al. 2006]. In

this study, it was demonstrated that tumor cells in a 3D fibronectin hydrogel matrix migrate quickly in highly elastic substrates. In contrast, tumor cells on 2D surfaces migrate quickly when the underlying substrate is nonelastic.

***Cell encapsulation and immunoisolation.***  Hydrogels can also be used to encapsulate cells in microcapsules. This can prevent cell aggregation, which can be useful for stirred bioreactor experiments. Furthermore, cell-laden hydrogels can be coated with various polymers to immunoisolate the encapsulated cells from the surrounding environment [Peppas et al. 2006].

Hydrogel materials express physical characteristics that are similar to the ECM and exhibit high permeability to oxygen, nutrients, and other metabolites, thus providing a favorable environment for cell survival. Typically, the procedures used to encapsulate cells within a hydrogel result in high cell viability, often only requiring that a cell suspension be mixed with the hydrogel precursor prior to crosslinking of the network.

When encapsulating cells within hydrogels, it is important to consider the photoinitiator concentration, UV exposure length, macromer concentration, and thermal exposure, since they all affect cell viability. When forming a gel, a balance is needed between the desired mechanical characteristics and long-term cell viability. Several studies have demonstrated long-term viability for hydrogel-encapsulated cells, especially in microgel structures which encourage effective nutrient and oxygen perfusion; see [Khademhosseini et al. 2006a; 2006b; 2006c]. These studies also show that hydrogel cell immunoisolation is useful because it can protect allogenic or xenogeneic cells from the host's immune system within a semipermeable membrane. For example, functional pancreatic cells may be immunoisolated in hydrogel and implanted into an allogenic host [Lim and Sun 1980].

## 5. Diagnostics and microdevices

Hydrogels can be used as functional components in microdevices and diagnostic tools. Due to the ease of photolithographic and micromolding techniques, it is possible to incorporate hydrogels cheaply into devices and sensors. The wide range of mechanically and chemically responsive *smart* hydrogels makes this integration particularly appealing.

***"Smart" hydrogels.***  Engineering the chemical or physical makeup of a hydrogel can predetermine their response to environmental stimuli. These so-called *smart* or *environmentally responsive* hydrogels can be designed to respond to a wide range of stimuli, such as changes in pH, $pI$, and temperature [Jeong et al. 2002; Miyata et al. 2002; Peppas 1997; Peppas and Khare 1993; Peppas et al. 2000].

Thermally responsive hydrogels, such as poly(N-isopropyl acrylamide) (PNIAAm) and its derivatives, have a highly reproducible response to temperatures. Generally, as the temperature of a hydrogel is increased, its volume will increase until it reaches a critical point, called the lower critical solution temperature (LCST). As the temperature of the gel exceeds the LCST, the gel undergoes a volumetric phase change and begins to shrink. This process is reversible; when the temperature is lowered below the LCST, the hydrogel will return to its original volume. For example, PNIPAAm exhibits a LCST around 33° C. PNIPAAm and other thermoresponsive hydrogels are being studied for a wide variety of tissue engineering and drug delivery applications [Jeong et al. 2002; Sershen and West 2003].

Another response mechanism is ionic activation. Examples of ionically responsive hydrogels are poly(acrylic acid), poly(methacrylic acid), polyacrylamide (PAam), poly(diethylaminoethyl methacrylate), and poly(dimethylaminoethyl methacrylate). In general, hydrogels with weakly acidic pendent groups will exhibit swelling as the pH of the surrounding medium increases, whereas hydrogels with weakly basic pendent groups will swell as the pH of the surrounding medium decreases. The determining factors for ionic swelling of hydrogels have been widely studied and include ionization equilibrium, ionic content and polymer structure [Khare and Peppas 1993; Podual and Peppas 2005; Scott and Peppas 1999].

***Hydrogels as components of microdevices.*** Environmentally responsive hydrogels, whether chemically, thermally, or mechanically activated, have been used in microdevices for a variety of purposes such as controlled microreactors, valves, and pumps [Beebe et al. 2000; Miyata et al. 2002; Yu et al. 2001]. For example, pH-sensitive photocrosslinkable PEG-based hydrogels have served as functional microvalves. As the pH of the microfluidic solution changes, so does the geometry of the valve, therefore allowing for effective sealing and opening of the microfluidic pathway [Beebe et al. 2000]. Another method used differential swelling between basic and acidic ionic gels to enable controllable valves [Yu et al. 2001]. By utilizing a bimetallic strip-like construct, it was possible to force a hydrogel construct to open in a particular direction, depending on the pH of the surrounding medium. Other signaling methods, such as photoactivity and thermal, chemical and electrical stimulation, have also been demonstrated [Beebe et al. 2000]. While valves are only one example of environmentally responsive hydrogel structures, the potential implication of microactuated hydrogel constructs could have far reaching applications. For example, chemically actuated hydrogel pumps may one day enable tissue engineering constructs that self perfuse.

Micropatterned PEG hydrogels also have applications in microdevices. For example, micropatterned PEG hydrogels embedded within microfluidic channels have been shown to enable control over the location of cells and proteins within the microfluidic channel. The ability to precisely control both cell and protein location can be used to perform cell- or protein-based assays or to create controlled microreactors [Heo et al. 2003; Zhan et al. 2002]. It has also been shown that PEG microstructures within microfluidic channels are capable of capturing and localizing cells in regions of low shear stress [Khademhosseini et al. 2004]. Capturing cells from flowing solutions is useful for many applications, such as sensing, cell separation, and cell-based microreactors.

***Hydrogels as integral components of microsensors.*** The incorporation of hydrogels into biological sensors could also result in a new class of sensing technologies. Hydrogels' perfusability enables the embedding of a large number of biological detection factors, such as antibodies, within a gel's 3D structure. When compared to antibody immobilization on a 2D surface, microgels should provide a significant sensing advantage by increasing the density of the receptor molecule [Zhan et al. 2002]. One example is a protein-sensitive, environmentally responsive hydrogel MEMS sensor (see Figure 7). In this sensing mechanism, an antibody-laden hydrogel is micropatterned onto a MEMS microcantilever [Bashir et al. 2002; Hilt et al. 2003]. Then, as the hydrogel absorbs the target protein, the hydrogel swells or contracts, causing the MEMS cantilever to deflect. The degree of deflection is measured using refractive optics.
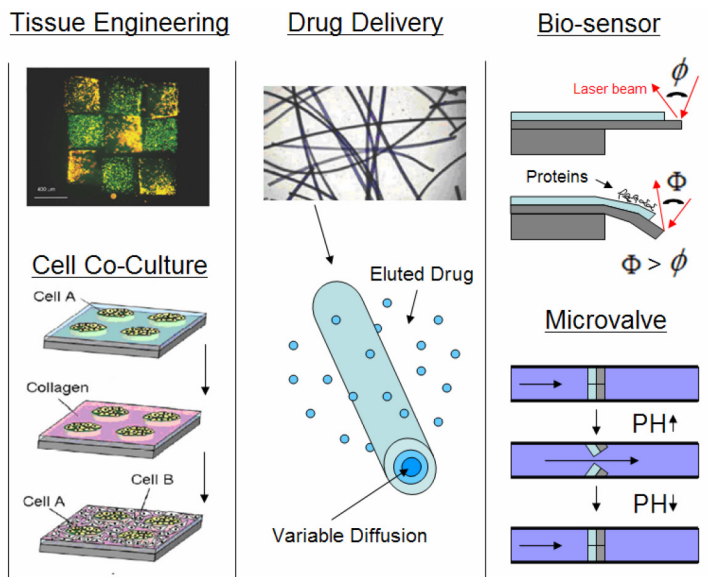
**Figure 7.** Applications of microscale and microfeatured hydrogels for tissue engineering, cell coculture, drug delivery, biosensors, and microfluidics.

Micropatterned hydrogel MEMS cantilever sensors have been used for a variety of sensing applications. For example, similar techniques have been demonstrated using pH- or thermally sensitive hydrogels, in which pH or temperature changes (respectively) cause swelling that deflects a microcantilever. Similar work has also demonstrated microcantilever hydrogel sensors capable of accurately sensing $CrO_4^{2-}$ [Zhang et al. 2003] and $Pb^{2+}$ [Liu and Ji 2004].

To develop analyte sensing technologies, several groups have micropatterned hydrogels onto MEMS electrodes using photolithography. By localizing oxidoreductase enzymes onto the microelectrodes, analyte levels can be accurately detected by measuring changes in the conductivity of the micropatterned hydrogel [Jimenez et al. 1997; Jobst et al. 1996; Sirkar et al. 2000].

***Cell-based diagnostics and screening.*** In addition to providing a source of viable cells for tissue replacement therapies, the use of microscale hydrogels for close regulation of the cellular microenvironment may also be utilized in high-throughput experimentation and diagnostic tools. Cells *in vivo* are exposed to various 3D microenvironmental conditions closely monitored by the body. *In vitro* culturing conditions often differ vastly from those experienced by cells in native organ systems. In traditional cell culture systems, cell-cell, cell-ECM and cell-soluble factor interactions are often too complicated to control, making it difficult to mimic the native spatial and temporal distribution of cell signaling. In addition, culture dishes offer only a 2D environment, as opposed to the 3D environments encountered by cells in the body.

Cells cultured in microscale hydrogels come into contact with a microenvironment much more comparable to that experienced by cells *in vivo*. As a result, this technique may provide a better tool for

*in vivo* studies on cell-environment interactions. The microscale nature of this technique permits combination with high-throughput technologies when studying many microenvironmental factors at once [Khademhosseini 2005].

One particularly promising application for microgels and micropatterned hydrogels is for cellular coculture experiments. By using natural hydrogel polymers such as HA and collagen, it has been demonstrated that effective cell cocultures can be performed using micropatterned hydrogels. In one example [Khademhosseini et al. 2006a; 2006b; 2006c], a microwell patterned layer of HA was used as a template to control cell-cell interactions (see Figure 7).

***Drug delivery.*** Many current drug delivery mechanisms are invasive, painful, or ineffective. Microscale hydrogels may provide an intelligent means of controlled drug delivery that solves these problems.

Drug-infused microscale hydrogels can deliver drug therapies in a sustainable and controllable manner [Langer 2000]. Furthermore, the drug release kinetics may be tailored by manipulating the shape, size, and density distribution of the microgels during the fabrication process. Microgels may also be fabricated from many different hydrogel polymers; this results in a dramatic variability of drug release mechanisms, many of which are environmentally responsive.

Hydrogels exhibiting pH sensitivity, temperature sensitivity, and swelling properties have all been exploited for drug release purposes. For example, pH-responsive microgels comprised of ionic networks containing PEG can be used for the oral delivery of medically relevant proteins such as insulin and calcitonin [Peppas et al. 2006]. Additionally, microgels with specific degradation characteristics can be induced to demonstrate pulsatile release responses upon breakdown. For instance, drugs encapsulated within alginate microgels can be released upon depolymerization of the alginate network, which is triggered through removal of divalent cations in the network.

Control over drug release systems can be used in the formation of intelligent materials, which may be utilized in targeted drug delivery methods [McCarthy et al. 2005; Peppas 1997; Peppas and Khare 1993]. By engineering the material composition, size, and shape of hydrogel drug delivery vehicles, not only can rates of drug diffusion be methodically managed, but release mechanisms can be made responsive to the surrounding environment. For example, *smart* microgels infused with cancer drugs could delay elution of their payload until they reach cancer cells. Such systems have great potential to increase the safety and effectiveness of future drugs, while decreasing the invasiveness of delivery mechanisms.

## 6. Future applications

It is widely expected that a majority of future tissue engineering techniques will be based on hydrogel technology. No other class of materials has the flexibility or biological compatibility to enable significant advances in tissue engineering. For example, microscale hydrogels let engineers precisely control the cellular microenvironment, which may lead to significantly more effective stem cell differentiation techniques. Additionally, the ability to create micropatterned, vascularized, cell-laden hydrogel scaffolds will enable more effective tissue engineering therapies. Finally, the versatile chemical and mechanical properties of microscale hydrogels provide a unique platform for the future development of more accurate and effective biological sensors and microdevices.

Many scientists believe that it may be possible one day to print an entire three-dimensional, functional organ. Novel 3D printing techniques, currently under development, may make this a reality. Due to the

exceptional mechanical and biological properties of hydrogels, many of these new technologies utilize hydrogel materials as their *ink*. By printing sequential layers of cell-laden hyrdogels, it may be possible to start to print entire ogranoids or tissues.

## 7. Conclusion

Microgels, as well as microfeatured hydrogels, have demonstrated great promise in biomedical engineering applications. Their unique, easily regulated mechanical and chemical characteristics solve many problems in tissue engineering, drug delivery and microdevice applications. In tissue engineering, microgels have shown promise for the construction of both scaffolds (for top-down methods) and the building blocks needed for bottom-up approaches. For drug delivery, the ability to fine-tune microgel drug release mechanisms has been shown widely effective for controlled-release applications. Finally, since hydrogels are easily customized, they make ideal components of microdevices and biosensors. Hydrogels, especially those with microscale features or sizes, have rapidly become an indispensable tool for solving some of the most difficult problems in medicine and biology. As research utilizing microgels progresses, it is expected that this platform will enable numerous advances in medicine and biology.

## 8. Acknowledgements

## References

[Alexakis et al. 1995]  T. Alexakis, K. Boadid, D. Guong, A. Groboillota, I. O'Neilli, D. Poncelet, and R. Neufeld, "Microencapsulation of DNA within alginate microspheres and crosslinked chitosan membranes for in vivo application", *Appl. Biochem. Biotech.* **50**:1 (1995), 93–106.

[Anseth et al. 1995]  K. S. Anseth, C. Browman, and L. Brannon-Peppas, "Mechanical properties of hydrogels and their experimental determination", *Biomaterials* **17**:17 (1995), 1647–1657.

[Bashir et al. 2002]  R. Bashir, J. Z. Hilt, O. Elibol, A. Gupta, and N. A. Peppas, "Micromechanical cantilever as an ultrasensitive pH microsensor", *Appl. Phys. Lett.* **81**:16 (2002), 3091–3093.

[Beebe et al. 2000]  D. J. Beebe, J. S. Moore, J. M. Bauer, Q. Yu, R. H. Liu, C. Devadoss, and B. H. Jo, "Functional hydrogel structures for autonomous flow control inside microfluidic channels", *Nature* **404**:6778 (2000), 588–590.

[Borenstein et al. 2002]  J. T. Borenstein, H. Terai, K. R. King, E. J. Weinberg, M. R. Kaazempur-Mofrad, and J. P. Vacanti, "Microfabrication technology for vascularized tissue engineering", *Biomed. Microdevices* **4**:3 (2002), 167–175.

[Bruck 1973]  S. Bruck, "Aspects of three types of hydrogels for biomedical applications", *J. Biomed. Mater. Res.* **7** (1973), 387–404.

[Burdick et al. 2004]  J. A. Burdick, A. Khademhosseini, and R. Langer, "Fabrication of gradient hydrogels using a microfluidics/photopolymerization process", *Langmuir* **20**:13 (2004), 5153–5156.

[Cabodi et al. 2005]  M. Cabodi, N. W. Choi, J. P. Gleghorn, C. S. Lee, L. J. Bonassar, and A. D. Stroock, "A microfluidic biomaterial", *J. Am. Chem. Soc.* **127**:40 (2005), 13788–9.

[Cohen et al. 1992]  Y. Cohen, O. Ramon, J. Kopelman, and S. Mizrahi, "Characterization of inhomogeneous polyacrylamide hydrogels", *J. Polym. Sci. B, Polym. Phys.* **30** (1992), 1055–1067.

[Dang and Zandstra 2005]  S. Dang and P. Zandstra, "Scalable production of embryonic stem cell-derived cells", *Meth. Mol. Biol.* **290** (2005), 353–364.

[Dang et al. 2004] S. Dang, S. Gerecht-Nir, J. Chen, J. Itskovitz-Eldor, and P. Zandstra, "Controlled, Scalable Embryonic Stem Cell Differentiation Culture", *Stem Cells* **22** (2004), 275–282.

[Davis 1989] H. Davis, "Studies on copolymeric hydrogels of N-vinyl-Z-pyrrolidone with 2-hydroxyethyl methacrylate", *Macromolecules* **22** (1989), 2824–2829.

[Demerci et al. 2003] U. Demerci, E. Haeggstrom, G. Percin, and B. T. Khuri-Yakub, *2D acoustically actuated micromachined droplet ejector array*, IEEE, 2003.

[Dendukuri et al. 2006] D. Dendukuri, D. Pregibon, J. Collins, A. Hatton, and P. Doyle, "Continuous-flow lithography for high-throughput microparticle synthesis", *Nat. Mater.* **5** (2006), 365–369.

[Engler et al. 2006] A. Engler, S. Sen, H. Sweeney, and D. Discher, "Matrix elasticity directs stem cell lineage specification", *Cell* **126** (2006), 677–689.

[Fukuda et al. 2006] J. Fukuda, A. Khademhosseini, Y. Yeo, X. Yang, J. Yeh, G. Eng, J. Blumling, C. F. Wang, D. S. Kohane, and R. Langer, "Micromolding of photocrosslinkable chitosan hydrogel for spheroid microarray and co-cultures", *Biomaterials* (2006).

[Greenberg 1980] K. Greenberg, "Viscoelastic behavior of highly crosslinked poly(acrylic acid)", *J. Polym. Sci.* **25** (1980), 2795–2805.

[Heo et al. 2003] J. Heo, K. J. Thomas, G. H. Seong, and R. M. Crooks, "A microfluidic bioreactor based on hydrogel-entrapped *E. coli*: cell viability, lysis, and intracellular enzyme reactions", *Anal. Chem.* **75**:1 (2003), 22–26.

[Hilt et al. 2003] J. Z. Hilt, A. K. Gupta, R. Bashir, and N. A. Peppas, "Ultrasensitive biomems sensors based on microcantilevers patterned with environmentally responsive hydrogels", *Biomed. Microdevices* **5**:3 (2003), 177–184.

[Jeong et al. 2002] B. Jeong, S. Kim, and Y. Bae, "Thermosensitive sol-gel reversible hydrogels", *Adv. Drug. Deliver. Rev.* **54**:1 (2002), 37–51.

[Jimenez et al. 1997] C. Jimenez, J. Bartrol, N. deRooij, and M. KoudelkaHep, "Use of photopolymerizable membranes based on polyacrylamide hydrogels for enzymatic microsensor construction", *Anal. Chim. Acta* **351**:1-3 (1997), 169–176.

[Jobst et al. 1996] G. Jobst, I. Moser, M. Varahram, P. Svasek, E. Aschauer, Z. Trajanoski, P. Wach, P. Kotanko, F. Skrabal, and G. Urban, "Thin-film microbiosensors for glucose-lactate monitoring", *Anal. Chem.* **68**:18 (1996), 3173–9.

[Kaihara et al. 2000] S. Kaihara, J. Borenstein, R. Koka, S. Lalan, E. R. Ochoa, M. Ravens, H. Pien, B. Cunningham, and J. P. Vacanti, "Silicon micromachining to tissue engineer branched vascular channels for liver fabrication", *Tissue Eng.* **6**:2 (2000), 105–17.

[Khademhosseini 2005] A. Khademhosseini, "Chips to hits: microarray and microfluidic technologies for high-throughput analysis and drug discovery", *Expert. Rev. Mol. Diagn.* **5**:6 (September 12-15 2005), 843–846.

[Khademhosseini et al. 2004] A. Khademhosseini, J. Yeh, S. Jon, G. Eng, K. Y. Suh, J. A. Burdick, and R. Langer, "Molded polyethylene glycol microstructures for capturing cells within microfluidic channels", *Lab. Chip.* **4**:5 (2004), 425–30.

[Khademhosseini et al. 2006a] A. Khademhosseini, G. Eng, J. Yeh, J. Fukuda, J. Blumling, R. 3rd, Langer, and J. A. Burdick, "Micromolding of photocrosslinkable hyaluronic acid for cell encapsulation and entrapment", *J. Biomed. Mater. Res. A.* (2006).

[Khademhosseini et al. 2006b] A. Khademhosseini, L. Ferreira, J. Blumling, J. 3rd, Yeh, J. M. Karp, J. Fukuda, and R. Langer, "Co-culture of human embryonic stem cells with murine embryonic fibroblasts on microwell-patterned substrates", *Biomaterials* (2006).

[Khademhosseini et al. 2006c] A. Khademhosseini, R. Langer, J. Borenstein, and J. P. Vacanti, "Microscale technologies for tissue engineering and biology", *Proc. Natl. Acad. Sci. U S A.* **103**:8 (2006), 2480–2487.

[Khare and Peppas 1993] A. R. Khare and N. A. Peppas, "Release behavior of bioactive agents from pH-sensitive hydrogels", *J. Biomater. Sci. Polym. Ed.* **4**:3 (1993), 275–89.

[Koh et al. 2003] W. G. Koh, L. J. Itle, and M. V. Pishko, "Molding of hydrogel multiphenotype cell microstructures to create microarrays", *Anal. Chem.* **75**:21 (2003), 5783–5789.

[Langer 2000] R. Langer, "Biomaterials in drug delivery and tissue engineering: one laboratory's experience", *Acc. Chem. Res.* **33**:2 (2000), 94–101.

[Langer and Peppas 2003] R. Langer and N. A. Peppas, "Advances in biomaterials, drug delivery, and bionanotechnology", *Aiche J.* **49**:12 (2003), 2990–3006.

[Langer and Vacanti 1993]  R. Langer and J. P. Vacanti, "Tissue Eng.", *Science* **260**:5110 (1993), 920–6.

[Lim and Sun 1980]  F. Lim and A. M. Sun, "Microencapsulated islets as a bioartificial endocrine pancreas", *Science* **210** (1980), 980–910.

[Liu and Bhatia 2002]  V. A. Liu and S. N. Bhatia, "Three-dimensional photopatterning of hydrogels containing living cells", *Biomed. Microdevices* **4**:4 (2002), 257–266.

[Liu and Ji 2004]  K. Liu and H. F. Ji, "Detection of Pb2+ using a hydrogel swelling microcantilever sensor", *Anal. Sci.* **20**:1 (2004), 9–11.

[McCarthy et al. 2005]  J. R. McCarthy, J. M. Perez, C. Bruckner, and R. Weissleder, "Polymeric nanoparticle preparation that eradicates tumors", *Nano Lett.* **5**:12 (2005), 2552–6.

[Miyata et al. 2002]  T. Miyata, T. Uragami, and K. Nakamae, "Biomolecule-sensitive hydrogels", *Adv. Drug. Deliver. Rev.* **54**:1 (2002), 79–98.

[Moussaid et al. 1994]  A. Moussaid, S. Candau, and J. Joosten, "Structural and dynamic properties of partially charged poly(acrylicacid) gels: nonergodicity and inhomogeneities", *Macromolecules* **27** (1994), 2102–2110.

[Nguyen 2002]  W. Nguyen, "Photopolymerizable hydrogels for tissue engineering applications", *Biomaterials* **22** (2002), 4307–4314.

[Nisisako et al. 2002]  T. Nisisako, T. Torii, and T. Higuchi, "Droplet formation in a microchannel network", *Lab. Chip.* **2** (2002), 24–26.

[Peppas 1997]  N. Peppas, "Hydrogels and drug delivery", *Curr. Opin. Colloid In.* **2**:5 (1997), 531–537.

[Peppas and Khare 1993]  N. A. Peppas and A. R. Khare, "Preparation, structure and diffusional behavior of hydrogels in controlled-release", *Adv. Drug. Deliver. Rev.* **11**:1-2 (1993), 1–35.

[Peppas et al. 2000]  N. A. Peppas, P. Bures, W. Leobandung, and H. Ichikawa, "Hydrogels in pharmaceutical formulations", *Eur. J. Pharm. Biopharm.* **50**:1 (2000), 27–46.

[Peppas et al. 2006]  N. Peppas, J. Z. Hilt, A. Khademhosseini, and R. Langer, "Hydrogels in biology and medicine", *Adv. Mater.* **18** (2006), 1–17.

[Podual and Peppas 2005]  K. Podual and N. Peppas, "Relaxational behavior and swelling-pH master curves of poly[(diethyl-aminoethyl methacrylate)-graft-(ethylene glycol)] hydrogels", *Polym. Int.* **54**:3 (2005), 581–593.

[Reis et al. 2006]  C. Reis, A. Ribeiro, R. Neufeld, and F. Veiga, "Alginate microparticles as novel carrier for oral insulin delivery", *Biotechnol. Bioeng.* (2006). In Press.

[Scott and Peppas 1999]  R. Scott and N. Peppas, "Kinetics of copolymerization of PEG-containing multiacrylates with acrylic acid", *Macromolecules* **32**:19 (1999), 6149–6158.

[Sefton and McGuigan 2006]  M. Sefton and A. McGuigan, "Vascularized organoid engineered by modular assembly enables blood perfusion", *PNAS.* **103**:31 (2006), 11461–11466.

[Sershen and West 2003]  S. Sershen and J. West, "Implantable, polymeric systems for modulated drug delivery (vol 54, pg 1225, 2002)", *Adv. Drug. Deliver. Rev.* **55**:3 (2003), 439–439.

[Sirkar et al. 2000]  K. Sirkar, A. Revzin, and M. V. Pishko, "Glucose and lactate biosensors based on redox polymer/oxido-reductase nanocomposite thin films", *Anal. Chem.* **72**:13 (2000), 2930–6.

[Stachowiak et al. 2005]  A. Stachowiak, A. Bershteyn, E. Tzatzalos, and D. Irvine, "Bioactive hydrogels with an ordered cellular structure combine interconnected macroporosity and robust mechanical properties", *Adv. Mater.* **17**:4 (2005), 399–403.

[Tweedie et al. 2005]  C. Tweedie, D. Anderson, R. Langer, and K. Van Vliet, "Combinatorial Material Mechanics: High-Throughput Polymer Synthesis and Nanomechanical Screening", *Adv. Mater.* **17** (2005), 2599–2604.

[Xu et al. 2005]  S. Xu, Z. Nie, M. Seo, P. Lewis, E. Kumacheva, H. A. Stone, P. Garstecki, D. B. Weibel, I. Gitlin, and G. M. Whitesides, "Generation of monodisperse particles by using microfluidics: control over size, shape, and composition", *Angew. Chem. Int. Ed. Engl.* **44**:25 (2005), 3799.

[Yeh et al. 2006]  J. Yeh, Y. Ling, J. M. Karp, G. Eng, J. Blumling Iii, R. Langer, and A. Khademhosseini, "Micromolding of shape-controlled, harvestable cell-laden hydrogels", *Biomaterials* **27**:31 (2006), 5391–5398.

[Yu et al. 2001] Q. Yu, M. Bauer, and J. Moore, "Responsive biomimetic hydrogel valve for microfluidics", *Appl. Phys. Lett.* **78**:17 (2001), 2589–2591.

[Zaman et al. 2006] M. Zaman, L. Trapani, A. Sieminski, D. MacKellar, H. Gong, R. Kamm, A. Wells, D. Lauffenburger, and P. Matsudaira, "Migration of tumor cell in 3D matrices is governed by matrix stiffness along with cell-matrix adhesion and proteolysis", *PNAS.* **103**:29 (2006), 10889–10894.

[Zhan et al. 2002] W. Zhan, G. H. Seong, and R. M. Crooks, "Hydrogel-based microreactors as a functional component of microfluidic systems", *Anal. Chem.* **74**:18 (2002), 4647–4652.

[Zhang et al. 2003] Y. Zhang, H. F. Ji, G. M. Brown, and T. Thundat, "Detection of CrO4(2−) using a hydrogel swelling microcantilever sensor", *Anal. Chem.* **75**:18 (2003), 4773–7.

CHRISTOPHER RIVEST: rivest.lab@gmail.com
*Department of Mechanical Engineering, Massachusetts Institute of Technology, Cambridge, MA 02139, United States*

DAVID W. G. MORRISON: morrisdw@mit.edu
*Harvard–MIT Division of Health Sciences and Technology, Massachusetts Institute of Technology, Cambridge, MA 02139, United States*

BIN NI: binni@mit.edu
*Department of Biological Engineering, Massachusetts Institute of Technology, Cambridge, MA 02139, United States*

JAMIE RUBIN: jamier@mit.edu
*Department of Biological Engineering, Massachusetts Institute of Technology, Cambridge, MA 02139, United States*

VIKRAMADITYA YADAV: vgyadav@mit.edu
*Department of Chemical Engineering, University of Waterloo, Waterloo, ON, N2L 3G1, Canada*

ALBORZ MAHDAVI: alborz@mit.edu
*Department of Chemical Engineering, Massachusetts Institute of Technology, Cambridge, MA 02139, United States*

JEFFREY M. KARP: jeffkarp@mit.edu
*Harvard–MIT Division of Health Sciences and Technology, Massachusetts Institute of Technology, Cambridge, MA 02139, United States*

and

*Center for Biomedical Engineering, Department of Medicine, Brigham and Women's Hospital, Harvard Medical School, Boston, MA 02115, United States*

ALI KHADEMHOSSEINI: alik@mit.edu
*Harvard–MIT Division of Health Sciences and Technology, Massachusetts Institute of Technology, Cambridge, MA 02139, United States*

and

*Center for Biomedical Engineering, Department of Medicine, Brigham and Women's Hospital, Harvard Medical School, Boston, MA 02115, United States*
http://www.tissueeng.net/lab/

# A MULTILEVEL NUMERICAL MODEL QUANTIFYING CELL DEFORMATION IN ENCAPSULATED ALGINATE STRUCTURES

KALYANI NAIR, KAREN CHANG YAN AND WEI SUN

Mechanical forces not only deform cells, but also alter their functions due to biological responses. While current biomanufacturing processes are capable of producing tissue scaffolds with cells encapsulated, it is essential to understand cell responses to process-induced mechanical disturbances. In this study the stresses and deformations of encapsulated cells under compressive loads are quantified via a multilevel nonlinear finite element approach. The macrolevel model is used to mechanically characterize the alginate-cell construct. At the microlevel, the effects of alginate concentration, cell model, and the microlevel geometric heterogeneity on cell deformation are examined. Cells are modeled as single phase inclusions containing only a nucleus phase; then as a two-phase inclusion comprised of a nucleus phase and cytoplasm phase. This study also analyzes the effects of two geometrical parameters—namely, cell size and cell distribution—on the local stress levels of the cell. Subsequent statistical analyses provide insight into the degree of influence of these factors. The study shows that cells embedded in a higher alginate concentration, 3% w/v, experience higher stress levels as compared to cells embedded in a lower alginate concentration, 1.5% w/v. Furthermore, analysis of the geometric heterogeneity indicates that there is a much higher stress concentration in areas where cells are clustered together as compared to areas where cells are relatively isolated.

## 1. Introduction

Tissue engineering is a multidisciplinary field involved in creating functional 3D tissues using cells along with scaffolds that facilitate cell growth, organization and differentiation [Griffith and Swartz 2006]. Cell functions are affected by a multitude of cues arising from the extracellular matrix (ECM) components, mechanical perturbations, surface chemistry, chemical and biological signals from neighboring cells. Studies have shown that mechanical forces are essential to living cells, especially for the bone and endothelium cells that are subjected to specific forces as a part of the native physiological environment [Bao and Suresh 2003]. Mechanical forces not only deform cells, but also induce biological responses, and result in altered functions [Ingber 1997; Breuls et al. 2002]. Furthermore, with the advent of biofabrication technology, tissue scaffolds can be fabricated with cell seeded and/or encapsulated. Experimental studies have demonstrated that the mechanical disturbance due to the fabrication processing affects cell viability in the formed scaffold construct [Khalil 2006]. In this connection, understanding the underlying mechanisms and developing mathematical models to predict cell behavior in a designed surrounding would aid in maintaining and controlling the phenotype of the cells to form functional tissue in an engineered construct.

Recently, there have been increasing efforts to study the effects of the microenvironment on cell morphology and function, both experimentally and numerically. Pelham and Wang [1997] investigated the cell responses to the stiffness of the substrates. NRK epithelial cells and 3T3 fibroblasts were cultured on the substrates with variable physical properties, but a controlled chemical environment. Both NRK epithelial cells and 3T3 fibroblasts were well spread and looked similar to cells cultured on glass or plastic substrates; NRK cells became less well spread and irregularly shaped when more flexible substrates were used.

Guilak and Mow [2000] developed a multilevel biphasic finite element model of the chondrocyte within an explant of cartilage to characterize and predict the biomechanical interactions between the chondrocyte and the extracellular matrix as well as determine the influence of cell and tissue properties on the local stress-strain environment. They assumed that cells do not contribute to the mechanical properties of the tissue and considered a single chondrocyte under unconfined compression. Breuls et al. [2002] have introduced a large-strain model based on a multilevel finite element approach that predicts the local cell deformations in engineered tissue constructs, subjected to macroscopic external loads. Although numerical analyses have demonstrated the presence of microlevel physical and geometrical heterogeneity in terms of the cell stress and deformation, the degree of effects as well as the dominance among various parameters remains unanswered. Caille et al. [2002] found that the nucleus and the cytoplasm have considerable differences in terms of material properties, which may not be negligible, especially at the microlevel. Furthermore, the effects of material stiffness on cells are critical when fabricating scaffolds for tissue engineering applications making it of great interest as well.

The objective of this study is to characterize the mechanical behavior of alginate tissue constructs in the macroscale and to quantify the local stresses and deformations at a cellular level when the tissue construct is subjected to macrolevel loads. Moreover, this study quantifies the effects of microlevel physical and geometrical heterogeneity on cell deformation. Specifically, it examines the effects of the cell substructure, the matrix material stiffness, and the cell geometric distribution in terms of location and size. Here we consider alginate as the matrix material owing to its excellent biocompatibility [Drury et al. 2004] and capability to fabricate three dimensional scaffolds [Khalil et al. 2005].

In conjunction with our initial experimental studies on alginate constructs with encapsulated endothelial cells, the present study also focuses on endothelial cells. Endothelial cells are usually present as linings in the entire circulatory system and are subjected to several different types of mechanical stimuli including hydrostatic pressure, fluid shear stress, and deformation [Cines et al. 1998]. The strain magnitudes in the aorta and large arteries range between 2%–10% [Dobrin 1978; Wedding et al. 2002]. Wille et al. [2004] have studied the effects of cyclic stretching as well as compression at strain rates of 2%–10% on the morphological responses of endothelial cells. This analysis is carried out to investigate the local stress/deformation of the cells when subjected to compression at the physiological level and beyond.

The analyses are conducted via a multilevel nonlinear finite element method. The macrolevel analysis is a nonlinear finite element model that characterizes the macroscopic behavior of alginate discs with encapsulated endothelial cells under load. The analysis simulates a compression test on the constructs and focuses on characterizing its mechanical properties. This, however, does not provide any insight of the stresses and deformations occurring at the cellular levels. Upon the results of the macroanalysis, a microlevel analysis is conducted to determine local stress/strain fields in a selected region with the
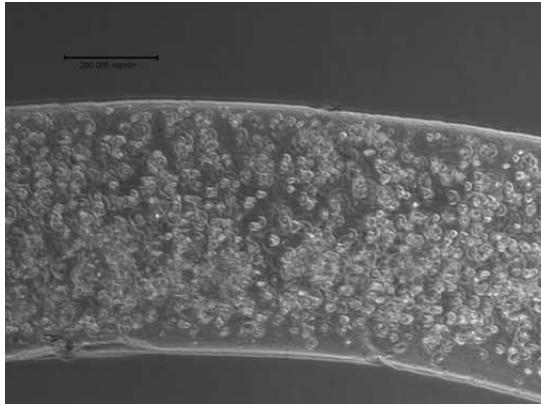
**Figure 1.** Fluorescent live/dead image of alginate construct with encapsulated rat heart endothelial cells.

encapsulated cells. Numerical results are determined and analyzed to quantify the effects from various sources on the local cell responses.

The paper is organized as follows. Section 2 describes the multilevel finite element approach that is applied in this study. Section 3 details the numerical procedure and model development, which includes the macrolevel and microscale analysis in Sections 3.1 and 3.2, respectively. In addition to the material model and cell model, three microfinite element models are developed to incorporate the geometrical heterogeneity, namely, encapsulated cells with random location and size, with random location and uniform size, and with uniform location and size. The latter two cases are presented for comparative purposes. The details of the results along with the discussions are given in Section 4.

## 2. Framework for analysis of cell encapsulated constructs: multilevel finite element approach

Alginate-based tissue scaffolds are fabricated using a proprietary multinozzle biopolymer deposition system [Khalil et al. 2005; Khalil 2006]. Upon examining the alginate scaffold with encapsulated endothelial cells, the size of cells is very small compared to the dimensions of the macrostructure (see Figure 1), therefore, multilevel analysis is necessary, especially for determining the cell responses. The paper focuses on the analysis of alginate-cell structures at three different scales.

At the macrolevel a nonlinear numerical model is developed to characterize the mechanical properties of the construct. For specific applications in tissue engineering it becomes necessary and indispensable to understand the stresses at the microenvironment of the encapsulated cells since cells respond to such stresses and their functions are highly dependent on such mechanical cues. Assuming statistical homogeneity, the multilevel finite element analysis may be utilized to determine the cell responses to the external load and further understand the effects of the system parameters from the different scales. A microlevel model has been developed to analyze the local effects around the cell boundaries, assuming that cells are inclusions within the alginate structure. The effects of physical and geometric heterogeneity on cells have been quantified as well. At the microlevel, the influence of substructures within the cell model contributes significantly to the stress distribution in the environment. Therefore, the study
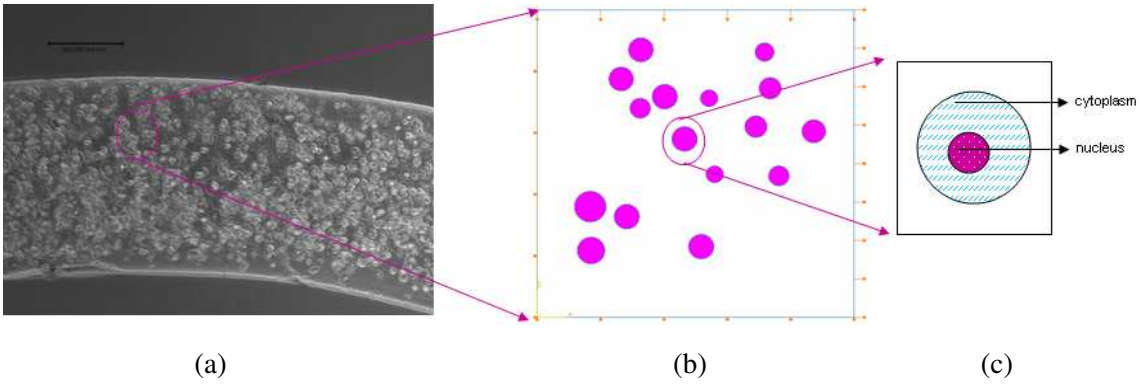
**Figure 2.** Multilevel approach applied to cell encapsulated alginate construct: (a) macrolevel analysis of discs under compression; (b) microlevel analysis incorporating random cell size and cell distribution; (c) analysis incorporating random cell size and cell distribution along with nucleus and cytoplasm.

attempts to analyze the microenvironment when including more specific cellular substructures such as the cytoplasm within the cell-model geometry. When analysis is conducted at the microscale, more information about cell membrane injury can be derived since the cytoplasm is less rigid than the nucleus and is prone to damage at lower levels of stress. Figure 2 indicates the multilevel approach along with the different microstructures integrated in the analysis. Experimental evidence suggests that the contribution of endothelial cells to the macroproperties is negligible

The multilevel finite element analysis has been developed and applied to link the microscopic behavior and the macroscopic phenomena of heterogeneous engineering materials [Smit et al. 1998; Kouznetsova et al. 2001; Wang and Yan 2005]. The fundamental assumption that enables this practice is statistical homogeneity. A heterogeneous body consisting of a blend of two materials, in general, possesses randomly distributed properties. For a complete description of the physical properties, each property is a random spatial function, and all of their joint probability distributions must be known. For instance, the microstructure can be described by the $n$-point phase probability function $S_n$, which is the probability of finding $n$ points simultaneously in phase 1 [Quintanilla and Torquato 1997] defined by

$$S_n(x_1, x_2, \ldots, x_n) = \left\langle \prod_{i=1}^{n} I(x_i) \right\rangle, \qquad I(x) = \begin{cases} 1, & x \text{ in phase 1,} \\ 0, & \text{otherwise,} \end{cases}$$

where $I(x)$ is the indicator function of phase 1, and the angular brackets denote an ensemble average over the possible realizations of the material. For statistical homogeneous media one can equate the ensemble averages with volume averages in the infinite volume limit, that is, ergodicity [Torquato 1998]. In practice a representative volume element (RVE) needs to be selected to represent the material adequately, to ensure, in particular, the one-to-one correspondence between the macro and microlevels. For a statistically homogeneous material under load, the local macroscopic deformation and stresses are equal to the averaged deformation and stresses of the RVE as given in equations below [Smit et al. 1998]. The deformation tensor $F(y_0)$ refers to the initially undeformed configuration at reference position $y_0$,
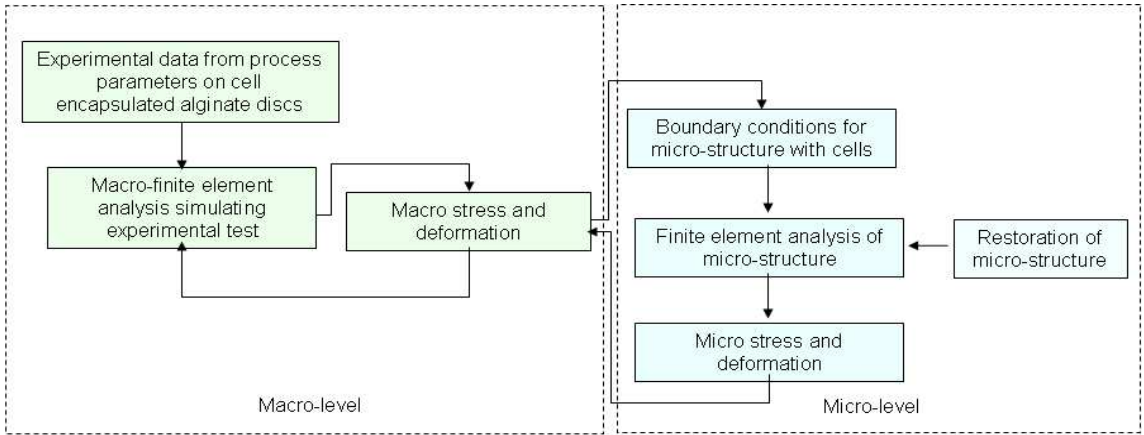
**Figure 3.** Flow chart of the multilevel finite element analysis procedure.

and the volume averaging is performed over the initial volume of the unit cell $V_0$.

$$F_{\text{macro}} = \overline{F}_{\text{RVE}} = \frac{1}{V_{0\,\text{RVE}}} \int_{y_0 \in V_{0\,\text{RVE}}} F(y_0) dV_0, \qquad \sigma_{\text{macro}} = \overline{\sigma}_{\text{RVE}} = \frac{1}{V_{\text{RVE}}} \int_{y \in V_{\text{RVE}}} \sigma(y) dV.$$

$F_{\text{macro}}$ and $\overline{F}_{\text{RVE}}$ are the macro and the RVE-averaged deformation gradient tensors, respectively, and $\sigma_{\text{macro}}$ and $\overline{\sigma}_{\text{RVE}}$ are the macro and the RVE-averaged stress tensor, respectively. The average stress in the RVE $\overline{\sigma}_{\text{RVE}}$ is the volume-averaged Cauchy stress tensor, where $\sigma(y)$ represents the stress tensor at position $y$. The averaging occurs over the current volume of the RVE because the Cauchy stress is defined in the current deformed configuration [Smit et al. 1998]. $F_{\text{macro}}$ and $\sigma_{\text{macro}}$ can be related through the material constitutive relation. In case of hyperelastic material [ABAQUS 2002], the material constitutive relation can be expressed as

$$\delta W = \int_{V_0} \det(F_{\text{macro}}) \sigma_{\text{macro}} : \delta D(F_{\text{macro}}) dV_0 = \int_{V_0} \delta U(F_{\text{macro}}) dV_0,$$

where $\delta W$ is the variation of work, and $\delta U$ is the variation of strain energy.

Figure 3 is a schematic of the multilevel modeling approach applied in this study. Initial experiments are conducted to characterize the overall/macro properties of the system under compressive load, and corresponding macrofinite element analyses are carried out to validate the experimental results and provide the macrodeformation and stresses. Detailed microstructures are restored to a region of interest, and microlevel analyses are then performed to determine the local deformation and stresses within the region.

## 3. Numerical procedure: macro and microlevel characterization of alginate-cell constructs

A nonlinear macrolevel numerical model has been developed to analyze the structural properties of three dimensional tissue engineering scaffolds. The model is also validated experimentally. Details of the

procedure are explained in Section 3.1. A nonlinear microlevel analysis is then conducted to capture the stress and deformation of the encapsulated cells in the scaffold when subjected to external compression. The physical and geometrical heterogeneity is modeled to analyze the degree of influence of these effects on the cell's microenvironment. Section 3.2 describes the microlevel modeling procedure in detail.

**3.1.** *Macrolevel analysis characterizing mechanical properties of cell encapsulated alginate discs.* Uniaxial compression tests are performed to measure the mechanical properties of alginate (Manugel) using a 4442 Instron mechanical tester. Gel samples are prepared in a cell culture 24-wellplate. Rat heart endothelial cells (500,000 cells/ml) are encapsulated in 1.5% w/v alginate concentration and are cross linked with 0.5% calcium chloride to form 2.1 mm thick 4.5 mm radii alginate discs. Six specimens are tested and a maximum compressive strain of up to 40% is applied to obtain the stress-strain curve as shown in Figure 4b. Previous experiments indicate that the stiffness of the alginate increases as the concentration increases, especially over the range of 1%–3% w/v [Khalil 2006].

Axisymmetric finite element models are developed simulating the virtual compression tests based on the experimental specimen geometry. With the obtained experimental data, the Marquardt Levenberg nonlinear least square optimization (MLNLS) algorithm is used to fit the experimental data with the neoHookean, Mooney–Rivlin and Ogden models. The three models have been used for comparative purposes to determine the most accurate material model that can best fit the experimental data. The constants are obtained by using the MLNLS optimization algorithm. The algorithm minimizes the error $E$ between the experimental stress, $T_{\exp}$, and the nominal stress, $T_i$, calculated from the strain energy polynomial [ABAQUS 2002], for each material model

$$E = \sum_{i=1}^{n} \left(1 - \frac{T_i}{T_{\exp}}\right)^2, \qquad T_i = \sum_{i=1}^{N} \frac{2\mu}{\alpha} \left(\lambda u^{\alpha-1} - \lambda u^{-0.5\alpha-1}\right).$$

Between the three models considered, the neoHookean model incorporates only a single material constant and has the simplest formulation for the strain energy density function. The Mooney–Rivlin model is capable of taking into account the deviations arising from other Gaussian and neoHookean models [Boyce 2000]. In these two models the strain energy density function is expressed in terms of the stretch variants. In the Ogden model [Boyce 2000; ABAQUS 2002], the strain energy is expressed in terms of the principal stretches ($\lambda_i = 1, 2, 3$) as

$$W_o = \sum_{i=1}^{n} \frac{2\mu_i}{\alpha_i^2} \left(\lambda_1^{-\alpha_i} + \lambda_2^{-\alpha_i} + \lambda_3^{-\alpha_i} - 3\right).$$

Here the hyperelastic Ogden material model is used for the alginate disc with embedded endothelial cells since it produces a much closer approximation to the test data of the nonlinear hydrogel than the other strain energy density functions. Here, $\mu_i$ and $\alpha_i$ are material-dependent constants, and $n$ is the degree of summation, which can be varied to best fit the data at hand allowing additional flexibility. In the present study the Ogden polynomial with $n = 4$ is used for an alginate concentration of 1.5% w/v, and $n = 3$ for 3% w/v.

Although physical meanings associated with the constants are often not clear in phenomenological models, the Ogden material constants can be related to the shear modulus as $G = \sum_{i=1}^{N} \mu_i$ [ABAQUS 2002].
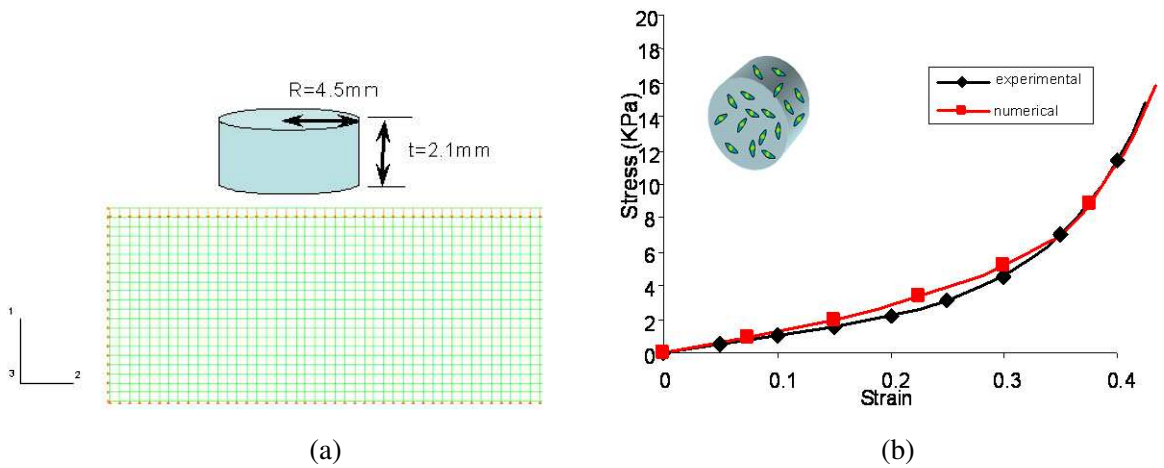
**Figure 4.** Macrolevel characterization of encapsulated bulk alginate discs: (a) axisymmetric FE model with loading and boundary conditions; (b) validation of numerical model with experimental data (nominal stress-strain).

The loading and boundary conditions are applied to simulate the experimental compression test, and the stress-strain curve is plotted to match up with the experimental curve. Figure 4(a) illustrates the macrolevel finite element model along with the loading and boundary conditions. Symmetric boundary conditions are applied along the vertical axis of symmetry, and uniform displacement is applied on the top surface of the sample to simulate the experimental compression test. After running the analysis for 40% strain, the nominal stress-strain curve is plotted and compared with the experimental measurements as shown in Figure 4(b). In addition, it is assumed that alginate does not exhibit any viscoelastic properties because the model predicts the mechanical properties of the scaffold at the instant it has been fabricated.

**3.2.** *Microlevel analysis: effects of physical and geometrical variations on local cell environment.* Microlevel numerical models are developed to determine the microstress and deformation fields and the effects of microenvironment on cell responses. Ideally, the microlevel analysis should be done with realistic 3D representation of the microstructure. However, the computation of such a model involving enormous number of degree of freedom is extremely demanding, hence two-dimensional approximations are often used to circumvent the difficulty [Smit et al. 1999]. In the present study, a two-dimensional simplification (axisymmetry) is utilized. This particular simplification can be justified with two assumptions. First, we assume that the presence of cells does not influence the overall mechanical properties of the scaffold. Secondly, the cells are randomly distributed in the cylindrical specimen. Now consider any given vertical plane cutting through the center of the specimen. From the latter, the circular intersections of the cells and the cutting plane are randomly distributed on the resulting cross section in terms of location and size. Hence a 2D model with a random distribution of cells modeled as inclusions is considered as an approximated representation of a given cross section.

The loading and boundary conditions are extracted from the macrolevel analyses of the alginate specimen with 20% and 30% compression. Although such strain magnitudes are beyond the physiological levels (for instance, for the aorta and large arteries one has 2%–10% [Dobrin 1978; Wedding et al. 2002]),

they may be induced by fabrication process. The study includes such conditions to understand the effects of large strain on the cell, which may provide information with respect to cell damage. For adequate representation of the alginate disc with encapsulated endothelial cells, a region of $400\,\mu$m $\times\,400\,\mu$m is selected; based on the cell volume fraction, sixteen cells are included. Two alginate concentrations, 1.5% w/v and 3% w/v, are considered due to the stiffness variation. Again, the Ogden material model is used to accurately capture the nonlinearity of the alginate.

The endothelial cells are treated first as single-phase inclusions, and then as two-phase inclusions. While the former simplifies the cell as a nucleus, the latter captures the contributions from both the nucleus and cytoplasm. The neoHookean material model is adopted for the nucleus, as well as the cytoplasm [Breuls et al. 2002; Caille et al. 2002; Haider et al. 2006]. The strain energy function for the neoHookean model [ABAQUS 2002] is given by $W_{NH} = a_1(I_1 - 3)$, where $a_1$ is a material parameter and $I_1$ is the first stretch invariant. The constant $a_1$ can be derived from the elastic modulus and Poisson's ratio as

$$a_{1\,\text{nucleus}} = \frac{4(1 + \nu_{\text{nucleus}})}{E_{\text{nucleus}}}, \qquad a_{1\,\text{cytoplasm}} = \frac{4(1 + \nu_{\text{cytoplasm}})}{E_{\text{cytoplasm}}}. \tag{1}$$

Here, the elastic moduli $E$ of the nucleus and the cytoplasm are assumed to take the value of $4462\,\text{N/m}^2$ and $323\,\text{N/m}^2$, respectively, and Poisson's ratio is 0.5 since the material is assumed to be incompressible [Caille et al. 2002]. Note that the cytoplasm is at least ten times less stiff than the nucleus. Modeling the cytoplasm and nucleus separately gives us additional information regarding damage to the cells since the cytoplasm could withstand much lower stress levels or deformations compared to the nucleus.

It is generally believed that the geometric heterogeneity at the microlevel leads to additional nonuniformity of the local stress/deformation fields; hence, it is necessary to address this for the microstructure restoration. In the present study, it is of interest to quantify this effect; therefore, three different microstructures are identified. Corresponding micro FE models are generated and analyzed, and the results so rendered are compared. Considering a realistic representation of alginate specimen with encapsulated cells, it can be observed from the microscopic image that the endothelial cells are randomly distributed with varying size. In the first assumption, the randomness in both location and size are represented and are characterized via a stochastic mean. Specifically, the random location is generated based on the equal probability and overlap constraints, while the radius is calculated using a normal distribution with a mean value $\mu = 15$ and a standard deviation $\sigma = 3$. The probability density function at position $x$ is given by

$$f(x) = \frac{1}{\sqrt{2\pi\sigma^2}}\exp\left[-\frac{(x - \mu)^2}{2\sigma^2}\right].$$

The average diameter of endothelial cells has been reported to be in the range of 20–30 $\mu$m [Bain 2001]. The location of the cells within the microstructure is calculated by generating a uniformly distributed pseudorandom number, lying in the specified range of 0.05 to 0.035 microns. The probability density function for a continuous uniform distribution on the interval $[a, b]$ is given by

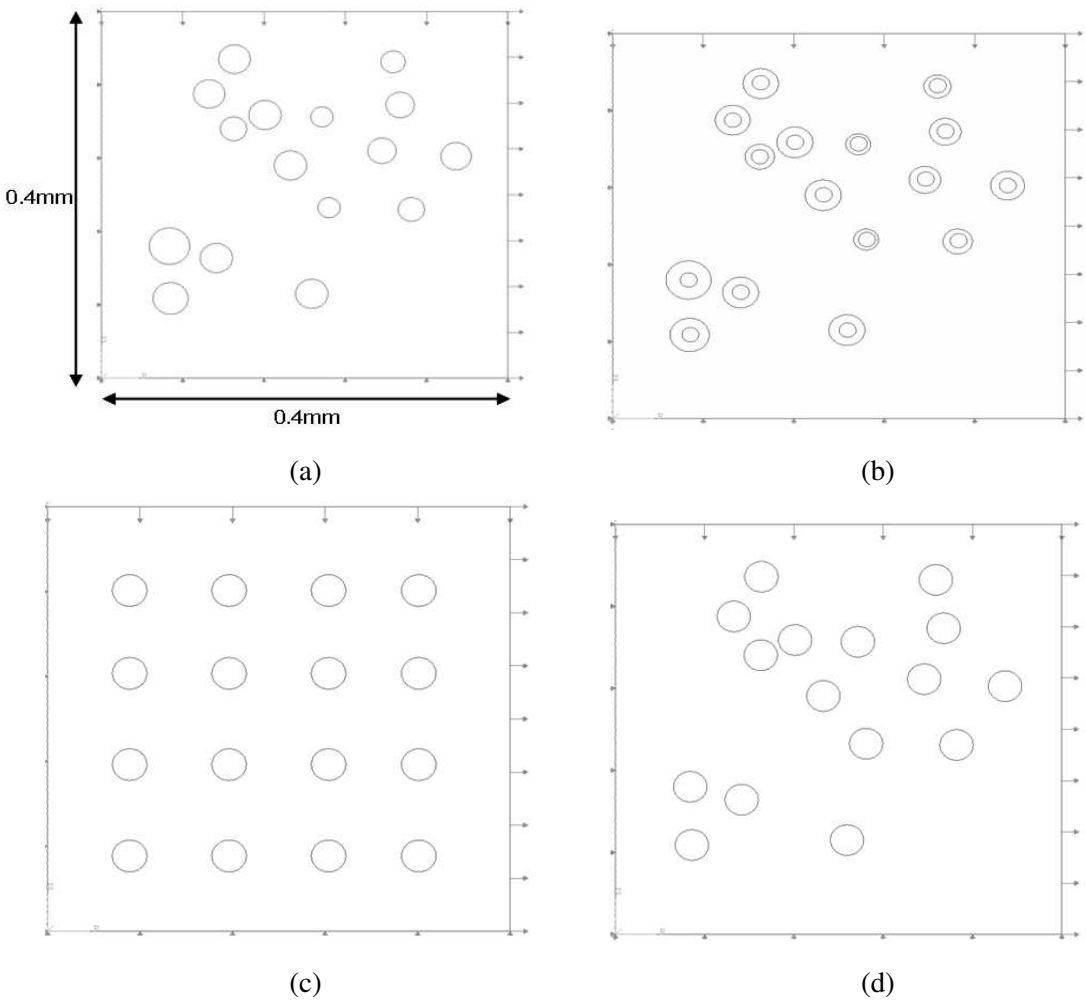$$f(x) = \begin{cases} \dfrac{1}{b - a}, & a \le x \le b, \\ 0, & \text{otherwise.} \end{cases}$$

**Figure 5.** Microlevel analysis: (a) random cell size and cell distribution; (b) random cell size and cell distribution along with cytoplasm; (c) uniform cell size and cell distribution; (d) uniform cell size and random cell distribution.

A subset of a random set can be identified via $\sqrt{(x_i - x_k)^2 + (y_i - y_k)^2} \geq (r_i + r_k)$. Here, $(x_i, y_i)$ is the location of any given cell, and $r_i$ is the radius; $(x_k, y_k)$ are the location of the cells that are adjacent to the cell $i$, and $r_k$ is the corresponding radius. This is computed using a commercial mathematic tool (Mathematica ver5.2). The approach allows for closely characterizing the heterogeneity of the microstructure, especially for the cases where the cells form clusters during fabrication. Figure 5 illustrates the restored microstructure with random characteristics along with the loading of the microstructure under analysis.

The geometrical heterogeneity within the microstructure has been carried out by formulating models with varying cell size and distribution. The first model involves a geometry including uniform cell location and uniform cell size; see Figure 5c. The next model assumes a geometry incorporating random location of the cells while assuming constant cell radii; see Figure 5d. Note that both random location

and random size are considered for the microlevel model with the cell modeled as two-phase inclusions with the cytoplasm and the nucleus, see Figures 5a and 5b. The size ratio between the nucleus and the cytoplasm is assumed to be constant.

## 4. Results and discussion

In the present study, a macrolevel model is developed to characterize the mechanical properties of alginate-cell constructs based on experimental data. A microlevel model is also developed based on information derived from the macrolevel model, and the stresses and deformations at the local cellular level are analyzed as well. Moreover, the microlevel analysis also quantifies how the stiffness of matrix material, the microstructure of the cell, and the geometric heterogeneity at the microlevel affect the local stress and deformation in the cell's microenvironment. This information leads to a better understanding of the cell responses to the mechanical force induced by the environment and a better mathematical model to predict cell viability, as well as cell damage.

Figures 6a and 6b indicate the macrolevel and the microlevel stress contours, respectively, when a 20% compressive strain is applied. As seen in Figure 6a, the macrolevel model shows uniform stress distribution and does not provide any information about the local stresses experienced by the cells. For applications in tissue engineering, it is imperative to understand the local stress levels at the cellular level since cell response to these stresses could lead to altered functions.

Figure 6b shows the stress contours at the cellular level wherein cells have been modeled as inclusions with the material properties assumed to be that of the nucleus. This analysis gives details regarding the microlevel stress distribution around the cells. To derive more information at this level, it is necessary to incorporate more substructures within the cell model. Figure 6c demonstrates the stress contours of the microlevel analysis where the microstructure incorporates the cell nucleus and the cytoplasm. At this level, the geometry, the density (the number of cells per unit area) and the material properties of the cell all contribute to the overall stress distribution. This analysis provides useful information about the stresses experienced by the cells in a random distribution.

**4.1.** *Effects of matrix stiffness on cell deformation and local stress distribution.* In order to study the effect of stiffness of the matrix material, alginate concentrations of 1.5% w/v and 3% w/v are considered. The stress contour plots rendered from the multilevel analysis are shown in Figure 7. The alginate gel with 1.5% w/v concentration is less stiff compared to the 3% w/v concentration. Therefore, less stress concentrations due to stiffness mismatch between the cell and matrix are introduced. We additionally observe that stresses are higher in areas where there are more cells compared to areas where the cells are isolated. The corresponding logarithmic strain contours from the analyses are given in Figure 8.

To further quantify the effect, nodal stress $S_{22}$ along the cell boundary (90° from the horizontal direction) is considered for statistical analysis. A set of sample data for $S_{22}$ is generated, and fitted to a normal distribution. Figure 9 plots the probability density function of $S_{22}$ on the cell boundary for the alginate concentrations of 1.5% w/v and 3% w/v. The shift in the curves clearly indicates the difference in terms of the mean stress value. Moreover, the mean value for the stresses is about 20% higher for alginate of 3% w/v concentration than that of 1.5% w/v. Though this quantifies the stress and deformation of the cells in the different environments, this paper does not attempt to explain how these stresses or deformations affect the functionality of the cell concerned.
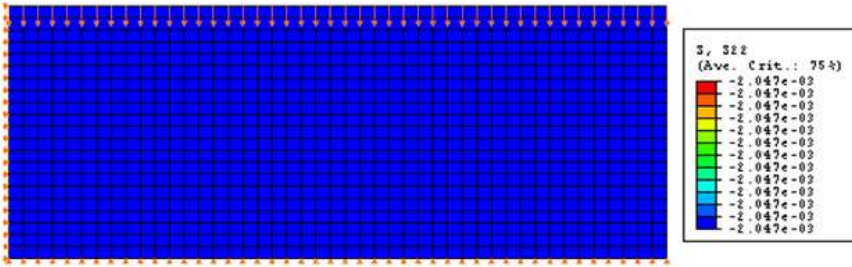
(a)
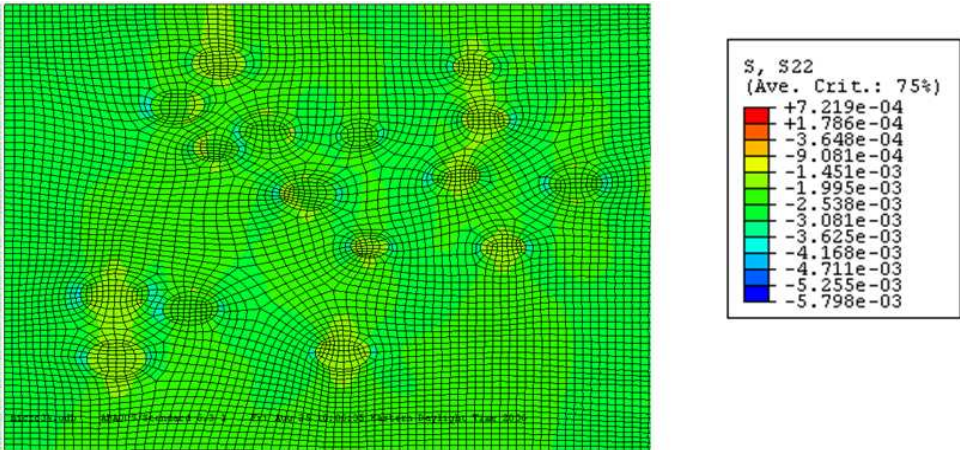


(b)
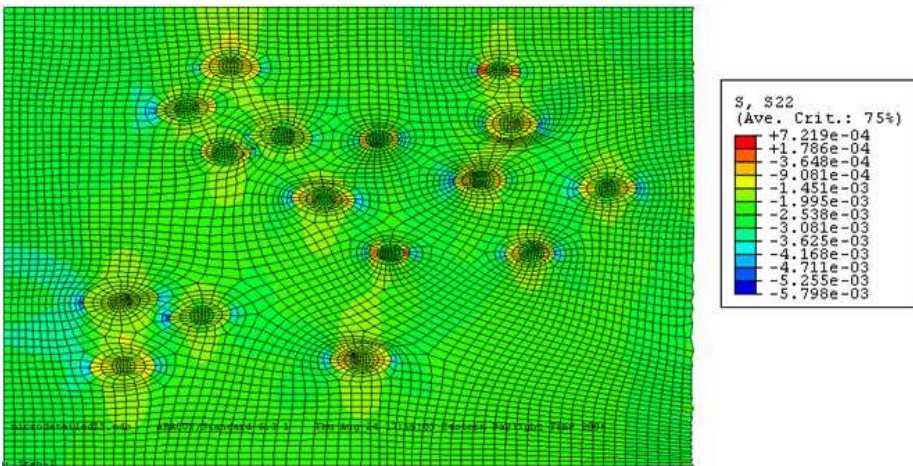


(c)

**Figure 6.** Stress (in MPa) contours for cell encapsulated alginate under 20% compressive strain: (a) macromodel for bulk discs; (b) microlevel model with cells; (c) microlevel model with cytoplasm and nucleus.
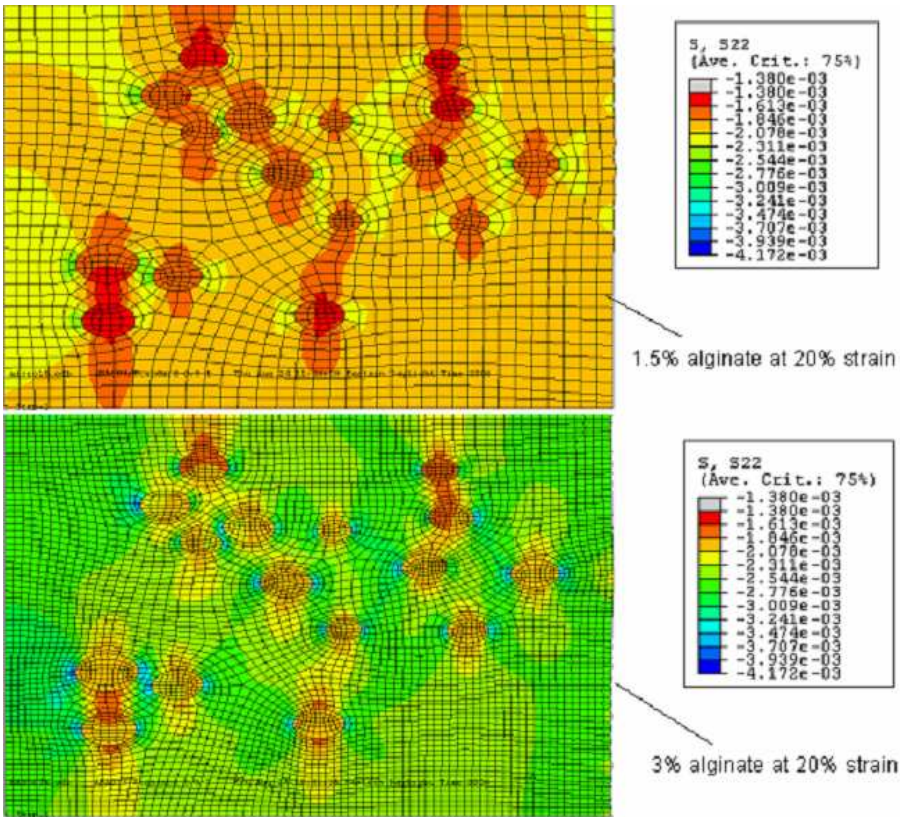
**Figure 7.** Stress (in MPa) contour plots for cells embedded in 1.5% w/v and 3% w/v alginate concentrations.

**4.2.** *Effects of incorporating cytoplasm within the cell model on the local cell environment.* The second factor the analysis takes into consideration is the significance of incorporating the nucleus and the cytoplasm within the cell model. It is known from literature that the material properties of the nucleus and cytoplasm are significantly different. For instance, the nucleus is about ten times stiffer than the cytoplasm [Caille et al. 2002]. Figure 10 shows a large degree of strain difference in the logarithmic strain contours between the two cases. Statistical analyses are conducted for both the stress and strain components, and the corresponding probability density function plots are shown in Figures 11 and 12, respectively. Figure 11 shows that the bell curve for the model with the nucleus and the cytoplasm has a larger standard deviation, but similar mean stress compared with the model that does not include the cytoplasm. The large deviation is due to the three phases of varying material stiffness. One can see from Figure 12 that the strains are significantly different in both cases. The shift in the curves indicates the difference in the mean strain in both cases. The model with the nucleus and cytoplasm has a higher value for the mean strain and a larger standard deviation compared with the case of only the nucleus. This can be attributed to the high degree of material property mismatch among the three regions: cell nucleus,
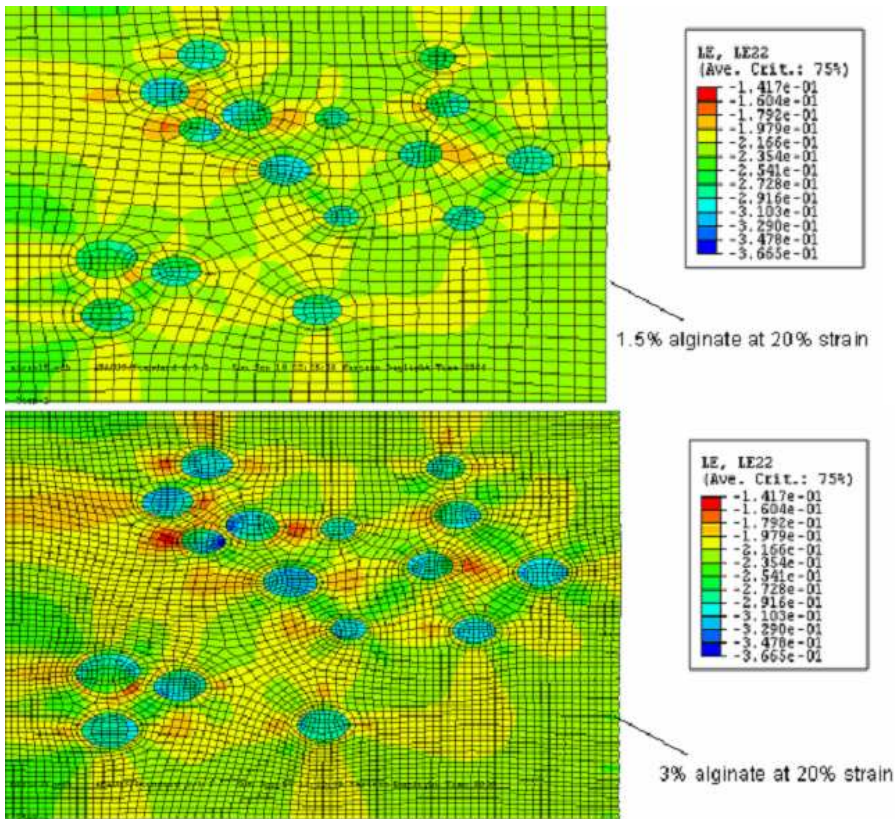
**Figure 8.** Logarithmic strain contour plots for cells embedded in 1.5% w/v and 3% w/v alginate concentration.

cytoplasm and surrounding alginate. Clearly analysis of the cell model incorporating the nucleus and cytoplasm provides more information that is critical to cell viability and cell function.

**4.3.** *Effects of cell size and position on the stress distributions at the cellular level.* The present study also looked into the effects of geometrical parameters, such as distributions in cell size and cell location, on the local stress at the cellular level. Specifically, the analysis aims to understand whether cell size and cell distributions in the construct adversely affect the local stresses and deformations in the cell's surroundings. Figure 13 shows the stress contours of the three cases where the variations have been made in parameters pertaining to cell geometry and cell distribution. The stress concentrations are significantly different between the model with uniform radius and distribution and that with random cell radii and distribution. Additionally, there is a small effect on cell sizes in the analysis. Regarding cell-cell interaction, there is much higher stress concentration in areas where cells are clustered together compared to the areas where cells are relatively isolated.

Three probability density function plots of $S_{22}$ are shown in Figure 14 for models with uniform cell size and cell distribution, with uniform cell size and random cell distribution, and with random cell size and cell distribution. The difference is clear between the model with uniform cell size/cell distribution
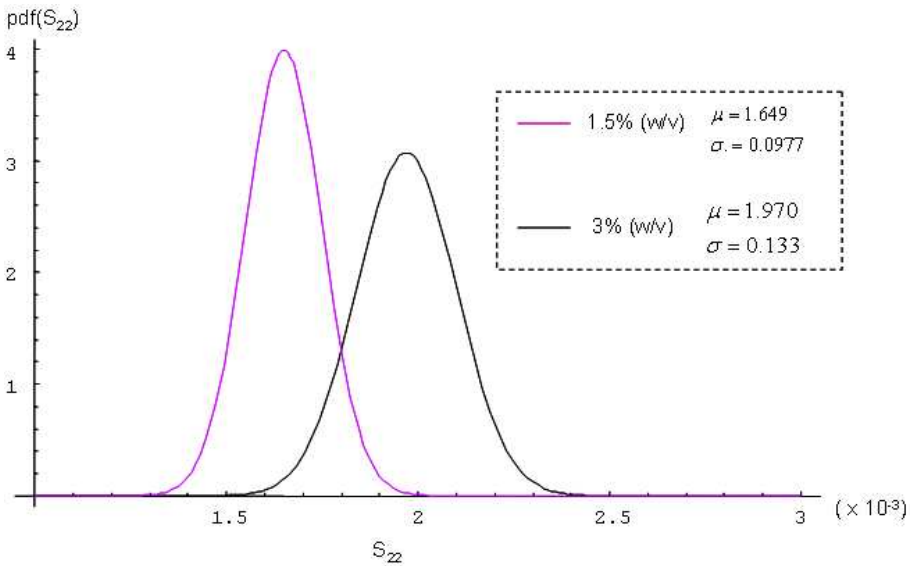
**Figure 9.** PDF plot of $S_{22}$ (in MPa) with mean $\mu = 1.97 \times 10^{-3}$ and standard deviation $\sigma = 0.13 \times 10^{-3}$ for cells embedded in 1.5% w/v and 3% w/v alginate concentrations.

and the random cell distribution model. There is little variation between the two cases where the cell size is constant and is variable. We conclude, then, that cell size does not affect the results too much. Similar trend can be observed in the strain contour plots in the form of deformation. Hence, the cell distribution affects the analysis in a significant manner.

This work uses the multilevel finite element approach to analyze the cell's microenvironment when tissue scaffolds are subjected to macrolevel loads. Previous works of Breuls et al. [2002] and Guilak and Mow [2000] have also used the same approach to analyze the local deformations in the cell's surroundings. However, these studies do not provide an in-depth analysis in terms of the effects of the microlevel physical and geometrical heterogeneity on cell stress and deformation. This paper aims to address these factors and aids in estimating the degree of influence as well as the dominance among various parameters using a statistical approach. It must be noted that this paper does not attempt to explain how the computed stresses or deformations affect the function or the phenotype of the cell concerned. Our future studies will be aimed at validating this model by conducting biological experiments that can examine the function of the cells under different stress environments.

## 5. Conclusion

In this work we focus on quantifying the effects of microphysical and geometric heterogeneity on the endothelial cells encapsulated in alginate gel under load using the multilevel finite element approach. The macrolevel properties of cell encapsulated alginate discs have been characterized. The microlevel stresses and deformations that cells are subjected to under macrolevel loads are analyzed. Two different concentrations of alginate gel create different mechanical environments; the effects of material stiffness have been modeled to quantify cell deformation and stress distribution within the constructs. This is
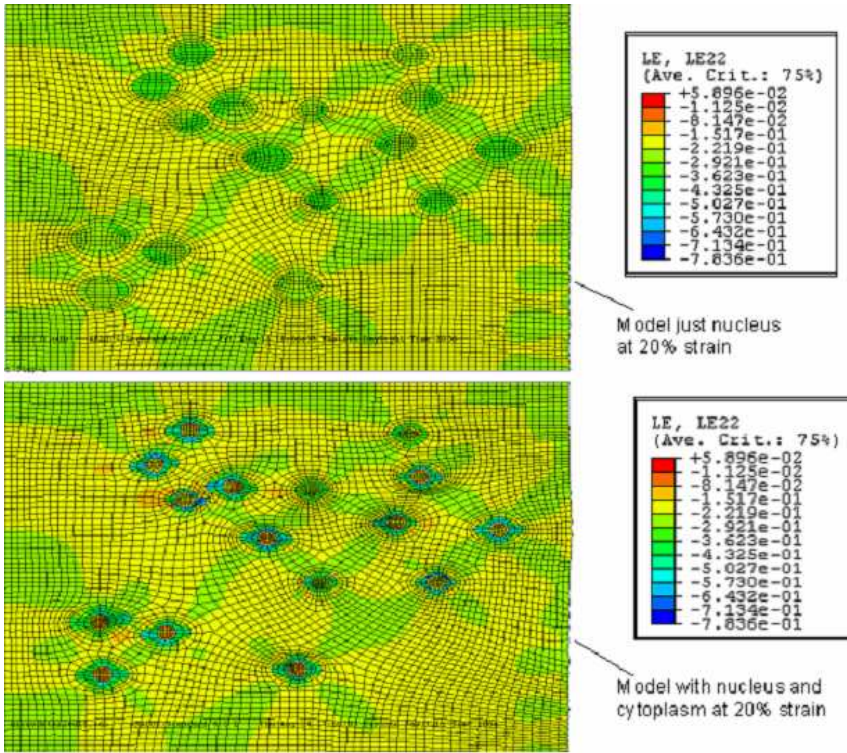
**Figure 10.** Logarithmic strain contour for analyzing effects of detailed microstructure.
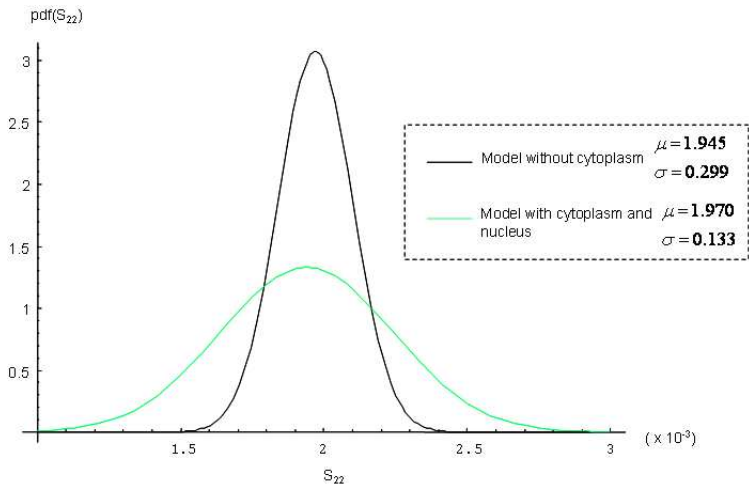


**Figure 11.** PDF plot of $S_{22}$ (in MPa) with mean $\mu$ and standard deviation $\sigma$ for analyzing effects of detailed microstructure.
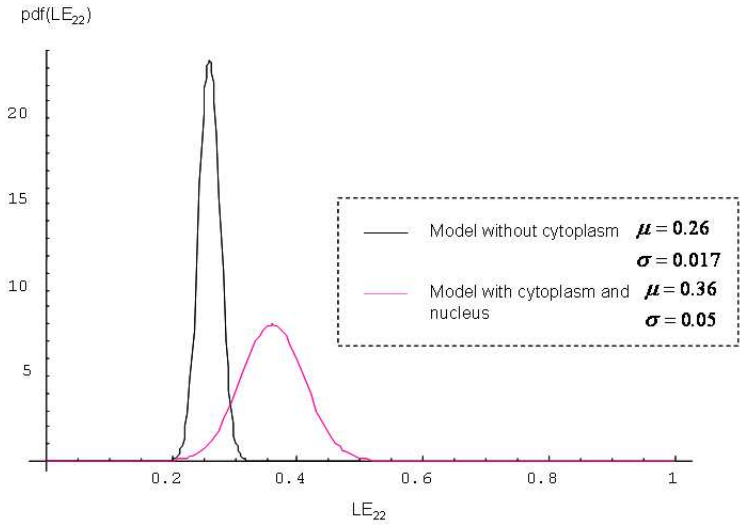
**Figure 12.** PDF plot of $L_{22}$ with mean $\mu$ and standard deviation $\sigma$ analyzing effects of detailed microstructure.
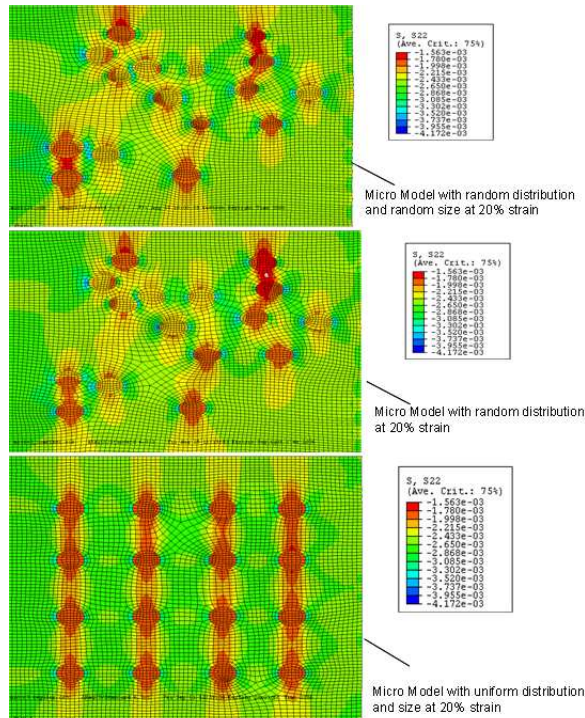


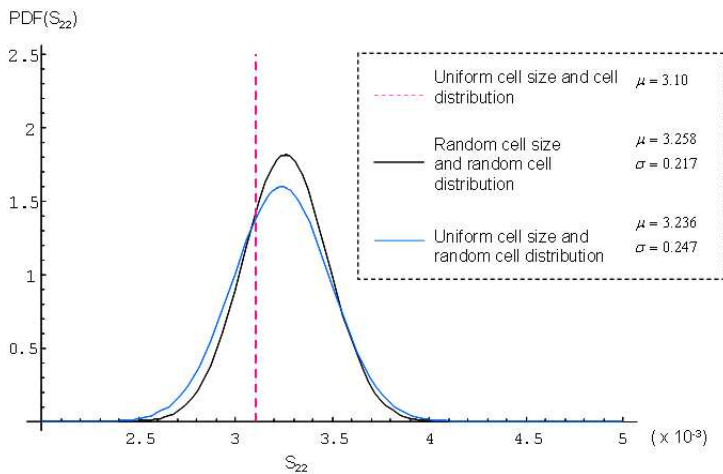**Figure 13.** Stress (in MPa) contour analyzing effects of geometrical distribution in size and location of cells within the microstructure.

**Figure 14.** PDF plot of $S_{22}$ (in MPa) with mean $\mu$ and standard deviation $\sigma$ analyzing effects of geometrical distribution in size and location of cells within the microstructure.

critical in determining the right material parameters, specifically alginate concentration in this case, when fabricating three-dimensional scaffolds.

Secondly, the paper examined the modeling of the cell, with and without a distinction between the cytoplasm and nucleus in terms of material properties. From the single phase model, the cell can withstand higher stresses since the nucleus is much stiffer than the cytoplasm. However, in order to look into cell damage, it becomes imperative to identify the stresses at the cytoplasm which is much less stiff than the nucleus. Additional information obtained from the detailed model may be linked to membrane damage and cell injury.

Finally, this study also analyzes the effects of two geometrical parameters, cell size and cell distribution, on the local stress levels of the cell. This further allows us to understand the differences in terms of stresses and deformations at the cellular levels between the cases where the cells are isolated versus those where they are clustered. To some extent this helps in understanding cell-cell interactions as well. Additionally, studies aiming to understand how the computed stresses and/or deformations affect cell function or behavior will greatly strengthen the analysis. Future studies will include experimental validation of these models.

## References

[ABAQUS 2002] *ABAQUS user manual*, Version 6.3-1, Hibbitt Karlsson Sorensen Inc., Providence, RI, 2002.

[Bain 2001] B. J. Bain, *Blood cells: a practical guide*, 3rd ed., Blackwell Science, Oxford, 2001.

[Bao and Suresh 2003] G. Bao and S. Suresh, "Cell and molecular mechanics of biological materials", *Nat. Mater.* **2**:11 (2003), 715–725.

[Boyce 2000] M. Boyce, "Constitutive models of rubber elasticity: a review", *Rubber Chem. Technol.* **73**:3 (2000), 504–523.

[Breuls et al. 2002] R. G. M. Breuls, B. G. Sengers, C. W. J. Oomens, C. V. C. Bouten, and F. P. T. Baaijens, "Predicting local cell deformations in engineered tissue constructs: a multilevel finite element approach", *J. Biomech. Eng.* (*Trans. ASME*) **124**:2 (2002), 198–207.

[Caille et al. 2002] N. Caille, O. Thoumine, Y. Tardy, and J. J. Meister, "Contribution of the nucleus to the mechanical properties of endothelial cells", *J. Biomech.* **35**:2 (2002), 177–187.

[Cines et al. 1998] D. B. Cines, E. S. Pollak, C. A. Buck, J. Loscalzo, G. A. Zimmerman, R. P. McEver, J. S. Pober, T. M. Wick, B. A. Konkle, B. S. Schwartz, E. S. Barnathan, K. R. McCrae, B. A. Hug, A. M. Schmidt, and D. M. Stern, "Endothelial cells in physiology and in the pathophysiology of vascular disorders", *Blood* **91**:10 (1998), 3527–3561.

[Dobrin 1978] P. B. Dobrin, "Mechanical properties of arterises", *Physiol. Rev.* **58**:2 (1978), 397–460.

[Drury et al. 2004] J. L. Drury, R. G. Dennis, and D. J. Mooney, "The tensile properties of alginate hydrogels", *Biomaterials* **25**:16 (2004), 3187–3199.

[Griffith and Swartz 2006] L. G. Griffith and M. A. Swartz, "Capturing complex 3D tissue physiology in vitro", *Nat. Rev. Mol. Cell Biol.* **7**:3 (2006), 211–224.

[Guilak and Mow 2000] F. Guilak and V. C. Mow, "The mechanical environment of the chondrocyte: a biphasic finite element model of cell-matrix interactions in articular cartilage", *J. Biomech.* **33**:12 (2000), 1663–1673.

[Haider et al. 2006] M. A. Haider, R. C. Schugart, L. A. Setton, and F. A. Guilak, "A mechano-chemical model for the passive swelling response of an isolated chondron under osmotic loading", *Biomech. Modeling Mechanobiol.* **5**:2-3 (2006), 160–171.

[Ingber 1997] D. E. Ingber, "Tensegrity: the architectural basis of cellular mechanotransduction", *Annu. Rev. Physiol.* **59** (1997), 575–599.

[Khalil 2006] S. Khalil, *Deposition and structural formation of 3D alginate tissue scaffolds*, Ph.D. thesis, Drexel University, Philadelphia, PA, 2006, Available at http://hdl.handle.net/1860/664.

[Khalil et al. 2005] S. Khalil, J. Nam, and W. Sun, "Multi-nozzle deposition for construction of 3D biopolymer tissue scaffolds", *Rapid Prototyping J.* **11**:1 (2005), 9–17.

[Kouznetsova et al. 2001] V. Kouznetsova, W. A. M. Brekelmans, and F. P. T. Baaijens, "An approach to micro-macro modeling of heterogeneous materials", *Comput. Mech.* **27**:1 (2001), 37–48.

[Pelham and Wang 1997] J. R. Pelham and Y. Wang, "Cell locomotion and focal adhesions are regulated by substrate flexibility", *P. Natl. Acad. Sci. USA* **94**:25 (1997), 13661–13665.

[Quintanilla and Torquato 1997] J. Quintanilla and S. Torquato, "Local volume fraction fluctuations in random media", *J. Chem. Phys.* **106**:7 (1997), 2741–2751.

[Smit et al. 1998] R. J. M. Smit, W. A. M. Brekelmans, and H. E. H. Meijer, "Prediction of the mechanical behavior of nonlinear heterogeneous systems by multi-level finite element modeling", *Comput. Methods Appl. Mech. Eng.* **155**:1–2 (1998), 181–192.

[Smit et al. 1999] R. J. M. Smit, W. A. M. Brekelmans, and H. E. H. Meijer, "Prediction of the large-strain mechanical response of heterogeneous polymer systems: local and global deformation behaviour of a representative volume element of voided polycarbonate", *J. Mech. Phys. Solids* **47**:2 (1999), 201–221.

[Torquato 1998] S. Torquato, "Morphology and effective properties of disordered heterogeneous media", *Int. J. Solids Struct.* **35**:19 (1998), 2385–2406.

[Wang and Yan 2005] A. S. D. Wang and K. C. Yan, "On modeling matrix failures in composites", *Compos. A Appl. Sci. Manuf.* **36**:10 (2005), 1335–1346.

[Wedding et al. 2002] K. L. Wedding, M. T. Draney, R. J. Herfkens, C. K. Zarins, C. A. Taylor, and N. J. Pelc, "Measurement of vessel wall strain using cine phase contrast MRI", *J. Magn. Reson. Imaging* **15**:4 (2002), 418–428.

[Wille et al. 2004] J. J. Wille, C. M. Ambrosi, and F. C. P. Yin, "Comparison of the effects of cyclic stretching and compression on endothelial cell morphological responses", *J. Biomech. Eng.* (*Trans. ASME*) **126**:5 (2004), 545–551.

KALYANI NAIR: kn43@drexel.edu
*Department of Mechanical Engineering and Mechanics, Drexel University, 32nd and Chestnut Street, Philadelphia, PA 19104, United States*

KAREN CHANG YAN: yan@tcnj.edu
*Department of Mechanical Engineering, The College of New Jersey, Ewing, NJ 08628, United States*

WEI SUN: sunwei@drexel.edu
*Department of Mechanical Engineering and Mechanics, Drexel University, 32nd and Chestnut Street, Philadelphia, PA 19104, United States*

# MODELING BONE RESORPTION USING MIXTURE THEORY WITH CHEMICAL REACTIONS

GHOLAMREZA ROUHI, MARCELO EPSTEIN, LESZEK SUDAK AND WALTER HERZOG

The increasing rate of osteoporosis in an aging population calls for a greater understanding of the cellular mechanism of bone resorption. We propose a biphasic mixture model. The solid phase (matrix) is assumed to be elastic and isotropic, and the fluid phase is assumed to be a linear viscous fluid. We give conservation equations for each constituent and for the whole mixture, and write new constitutive equations for the system. The rate of mass supply to constituents, caused by chemical reactions, is taken from an empirical relation of dissolution kinetics. We derive the biochemomechanical affinity in terms of biological, chemical, and mechanical factors. The strain energy density, hydrostatic pressure, and concentration of different ions present in the mixture are shown to affect the rate of bone resorption.

## 1. Introduction

Resorption of extra-cellular matrices by osteoclasts [Teitelbaum and Ross 2003] is followed by osteoblastic invasion of the cavity, and subsequent secretion of extra-cellular matrix that is then mineralized [Ducy et al. 2000]. These two processes, which together are called bone remodeling, occur continuously and are in balance in healthy bone [Riggs et al. 2002]. Optimal remodeling is responsible for bone health and strength throughout life. An imbalance in bone remodeling may cause diseases such as osteoporosis. Osteoporosis is characterized by extensive bone resorption. This leads to a disturbance in the bone's microarchitecture, which increases the probability of fractures. It is often called a "silent disease" because there are no symptoms until a bone breaks.

An early hypothesis about the dependence of the structure and form of bones, and the mechanical loads they carry, was proposed by Galileo in 1638 [Ascenzi 1993], and was first described in a semiquantitative manner by Wolff [1892]. Today, it is well accepted that bone growth, maintenence, degeneration, and remodeling are biochemically regulated processes influenced by mechanical loading [Carter 1987; 1996]. There are several theories about the mechanisms of bone adaptation, each with its own governing equation for the process of remodeling (i.e., resorption and formation). They are typically based on a single-phase continuum mechanics approach [Cowin and Hegedus 1976; Hegedus and Cowin 1976; Beaupré et al. 1990; Jacobs et al. 1997; Huiskes et al. 2000; Ramtani and Zidi 2001; 2002; Doblaré and García 2001; Garcia et al. 2002; Ruimerman et al. 2005; Rouhi et al. 2006]. In these models, bone resorption and formation are modeled as a single process. Considering the time duration of bone resorption (1 to 3 weeks [Recker 1983]), its high importance in osteoporosis disease [Aguado et al. 1997], and the prevalence of treating osteoporosis with anti-bone-resorption drugs [Arnaud 2001], only the resorption process is modeled here.

---

We treat bone as a biphasic mixture of matrix and fluid, and model resorption as an exchange of mass between the solid and fluid phases. This exchange is caused by the secretion of $H^+$ and $Cl^-$ from osteoclasts, which creates an acidic environment in a sealed zone [Blair 1998; Rousselle and Heymann 2002]. In our model, demineralization depends on the rate of surface processes. Mixture theory with chemical reactions will be used to derive conservation laws of mass, linear and angular momentum, energy, and the entropy inequality. In the conservation of mass equations, the rate of mass transferred to different constituents is assumed given by an empirical relation arising from the dissolution kinetics of the solid phase. The governing equations for bone resorption are derived using the conservation laws, as well as entropy inequality and the appropriate constitutive equations. In the constitutive equations, it is assumed that dependent variables (e.g., free energy) are functions of temperature, deformation gradient, rate of deformation gradient, and the extent of chemical reactions.

To develop a general framework for the description of biochemomechanically driven bone resorption, we made the following assumptions:

(1) Bone is a biphasic mixture of a solid phase (bone matrix) and a fluid phase (bone fluid).

(2) The transfer of mass, energy and entropy between the solid and the fluid phases are a result of biochemical reactions that occur between the osteoclasts and the matrix.

(3) The chemical reactions between osteoclasts and bone matrix are at the interface of the solid and fluid phase.

(4) The characteristic time of chemical reactions is several orders of magnitude greater than the characteristic time associated with a complete perfusion of the blood plasma in bone; hence any excess heat generated by chemical reactions is quickly carried away by circulation, and bone resorption is considered isothermal.

(5) The bone matrix obeys small deformation theory [Fritton et al. 2000] and is isotropic and linearly elastic.

(6) The velocity of the bone matrix is zero.

(7) The fluid phase is nonrotational, and viscous and inertial effects are neglected because of the slow velocities that are at play.

(8) A nonpolar mixture assumption is made, thus the stress tensor and the inner part of the stress tensor are symmetric [Bowen 1971].

(9) Both mechanical and chemical factors affect the rate of bone resorption, thus they both appear in the biochemomechanical affinity as driving forces of the chemical reactions.

(10) The degree of saturation is a function of the biochemomechanical affinity which contains mechanical (strain energy density and hydrostatic pressure), biological (chemical potential generated by the resorbing cells), and chemical (concentration of different ions in the reaction) factors.

(11) This biphasic system is closed with respect to mass transfer but open with respect to momentum, energy and entropy transfer.

(12) The mechanical properties of the matrix are determined by the properties of the mineral phase.

(13) Dissolution of the matrix is the same as resorption of the mineral phase.

## 2. Field equations

In this section, conservation equations (mass, linear and angular momentum and energy), biochemo-mechanical affinity and entropy inequality will be derived for a biphasic model of bone resorption. The conservation equations consist of balance for each constituent and a balance for the mixture as a whole.

*Axiom of mass balance.* Conservation of mass equations for each constituent and for the whole mixture, respectively, can be expressed as follows:

$$\frac{\partial \rho_s}{\partial t} = \widehat{C}_S, \tag{1}$$

$$\frac{\partial \rho_f}{\partial t} + \operatorname{grad} \rho_f \cdot V_f + \rho_f \operatorname{div} V_f = \widehat{C}_f, \tag{2}$$

$$\widehat{C}_S = -\widehat{C}_f = \widehat{C}, \tag{3}$$

where $\rho_a$ is the density of the $a$-th constituent, $V_f$ is the fluid velocity, grad denotes gradient with respect to spatial coordinates, $t$ is the time, and $\widehat{C}_a$ is the rate of mass supplied to the $a$-th constituent caused by the chemical reactions between the $a$-th constituent and other constituents of the mixture. The velocity of the matrix is assumed negligible.

*Biochemomechanical affinity and dissolution kinetics.* Bone matrix consists of 65% mineral and 35% organic matrix. The mineral phase is largely impure hydroxyapatite, $Ca_{10}(PO_4)_6(OH)_2$. The organic matrix is 90% collagen and 10% various noncollagenous proteins [Jee 2001]. It has been shown that the mineral phase is an important determinant of bone elasticity, whereas the organic phase is responsible for the bone post-yield behavior [Reilly and Burstein 1975]. Bone mineral (hydroxyapatite) and organic (collagen I) matrix are degraded independently. Thus a bone resorption model needs two separate expressions, one for each phase. For lack of information about the dissolution of the organic phase, we only consider the mineral phase dissolution and assume that it is equivalent to the dissolution of the bone matrix. Microscopic observations suggest that degradation of collagen closely follows mineral degradation [Chambers et al. 1984], so our assumption may be justified.

Dissolution of minerals occurs at the surface. A major source of uncertainty is the surface reactivity, which depends on chemical composition, atomic structure, and surface topography (including surface curvature). The free energy of surface sites changes as a function of the aforementioned factors. Thus, no universal expression for the dissolution kinetics exists and experimental studies are needed to derive a dissolution kinetics relation for each case. The dissolution kinetics of hydroxyapatite has been the subject of numerous publications [Christoffersen et al. 1996; Dorozhkin 1997a; 1997b; 1997c; Thomann et al. 1989; 1990; 1991; Margolis and Moreno 1992; Hankermeyer et al. 2002; Fulmer et al. 2002; Chow et al. 2003]. Under certain conditions, dissolution is diffusion-limited and occurs with the formation of a calcium-rich boundary at the surface [Thomann et al. 1991]. Because of the small dimensions of the resorption microenvironment (between the osteoclasts and the bone matrix), we assume that dissolution is governed by the reaction kinetics. Bone resorption can then be simplified to (see [Blair 1998; Dorozhkin 1997a; 1997b; 1997c])

$$Ca_{10}(PO_4)_6(OH)_2 + 2H^+ \leftrightarrow 10Ca^{2+} + 6PO_4^{3-} + 2H_2O. \tag{4}$$
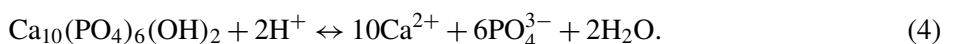
The chemical driving force for bone resorption (i.e., the chemical reaction shown in Equation (4)) can be expressed by the Gibbs free energy variation per mole

$$\Delta G = \sum_{i=1}^{n} \nu_i \mu_i = 10\mu_{\text{Ca}^{2+}} + 6\mu_{\text{PO}_4^{3-}} - 2\mu_{\text{H}^+} - \mu_{\text{Mineral}}, \tag{5}$$

where $\nu_i$ and $\mu_i$ represent the stoichiometric coefficients and chemical potential of the substances involved in the chemical reactions, respectively. The quantity $\Delta G$, can also be expressed as

$$\Delta G = RT \ln \frac{[\text{Ca}^{2+}]^{10} [\text{PO}_4^{3-}]^6 [\text{H}^+]_0^2}{[\text{Ca}^{2+}]_0^{10} [\text{PO}_4^{3-}]_0^6 [\text{H}^+]^2}, \tag{6}$$

where $[X]$ and $[X]_0$ are concentrations of ion $X$ at time $t$ and at equilibrium states, respectively. We hypothesize that *the rate of mass supplied to the a-th constituent caused by chemical reactions with other constituents, $\widehat{C}_a$, can be found using experimental approaches of dissolution kinetics.*

Margolis and Moreno [1992] performed dissolution experiments with hydroxyapatite crystals, in which they measured pH, calcium and phosphate concentrations at a constant temperature. Assuming electroneutrality and congruent dissolution, kinetic data can be derived directly by measuring pH. They proposed the following equation for the rate of dissolution of the mineral phase of the bone matrix:

$$J = k(1 - DS)^m [\text{H}^+]^n, \tag{7}$$

where $J$ is the mineral flux across the real surface of the mineral phase, $DS$ is the degree of saturation, $[\text{H}^+]$ is is the concentration of hydrogen ion, and $k$, $m$, and $n$ are empirical constants. As stated earlier, it is assumed that $J$ is almost equal to the dissolution rate of the solid phase, i.e. hydroxyapatite + collagen I.

The degree of saturation ($DS$) is expressed as

$$DS = \left( \frac{[\text{Ca}^{2+}]^5 [\text{PO}_4^{3-}]^3 [\text{OH}^-]}{K_{so}} \right)^{1/9} = \exp \frac{\Delta G}{18RT}, \tag{8}$$

where $[X]$ is the concentration of ion $X$, $K_{so}$ is the solubility product of hydroxyapatite, $R$ is the universal gas constant, and $T$ is the absolute temperature [Margolis and Moreno 1992].

Since biological, chemical, and mechanical factors have a definite effect on the rate of dissolution, we hypothesize that a biochemomechanical driving force should be considered in the dissolution relation, instead of just a chemical driving force: see Equation (6). We will use a dissipation law to find the biochemomechanical affinity. Dissipation in the system is defined as the difference between the external work rate and the rate of change in free energy. According to the Second Law of Thermodynamics, this quantity should be nonnegative, that is

$$\frac{dD}{dt} = \frac{dW_{\text{ext}}}{dt} - \frac{d\psi}{dt} \geq 0. \tag{9}$$

For a solid-fluid mixture, in a nonequilibrium state, a chemical process will occur on the interface of the solid and fluid phase, resulting in a flow of mass through the boundary and a change in boundary position. In the presence of chemical reactions, the external work rate can be separated into a mechanical

term $W_{\text{ext}}^{\text{mech}}$ and a chemical term $W_{\text{ext}}^{\text{chem}}$:

$$\frac{dW_{\text{ext}}}{dt} = \frac{dW_{\text{ext}}^{\text{mech}}}{dt} + \frac{dW_{\text{ext}}^{\text{chem}}}{dt}. \tag{10}$$

The mechanical work rate can be expressed as

$$\frac{dW_{\text{ext}}^{\text{mech}}}{dt} = \int_{V_s} v^s \cdot b \, dv + \int_{\Gamma} V^s \cdot T \, da, \tag{11}$$

where $b$ is the bulk body force, $T$ is the traction on the surface, $V_s$ is the normal velocity at which the boundary is moving, and $v^s$ is the material velocity of a point at the current boundary position [Silva and Ulm 2002].

Assuming that dissolution occurs only at the solid-fluid interface, then $T = -Pn$ at $\Gamma$. Using the equilibrium equation, the divergence theorem, and the definition of strain rate, one can conclude that

$$\frac{dW_{\text{ext}}^{\text{mech}}}{dt} = \int_{V_S} \text{tr}(\sigma D) dv - \int_{\Gamma} p v^c da, \tag{12}$$

where $D$ is the rate of deformation tensor, tr denotes trace, and $v^c$ is the chemical velocity which is defined by

$$v^c = V^s - v^s \cdot n, \tag{13}$$

where $n$ is the outward unit vector normal to the solid-fluid interface.

The chemical work rate can be expressed as the chemical energy associated with the flow through the surface ($J_\rho = \rho(v^s \cdot n - V^S) = -\rho v^c$), which is proportional to the external chemical potential, $\mu_{\text{ext}}$. External chemical potential, $\mu_{\text{ext}}$, is the chemical potential generated by the resorbing cells and is also called the biologically generated potential [Silva and Ulm 2002]:

$$\frac{dW_{\text{ext}}^{\text{chem}}}{dt} = -\int_{\Gamma} \frac{\mu_{\text{ext}} J_\rho}{M} da = \int_{\Gamma} \mu_{\text{ext}} C_s v^c da. \tag{14}$$

$C_s$ is defined as

$$C_s = \frac{\rho}{M}, \tag{15}$$

where $\rho$ and $M$ are the density and the molar mass of the matrix, respectively.

The rate of free energy variation can be written as

$$\frac{d\psi}{dt} = \frac{d}{dt} \int_{V_s} \psi \, dv = \int_{V_s} \left( \frac{\partial \psi}{\partial t} + \text{div}(\psi v^s) \right) dv + \int_{\Gamma} \psi v^c \, da. \tag{16}$$

Using (12), (14), (10), and (16) in (9), one obtains for the dissipation rate

$$\frac{dD}{dt} = \int_{V_s} \left( \text{tr}(\sigma D) - \frac{\partial \psi}{\partial t} x - \text{div}(\psi v^s) \right) dv - \int_{\Gamma} (\psi + P - \mu_{\text{ext}} C_s) v^c \, da. \tag{17}$$

Equation (17) allows the identification of the driving force in the dissolution process ($A$):

$$A = \psi + P - \mu_{\text{ext}} C_s. \tag{18}$$

The free energy ($\psi$) can be expressed as a sum of the mechanical and the chemical energies:

$$\psi = \psi^{\text{mech}} + \psi^{\text{chem}}. \tag{19}$$

The chemical free energy, $\psi^{\text{chem}}$, can be expressed as

$$\psi^{\text{chem}} = C_S \mu_S, \tag{20}$$

where $\mu_S$ is the chemical potential of the solid phase in the unstressed condition.

Thus, the driving force for the dissolution process can be written as

$$A = \psi^{\text{mech}} + P + C_s(\mu_s - \mu_{\text{ext}}). \tag{21}$$

$A$ in Equation (21) is the biochemomechanical driving force.

Thus, the Second Law defines the following dissipation condition at the surface:

$$-A u^C \geq 0 \quad \text{at } \Gamma. \tag{22}$$

It is well accepted that biological, chemical and mechanical factors affect the rate of chemical reactions, generally, and the degree of saturation, specifically. By substituting the biochemomechanical driving force $A$ in (21) into the rate of dissolution of the mineral phase, given by Equation (7), one can derive

$$
\begin{aligned}
J &= k\left(1 - \exp\frac{-A}{18RTC_s}\right)^m [\text{H}^+]^n \\
&= k\left(1 - \left(\frac{[\text{Ca}^{2+}]}{[\text{Ca}^{2+}]_0}\right)^{10/18}\left(\frac{[\text{PO}_4^{3-}]}{[\text{PO}_4^{3-}]_0}\right)^{1/3}\left(\frac{[\text{H}^+]_0}{[\text{H}^+]}\right)^{1/9}\exp\left(\frac{\psi_{\text{mech}} + P}{-18RTC_s}\right)\right)^m [\text{H}^+]^n.
\end{aligned} \tag{23}
$$

The rate of mass supplied to the fluid phase, i.e. $\widehat{C}_f$, which is equal to $-\widehat{C}_s$, can be related to $J$ (Equation (23)) using the relation

$$\widehat{C}_f = -\widehat{C}_s = \widehat{C} = \frac{M S_{\text{act}}}{V_{\text{tot}}} J, \tag{24}$$

where $S_{\text{act}}$ is the total active area available for the resorption process, $V_{\text{tot}}$ is the total volume of the mixture. Since $\widehat{C}_a$ is expressed per unit volume, $V_{\text{tot}}$ is assumed to be one.

Now, one can write the conservation of mass equation for the solid phase:

$$
\begin{aligned}
\frac{\partial \rho_s}{\partial t} &= \widehat{C}_S = -\widehat{C} = k\left(1 - \exp\frac{-A}{18RTC_s}\right)^m [\text{H}^+]^n \\
&= -k S_{\text{act}} M\left(1 - \left(\frac{[\text{Ca}^{2+}]}{[\text{Ca}^{2+}]_0}\right)^{10/18}\left(\frac{[\text{PO}_4^{3-}]}{[\text{PO}_4^{3-}]_0}\right)^{1/3}\left(\frac{[\text{H}^+]_0}{[\text{H}^+]}\right)^{1/9}\exp\left(\frac{\psi_{\text{mech}} + P}{-18RTC_s}\right)\right)^m [\text{H}^+]^n.
\end{aligned} \tag{25}
$$

To solve Equation (25), we need the area available for resorption, the ion concentrations in the mixture, and the strain energy density of the solid phase and the hydrostatic pressure exerted by the fluid on the solid phase.

Equation (25) shows that increasing the concentration of $\text{Ca}^{2+}$ with respect to the initial concentration decreases the rate of resorption. This agrees with experimental observations [Lorget et al. 2000]. The same equation demonstrates that increasing the $\text{H}^+$ concentration increases the rate of resoption; we

can increase the $H^+$ concentration by changing the activity of proton pumps in osteoclasts. Another corollary of Equation (25) addresses a crucial question: Are mechanical factors alone at play in the bone resorption process, or are other factors (e.g., chemical and biological) important as well? As Equation (25) shows, not only the mechanical factors (strain energy density $\psi_{\text{mech}}$ and hydrostatic pressure $p$) but also chemical and biological factors (ion concentration) affect the rate of bone resorption.

If one only considers the effects of chemical factors and ignores the mechanical ones, the conservation of mass equation for the bone matrix will become

$$\frac{\partial \rho_s}{\partial t} = -k S_{\text{act}} M \left( 1 - \left( \frac{[\text{Ca}^{2+}]}{[\text{Ca}^{2+}]_0} \right)^{10/18} \left( \frac{[\text{PO}_4^{3-}]}{[\text{PO}_4^{3-}]_0} \right)^{1/3} \left( \frac{[\text{H}^+]_0}{[\text{H}^+]} \right)^{1/9} \right)^m [\text{H}^+]^n. \tag{26}$$

On the other hand, if one only considers mechanical factors and discards the chemical ones, the conservation of mass equation for the matrix will become

$$\frac{\partial \rho_s}{\partial t} = -k S_{\text{act}} M \left( 1 - \exp\left( \frac{\psi_{\text{mech}} + P}{-18 R T C_s} \right) \right)^m. \tag{27}$$

***Axiom of linear and angular momentum.*** Assuming that the body forces and inertia effects are negligible compared to other forces, the solid phase velocity is negligible and it is linearly elastic. Also, the fluid is viscous; the linear momentum equations for the solid, fluid, and the whole mixture are, respectively,

$$\text{div}(2\mu E + \lambda \, \text{tr} \, E) + \hat{p}_s = 0, \tag{28}$$

$$\frac{\partial (\rho_f V_f)}{\partial t} + \text{div}(\rho_f V_f \otimes V_f) = \text{div}(-pI + 2\eta D) + \hat{p}_f - \widehat{C} V_f, \tag{29}$$

$$\text{div}(2\mu E + \lambda \, \text{tr} \, E + -pI + 2\eta D) = 0, \tag{30}$$

where $\hat{p}_a$ is the momentum supply to the $a$-th constituent, $p$ is the hydrostatic pressure in the fluid phase, $\mu$, $\eta$, and $\lambda$ are Lamé's constants, and $E$ and $D$ are strain and rate of deformation tensors, respectively.

Assuming a nonpolar mixture for bone, the axiom of moment of momentum for the $a$-th constituent can be reduced to

$$T_a = T_a^T. \tag{31}$$

Conservation of angular momentum for the whole mixture can be written as

$$\text{div}\left( x \times (2\mu E + \lambda \, \text{tr} \, E + T_c - pI + 2\eta D) \right) = 0. \tag{32}$$

Using compatibility requirements for the linear momentum of each constituent and the whole mixture, one obtains

$$\widehat{P}_s + \widehat{P}_f = \widehat{C} V_f, \tag{33}$$

where the parameters in Equation (33) have been introduced earlier.

***First and Second Laws of Thermodynamics.*** Using the First Law of Thermodynamics and assuming that the resorption process is isothermal, the following relations can be derived for the matrix, the fluid,

and the whole mixture, respectively:

$$\rho_s \frac{\partial \varepsilon_s}{\partial t} = \hat{\varepsilon}_s, \tag{34}$$

$$\rho_f \left( \frac{\partial \varepsilon_f}{\partial t} + \operatorname{grad} \varepsilon_f \cdot V_f \right) = \tfrac{1}{2} \operatorname{tr}(-p D_f + 2\eta D_f^2) + \hat{\varepsilon}_f, \tag{35}$$

$$(\rho_s + \rho_f) \left( \frac{\partial \varepsilon_I}{\partial t} + \operatorname{grad} \varepsilon_I \cdot \frac{\rho_f V_f}{\rho_f + \rho_s} \right) = \operatorname{tr}(2\mu E + \lambda \operatorname{tr} E + T_c - pI + 2\eta D), \tag{36}$$

where $\varepsilon_a$ is the internal energy density, $\hat{\varepsilon}_a$ is the energy supplied to the $a$-th constituent, and $\varepsilon_I$ is the inner part of the internal energy density.

The inner part of the internal energy density, assuming that the product of the diffusion velocities is negligible, can be written as

$$\varepsilon_I = \frac{1}{\rho_s + \rho_f}(\rho_s \varepsilon_s + \rho_f \varepsilon_f). \tag{37}$$

In Equations (34)–(36) it is assumed that the external heat supply to the solid and fluid phase is zero and that the products of the diffusion velocities can be neglected.

The second axiom of thermodynamics for a mixture of $N$ reacting materials without diffusion is the postulate that for every admissible thermodynamical process [Bowen 1968],

$$-\rho(\dot{\psi} + \eta\dot{\theta}) + \operatorname{tr}(TL) - \frac{\operatorname{grad} \theta \cdot q}{\theta} \geq 0. \tag{38}$$

From the consistency requirement for energy balance for the constituents and the whole mixture, we obtain for the biphasic model

$$\widehat{C} = \frac{\hat{\varepsilon}_s + \hat{\varepsilon}_f + V_f \widehat{P}_f}{\varepsilon_f - \varepsilon_s + \tfrac{1}{2} V_f^2}. \tag{39}$$

Equation (39) shows that in a bone with high value of porosity, the rate of resorption decreases with increasing fluid velocity. In agreement with the aforementioned point, experimental evidence shows that by exerting intermittent forces on bone (i.e., increasing bone fluid velocity and pressure), rate of resorption decreases [Flieger et al. 1998; Rubin et al. 1998; 2001a; 2004].

Using the Second Law of Thermodynamics, one can find the maximum amount of the rate of bone resorption for this biphasic, isothermal process:

$$\widehat{C}_{\mathrm{Max}} = \frac{\rho_s \dfrac{\partial \eta_s}{\partial t} + \rho_f \left( \dfrac{\partial \eta_f}{\partial t} + \operatorname{grad} \eta_f \cdot V_f \right)}{\eta_f - \eta_s}. \tag{40}$$

Because of the greater value of $\eta_f - \eta_s$ in cancellous than in cortical bone, Equation (40) predicts that the maximum rate of resorption in cortical bone will be greater than in trabecular bone. This behavior of cortical and trabecular bone, which is well accepted experimentally [Martin and Burr 1989], can be predicted using the conservation of mass equation (27), as well. More research is needed to find the clinical implications of Equation (40) and explore different methods to control it.

### 3. Damage, pressure, and rate of bone resorption

It is well accepted that physiologic strains produce fatigue damage in bone [Burr and Martin 1993; Mori and Burr 1993; Martin 2003; Taylor et al. 2003]. Damage, in turn, is associated with osteocyte apoptosis and activation of the remodeling process (i.e., resorption and formation) which repairs the damage [Martin 2003]. Experimental studies in which damage is produced by cyclic loading demonstrated that resorption is primarily associated with microcracks [Burr and Martin 1993; Mori and Burr 1993]. It has also been observed that resorption in the vicinity of microcracks occurs more often than expected [Li et al. 2001]. Also, experimental evidence shows that intermittent forces can increase the rate of bone remodeling [Rubin et al. 1998; 2001a; 2001b; 2002; 2004].

Equation (27) can be used to find a theoretical explanation for the experimental observations mentioned. It is well known that there is a stress concentration in the vicinity of cracks and thus an increase in the strain energy density. Using (27), we see that by increasing strain energy density (in the vicinity of cracks), there will be an increase in the biochemomechanical affinity — see (21) — and, as a result, an increase in the rate of resorption. Also, (27) can be used to find a theoretical support for a greater rate of resorption in cortical than trabecular bone [Martin and Burr 1989]. In cortical bone, osteoclasts come into contact with the surface, eroding the bone and producing cavities called cutting cones. In trabecular bone, osteoclasts erode flat surfaces of the bone and produce Howship's lacunae [Eriksen and Kassem 1992]. The stress and strain energy magnifications in the cutting cones of cortical bone are much greater than in the Howship's lacunae of trabecular bone. This can lead to a bigger strain energy density for cortical bone and thus — see (27) — a higher rate of resorption than for trabecular bone.

To the best of our knowledge, there is no theoretical model that incorporates hydrostatic pressure of the bone fluid phase with the rate of bone resorption. But there is experimental evidence in favor of the idea that increasing hydrostatic pressure of the bone fluid can enhance rate of bone resorption; see, for example, [Van Der Vis et al. 1998; Skripitz and Aspenberg 2000; Astrand et al. 2003]. If one discards the chemical factors (Equation (27)), effects of both hydrostatic pressure, $P$, and strain energy density, $\psi_{\text{mech}}$, on the rate of bone resorption can be observed (Figure 1). This figure shows that increasing either $P$ or $\psi_{\text{mech}}$ has a direct effect on the rate of bone resorption. The following values have been considered
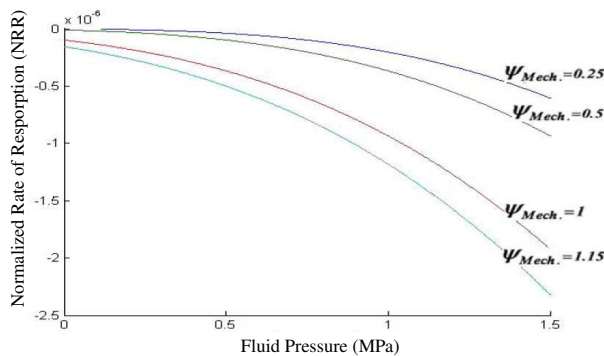


**Figure 1.** Normalized rate of resorption (NRR) versus fluid pressure for four different values of strain energy density ($k S_{\text{act}} M$ is considered a constant). Increasing either fluid pressure $P$ or free energy density of the $\psi_{\text{mech}}$ of the solid phase enhances the rate of bone resorption.

for $R$, $T$ and $C_s$, respectively: $8.3145\,\mathrm{J\,mol^{-1}K^{-1}}$, $310.15\,\mathrm{K}$ and $2988.05\,\mathrm{mol\cdot m^{-3}}$; the vertical axis, representing $((\partial\rho_s/\partial t)(kS_{\mathrm{act}}M)^{-1})$, has been normalized.

## 4. Constitutive assumptions and restrictions imposed by the Second Law of Thermodynamics

We assume that the Helmholtz free energy $\psi$, specific entropy $\eta$, stress tensor $T$, heat flux vector $q$, and the reaction vector $\omega$ are functions of temperature $\theta$, deformation gradient $F$, and the extent of the chemical reaction vector $\zeta$. Bowen [1968] makes a similar assumption for chemically reacting mixtures. Since the characteristic time for bone resorption (1 to 3 weeks, according to Recker [1983]) is much longer than the frequency of mechanical loading, one can assume that each dependent variable ($\psi$, $\eta$, $T$, $q$, and $\omega$) in the constitutive equations is a function of $\theta$, $\mathrm{grad}\,\theta$, $F$, $\dot{F}$, and $\zeta$:

$$
\begin{aligned}
\psi &= \bar{\psi}(\theta, \theta_{,i}, F, \dot{F}, \zeta); \\
\eta &= \bar{\eta}(\theta, \theta_{,i}, F, \dot{F}, \zeta); \\
T &= \bar{T}(\theta, \theta_{,i}, F, \dot{F}, \zeta); \\
q &= \bar{q}(\theta, \theta_{,i}, F, \dot{F}, \zeta); \\
\omega &= \bar{\omega}(\theta, \theta_{,i}, F, \dot{F}, \zeta).
\end{aligned}
\tag{41}
$$

Taking the material time derivative of $(41)_1$, we obtain

$$
\dot{\psi} = \frac{\partial\bar{\psi}((\theta, \theta_{,i}, F, \dot{F}, \zeta)}{\partial\theta}\dot{\theta} + \psi_{,g}(\theta, \theta_{,i}, F, \dot{F}, \zeta)\cdot\dot{g}
$$
$$
+\,\mathrm{tr}\!\left(\frac{\partial\psi(\theta, \theta_{,i}, F, \dot{F}, \zeta)}{\partial F}\dot{F}\right) + \mathrm{tr}\!\left(\frac{\partial\psi(\theta, \theta_{,i}, F, \dot{F}, \zeta)}{\partial\dot{F}}\ddot{F}\right) + \frac{\partial\psi(\theta, \theta_{,i}, F, \dot{F}, \zeta)}{\partial\zeta}\dot{\zeta}. \tag{42}
$$

Using Equation (42) in the entropy inequality (38) and making use of standard arguments [Coleman and Gurtin 1967], one can obtain the following relations for the specific Helmholtz free energy, specific entropy, and stress tensor:

$$
\psi = \bar{\psi}(\theta, F, \zeta), \tag{43}
$$

$$
\eta = \bar{\eta}(\theta, F, \dot{F}, \zeta) = -\frac{\partial\bar{\psi}(\theta, F, \zeta)}{\partial\theta}, \tag{44}
$$

$$
T = \rho\frac{\partial\bar{\psi}(\theta, F, \zeta)}{\partial F}F^T. \tag{45}
$$

As a result, entropy inequality reduces to the form

$$
-\frac{\mathrm{grad}\,\theta\cdot q}{\theta} + A(\theta, F, \zeta)\cdot\dot{\zeta} \geq 0, \tag{46}
$$

where $A$ is the *chemical affinity* as defined in [Prigogine and Defay 1954]:

$$
A = -\frac{\partial\psi(\theta, F, \zeta)}{\partial\zeta}\bigg|_{V\&\theta=\mathrm{const.}} \tag{47}
$$

If $q$ is independent of $\operatorname{grad}\theta$, then the entropy inequality takes the form

$$A(\theta, F, \zeta) \cdot \dot{\zeta} \geq 0. \tag{48}$$

The affinity $A$ is acting as a driving force for the chemical reactions. When $A$ is zero, there will be a thermodynamic equilibrium state. For bone resorption, an expression for $A$, as a biochemomechanical driving force was derived (Equation (21)). The role of biological (concentration of $H^+$ produced by proton pumps in osteoclasts), chemical (chemical potential of the matrix), and mechanical (strain energy density, and hydrostatic pressure) factors is to change the magnitude and polarity of the affinity. When Equation (21) is equal to zero, there will be a resorption equilibrium state analogous with the remodeling equilibrium state in bone remodeling process. Considering Equation (21) as a driving force of resorption process, it seems more reasonable to assume that resorption is controlled by not only mechanical, but also, chemical, and biological factors, simultaneously.

## 5. Conclusion and discussion

In this paper, a mixture theory model with chemical reactions for bone resorption process has been presented. A biphasic model, composed of a solid phase (bone matrix), and a fluid phase (bone fluid) is developed. General expression for a driving force of the bone resorption process which contains biological, mechanical and chemical factors is concluded. In the mass conservation equations, rate of mass supplied to the fluid phase by chemical reactions between the matrix and fluid is assumed to be equal to an empirical relation of the dissolution kinetics of the mineral phase of the bone matrix. Degree of saturation is assumed to be a function of the biochemomechanical affinity (Equation (21)), but not only of the Gibbs free energy (Equation (6)). As a result, mechanical, biological and chemical factors appear in the conservation equations, the constitutive assumptions, and the entropy inequality.

Strain energy density has been shown experimentally to be a likely stimulus for bone remodeling [Brown et al. 1990] and was used extensively in many theoretical modeling of bone adaptation; see, for instance, [Jacobs et al. 1997; Huiskes et al. 2000; Doblaré and García 2001; Garcia et al. 2002; Ruimerman et al. 2005]. Here, it is theoretically shown to be an effective mechanical stimulus for the bone resorption. Also, hydrostatic pressure is introduced as another mechanical stimulus for the bone resorption. Using this model, it is also shown that increasing either strain energy density or hydrostatic pressure will enhance rate of bone resorption (Figure 1). The last point can be used as a theoretical justification for many experimental observations [e.g., [Burr et al. 1985; Burr and Martin 1993; Mori and Burr 1993; Schaffler and Jepsen 2000; Li et al. 2001; Martin 2003; Van Der Vis et al. 1998; Skripitz and Aspenberg 2000; Astrand et al. 2003]. This model also shows that an increase in the concentration of $H^+$ or a decrease in the concentrations of $PO_4^{3-}$ and $Ca^{2+}$ can cause a reduction of the rate of bone resorption. Experimental data can be found in support of this model's predictions of the effect of $Ca^{2+}$ concentration on the rate of bone resorption [Lorget et al. 2000].

Biological tissues are all composed of multiphase constituents, and there are chemical reactions and/or diffusions between different components of them. Cells as live organs in the biological tissues can dictate rate of growth and adaptation, and their activities are affected by different factors (e.g., mechanical, chemical, and biological factors). One purpose of this research was using a mixture theory approach for modeling bone resorption. By this, we hoped to gain new insight about engineering and biological

factors which can change the rate of bone resorption, especially in the osteoporotic cases. Nowadays, the most common method in treating osteoporosis is anti-bone-resorption drugs which inhibit or reduce the bone resorbing cells (i.e. osteoclasts) activity. The reason for using this way of treatment is the lack of information about all the factors affecting osteoclasts' activity. This preliminary theoretical research shows that the activity of osteoclasts and, thus, the rate of bone resorption are not only dictated by biological factors (e.g., hormone levels), but also by engineering factors (hydrostatic pressure, strain energy density, and concentration of different ions present in the resorption process); see Equations (21), (25) and (48). Another goal was to make a novel attempt to combine mixture theory with chemical kinetics. This could be useful not only for modeling growth and adaptation of biological tissues such as bone, cartilage, and muscle, but also for modeling nonbiological processes such as stress corrosion. In order to attain the second goal, more theoretical and experimental research is in progress.

# References

[Aguado et al. 1997] F. Aguado, M. Revilla, L. F. Villa, and H. Rico, "Cortical bone resorption in osteoporosis", *Calcified Tissue Int.* **60**:4 (1997), 323–326.

[Arnaud 2001] C. Arnaud, "New drug revolutionizes osteoporosis treatment", *FOREFront* (newsletter of Foundation for Osteoporosis Research and Education) **8**:2 (2001), 1–2.

[Ascenzi 1993] A. Ascenzi, "Biomechanics and Galileo Galilei", *J. Biomech.* **26**:2 (1993), 95–100.

[Astrand et al. 2003] J. Astrand, R. Skripitz, B. Skoglund, and P. Aspenberg, "A rat model for testing pharmacologic treatments of pressure-related bone loss", *Clin. Orthop. Relat. Res.* **409** (2003), 296–305.

[Beaupré et al. 1990] G. S. Beaupré, T. E. Orr, and D. R. Carter, "An approach for time-dependent bone modeling and remodeling- theoretical development", *J. Orthopaed. Res.* **8**:5 (1990), 651–661.

[Blair 1998] H. C. Blair, "How the osteoclast degrades bone", *BioEssays* **20**:10 (1998), 837–846.

[Bowen 1968] R. M. Bowen, "Thermochemistry of reacting materials", *J. Chem. Phys.* **49**:4 (1968), 1625–1637.

[Bowen 1971] R. M. Bowen, "Theory of mixtures", pp. 2–122 in *Continuum physics*, vol. 3, edited by A. C. Eringen, Academic Press, New York, 1971.

[Brown et al. 1990] T. D. Brown, D. R. Pedersen, M. L. Gray, R. A. Brand, and C. T. Rubin, "Toward an identification of mechanical parameters initiating periosteal remodeling: a combined experimental and analytic approach", *J. Biomech.* **23**:9 (1990), 893–897.

[Burr and Martin 1993] D. B. Burr and R. B. Martin, "Calculating the probability that microcracks initiate resorption spaces", *J. Biomech.* **26**:4-5 (1993), 613–616.

[Burr et al. 1985] D. B. Burr, R. B. Martin, M. B. Schaffler, and E. L. Radin, "Bone remodeling in response to in vivo fatigue microdamage", *J. Biomech.* **18**:3 (1985), 189–200.

[Carter 1987] D. R. Carter, "Mechanical loading history and skeletal biology", *J. Biomech.* **20**:11-12 (1987), 1095–1109.

[Carter et al. 1996] D. R. Carter, M. C. Van der Meulen, and G. S. Beaupré, "Mechanical factors in bone growth and development", *Bone* **18**:1 Suppl.1 (1996), S5–S10.

[Chambers et al. 1984] T. J. Chambers, P. A. Revell, K. Fuller, and N. A. Athanasou, "Resorption of bone by isolated rabbit osteoclasts", *J. Cell Sci.* **66**:1 (1984), 383–399.

[Chow et al. 2003] L. C. Chow, M. Markovic, and S. Takagi, "A dual constant-composition titration system as in vitro resorption model for comparing dissolution rates of calcium phosphates biomaterials", *J. Biomed. Mater. Res.* **65B**:2 (2003), 245–251.

[Christoffersen et al. 1996] J. Christoffersen, M. R. Christoffersen, and T. Johansen, "Kinetics of growth and dissolution of fluorapatite", *J. Cryst. Growth* **163**:3 (1996), 295–303.

[Coleman and Gurtin 1967] B. D. Coleman and M. E. Gurtin, "Thermodynamics with internal state variables", *J. Chem. Phys.* **47**:2 (1967), 597–613.

[Cowin and Hegedus 1976] S. C. Cowin and D. H. Hegedus, "Bone remodeling,I: theory of adaptive elasticity", *J. Elasticity* **6**:3 (1976), 313–326.

[Doblaré and García 2001] M. Doblaré and J. M. García, "Application of an anisotropic bone-remodeling model based on a damage-repair theory to the analysis of the proximal femur before and after total hip replacement", *J. Biomech.* **34**:9 (2001), 1157–1170.

[Dorozhkin 1997a] S. V. Dorozhkin, "Acidic dissolution mechanism of natural fluorapatite,I: milli- and microlevels of investigations", *J. Cryst. Growth* **182**:1-2 (1997), 125–132.

[Dorozhkin 1997b] S. V. Dorozhkin, "Acidic dissolution mechanism of natural fluorapatite,II: nanolevel of investigations", *J. Cryst. Growth* **182**:1-2 (1997), 133–140.

[Dorozhkin 1997c] S. V. Dorozhkin, "Surface reactions of apatite dissolution", *J. Colloid Interf. Sci.* **191**:2 (1997), 489–497.

[Ducy et al. 2000] P. Ducy, T. Schinke, and G. Karsenty, "The osteoblast: a sophisticated fibroblast under central surveillance", *Science* **289**:5484 (2000), 1501–1504.

[Eriksen and Kassem 1992] E. F. Eriksen and M. Kassem, "The cellular basis of bone remodeling", *Triangle* **31**:2/3 (1992), 45–57.

[Flieger et al. 1998] J. Flieger, T. Karachalios, L. Khaldi, P. Raptou, and G. Lyritis, "Mechanical stimulation in the form of vibration prevents postmenopausal bone loss in ovariectomized rats", *Calcified Tissue Int.* **63**:6 (1998), 510–514.

[Fritton et al. 2000] S. P. Fritton, K. J. McLeod, and C. T. Rubin, "Quantifying the strain history of bone: spatial uniformity and self similarity of low magnitude strains", *J. Biomech.* **33**:3 (2000), 317–325.

[Fulmer et al. 2002] M. T. Fulmer, I. C. Ison, C. R. Hankermayer, B. R. Constantz, and J. Ross, "Measurements of the solubilities and dissolution rates of several hydroxyapatites", *Biomaterials* **23**:3 (2002), 751–755.

[Garcia et al. 2002] J. M. Garcia, M. Doblare, and J. Cegonino, "Bone remodeling simulation: a tool for implant design", *Comput. Mater. Sci.* **25**:1–2 (2002), 100–114.

[Hankermeyer et al. 2002] C. R. Hankermeyer, K. L. Ohashi, D. C. Delaney, J. Ross, and B. R. Constantz, "Dissolution rates of carbonated hydroxyapatite in hydrochloric acid", *Biomaterials* **23**:3 (2002), 743–750.

[Hegedus and Cowin 1976] D. H. Hegedus and S. C. Cowin, "Bone remodeling, II: small strain adaptive elasticity", *J. Elasticity* **6**:4 (1976), 337–352.

[Huiskes et al. 2000] R. Huiskes, R. Ruimerman, G. H. Van Lenthe, and J. D. Janssen, "Effects of mechanical forces on maintenance and adaptation of form in trabecular bone", *Nature* **405**:6787 (2000), 704–706.

[Jacobs et al. 1997] C. R. Jacobs, J. C. Simo, G. S. Beaupré, and D. R. Carter, "Adaptive bone remodeling incorporating simultaneous density and anisotropy considerations", *J. Biomech.* **30**:6 (1997), 603–613.

[Jee 2001] W. S. S. Jee, "Integrated bone tissue physiology: anatomy and physiology", pp. 1–68 in *Bone mechanics handbook*, 2nd ed., edited by S. C. Cowin, CRC Press, Boca Raton, FL, 2001.

[Li et al. 2001] J. Li, T. Mashiba, and D. B. Burr, "Bisphosphonate treatment suppresses not only stochastic remodeling but also the targeted repair of microdamage", *Calcified Tissue Int.* **69**:5 (2001), 281–286.

[Lorget et al. 2000] F. Lorget, S. Kamel, R. Mentaverri, A. Wattel, M. Naassila, M. Maamer, and M. Brazier, "High extracellular calcium concentrations directly stimulate osteoclast apoptosis", *Biochem. Biophys. Res. Commun.* **268**:3 (2000), 899–903.

[Margolis and Moreno 1992] H. C. Margolis and E. C. Moreno, "Kinetics of hydroxyapatite dissolution in acetic, lactic, and phosphoric-acid solutions", *Calcified Tissue Int.* **50**:2 (1992), 137–143.

[Martin 2003] R. B. Martin, "Fatigue microdamage as an essential element of bone mechanics and biology", *Calcified Tissue Int.* **73**:2 (2003), 101–107.

[Martin and Burr 1989] R. B. Martin and D. B. Burr, *Structure, function and adaptation of compact bone*, Raven Press, New York, 1989.

[Mori and Burr 1993] S. Mori and D. B. Burr, "Increased intracortical remodeling following fatigue damage", *Bone* **14**:2 (1993), 103–109.

[Prigogine and Defay 1954] I. Prigogine and R. Defay, *Chemical thermodynamics*, Wiley, New York, 1954.

[Ramtani and Zidi 2001] S. Ramtani and M. Zidi, "A theoretical model of the effect of continuum damage on a bone adaptation model", *J. Biomech.* **34**:4 (2001), 471–479.

[Ramtani and Zidi 2002] S. Ramtani and M. Zidi, "Damaged-bone adaptation under steady homogeneous stress", *J. Biomech. Eng.*(*Trans. ASME*) **124**:3 (2002), 322–327.

[Recker 1983] R. R. Recker, *Bone histomorphometry: techniques and interpretation*, CRC Press, Boca Raton, FL, 1983.

[Reilly and Burstein 1975] D. T. Reilly and A. H. Burstein, "The elastic and ultimate properties of compact bone tissue", *J. Biomech.* **8**:6 (1975), 393–396.

[Riggs et al. 2002] B. L. Riggs, S. Khosla, and L. J. Melton, "Sex steroids and the construction and conservation of the adult skeleton", *Endocr. Rev.* **23**:3 (2002), 279–302.

[Rouhi et al. 2006] G. Rouhi, M. Epstein, L. Sudak, and W. Herzog, "Free surface density and microdamage in the bone remodeling equation: theoretical considerations", *Int. J. Eng. Sci.* **44**:7 (2006), 456–469.

[Rousselle and Heymann 2002] A. V. Rousselle and D. Heymann, "Osteoclastic acidification pathways during bone resorption", *Bone* **30**:4 (2002), 533–540.

[Rubin et al. 1998] C. Rubin, S. Turner, C. Jerome, M. Strachan, S. Bain, and K. McLeod, "Low magnitude, high frequency mechanical stimulation increases trabecular density of the proximal femur", *Amer. Soc. Bone Miner. Res.* **23** (1998), 1126–1132.

[Rubin et al. 2001a] C. Rubin, D. W. Sommerfeldt, S. Judex, and Y. X. Qin, "Inhibition of osteopenia by low magnitude, high frequency mechanical stimuli", *Ther. Focus* **6**:16 (2001), 848–858.

[Rubin et al. 2001b] C. Rubin, A. Turner, S. Bain, C. Mallinckrodt, and K. McLeod, "Anabolism: low mechanical signals strengthen long bones", *Nature* **412**:6847 (2001), 603–604.

[Rubin et al. 2002] C. Rubin, A. Turner, R. Muller, E. Mittra, K. McLeod, W. Lin, and Y. Qin, "Quantity and quality of trabecular bone in the femur are enhanced by a strongly anabolic, noninvasive mechanical intervention", *J. Bone Miner. Res.* **17** (2002), 349–357.

[Rubin et al. 2004] C. Rubin, R. Recker, D. Cullen, J. Ryaby, J. McCabe, and K. McLeod, "Prevention of postmenopausal bone loss by a low magnitude, high-frequency mechanical stimuli: a clinical trial assessing compliance, efficacy, and safety", *J. Bone Miner. Res.* **19**:3 (2004), 343–351.

[Ruimerman et al. 2005] R. Ruimerman, P. Hilbers, B. van Rietbergen, and R. Huiskes, "A theoretical framework for strain-related trabecular bone maintenance and adaptation", *J. Biomech.* **38**:4 (2005), 931–941.

[Schaffler and Jepsen 2000] M. B. Schaffler and K. J. Jepsen, "Fatigue and repair in bone", *Int. J. Fatigue* **22**:10 (2000), 839–846.

[Silva and Ulm 2002] E. C. C. M. Silva and F. J. Ulm, "A bio-chemo-mechanics approach to bone resorption and fracture", pp. 355–366 in *IUTAM symposium on advanced and computational fracture mechanics of non-homogeneous materials*, Kluwer, Dordrecht, 2002.

[Skripitz and Aspenberg 2000] R. Skripitz and P. Aspenberg, "Pressure-induced periprosthetic osteolysis: a rat model", *J. Orthopaed. Res.* **18**:3 (2000), 481–484.

[Taylor et al. 2003] D. Taylor, J. G. Hazenberg, and T. C. Lee, "The cellular transducer in damage-stimulated bone remodeling: a theoretical investigation using fracture mechanics", *J. Theor. Biol.* **225**:1 (2003), 65–75.

[Teitelbaum and Ross 2003] S. L. Teitelbaum and F. P. Ross, "Genetic regulation of osteoclast development and function", *Nat. Rev. Genet.* **4**:8 (2003), 638–649.

[Thomann et al. 1989] J. M. Thomann, J. C. Voegel, M. Gumper, and P. Gramain, "Dissolution kinetics of human enamel powder, II: a model based on the formation of a self-inhibiting surface layer", *J. Colloid Interf. Sci.* **132**:2 (1989), 403–412.

[Thomann et al. 1990] J. M. Thomann, J. C. Voegel, and P. Gramain, "Kinetics of dissolution of calcium hydroxyapatite powder, III: PH and sample conditioning effects", *Calcified Tissue Int.* **46**:2 (1990), 121–129.

[Thomann et al. 1991] J. M. Thomann, J. C. Voegel, and P. Gramain, "Kinetics of dissolution of calcium hydroxyapatite powder, IV: interfacial calcium diffusion controlled process", *Colloids Surf.* **54**:1-2 (1991), 145–159.

[Van Der Vis et al. 1998] H. M. Van Der Vis, P. Aspenberg, R. K. Marti, W. Tigchelaar, and C. J. Van Noorden, "Fluid pressure causes bone resorption in a rabbit model of prosthetic loosening", *Clin. Orthop. Relat. Res.* **350** (1998), 201–208.

[Wolff 1892] J. Wolff, *Das Gesetz der Transformation der Knochen*, August Hirschwald, Berlin, 1892. Translated as *The law of bone remodeling*, Springer, Berlin, 1986.

GHOLAMREZA ROUHI: grouhi@uottawa.ca
*Department of Mechanical Engineering, University of Ottawa, 161 Louis Pasteur, Room A017 Ottawa, Ontario, Canada
K1N 6N5, Canada*

MARCELO EPSTEIN: mepstein@ucalgary.ca
*Department of Mechanical and Manufacturing Engineering, University of Calgary, 2500 University Dr. NW,
Calgary, Alberta T2N 1N4, Canada*

LESZEK SUDAK: lsudak@ucalgary.ca
*Department of Mechanical and Manufacturing Engineering, University of Calgary, 2500 University Dr. NW,
Calgary, Alberta T2N 1N4, Canada*

WALTER HERZOG: walter@kin.ucalgary.ca
*Faculty of Kinesiology, University of Calgary, 2500 University Drive NW, Calgary, Alberta T2N 1N4, Canada*

# THE MECHANICS OF TIP GROWTH MORPHOGENESIS: WHAT WE HAVE LEARNED FROM RUBBER BALLOONS

Roberto Bernal, Enrique R. Rojas and Jacques Dumais

*If you can't demonstrate it with balloons, it's probably not important anyway.*

Stephen A. Wainwright, quoted in [Vogel 2003].

Morphogenesis of plant, fungal, and bacterial cells depends heavily on surface mechanics and in particular on the stiff wall that surrounds these cells. In this paper, we show that tubular rubber balloons offer a useful physical model of tip growth morphogenesis. In particular, the balloons reproduce accurately the inhomogeneity and anisotropy of surface expansion observed during tip growth. Comparison between the two systems has led to a simple model of tip growth that assumes linear constitutive relations with inhomogeneous material properties. The strain rate profile predicted by the model is a surprisingly good fit to the data given the model's simplicity. We suggest that a meridional gradient of compliance or extensibility is the key mechanical feature that explains the similar strain rate profiles in tip-growing cells across broad taxonomic groups as well as in rubber balloon analogs.

## 1. Introduction

Cells come in a variety of shapes that are often finely adapted to fulfill specific functions. A familiar example is the human red blood cell whose flexible biconcave geometry allows it to squeeze through narrow capillaries. The morphogenetic mechanisms that control the development of shape appear to be quite diverse [Harold 1990] and few are particularly well understood.

In bacteria, fungi, and plants, cell shape is to a large extent determined by the stiff extracellular matrix or cell wall surrounding the cell. The cell wall is a thin layer of polysaccharides and proteins assembled outside the plasma membrane. The architecture of cell walls can vary greatly although it typically takes the form of a fiber-reinforced composite where fibrils of cellulose (in plants) provide stiffness to the wall while an amorphous matrix of pectins helps maintain the cohesion between the different wall components.

This paper focuses on one important mode of cell morphogenesis called tip growth. The shape of tip-growing cells is characterized by a long cylinder capped by a prolate dome (Figure 1). Kinematics studies using cell surface markers have established that wall expansion is limited to the tip of the cell [Reinhardt 1892; Hejnowicz et al. 1977; Shaw et al. 2000; Dumais et al. 2004]. Expansion at the tip is maintained by two complementary processes: the addition of cell surface material and the mechanical deformation of the cell surface into the characteristic cylindrical shape. Vesicle exocytosis and polysaccharide synthesis
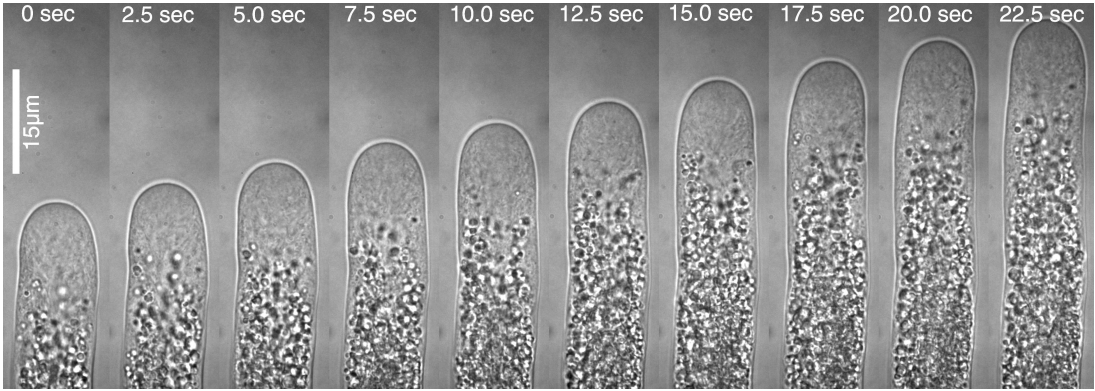
**Figure 1.** Tip growth morphogenesis of a lily pollen tube.

at the plasma membrane provide the material necessary to expand the surface. However, secretion of building material does not expand the cell surface unless the material is subsequently deformed and integrated into the preexisting extracellular matrix. This step requires mechanical work provided by the internal hydrostatic pressure of the cell.

Although models of tip growth are available, few have attempted an explicit comparison with the kinematics of these cells. The goal of this paper is to introduce a simple mechanical model that reproduces the key features of tip growth morphogenesis.

## 2. The kinematics of tip growth

Over a period of minutes or hours, the elongation of tip-growing cells is surprisingly steady both in terms of geometry and the rate of elongation, as shown in Figure 1 [Shaw et al. 2000]. Kinematics studies of tip growth have been performed using time-lapse imaging of marked cells [Castle 1958; Chen 1973; Hejnowicz et al. 1977; Shaw et al. 2000; Dumais et al. 2004]; see Figures 2 and 3. Given the axisymmetric geometry of these cells, two variables are sufficient to describe the entire morphogenetic
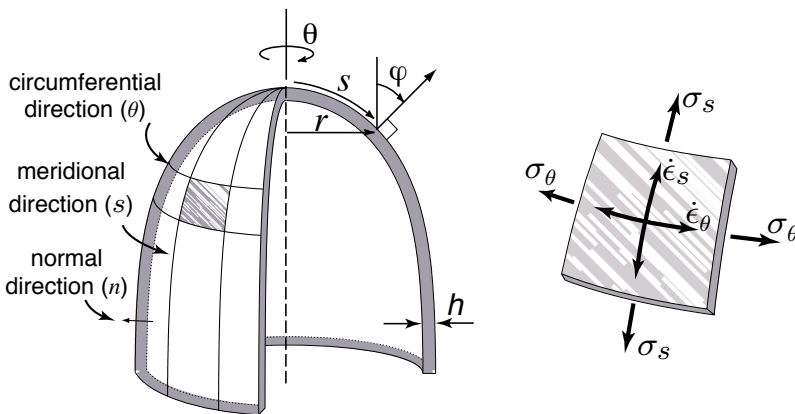


**Figure 2.** Key geometrical variables for the description of tip growth.
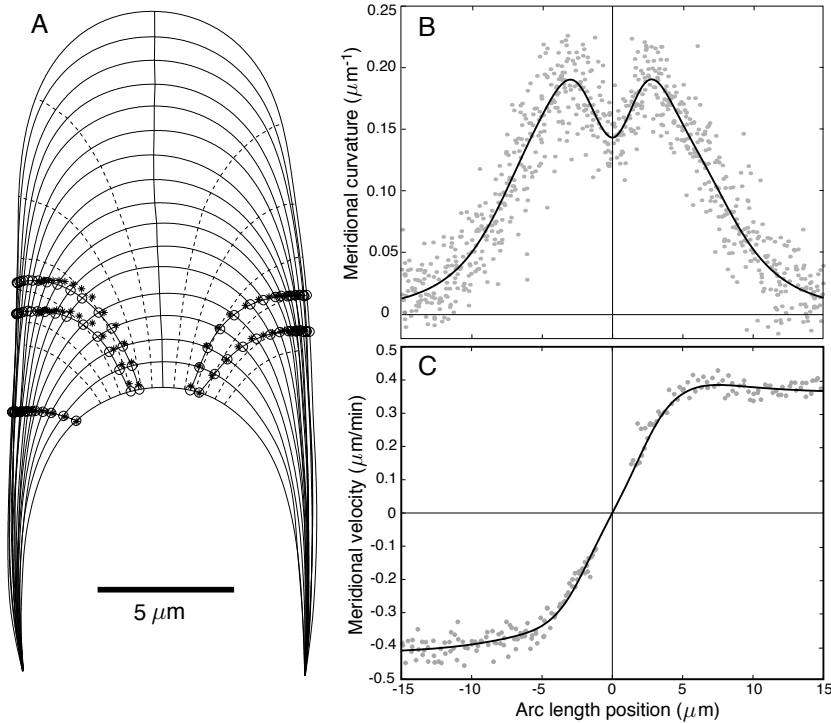
**Figure 3.** Growth kinematics of a *Medicago truncatula* root hair. (A) The cell outline captured at a 3 min time interval. The displacement of five surface markers is shown (circles). The dotted lines indicate trajectories that are normal to the cell surface. (B) The meridional curvature of the cell. (C) The meridional velocity of material points. Modified from [Dumais et al. 2004].

process. The cell geometry is given by the meridional curvature ($\kappa_s$) (Figure 3B) while the rates of surface expansion can be derived from the meridional velocity ($v$) of material points with respect to the pole of the cell (Figure 3C). Given these variables, the strain rates are defined as [Hejnowicz et al. 1977; Dumais et al. 2004]:

$$\dot{\epsilon}_s = \frac{d}{ds}\frac{ds}{dt} = \frac{dv}{ds}, \qquad \dot{\epsilon}_\theta = \frac{1}{r}\frac{dr}{dt} = \frac{1}{r}\frac{dr}{ds}v, \tag{1}$$

where the variables are illustrated in Figure 2.

Studies of cellular tip growth have revealed two fundamental features of wall expansion: surface expansion is inhomogeneous and anisotropic (Figure 4). The inhomogeneity is seen in the sharp decline of the strain rates from a maximal value near the pole of the cell to zero on the side of the cell. Surface expansion also shows a characteristic anisotropy with meridional anisotropy ($\dot{\epsilon}_s > \dot{\epsilon}_\theta$) within two to three microns of the pole and extensive circumferential anisotropy ($\dot{\epsilon}_\theta > \dot{\epsilon}_s$) on the flanks of the tip (Figure 4).

The strain profile observed in root hairs is similar to those reported for other tip-growing cells including the *Chara* rhizoid [Hejnowicz et al. 1977], the *Nitella* rhizoid [Chen 1973], and the sporangiophore of *Phycomyces* [Castle 1958]. Since these systems include representatives of fungi, plants and algae, that differ greatly in wall chemistry and cell biology, one is tempted to attribute the similarities in the
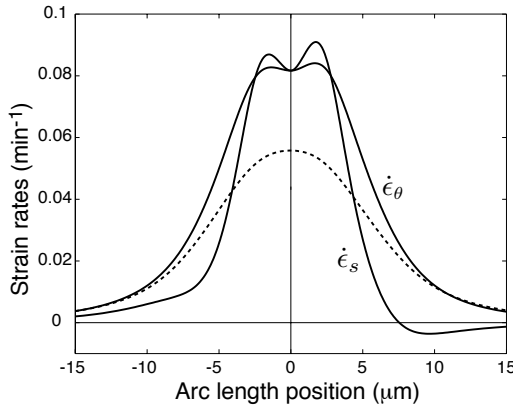
**Figure 4.** Strain rate profile for the cell shown in Figure 3. A slight meridional anisotropy ($\dot{\epsilon}_s > \dot{\epsilon}_\theta$) near the pole is followed by long shoulders of circumferential anisotropy ($\dot{\epsilon}_\theta > \dot{\epsilon}_s$). For comparison, the isotropic strain solution for the same geometry is shown (dotted line). Modified from [Dumais et al. 2004].

kinematics of these cells to some broadly shared processes. Therefore, the first question to ask is whether the observed strain rate profile is a geometrical requirement for all tip-growing cells. Although geometry certainly constrains kinematics, the statement above cannot be generally true since there is an infinite number of strain rate profiles that are compatible with the geometry of the system.

A comparison with the profile corresponding to an isotropic deformation of the surface reveals what is unique about the observed strain rate pattern. Setting the two equations in (1) equal to one another leads to the differential equation

$$\frac{1}{v}\frac{dv}{ds} = \frac{1}{r}\frac{dr}{ds},$$

which has as a general solution $v(s) = \frac{v_c}{r_c}r(s)$, where $v_c$ is the tip velocity and $r_c$ is the radius of the cylindrical region of the cell. The isotropic strain rates associated with this velocity profile are: $\dot{\epsilon}^i = \dot{\epsilon}_s = \dot{\epsilon}_\theta = \frac{v_c}{r_c}\frac{dr}{ds}$. The solution is shown in Figure 4 alongside the measured strain rates. Strain isotropy, in itself, is not a good model for the observed strain rates. However, three kinematic constraints can help explain some of the features of the observed strain rates:

(i) rotational symmetry requires that $\dot{\epsilon}_s(0) = \dot{\epsilon}_\theta(0)$;

(ii) the area under the $\dot{\epsilon}_s$ curve and the isotropic strain rate solution must be equal since it is set by the velocity of the tip, i.e. $\int_0^\infty \dot{\epsilon}_s ds = \int_0^\infty \dot{\epsilon}^i ds = v_c$;

(iii) the circumferential strain rate is asymptotic to the isotropic solution near the base of the dome, i.e.,

$$\dot{\epsilon}_\theta = \frac{v}{r}\frac{dr}{ds} \simeq \frac{v_c}{r_c}\frac{dr}{ds} = \dot{\epsilon}^i, \quad \text{for } r \to r_c.$$

Given these constraints, the main differences between the observed strain rates and the isotropic solution can be encapsulated into one observation: tip-growing cells show relatively more surface expansion near the pole than what is predicted by the isotropic solution. Since $\dot{\epsilon}_s$ exceeds $\dot{\epsilon}^i$ near the pole, it must drop below $\dot{\epsilon}^i$ away from the pole so that the second constraint is fulfilled. This feature explains the sharp

decline in $\dot{\epsilon}_s$ observed in Figure 4. The circumferential anisotropy is also predicted since while $\dot{\epsilon}_s < \dot{\epsilon}^i$ on the flanks of the tip, the third constraint requires that $\dot{\epsilon}_\theta \to \dot{\epsilon}^i$ at that location. Therefore, high strain rate (relative to the isotropic solution) near the pole of the cell implies circumferential anisotropy on the flanks of the dome. A similar argument was made by Green and King [1966], who demonstrated the validity of their result using locally reinforced rubber membranes. These statements will be made more precise when we discuss our model in Section 4, but first we look at the kinematics of rubber balloons from which the model was inspired.

## 3. Analysis of rubber balloon expansion

D'Arcy W. Thompson [1942] is widely credited for popularizing the idea that many seemingly complex biological phenomena, including cell morphogenesis, are governed by simple geometrical and physical principles. It is in this spirit that Hejnowicz et al. [1977] drew a parallel between tip growth morphogenesis and the growth of cylindrical rubber balloons. These balloons undergo an instability [Chater and Hutchinson 1984] whereby two cylindrical solutions can coexist at the given internal pressure, as shown in Figure 5. Inflation of the balloon pushes forward the zone of transition between these two cylindrical solutions. According to Hejnowicz and coworkers, the migration of the front is analogous to tip growth. The small-radius tail that precedes the front is regarded as a source of new material on which the large-radius solution feeds during growth. The narrow tail could well be pushed inside the inflating balloon to become an "internal" source of material as in tip growth. An analysis of the deformation process in rubber balloons shows that the parallels go beyond the simple geometrical analogy.

**3.1.** *Experimental setup.* We used an experimental configuration similar to that of Kyriakides and Chang [1991] to follow the steady-state growth of cylindrical rubber balloons (Qualatex 160Q) under constant
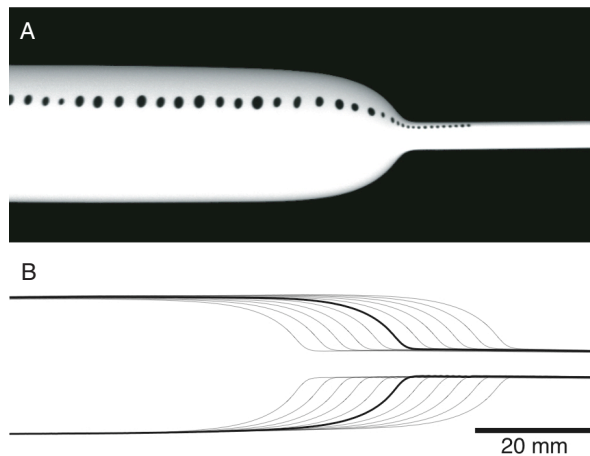


**Figure 5.** (A) Snapshot of the inflated balloon with its fiducial points. (B) Propagation of the growth front during inflation. The velocity of the material entering the front is $V = 2.55$ mm/s assuming that the front is fixed in space. The velocity of the material that exits the front is $v_c = \lambda_s^{\max} V = 3.74 \times 2.55$ mm/s $= 9.54$ mm/sec, where $\lambda_s^{\max}$ is the maximal meridional stretch.
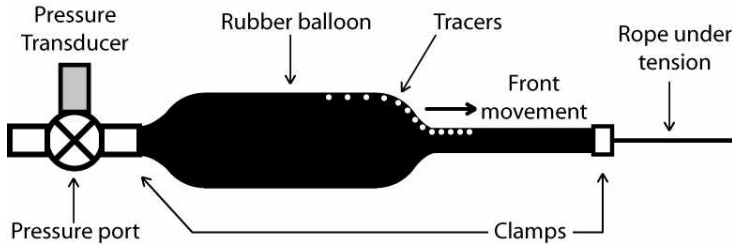
**Figure 6.** Diagram of the experimental setup for the rubber balloon deformation under constant internal pressure.

internal pressure $P$ of 24.3 kPa, measured with an OMEGA PX26-005GV pressure transducer (Figure 6). To get a uniform and straight advance of the growth front, the balloon was maintained under slight axial tension by pulling with a mass $M \simeq 20$ g. The axial stress in the elastic membrane associated with this tension was approximately 50 kPa, which is negligible compared to the membrane stresses imposed by the internal pressure (210 kPa $<$ Pr/h $<$ 21 MPa). Time-lapse sequences were recorded at 10 frames per second with a PIXELINK PL-A781 camera. The meridional curvature was measured using the outline of the balloon and the stretches were computed by tracking the position of fiducial points applied to one side of the balloon (Figure 5). All further analyses were done in Matlab 7.3 and assumed an axisymmetric geometry. These data provide the information to characterize the kinematics of the balloon.

**3.2. *Kinematics*.** As the rubber balloon deforms under the internal pressure, the growth front pushes forward, delimiting two cylindrical regions in which the radii of the balloon are $r_{min} = 2.32$ mm and $r_{max} = 11.2$ mm, respectively. The undeformed radius (i.e. at $P = 0$) is $R = 2.12$ mm. The separation of the fiducial points was on average $dS \simeq 1$ mm before stretching and reached a maximum of 3.7 mm in the deformed region. The undeformed thickness of the membrane was $H = 0.27$ mm.

The kinematics of the balloon is formulated in terms of stretches. The meridional, circumferential and normal stretches are ratios of length elements before and after the deformation:

$$\lambda_s = ds/dS, \quad \lambda_\theta = r/R, \quad \lambda_n = h/H,$$

where capital letters stand for undeformed lengths. These stretches are generally not completely independent. For an incompressible material, we have $\lambda_s \lambda_\theta \lambda_n = 1$ or, alternatively, $\lambda_n = (\lambda_\theta \lambda_s)^{-1}$.

The meridional curvature is $\kappa_s = d\varphi/ds$, where $\varphi$ is the angle between the normal to the surface and the axis of the balloon (Figure 2). The meridional curvature defines two regions (Figure 7A). A core region within 7 mm of the axis shows negative curvature. It corresponds to the source of material for the advance of the front. An outer region extends from a distance of 7 mm onwards. In our analogy with tip growth morphogenesis, this region stands for the deforming cell surface and is thus of special interest.

Using the balloon outline and the position of fiducial points, we computed the stretches of the elastic membrane (Figure 7B). The maximal circumferential stretch is $\lambda_\theta = 5.63$ while the maximal meridional stretch is $\lambda_s = 3.74$. For comparison with tip-growing cells, we need to define strain rates for the elastic deformation of the membrane. The velocity of material points, assuming that the front is fixed in space while material flows through it, is given by $v(s) = \lambda_s(s)V$, where $V$ is the velocity at which underformed
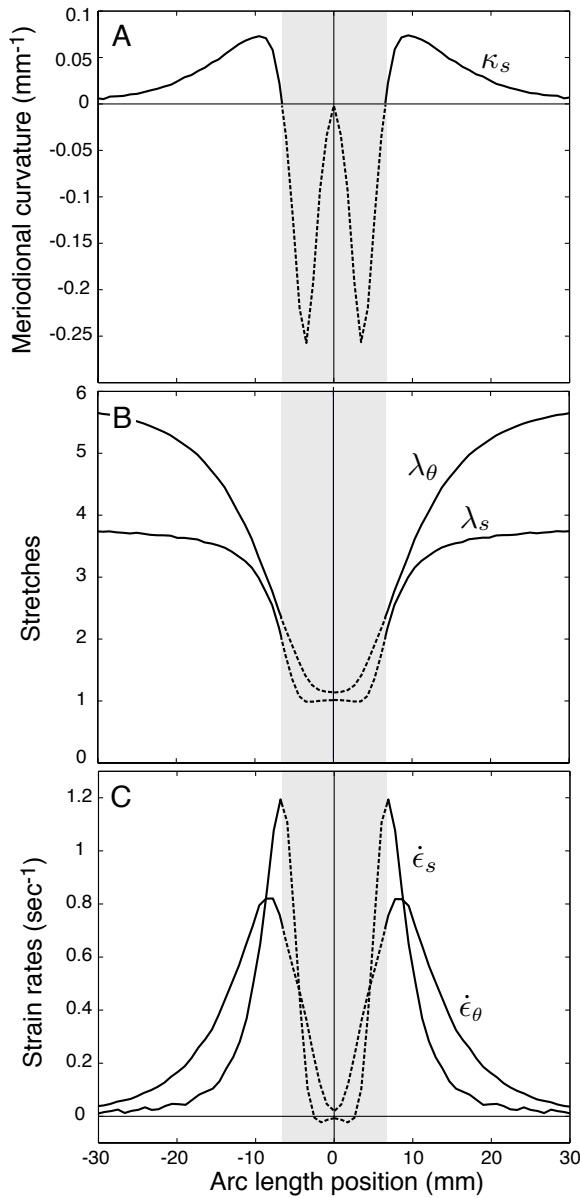
**Figure 7.** (A) Meridional curvature $\kappa_s$ as a function of arc length $s$. The shaded area delimits the core region ($\kappa_s < 0$) corresponding to the "source" of material and an outer region ($\kappa_s > 0$) analogous to the dome of tip-growing cells. (B) Meridional and circumferential stretches as a function of arc length. The maximum circumferential and meridional stretches are $\lambda_\theta = 5.63$, $\lambda_s = 3.74$ respectively. (C) Meridional and circumferential strain rates as a function of arc length.
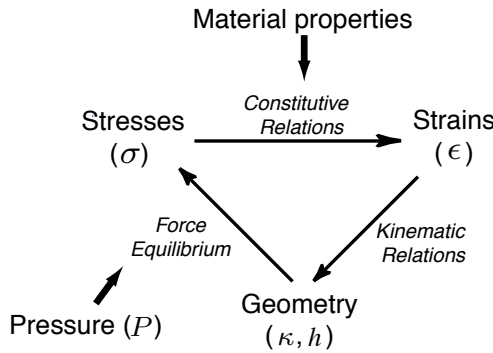
**Figure 8.** Three fundamental relations for thin pressurized shells.

material feeds into the front. Accordingly, the strain rates are

$$\dot{\epsilon}_s = \frac{d}{ds} v = \frac{d\lambda_s}{ds} V, \qquad \dot{\epsilon}_\theta = \frac{1}{r} \frac{dr}{dt} = \frac{R}{r} \frac{d(r/R)}{ds} \frac{ds}{dS} \frac{dS}{dt} = \frac{\lambda_s}{\lambda_\theta} \frac{d\lambda_\theta}{ds} V. \tag{2}$$

The measured strain rates show substantial variation (Figure 7C). In the polar region, the two strain rates increase rapidly to a near maximal value as the material is about the exit this region. In the outer region, the strain rates decline gradually. The strain rate anisotropy first favors meridional stretching followed by long shoulders where circumferential stretching dominates. The similarities with the strain rates reported for plant cells is striking. In particular, the strain rate anisotropy and inhomogeneity follow the same trends and are mapped to the same regions in the two systems.

## 4. A model of tip growth

The similarities between cellular tip growth and the balloon analog prompted us to look for a simple model that could be applied to both systems. Given the sharp differences between the material properties of rubber (nonlinear elasticity) and plant cell walls (viscoplasticity), we postulate that the strain rate profile does not depend strongly on the details of the constitutive behavior. Our focus therefore is on features that are known to be shared between rubber balloons and tip-growing cells. The two systems are thin pressurized shells whose material properties are spatially varying.

The mechanics of thin shells is well understood particularly those with axisymmetric geometry [Flügge 1973]. A set of three fundamental relations connect the stresses $\sigma$, the strains $\epsilon$, and geometrical variables such as the curvature $\kappa$ of the surface and the shell thickness $h$; see Figure 8. The kinematic relations are already encapsulated in Equations (1) and (2). Equations are also needed for the balance of forces between the membrane stresses and the internal pressure. The wall stresses are given by

$$\sigma_s = \frac{P}{2h\kappa_\theta}, \qquad \sigma_\theta = \frac{P}{2h\kappa_\theta} \left( 2 - \frac{\kappa_s}{\kappa_\theta} \right), \tag{3}$$

[Steele 2000; Dumais et al. 2006], where $P$ is the internal hydrostatic pressure, $h$ is the wall thickness, and $\kappa_s$ and $\kappa_\theta$ are the meridional and circumferential curvatures. Note that the normal stress, $\sigma_n \sim P$,

is much smaller than the plane stresses, $\sigma_s$ and $\sigma_\theta$. We can therefore neglect the normal stress in the following treatment.

Next we must select a constitutive model to relate the strains and stresses. Several constitutive models have been suggested for the plant cell wall (see [Dumais et al. 2006], for instance) and rubber elasticity (see [Ogden 1972; Treloar et al. 1976], for example). These models are very different except in the limit of small deformation where a linear set of equations can be applied to most materials. We therefore adopt a simple linear constitutive model:

$$\begin{pmatrix} \epsilon_s(s) \\ \epsilon_\theta(s) \end{pmatrix} = \alpha(s) \begin{pmatrix} 1 & -\nu \\ -\nu & 1 \end{pmatrix} \begin{pmatrix} \sigma_s(s) \\ \sigma_\theta(s) \end{pmatrix}, \tag{4}$$

where $\alpha(s)$ is a spatially varying elastic compliance and $\nu$ is a fixed Poisson's ratio. In this model, the complexity of the material's response to stress is encapsulated in the compliance $\alpha$ rather than in a more complex functional form for the model. One important advantage of this model is that it can be solved analytically for a given tip geometry.

Substituting for the strains and stresses in Equation (4) yields

$$\begin{aligned} \epsilon_s &= \frac{ds}{dS} - 1 = \alpha\left(\frac{P}{2h\kappa_\theta} - \nu\frac{P}{2h\kappa_\theta}\left(2 - \frac{\kappa_s}{\kappa_\theta}\right)\right), \\ \epsilon_\theta &= \frac{r}{R} - 1 = \alpha\left(\frac{P}{2h\kappa_\theta}\left(2 - \frac{\kappa_s}{\kappa_\theta}\right) - \nu\frac{P}{2h\kappa_\theta}\right). \end{aligned} \tag{5}$$

Dividing the first equation by the second and rearranging, we get

$$ds = \left(\left(\frac{r}{R} - 1\right)\frac{(1 - 2\nu)\kappa_\theta + \nu\kappa_s}{(2 - \nu)\kappa_\theta - \kappa_s} + 1\right)dS. \tag{6}$$

Finally, dividing both sides of this equation by $dt$, we get

$$v(s) = \left(\left(\frac{r}{R} - 1\right)\frac{(1 - 2\nu)\kappa_\theta + \nu\kappa_s}{(2 - \nu)\kappa_\theta - \kappa_s} + 1\right)V = \lambda_s V = \frac{\lambda_s}{\lambda_s^{\max}}v_c. \tag{7}$$

From (7) it is possible to determine the velocity profile based solely on the shell geometry ($r(s)$ or $\kappa_s(s)$) and two parameters, the Poisson's ratio ($\nu$) and a characteristic velocity ($V$ or $v_c$). $v_c$ is the velocity of the front with respect to the deformed region. We adopt this parameter since it has a natural parallel with the velocity for tip growth. The Poisson's ratio of rubber is close to 0.5 for small deformations but for strains above one it quickly drops to 0.3 [Vincent 1990]. Since the balloon strains go beyond a value of 4, we use $\nu = 0.3$.

Using the values for $\nu$ and $v_c$ in (7) and substituting into (2) allows us to predict the strain rates for the balloon (Figure 9A). A comparison with the measured strain rates (Figure 7C) reveals that the model is surprisingly accurate despite its simplicity. In particular, the model captures the switch in strain rate anisotropy as well as the magnitude of the maximal strain rates.

The constitutive model can be modified easily to account for tip growth. Since the wall material deforms irreversibly, we must now relate stresses with strain rates rather than strains. Equations (5) then
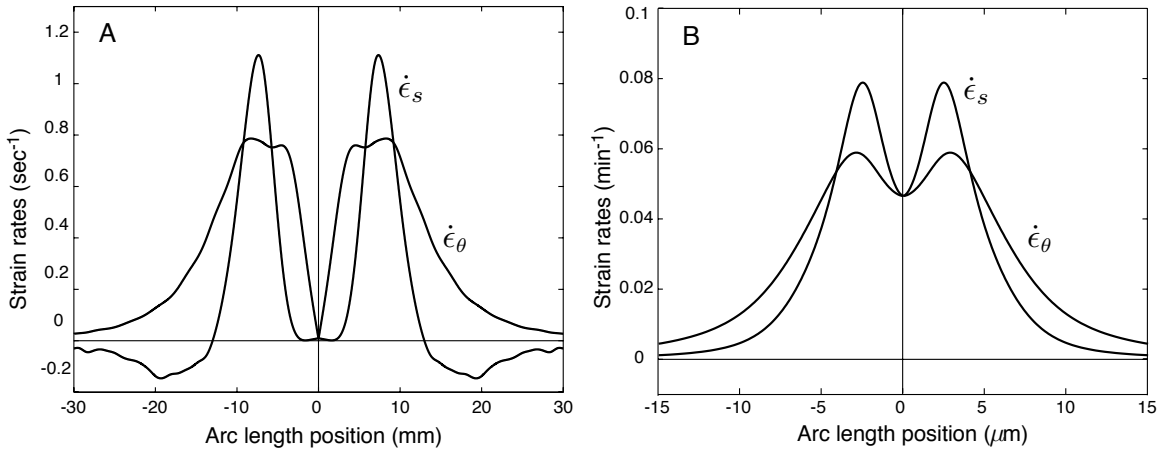
**Figure 9.** Predicted strain rates for the rubber balloon (A) and root hair (B) using the isotropic model.

become

$$\dot{\epsilon}_s = \frac{dv}{ds} = \alpha \left( \frac{P}{2h\kappa_\theta} - v \frac{P}{2h\kappa_\theta} \left( 2 - \frac{\kappa_s}{\kappa_\theta} \right) \right), \tag{8}$$

$$\dot{\epsilon}_\theta = \frac{1}{r} \frac{dr}{ds} v = \alpha \left( \frac{P}{2h\kappa_\theta} \left( 2 - \frac{\kappa_s}{\kappa_\theta} \right) - v \frac{P}{2h\kappa_\theta} \right). \tag{9}$$

Here $\alpha$ can be interpreted as an extensibility (inverse viscosity). Dividing the first equation by the second and rearranging gives

$$\frac{1}{v} \frac{dv}{ds} = \frac{1}{r} \frac{dr}{ds} \frac{(1 - 2v)\kappa_\theta + v\kappa_s}{(2 - v)\kappa_\theta - \kappa_s} \tag{10}$$

This differential equation for $v$, with boundary condition $v(0) = 0$, has for solution

$$v(s) = \gamma r(s) \exp\left( \int_0^s G(s) \, ds \right), \qquad G(s) = \frac{1}{r} \frac{dr}{ds} \frac{(1 + v)(\kappa_s - \kappa_\theta)}{(2 - v)\kappa_\theta - \kappa_s}, \tag{11}$$

where $\gamma$ is a constant set by the geometry and elongation rate of the tip. We used this equation and $v = 0.3$ to predict the strain rates for tip growth (Figure 9B). Again, the predicted strain rates are very similar to the observed strain rates (Figure 4). It is surprising that a model that does not include material anisotropy can nonetheless account for strain rate anisotropy so accurately. We must conclude that the observed anisotropy in the strain rates results from a similar anisotropy in the membrane stresses.

Finally, we computed the material property $\alpha(s)$ predicted by the model (Figure 10). This parameter represents a compliance for the rubber material or an extensibility for the cell wall. Given the simplicity of the model, it is unlikely that $\alpha$ represents a true material property. We interpret it more generally as the responsiveness of the system to the internal pressure. The parameter $\alpha$ maps out the polar zone that serves as a source of material ($d\alpha/ds > 0$) and the flanks of the tip, where the material is actively stretched and therefore stiffening ($d\alpha/ds < 0$). The similarity between the balloon analog and tip-growing cells is again quite remarkable.
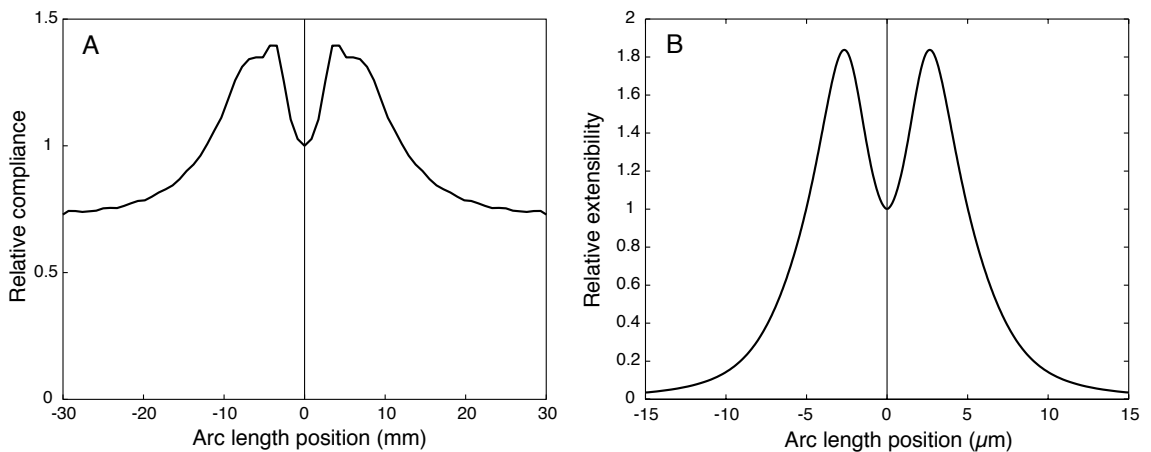
**Figure 10.** Predicted compliance for the rubber balloon (A) and extensibility for the root hair (B). Compliance and extensibility were normalized with respect to the value at the pole.

## 5. Conclusions

The similar pattern of surface expansion in tip-growing cells and rubber balloons calls for an explanation. The first explanation to consider is whether there is only a limited set of strain patterns that can maintain tip growth; that is, shared kinematics constraints could explain the similarities. As indicated above, and illustrated in Figure 4, very different strain patterns are compatible with a given tip geometry and elongation velocity. Therefore, kinematics alone is not a sufficient explanation for the similar expansion pattern. Tip-growing cells and rubber balloons must share features at a more fundamental level. We propose that the presence of a source of soft material in the polar region is one likely common feature. In the balloon, the rapid stiffening of the material as it is stretched can explain the characteristic geometry of the growing front. Strain stiffening has also been proposed for tip growth morphogenesis [Green and King 1966]. The stiff cellulose microfibrils that make up a large volume fraction of plant cell walls are synthesized in the polar region presumably in a relaxed state. As the tip surface deforms, the fibrils would be progressively put under tension thus increasing rapidly the stiffness of the wall. Clearly, plant cell expansion is *not* an elastic phenomenon but the presence of long cellulose microfibrils in the wall means that the cell possesses some memory of past deformation.

The main conclusion of this work is that many aspects of cell morphogenesis, despite their complex biological underpinning, may still be explained via relatively simple physical principles. For the case of tip growth morphogenesis, we have shown that a simple constitutive model with isotropic material properties is sufficient to explain the observed strain rate anisotropy. We postulate that strain stiffening of the wall's molecular fabric accounts for the meridional variation of the wall extensibility.

## References

[Castle 1958] E. S. Castle, "The topography of tip growth in a plant cell", *J. Gen. Physiol.* **41**:5 (1958), 913–926.

[Chater and Hutchinson 1984] E. Chater and J. W. Hutchinson, "On the propagation of bulges and buckles", *J. Appl. Mech.* (*Trans. ASME*) **51** (1984), 269–277.

[Chen 1973] J. C. W. Chen, "The kinetics of tip growth in the *Nitella* rhizoid", *Plant Cell Physiol.* **14**:4 (1973), 631–640.

[Dumais et al. 2004] J. Dumais, S. R. Long, and S. L. Shaw, "The mechanics of surface expansion anisotropy in *Medicago truncatula* root hairs", *Plant Physiol.* **136** (2004), 3266–3275.

[Dumais et al. 2006] J. Dumais, S. L. Shaw, C. R. Steele, S. R. Long, and P. M. Ray, "An anisotropic-viscoplastic model of plant cell morphogenesis by tip growth", *Int. J. Dev. Biol.* **50** (2006), 209–222.

[Flügge 1973] W. Flügge, *Stresses in shells*, 2nd ed., Springer, Berlin, 1973.

[Green and King 1966] P. B. Green and A. King, "A mechanism for the origin of specifically oriented textures in development with special reference to *Nitella* wall texture", *Aust. J. Biol. Sci.* **19** (1966), 421–437.

[Harold 1990] F. M. Harold, "To shape a cell: an inquiry into the causes of morphogenesis of microorganisms", *Microbiol. Rev.* **54**:4 (1990), 381–431.

[Hejnowicz et al. 1977] Z. Hejnowicz, B. Heinemann, and A. Sievers, "Tip growth: Patterns of growth rate and stress in the *Chara* rhizoid", *Zeitung der Pflanzenphysiologie* **81** (1977), 409–424.

[Kyriakides and Chang 1991] S. Kyriakides and Y. C. Chang, "The initiation and propagation of a localized instability in an inflated elastic tube", *Int. J. Solids Struct.* **27**:9 (1991), 1085–1111.

[Ogden 1972] R. W. Ogden, "Large deformation isotropic elasticity: on the correlation of theory and experiment for incompressible rubberlike solids", *P. Roy. Soc. Lond. A Mat.* **326**:1567 (1972), 565–584.

[Reinhardt 1892] M. O. Reinhardt, "Das Wachsthum der Pilzhyphen", *Jahrbücher für wissenschaftliche Botanik* **23** (1892), 479–566.

[Shaw et al. 2000] S. L. Shaw, J. Dumais, and S. R. Long, "Cell surface expansion in polarly growing root hairs of *Medicago truncatula*", *Plant Physiol.* **124** (2000), 959–970.

[Steele 2000] C. R. Steele, "Shell stability related to pattern formation in plants", *J. Appl. Mech.*(*Trans. ASME*) **67**:2 (2000), 237–247.

[Thompson 1942] D. W. Thompson, *On growth and form*, 2nd ed., Cambridge Univ. Press, Cambridge, 1942. Reprinted by Dover, New York, 1992.

[Treloar et al. 1976] L. R. G. Treloar, H. G. Hopkins, R. S. Rivlin, and J. M. Ball, "The mechanics of rubber elasticity", *P. Roy. Soc. Lond. A Mat.* **351**:1666 (1976), 301–330.

[Vincent 1990] J. F. V. Vincent, *Structural biomaterials*, Princeton University Press, Princeton, 1990.

[Vogel 2003] S. Vogel, *Comparative biomechanics: life's physical world*, Princeton University Press, Princeton, 2003.

ROBERTO BERNAL: rbernal@oeb.harvard.edu
*Department of Organismic and Evolutionary Biology, Harvard University, 16 Divinity Ave., Cambridge, MA 02138, United States*

ENRIQUE R. ROJAS: errojas@fas.harvard.edu
*Department of Physics, Harvard University, 17 Oxford St., Cambridge, MA 02138, United States*

JACQUES DUMAIS: jdumais@oeb.harvard.edu
*Department of Organismic and Evolutionary Biology, Harvard University, 16 Divinity Ave., Cambridge, MA 02138, United States*

# CONTINUUM-BASED COMPUTATIONAL MODELS FOR CELL AND NUCLEAR MECHANICS

ASHKAN VAZIRI, ARVIND GOPINATH AND VIKRAM S. DESHPANDE

Deciphering the relationship between cellular processes and the structure of living cells is a key step toward understanding and predicting cell functions with direct implications for understanding human health and disease. The active nature of these cellular processes, which span several decades of spatial and temporal scales, pose significant challenges to unraveling this complex structure-function paradigm. Complementing novel experimental techniques with robust computational approaches capable of modeling mechanical response at varying scales provides new avenues to resolving this paradigm. We provide an overview of continuum-based computational approaches used in studying and interpreting responses of individual cells and nuclei, we outline techniques used for measuring the mechanical characteristics of living cells, and we discuss some of the key insights provided by these approaches.

## 1. Introduction

Recent developments in the field of nanotechnology have delivered sophisticated experimental tools for measuring forces as small as piconewtons and deformations as small as microns or less. These developments have enabled accurate measurement and monitoring of the mechanical properties and function of living cells, subcellular structures and even single biomolecules [Bao and Suresh 2003; Van Vliet et al. 2003; Huang et al. 2004; Yu et al. 2006]. Specifically, work done over the last two decades at cellular scales has led to the formulation of experimental frameworks for measuring the mechanical response of cells in vitro. Quantifying the mechanical characteristics of subcellular structures based on these frameworks, a key step towards understanding the structure-function paradigm of living cells, is a fundamental challenge facing the biomechanics, biomaterials, and biophysics communities. This challenge arises due to the intricate nature of the cell, a delicate assembly of numerous subcellular components with vastly different geometrical, material, and biochemical characteristics; see, for example, Figure 1. These subcellular components evolve during various cell functions at temporal scales that extend over several decades. Figure 2a illustrates the mapping between length scales and time scales via selected functionality of living cells and various organelles. While most short-term cellular responses are locally mediated, long-term events generally involve alterations in gene expression [Kamm and Kaazempur-Mofrad 2004]. Even what is seemingly a single cell function can be governed by completely different mechanisms at different time scales, as illustrated recently for cell adhesion to substrates [Cuvelier et al. 2007].
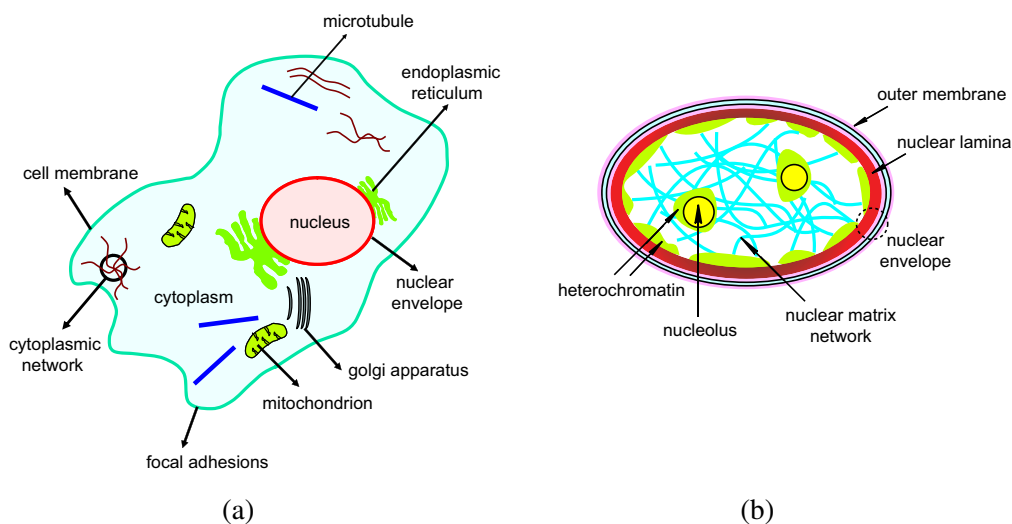
**Figure 1.** Schematics of (a) an eukaryotic cell and (b) its nucleus.

In the process of modeling the deformation and mechanics of cells, subcellular structures, and constituent biomolecules, the method of choice depends on the length and time scales of interest. Computational approaches can be classified into two main categories: continuum-based approaches and micro/nanostructural approaches [Vaziri and Gopinath 2007]. Integrated models that combine aspects of these two approaches and are useful in predicting the response of living cells at physiologically relevant temporal and spatial scales are still in their infancy.

This article reviews continuum-based computational models in cell and nuclear mechanics. Our aim is to provide an overview of the current state of the art in such approaches and comment on their applicability in interpreting as well as predicting the deformation and mechanics of living cells and organelles. The advantages and deficiencies of the more commonly used models are emphasized. Insights provided by these approaches, specifically in understanding the connection to human health and disease, are discussed. This article complements a recent review by Vaziri and Gopinath [2007] that focuses on the insights provided by micro/nanostructural and continuum computational approaches in cell and biomolecular mechanics. We will highlight computational studies on both whole cell response as well as studies on isolated nuclei, which have been the subject of much research in recent years.

Continuum methods are applicable when the length scales of interest are much larger than microscopically relevant structural features that act as small perturbations to global variations in properties. To illustrate this, consider, for instance, steady AFM indentation of the individual cells at micron level in which the length scale characterizing the deformation field is typically larger than the spatial dimensions of individual cellular elements. Consequently, a continuum description is appropriate when studying the nature of this deformation field. The same picture holds for studies on cell migration and flow and deformation of red blood cells in capillaries. Even though microscopic features affect the cell shape and behavior at small length scales, the overall response of a blood cell to flow or stress as it moves in and out of capillaries is amenable to a macroscopic analysis. On the other hand, when studying the
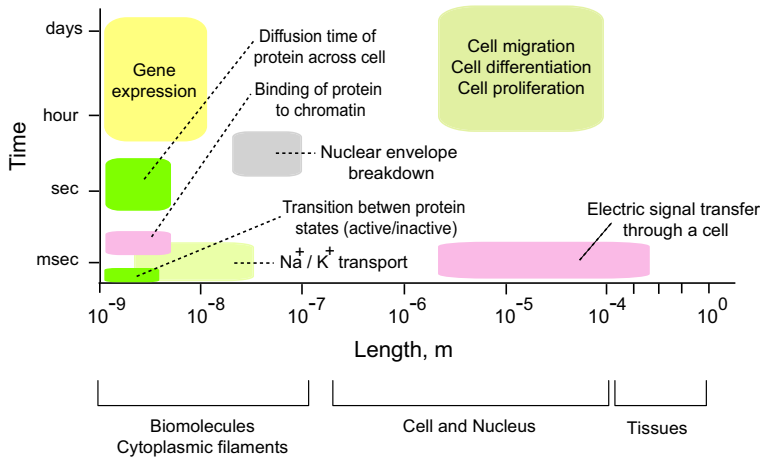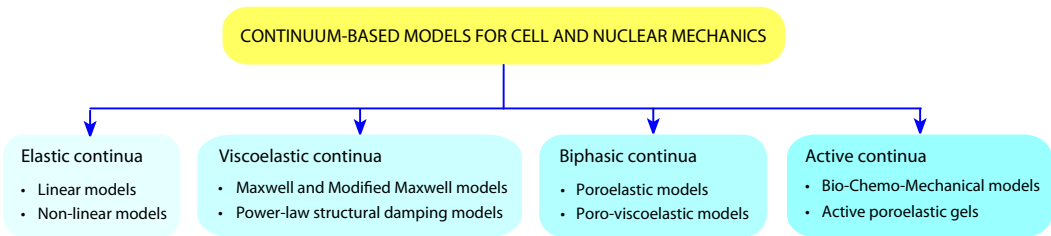
**Figure 2.** (a) Mapping between length and time scales in cell and biomolecular mechanics via selected functions. Shown is the vast difference in length scales from biomolecules to tissues as well as concomitant time scales for some processes and function at biomolecular/cellular level. (b) Computational toolbox encapsulating current continuum-based computational approaches for living cells and isolated nuclei.

mechanics of individual biomolecules, as in protein folding and fracture, the length scales of interest, for example, spatial scales characterizing the deformation field, are comparable to the molecular size. In this case, continuum-based models are inappropriate, and atomistic and molecular simulations should be employed. Most of the atomistic and molecular simulations in biomechanics are based on Monte Carlo or Molecular Dynamics algorithms reviewed in a recent article by Vaziri and Gopinath [2007].

Most continuum-based computational models in cell mechanics, and more generally in biomechanics, are based on the finite element method. Significant reasons for its popularity are its efficiency, ease of computation, and speed of implementation. In addition, material as well as geometric nonlinearities can be easily incorporated. Numerical schemes associated with this method are also well-developed and have been implemented in various commercially available software. It must be pointed out, however, that alternative computational approaches have also been used when appropriate for particular applications. For instance, the boundary element method, which is also based on fundamental solutions of the governing partial differential equations and requires discretization on only the domain boundary, has the

potential to reduce significantly the computation time specifically for complex geometries. Such alternate computational approaches offer advantages in certain specific problems in cell mechanics [Discher et al. 1998; Haider and Guilak 2002; Cristini and Kassab 2005], but the finite element method seems to be the algorithm of choice in most applications.

The perspectives and overview presented here are necessarily brief and are intended to convey only broad concepts. The readers are encouraged to consult the papers cited in this review for details on the topics addressed here including the list of key references.

## 2. Cell and nuclear mechanics: insight from computational approaches

Advances and development of new techniques in numerical methods over the last decade have provided reliable tools to model materials with complex characteristics. A key challenge in developing appropriate computational models in cell mechanics is the selection of material laws capable of representing the multiaxial and highly nonlinear stress-strain relationships as well as their alteration due to mechanical, biochemical, or electrical stimuli with high fidelity. Figure 2b displays material laws ranging from simple linear elasticity to more complex biphasic models and active continua that have been employed in various computational models in cell and nuclear mechanics. Most of these models, with the exception of those in the *active continua* category, assume that the cell and its subcellular structures respond passively to the stimulus. The material constants associated with these models are usually obtained by measuring the overall response of a cell (or isolated nuclei) using experimental techniques such as micropipette aspiration and atomic force microscopy (AFM) indentation experiments, and comparing these experimental results with computational predictions. Table 1 shows the available computational models developed for common experimental techniques that are typically performed on whole cells. A companion list of the computational methodologies developed for modeling the deformation and response of an isolated nucleus is provided in Table 2.

An illustration of the method by which material constants are obtained is shown in Figure 3 for microplate compression tests on a round endothelial cell and an isolated nucleus extracted from cell cultures by chemical treatment [Caille et al. 2002]. The corresponding computational simulations at each stage of deformation are also shown and performed by assuming that the cell and the nucleus are separate homogeneous isotropic materials and calculating the response to compression. Interpreting the experimental measurements using simulations shows that the nucleus of an endothelial cell is about 10 times stiffer than its cytoplasm (Figures 3c and 3d).

Characteristic properties of cells have been experimentally obtained by considering responses over a limited range of excitation frequencies. Recent studies have indicated that the cytoskeleton response is governed by a ubiquitous mechanical behavior called power law rheology over a broad frequency spectrum [Fabry et al. 2001; 2003; Alcaraz et al. 2003; Lenormand et al. 2004; Desprat et al. 2005; Bursac et al. 2005; Hoffman et al. 2006]. Investigations of the rheology of actin gels containing a single actin crosslinking protein indicate that that the power law behavior might be an intrinsic feature of actin systems with only one or two binding proteins present [Gardel et al. 2006]. The emergence of this relatively simple power law behavior for complex structures such as the cytoskeleton and actin gels has motivated both theoretical and computational efforts to interpret these experimental observations. In Section 2.1, we provide an overview of such a computational model developed by Vaziri et al. [2007].
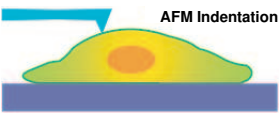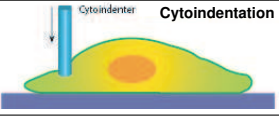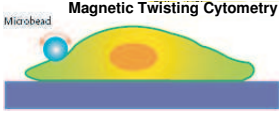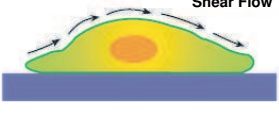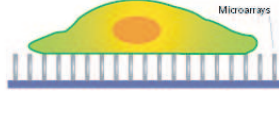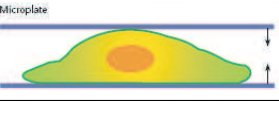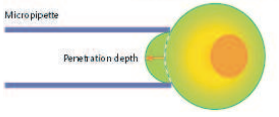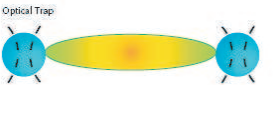
| Experiment | Material model | References |
|---|---|---|
|  **AFM Indentation** | Linear elastic | [Costa and Yin 1999] [Ohashi et al. 2002; Ng et al. 2007] |
| | Nonlinear elastic | [Costa and Yin 1999] |
| | Nonlinear elastic | [McElfresh et al. 2002] |
|  **Cytoindentation** | Linear elastic | [Shin and Athanasiou 1999] |
| | Poroelastic | [Shin and Athanasiou 1999] |
|  **Magnetic Twisting Cytometry** | Linear elastic | [Mijailovich et al. 2002] [Charras and Horton 2002] |
| | Nonlinear elastic | [Ohayon et al. 2004] |
| | Maxwell viscoelastic | [Karcher et al. 2003] |
| | Power law structural damping | [Vaziri and Gopinath 2007] |
|  **Shear Flow** | Linear elastic | [Charras and Horton 2002] [§] [Cao et al. 2007; Ferko et al. 2007] [§] |
| | Nonlinear elastic | [Jadhav et al. 2005] |
|  **Cell Contraction (Microarrays/substrate)** | Linear elastic | [Nelson et al. 2005] |
| | Modified Maxwell viscoelastic | [McGarry et al. 2005] [§] |
| | Biochemomechanical | [Deshpande et al. 2006; 2007a; 2007b] [Wei et al. 2007] |
|  **Microplate Compression** | Nonlinear elastic | [Caille et al. 2002] |
|  **Micropipette Aspiration** | Linear elastic | [Haider and Guilak 2002] |
| | Nonlinear elastic | [Zhou et al. 2005; Baaijens et al. 2005] |
| | Maxwell viscoelastic | [Baaijens et al. 2005; Trickey et al. 2006] |
| | Modified Maxwell viscoelastic | [Haider and Guilak 2000] |
| | Poroelastic | [Baaijens et al. 2005] |
| | Poroviscoelastic | [Baaijens et al. 2005; Trickey et al. 2006] |
|  **Optical Tweezers** | Nonlinear elastic | [Dao et al. 2003; Mills et al. 2004] [Suresh et al. 2005] |
| | Modified Maxwell viscoelastic | [Mills et al. 2004] |

**Table 1.** Computational models for whole cell deformation in common experimental techniques in cell mechanics. Most of the current models are based on the finite element method. Alternate approaches include studies based on boundary integral methods as in [Haider and Guilak 2000; 2002]. ([§]The model of the cell in [Caille et al. 2002; McGarry et al. 2005; Ferko et al. 2007] includes a separate component representing the nucleus.)
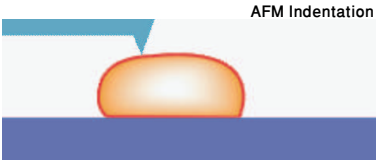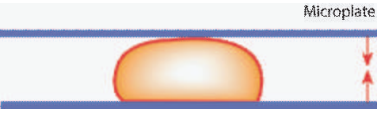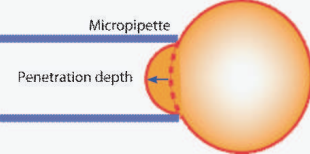
| Experiment | Material model | Reference |
|---|---|---|
|  AFM Indentation | Maxwell viscoelastic | [Vaziri et al. 2006] |
|  Microplate Compression | Nonlinear elastic | [Caille et al. 2002] |
| | Maxwell viscoelastic | [Vaziri et al. 2006] |
|  Micropipette Aspiration | Modified Maxwell viscoelastic | [Vaziri et al. 2007] |

**Table 2.** Available computational models for the deformation of an isolated nucleus.

Most material models presented in Figure 2b assume a passive nature for the response of cells and subcellular components to mechanical stimuli. In a living cell, however, the cytoskeletal structure undergoes active changes in response to mechanical stimuli and chemical signals [Wang et al. 2000; Bao and Suresh 2003; Kaunas et al. 2005; Chien 2006; Kumar et al. 2006]. Recent efforts by several groups have led to the development of biochemomechanical models for cells in an effort to capture this active mechanical response [Deshpande et al. 2006; 2007a; Deshpande et al. 2007b; Pathak et al. 2007; Yang and Saif 2007]. These new approaches can help immensely in understanding the interplay of mechanics and biochemistry during the active cellular response and cell function as explained in Section 2.2. Recent theoretical efforts have also focused on developing a general framework for describing the largescale dynamics of an active-filament network as is found in the cytoskeleton [Kruse and Julicher 2006]. Using pairwise interactions between active filaments and general conservation principles, effective medium expressions are developed for the stresses generated in such a filamentous structure. This description may be linked to continuum theories of active polar gels and provides a useful starting point for the numerical modeling of such systems.

An additional property of the deformation response to mechanical forces, present even in the passive limit, is the inherent inhomogeneity in cell structure. Computational models that treat the cell and its nucleus as a homogeneous isotropic material have proven successful in modeling certain aspects of the cell behavior. This approximate treatment however fails to predict some major physiological observations such as transmission of the forces applied via focal adhesions to long distances in the cytoskeleton [Maniotis et al. 1997; Hu et al. 2003]. Developing computational biomechanical models which account for inhomogeneity of the cell and nuclear structure constitutes another important step towards understanding the behavior and functions of living cells and their relationship with mechanics. In Section 2.3, we
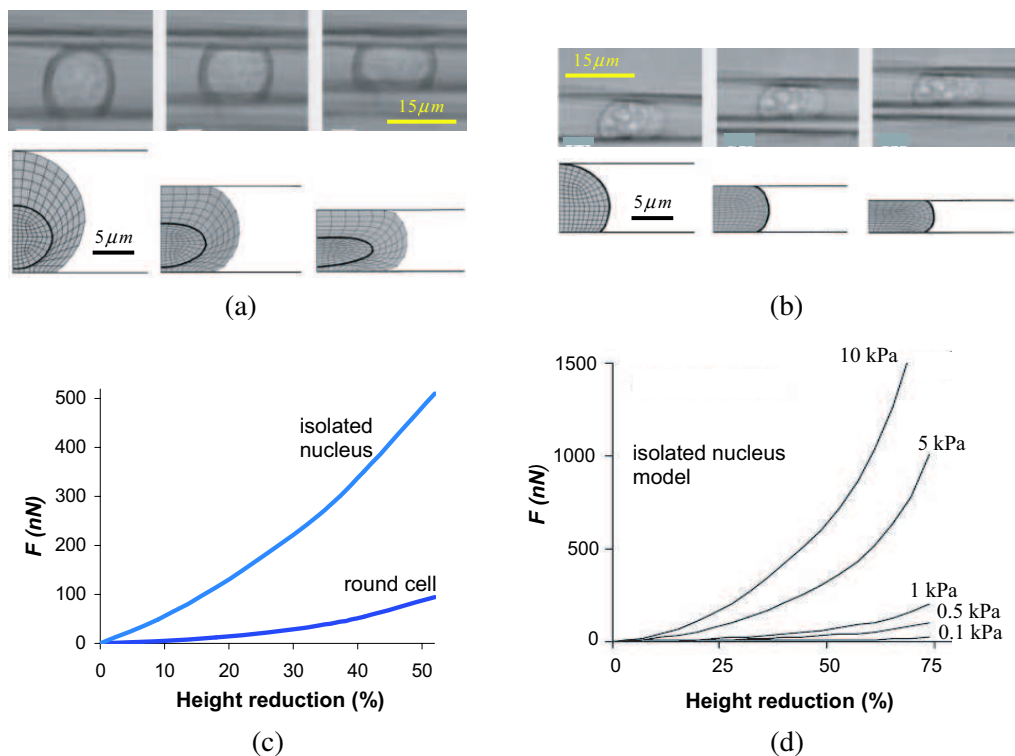
**Figure 3.** (a) Top panels show digitized images of a round endothelial cell compressed by flexible microplates. Left: cell at rest; middle: 30% compression of cell height; right: 50% compression of cell height. Bottom panels show the finite element model of the compression test at same stages; the nucleus within the cell is distinguished by the bold line and was modeled as a separate element with different mechanical properties. (b) Same as (a) for an isolated nucleus extracted from endothelial cell by chemical treatment. (c) Average force-height reduction of round endothelial cells ($n = 17$) and isolated nuclei ($n = 21$) measured experimentally. (d) Numerical simulation of force-height reduction of an isolated nucleus for various values of the nuclear elastic modulus. Fitting to experimental data indicates that the nucleus is about 10 times stiffer than the cytoplasm in endothelial cells. In numerical simulations both cytoplasm and nucleus are modeled as homogeneous, incompressible, isotropic, hyperelastic materials. (Figures and data are modified from [Caille et al. 2002]. Copyright © 2002, Elsevier Science. Reprinted with permission.)

discuss the details of a new computational model proposed for studying the deformation and mechanics of isolated nuclei.

Complete characterization of the biomechanics of the cell and its subcellular structures cannot be achieved by a single experiment and requires combinations of several experimental techniques and detailed computational simulations. For example, Baaijens et al. [2005] show that computational models using a viscoelastic material model or a biphasic viscoelastic material model are capable of accurately

simulating the experimentally measured creep response of chondrocytes aspired into a micropipette. A similar discussion is provided by Vaziri and Kaazempur-Mofrad [2007] for the deformation of an isolated nucleus in micropipette aspiration experiment.

**2.1.** *Power law rheology based models.* The power law rheology exhibited by emulsions, pastes, foams, and colloids is an intrinsic feature of materials composed of numerous discrete elements that experience weak interactions with inherently disordered and metastable microstructural geometry. Surprisingly, recent experiments have indicated that under certain conditions this rheological law is also valid for the cytoplasm as described in Section 2. A computational model of the magnetic twisting cytometry experiment has been recently developed in which the material law associated with this power law rheology is incorporated. In Figure 4, results from the computational simulations based on this coarse-grained model are compared with experimental observations on HASM cells from Fabry et al. [2003]. Interpreting these observations using the computational model yields an accurate assessment of the material constants associated with the power law rheology. It should be noted that this computational model is phenomenological, and fails to provide any physical insight into the mechanisms responsible for the emergence of this peculiar behavior of the cytoskeleton.

When the simple law described above proves inadequate, the framework may be extended to incorporate more complex frequency dependent viscoelastic behavior. As an example, the intranuclear region of Swiss 3T3 fibroblasts is shown to have a frequency dependent viscoelastic characteristic that in general does not follow the power law rheology over a wider range of excitation frequencies [Tseng et al. 2004]. Another example is the additional Newtonian viscosity term suggested by Fabry et al. [2003] to account for the complex behavior of the cytoplasm at relatively high frequencies of excitation. Alternatively, mechanical prestress in the active cytoskeleton, generated in part due to the activity of molecular motors, also significantly influences its rheology and behavior of the cell [Stamenovic et al. 2002; Wang and Suo 2005]. This prestress regulates the transition between solid-like and fluid-like behavior in cells, and is indicated in the power law rheology as a decrease in the power law exponent with increasing prestress [Stamenovic et al. 2002; Stamenovic et al. 2004]. The developed computational model is capable of incorporating the mechanical prestressing and can provide insight into the role of this mechanical factor.

**2.2.** *Active continua computational models.* The cytoskeleton is a protein scaffold found inside most eukaryotic cells. It consists of three major classes of filaments: actin, microtubules, and intermediate filaments along with accessory proteins that crosslink the filaments to the plasma membrane. In mammalian cells with compliant cell membranes (no cell walls), *the dynamic structure and active nature of the cytoskeleton largely determine the morphology of a cell and its mechanics* [Howard 2001]. Here we briefly review the main features of computational approaches that attempt to account for the active nature of the cytoskeleton and its effect on the mechano-sensitivity of cell adhesion.

**2.2.1.** *Cytoskeletal contractility.* The tension generated inside the contractile microfilaments in the cytoskeleton plays a critical role in control of cell morphology and function [Ingber 1997]. Contractile bundles composed of actin and myosin proteins form and dissociate in response to external mechanical or chemical stimuli. Typically, these contractile bundles are found in three forms: (i) circumferential belts (in epithelial cells), (ii) stress fibers along the ventral surfaces, and (iii) contractile rings at the equator that form during cytokinesis. A suitable model must incorporate the following basic biomechanochemical
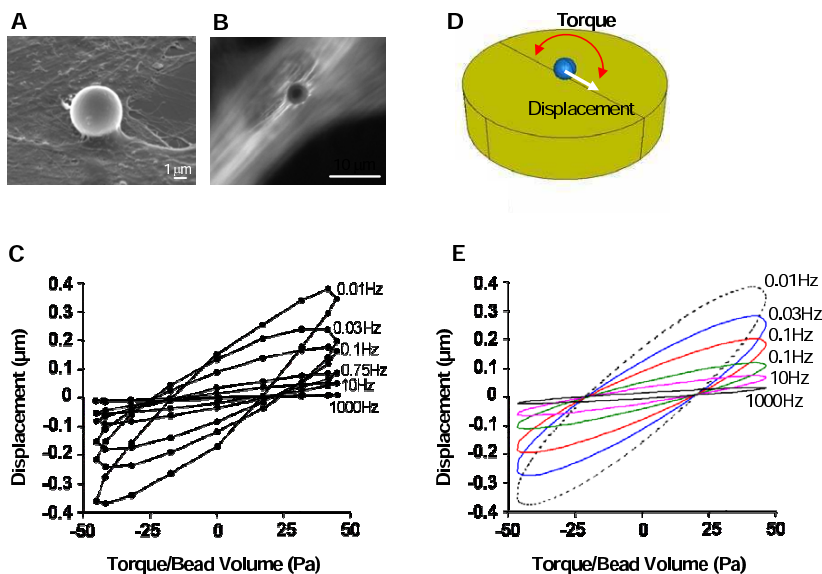
**Figure 4.** Power law rheology of the cytoskeleton. (a) Scanning electron microscopy of a magnetic microbead bound to surface of a human airway smooth muscle cell (HASMc) in magnetic twisting cytometry (MTC) experiments (see Table 1 for the schematic of the experiment). (b) Ferromagnetic beads bind to the actin cytoskeleton (stained with fluorescently labeled phalloidin) of HASM cells via cell adhesion molecules (integrins). (c) Microbead displacement versus specific torque (mechanical torque/bead volume) of the cytoskeleton at different frequencies of excitation of the microbead in MTCE for HASMc. (d) Geometry of computational model of MTC experiment. (e) Numerical results for response in MTC experiment at various excitation frequencies of rigid microbead. Both average radius of ferromagnetic microbeads in experiment and of rigid spheres in numerical simulations is 2.25 $\mu m$. See Table 1 for alternative computational models developed for understanding cytoskeletal response in MTC experiment. (A, B and C are taken from [Fabry et al. 2003]. Copyright © 2003, American Physical Society. Reprinted with permission. D and E are modified from [Vaziri et al. 2007]. Copyright © 2007, Elsevier Science (D and E). Reprinted with permission.)

processes [Deshpande et al. 2006; 2007a]: (i) the formation of stress fibers induced by an activation signal, (ii) polymerization of actin filaments and the phosphorylation of myosin II that promotes the assembly of myosin II into bipolar filaments triggered by the activation signals. These myosin filaments enter into the $\alpha$ actinin bound actin filament bundles, resulting in the formation of stress fibers, and (iii) tension generated in stress fibers by crossbridge cycling between the actin and myosin filaments. When the tension is allowed to relax, the actin filaments are no longer held in place by the bipolar myosin filaments and the stress fibers disassemble.

Motivated by these processes, Deshpande et al. [2006; 2007a] have proposed a model for the contractility of the cytoskeleton that supersedes oversimplified models in which the cytoskeleton is regarded as a passive mechanical structure augmented only by a thermal contraction induced by a deus ex machina
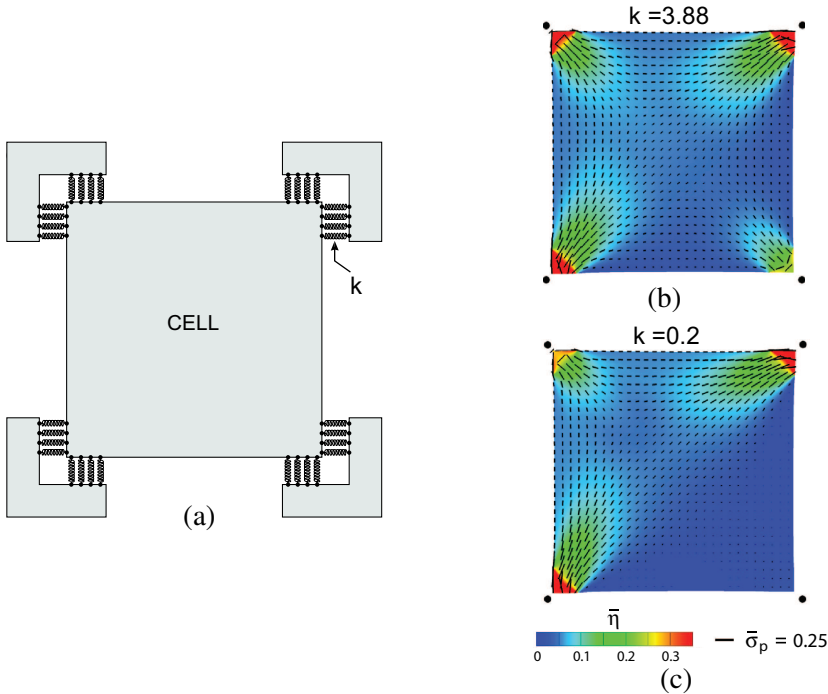
**Figure 5.** (a) Schematic of the cell on 4 *posts*. Effect of reducing stiffness of top right support (denoted by $k$) is illustrated in (b) and (c), wherein contours of stress fiber concentration $\bar{\eta}$ are plotted along with line segments indicating direction of maximum principal stress. (The figures are modified from [Deshpande et al. 2006]. Copyright © 2006, National Academy of Sciences, USA.)

[Satcher and Dewey 1996; Nelson et al. 2005; Mohrdieck et al. 2005]. In the model, the mechanical response of the stress fibers comprises three coupled phenomena: (i) an activation signal that triggers the formation of stress fibers; (ii) a fiber formation rate dependent on the activation signal, coupled with a dissociation rate dependent on the tension; and (iii) a contraction rate (contractility) for the stress fiber that depends on the tension through the crossbridge dynamics. Simple phenomenological relations are used to model these coupled phenomena for a single stress fiber, and thereafter the relations are generalized to two and three dimensional cytoskeletal networks by homogenizing over all possible fiber orientations at each point in the cell. Simulation of the cell response is carried out by solving the equations of force equilibrium as the cytoskeleton forms to create a contractile network consistent with the tensegrity hypothesis [Ingber 1997]. By considering a square cell fixed between four support posts (see Figure 5a), the model predicts reconstruction of the cytoskeleton in a manner dependent on the external mechanical constraints. Predictions of the distributions of the stress fibers (Figures 5b and 5c) are in line with experimental findings that the stress fiber network is dependent on the spring constants of the supports with a higher concentration of fibers located adjacent to stiffer supports. Moreover, the model captures the many key features observed in experimental studies including: (a) the decrease of the forces generated by the cell with increasing substrate compliance, and (b) the influence of cell shape and boundary conditions on the development of structural anisotropy. It is apparent from these studies that
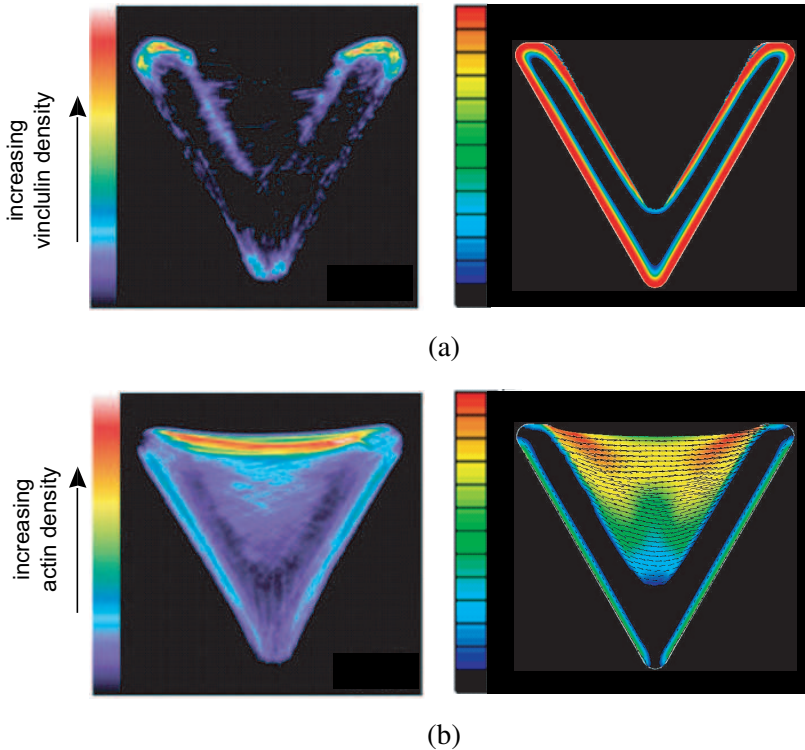
(a)



(b)

**Figure 6.** Observations (left) and predictions (right) of the vinculin (a) and actin (b) distributions in infinity telomerase-immortalized retinal pigment epithelial human cells placed on a V-shaped fibronectin pattern. The edge of the V is $46\,\mu$m. Observations are reproduced from [Théry et al. 2006], while the predictions are from [Pathak et al. 2007].

mechanics and the conditions of force equilibrium play a central role in the processes of cytoskeleton formation and contractility.

**2.2.2.** *Cooperativity between cell adhesion and cytoskeletal contractility.* Cell adhesion to the extracellular matrix (ECM) is critical to functions ranging from migration and proliferation to apoptosis. The primary subcellular structures that mediate the regulatory effects of ECM adhesion are the focal adhesions (FAs). These macromolecular complexes not only mediate cell anchorage by physically coupling integrins to the contractile actin cytoskeleton but also orient and concentrate numerous signaling proteins at sites of integrin binding and clustering. Because FAs function not only as the mechanical linkages but also as biochemical signaling hubs for many regulatory pathways, regulation of their assembly and disassembly is a critical mechanism for controlling cell function. FA formation is itself controlled mechanically with the tractions generated at the contact sites increasing the rate of assembly of the focal adhesions [Balaban et al. 2001]. Moreover, FA formation can be increased or decreased by respectively raising or lowering cytoskeletal tension using pharmacological agents such as BDM that curtail actomyosin activity [Chen et al. 2003]. The global shape of cells and their internal cytoskeletal structure also play an important role in constraining the magnitude, distribution, and direction of such tractions across the cell surface [Parker et al. 2002; Chen et al. 2003], and thereby control local FA assembly

and organization. The fact that many proteins perform both structural and signaling functions [Burridge and Chrzanowska-Wodnicka 1996] hinders the ability of traditional approaches to parse the mechanisms that regulate FA dynamics: for example, knocking out an adhesion protein by genetic manipulation may also eliminate an essential structural component. Consequently, a combination of critical experiments guided by computational models that include the salient features of the mechanics and biochemistry is needed in order to understand the observed behaviors. Théry et al. [2006] have investigated the effect of cell shape on the distribution of actin and vinculin at fixed cell area, as exemplified in the upper part of Figure 6, which visualizes a human endothelial cell placed on a V-shaped fibronectin ligand pattern. Such studies indicate a complex interaction among cell shape, ligand patch geometry, and cytoskeletal response with strong stress fibers forming along the nonadhesive edges and high focal adhesion densities (as exemplified by the vinculin density) along the edges of the ligand patch. Deshpande et al. [2007b] have developed a model that accounts for the cooperativity between cytoskeletal contractility and focal adhesion formation and growth. This thermodynamically-motivated computational approach has three essential features: (i) coexistence of the low and high affinity integrins in thermodynamic equilibrium, (ii) mobility of the low affinity integrins within the plasma membrane, and (iii) mechanical equilibrium of the contractile forces generated by the stress fibers; these forces affect the free energies of the integrins giving rise to a coupled thermomechanical response. An initial prediction based on the model of Deshpande et al. [2007b] is included in bottom part of Figure 6. The predictions show distributions of the normalized focal adhesion densities (as parameterized by the high affinity integrin concentration) and contours of the stress fiber density. Also included with the predicted stress fiber concentration distributions are line segments showing the effective direction of the stress fiber. The predictions are remarkably consistent with trends observed in the experiment: (i) since the cell exerts maximum tractions on the ECM near the edges of the ligand patch, high focal adhesion densities are predicted in this region, and (ii) aligned stress fibers form along the longest nonadhesive edge; see [Pathak et al. 2007] for details and interpretation of the analysis.

### 2.3. *Computational model of an isolated nucleus.*

The nucleus of eukaryotic cells, containing most of the cell's genetic material, is an assembly of numerous subnuclear components which work cooperatively to maintain the structural integrity and proper function of the nucleus, as shown in Figure 1b. The nuclear envelope is one of the major elements of the nucleus, and is comprised of inner and outer membranes, nuclear lamina, nuclear pore complexes, and the perinuclear region. The nuclear lamina is a polymeric network composed of coiled-coil proteins called lamins [Aebi et al. 1986; McKeon et al. 1986] and is known to play a critical role in maintaining the structural integrity of the nucleus. It is built of two types of proteins, lamin A/C and lamin B, and comprises the majority of the protein composition within the nucleus. Within the nucleoplasm are one or several nucleoli, responsible for the production of ribosomes that are then transported to the rough endoplasmic reticulum where protein synthesis occurs.

Continuum-based computations have also been used in studying the mechanical properties of isolated and intact nuclei. These studies can further our understanding of the mechanisms by which mechanical stresses are transmitted to biochemical reactions and ultimately alterations in gene expression and cell function. A continuum-based computational model of an isolated nucleus that incorporates the nuclear inner and outer membranes, nuclear lamina and nucleoplasm as separate components with different material characteristics has been developed recently by Vaziri et al. [2006]; see Figures 7a and 7b. Using
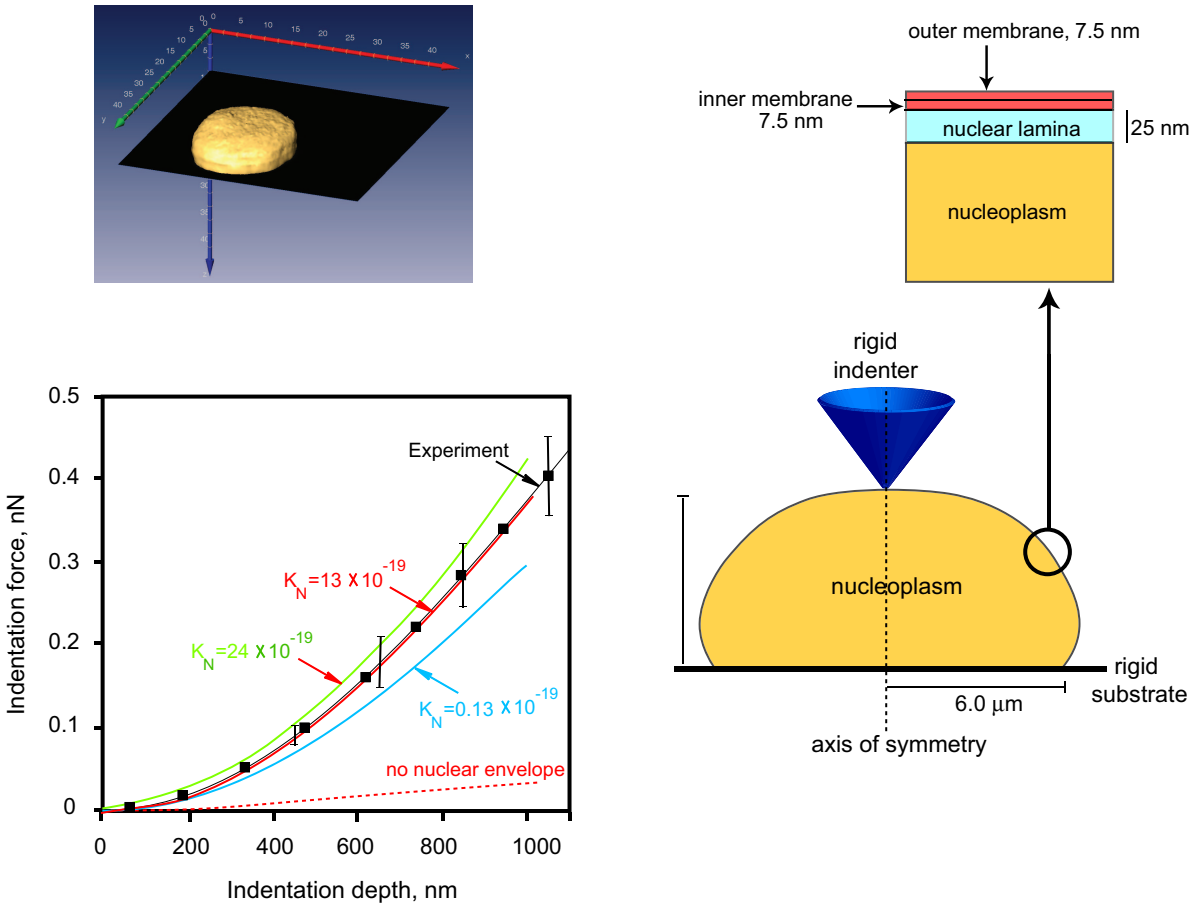
**Figure 7.** From top left clockwise: (a) three-dimensional images of isolated nuclei on a glass substrate (black in the image) via two-photon microscopy; (b) schematic of the computational model of an isolated nucleus in AFM indentation, consisting of nucleoplasm, inner and outer membranes, and nuclear lamina, with different material characteristics; and (c) dependence of force-indentation response of isolated nucleus on bending stiffness of nuclear lamina, $K_N$. Nuclear elements are modeled as linear elastic materials with following characteristics: Poisson ratio $\upsilon = 0.485$, nucleoplasm Young's modulus $= 25$ Pa, and bending stiffness of nuclear membrane $1.8 \times 10^{-19}$ Nm. Experimental result gives the average response of 23 nuclei from mouse embryo fibroblasts. Error bars give the standard error at specific values of indentation. (The figures are modified from [Vaziri et al. 2006]. Copyright © 2006, Materials Research Society.)

this approach, the contributions of individual nuclear elements to the overall response of an isolated nucleus can be calculated; this is shown for the case of AFM indentation in Figure 7c and discussed for the case of micropipette aspiration in [Vaziri and Kaazempur-Mofrad 2007]. Numerical simulation of the indentation of an isolated nucleus reveals that under localized indentation, the nuclear envelope transfers the force applied locally to a large portion of the nucleoplasm as the nuclear envelope undergoes
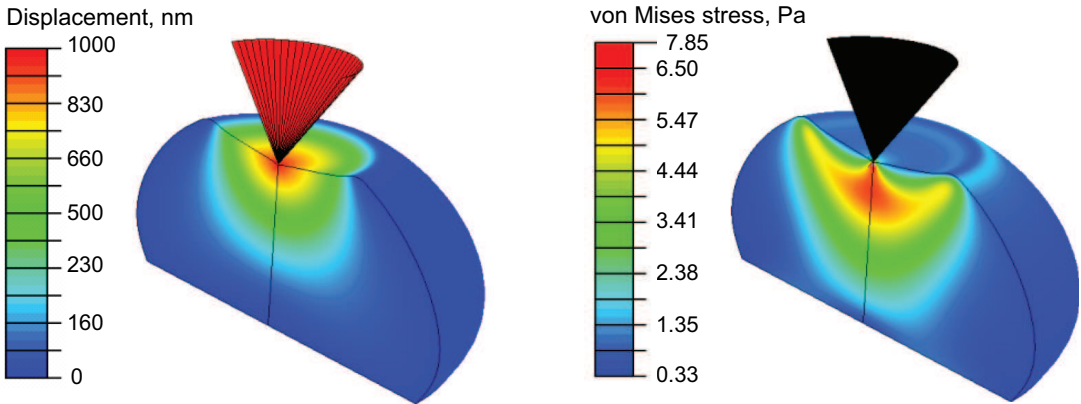
**Figure 8.** Distribution of nodal displacement and von Mises stress in the nucleoplasm at probe displacement of 1000 nm from the isolated nucleus model in Figure 7 for nuclear lamina bending stiffness of $K_{NL} = 13.6 \times 10^{-19}$ N.m. In computational simulations sharp probe has a half angle of $35°$, consistent with experiments. (The figures are modified from [Vaziri et al. 2006]. Copyright © 2006, Materials Research Society.)

bending and stretching; see Figure 8. The overall response of the nucleus to point indentation is predicted to be a complex function of the material characteristics of its individual elements. Similar theoretical and computational studies, carried out to study the mechanisms of response of living cells under point indentation, indicated the necessity of accounting for the mechanics of biomembrane in the response [McElfresh et al. 2002; Baesu et al. 2004]. These results clearly reveal the inadequacy of the commonly employed Hertzian contact model used in interpreting results from indentation experiments; see [Vaziri et al. 2006] for further discussion.

Recent experimental observations indicate that the nuclei of endothelial cells undergo permanent structural remodeling when shear stress is applied to the cell. This cytoskeleton-mediated deformation of the nucleus is hypothesized as a possible pathway through which shear stresses are transduced to gene regulating signals [Deguchi et al. 2005]. The underlying mechanisms of this process and the details of the mechanical connection between the cell membrane and its nucleus are still far from being understood, but it is known that subcellular structures play an important role in this process. Computational models capable of distinguishing and incorporating the structural role of different subcellular structures and nuclear elements can help immensely in understanding these mechanisms. Moreover, these computational models are robust tools that can help in resolving the apparent discrepancy of the current data on mechanical properties of cells and subcellular structures [Vaziri et al. 2006; Vaziri and Kaazempur-Mofrad 2007].

## 3. Implications in understanding the state of human health and disease

Initiation and progression of many diseases are associated with alterations in the structure and function of subcellular and subnuclear components which in turn modify the function of the cell [Cornhill and Roach 1974; Sinzinger et al. 1980; Athanasiou and Shieh 2002; Trickey et al. 2000; Suresh et al. 2005; Wilson 2005; Mattout et al. 2006; Suresh 2006; Cao et al. 2007]. For instance, mutations in gene

encoding lamin A and its binding partners have been associated with a variety of human diseases including Emery–Dreifuss muscular dystrophy, dilated cardiomyopathy, and Hutchinson–Gilford progeria syndrome [Lammerding et al. 2004; Wilson 2005; Mattout et al. 2006]. As another example, various cancer cells have altered nuclear structure and irregularity in shapes and spatial organization of subnuclear structures [Zink et al. 2004].

The exact role of mechanics in the progression of these diseases is still unclear and computational models can play a key role in unraveling this relationship. An example of such studies is the recent work on biomechanics of red blood cells infected by the parasite *P. falciparum* [Dao et al. 2003; Mills et al. 2004; Suresh et al. 2005]. This work, which combines novel experimental techniques and continuum-based computational models, has significantly enhanced our fundamental knowledge of the underlying mechanisms of disease progression at the cellular level and provides a template for extensions of this approach to other applications. Moreover, insights obtained from detailed computations that distinguish between the effects of subcellular structures can serve to guide further experiments for characterizing the mechanics of altered subcellular structures. For example, modeling the response of an isolated nucleus in micropipette aspiration and indentation experiments by employing the computational model of an isolated nucleus discussed in Section 2.3 indicated that the overall response of the nucleus in micropipette aspiration is highly sensitive to the stiffness of the nuclear envelope [Vaziri and Kaazempur-Mofrad 2007], while in the indentation experiment the overall response is more sensitive to the nucleoplasm material properties. This indicates that micropipette aspiration is robust enough to examine the influence of various alterations in the nuclear lamina such as mutations in gene encoding lamin A and its bindings.

Another example in which mechanics might play a role involves the development of atherosclerotic lesions. These lesions develop in the vicinity of branch points in the arterial vasculature, while straight unbranched regions tend to be protected [Cornhill and Roach 1974; Sinzinger et al. 1980]. Namely, the tubular geometry of the straight segments ensures that the cyclical rise and fall of blood pressure results in uniaxial stretch. Conversely, the complex geometry of artery branches promotes stretching of the blood vessel along more than one axis. These differences result in endothelial cells having nonaligned stress fibers at branch points, while those in the straight segments are aligned in the longitudinal direction [Davies 1995]. Isotropic or random cytoskeletal arrangements give rise to continued activation of Jun Kinase (JNK) [Kaunas et al. 2006] that triggers a cascade of events that eventually induce structural changes at the branch points including the increased deposition of ECM collagen and elastin. These changes lead to the atherosclerotic narrowing and hardening of coronary arteries at vessel branches. Wei et al. [2007] have shown that the biochemomechanical model discussed in Section 2.2 accurately predicts the cytoskeletal structures that evolve in endothelial cells due to a range of hemodynamic and mechanical stimuli. It is suggested that this model could be employed to investigate the onset of atherosclerotic lesions.

Applications are also seen in the field of viral studies and especially in studies on infectivity and its connection to structure. An excellent example is described in recent work by Kol et al. [2007]. This work deals with the internal morphological reorganization that HIV and some other retrovirus particles undergo following budding from a cell. During this maturation process, the immature HIV particle changes from being roughly spherically symmetric with a thick protein shell to a state characterized by a thin protein shell and a conical core. Nanoindentation experiments via AFM indicate that immature HIV particles are 14 times stiffer than mature particles and this difference is primarily due to the HIV

envelope cytoplasmic tail domain. Finite element simulations used to elucidate the effects of deleting the cytoplasmic tail domain offer strong evidence that changes in mechanical properties, in this case the softening of the viral particle, might be a crucial step in the infection process. Such studies offer immense scope in using computations to anticipate effects of changes in structure arising due to mutations or as a course of natural morphological change during the progression of disease. Once an understanding of this mechanical change is gained, attempts to block or change this process may be used as a means to circumvent this intrinsic morphological switch and retard infection.

Finally, the function of the cell and its nucleus is ultimately governed by the characteristics of appropriate biomolecules and their alteration by biochemical reactions. Therefore, understanding the mechanisms of the diseases associated with altered cell and nuclear function entails resolving the behavior at much smaller spatial scales. Computational approaches based on micro/nano approaches can help immensely in this regard. Examples are recent works on the effects of hyperglycemia on collagenolysis [Stultz and Edelman 2003; Stultz 2006].

## 4. Multiscale approaches: from cell mechanics to collective tissue behavior

The complexity of individual subcellular structures and the range of spatial and temporal scales associated with their interactions make it almost impossible to analyze these structures using a single theoretical or computational model. Complete characterization of the cell entails interconnecting several models each valid in a certain range of scales and forming a composite picture that reflects accurately mechanical and biochemical behavior at all scales. A major challenge in this process is to appropriately couple macroscale dynamics and cell kinetics to microscale deformation and mechanics; for example, protein mechanics, filament dynamics and active motor behavior. A significant complication arises due to the strongly nonlinear interactions as macroscopic mechanical effects provoke signal pathways that may give rise to both local effects and nonlocal cell-wide changes. In a living cell, the continuous consumption of fuel results in a constant state of nonequilibrium at all length scales. Even when considering properties and responses at macroscopic length scales it is imperative to take into account the cumulative effects of active microscopic processes.

Multiscale approaches developed in the field of cell mechanics can be classified into two categories. In the first category, micro/nano simulations at subcellular, microscopic, or single molecule level are used as input into macroscopic computations. A specific example would be using network simulations of erythrocytes to obtain effective elastic constants of the membrane and the underlying filamentous structure [Li et al. 2005; Dao et al. 2006]. This is discussed further in [Vaziri and Gopinath 2007]. In this article, we provide a selected set of examples regarding a second complementary multiscale approach wherein results from continuum computations at the single cell or subcellular level are used as input to study behavior and response at the tissue or organ level, as illustrated in Figure 9.

Multiscale computational approaches have been employed in understanding various aspects of the circulatory system from the mechanical properties of the heart muscle due to aging and plaque to cardio-vascular circulatory mechanics [Shim et al. 2006]. We expect that continuum based computations will be of use in coupling the dynamical characteristics of the circulation to the activation-induced mechanical contraction of the heart muscle. Another physiologically relevant example is studying the process by which air exchange occurs in the lung [Fredberg and Kamm 2006]. Evidence strongly suggests that
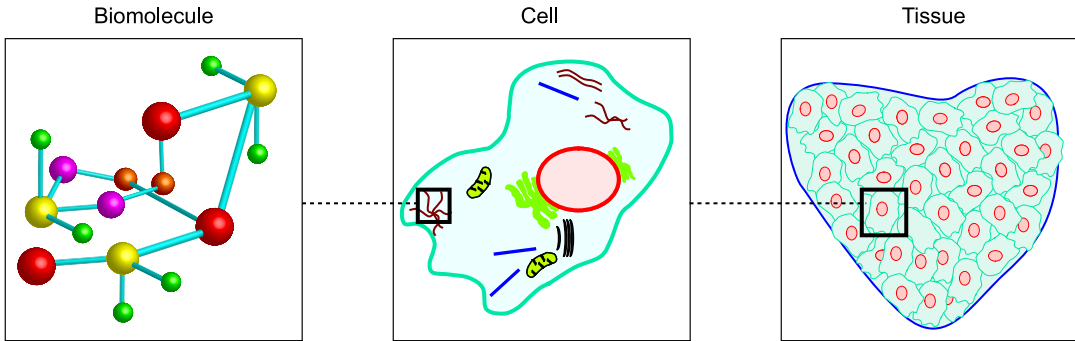
**Figure 9.** Multiscale approaches in biomechanics connecting microscopic characteristics of biomolecules to collective tissue behavior.

multiscale phenomena span the length scales that exist and govern integrative lung behavior. Another example of application of multiscale approaches is in understanding the underlying mechanisms of morphogenesis, a complex developmental phenomenon that involves cell growth, division, rearrangement, as well as flow in a well defined manner [Chaturvedi et al. 2005].

In tissue engineering, alginate hydrogels are increasingly used as biomaterials to develop new cell delivery methods as well as support matrices [Augst et al. 2006; Yeh et al. 2006; Khademhosseini et al. 2006; Rivest et al. 2007]. It is expected that these biomaterials play the role of an artificial extracellular matrix that will surround living tissues and provide space for repair, regeneration, or growth of new tissue as well as offering mechanical support and traction. These composite biomaterials are living analogues of inanimate composites that have been so intensively studied until now in materials science and engineering. The possibility of drug delivery from such materials is also of great interest [Khademhosseini and Langer 2006]. In all these applications, an accurate mechanical characterization is essential, and multiscale continuum methods offer a good route to such understanding. Numerical investigations of such composite biomaterials employ solutions to basic unit cell geometries coupled with homogenization techniques to probe macroscopic variations. Typically, the cells are treated as deformable inclusions responding to the macroscopically imposed external stress. The stress results in a macroscopic deformation field, the magnitude of which has to be self-consistently determined by solving a microscopic unit cell problem. Computations can then be used to quantify effects of scaffold stiffness and inclusion interactions on cell deformation. Such multiscale studies are critical in evaluating the effects of mechanical processing on the viability of tissue constructs. For example, Guilak and Mow [2000] used a biphasic FEM model to study biomechanical interactions between the chondrocyte and the extracellular matrix. In a similar vein, Breuls et al. [2002] introduced a large strain model to study the local deformation fields in tissue composites when subject to macroscopic external loads. A similar approach is possible in the analysis of naturally occurring composites like bone tissues [Kowalczyk 2006].

## 5. Concluding remarks

Mechanical characteristics of biological materials, although far more complex than the behavior of man-made materials, are still amenable to studies based on computational frameworks. Indeed, the steps toward a coherent synthesis of computations and experiments, with an aim to understanding cell and

subcellular mechanical characteristics, have already begun in earnest. Considering recent advances in computational efficiency and algorithms and the inclination of many researchers to enter interdisciplinary fields, fast progress in the utilization of computational approaches in the field of cell and nuclear mechanics is anticipated. This in turn can lead to the emergence of new applications in various fields such as tissue engineering, medicine, and nanobiotechnology, as well as novel avenues for treatment and diagnosis of diseases.

## References

[Aebi et al. 1986] U. Aebi, J. Cohn, L. Buhle, and L. Gerace, "The nuclear lamina is a meshwork of intermediate-type filaments", *Nature* **323**:6088 (1986), 560–564.

[Alcaraz et al. 2003] J. Alcaraz, L. Buscemi, M. Grabulosa, X. Trepat, B. Fabry, R. Farré, and D. Navajas, "Microrheology of human lung epithelial cells measured by atomic force microscopy", *Biophys. J.* **84** (2003), 2071–2079.

[Athanasiou and Shieh 2002] K. A. Athanasiou and A. C. Shieh, "Biomechanics of single chondrocytes and osteoarthritis", *Crit. Rev. Biomed. Eng.* **30**:4-6 (2002), 307–343.

[Augst et al. 2006] A. D. Augst, H. J. Kong, and D. J. Mooney, "Alginate hydrogels as biomaterials", *Macromol. Biosci.* **6**:8 (2006), 623–633.

[Baaijens et al. 2005] F. P. Baaijens, W. R. Trickey, T. A. Laursen, and F. Guilak, "Large deformation finite element analysis of micropipette aspiration to determine the mechanical properties of the chondrocyte", *Ann. Biomed. Eng.* **33**:4 (2005), 494–501.

[Baesu et al. 2004] E. Baesu, R. E. Rudd, J. Belak, and M. McElfresh, "Continuum modeling of cell membranes", *Int. J. Non-Linear Mech.* **39**:3 (2004), 369–377.

[Balaban et al. 2001] N. Q. Balaban, U. S. Schwarz, D. Riveline, P. Goichberg, G. Tzur, I. Sabanay, D. Mahalu, S. Safran, A. Bershadsky, L. Addadi, and B. Geiger, "Force and focal adhesion assembly: a close relationship studied using elastic micropatterned substrates", *Nat. Cell Biol.* **3** (2001), 466–472.

[Bao and Suresh 2003] G. Bao and S. Suresh, "Cell and molecular mechanics of biological materials", *Nat. Mater.* **2**:11 (2003), 715–725.

[Breuls et al. 2002] R. G. M. Breuls, B. G. Sengers, C. W. J. Oomens, C. V. C. Bouten, and F. P. T. Baaijens, "Predicting local cell deformations in engineered tissue constructs: a multilevel finite element approach", *J. Biomech. Eng.* (*Trans. ASME*) **124**:2 (2002), 198–207.

[Burridge and Chrzanowska-Wodnicka 1996] K. Burridge and M. Chrzanowska-Wodnicka, "Focal adhesions, contractility and signaling", *Annu. Rev. Cell Dev. Bi.* **12** (1996), 463–519.

[Bursac et al. 2005] P. Bursac, G. Lenormand, B. Fabry, M. Oliver, D. Weitz, V. Viasnoff, J. Butler, and J. J. Fredberg, "Cytoskeletal remodeling and slow dynamics in the living cells", *Nat. Mater.* **4**:7 (2005), 557–561.

[Caille et al. 2002] N. Caille, O. Thoumine, Y. Tardy, and J. J. Meister, "Contribution of the nucleus to the mechanical properties of endothelial cells", *J. Biomech.* **35**:2 (2002), 177–187.

[Cao et al. 2007] Y. Cao, R. Bly, W. Moore, Z. Gao, A. M. Cuitino, and W. Soboyejo, "On the measurement of human osteosarcoma cell elastic modulus using shear assay experiments", *J. Mater. Sci. Mater. M.* **18**:1 (2007), 103–109.

[Charras and Horton 2002] G. T. Charras and M. A. Horton, "Determination of cellular strains by combined atomic force microscopy and finite element modeling", *Biophys. J.* **83**:2 (2002), 858–879.

[Chaturvedi et al. 2005] R. Chaturvedi, C. Huang, B. Kazmierczak, T. Schneider, J. A. Izaguirre, T. Glimm, H. G. Hentschel, J. A. Glazier, S. A. Newman, and M. S. Alber, "On multiscale approaches to three dimensional modeling of morphogenesis", *J. Roy. Soc. Interface* **2**:3 (2005), 237–253.

[Chen et al. 2003] C. S. Chen, J. L. Alonso, E. Ostuni, G. M. Whitesides, and D. E. Ingber, "Cell shape provides global control of focal adhesion assembly", *Biochem. Biophys. Res. Comm.* **307**:2 (2003), 355–361.

[Chien 2006] S. Chien, "Molecular basis of rheological modulation of endothelial functions: importance of stress direction", *Biorheology* **43**:2 (2006), 95–116.

[Cornhill and Roach 1974] J. F. Cornhill and M. R. Roach, "Quantitative method for the evaluation of athero-sclerotic lesions", *Atherosclerosis* **20**:1 (1974), 131–136.

[Costa and Yin 1999] K. D. Costa and F. C. Yin, "Analysis of indentation: implications for measuring mechanical properties with atmic force microscopy", *J. Biomech. Eng.* (*Trans. ASME*) **121** (1999), 462–471.

[Cristini and Kassab 2005] V. Cristini and G. S. Kassab, "Computer modeling of red blood cell rheology in the microcirculation: a brief overview", *Ann. Biomed. Eng.* **33**:12 (2005), 1724–1727.

[Cuvelier et al. 2007] D. Cuvelier, M. Théry, Y. S. Chu, S. Dufour, J. P. Thiéry, M. Bornens, P. Nassoy, and L. Mahadevan, "The universal dynamics of cell spreading", *Curr. Biol.* **17** (2007), 694–699.

[Dao et al. 2003] M. Dao, C. T. Lim, and S. Suresh, "Mechanics of the human red blood cell deformed by optical tweezers", *J. Mech. Phys. Solids* **51**:11-12 (2003), 2259–2280.

[Dao et al. 2006] M. Dao, J. Li, and S. Suresh, "Molecularly based analysis of deformation of spectrin network and human erythrocyte", *Mater. Sci. Eng. C Biomim.* **26**:8 (2006), 1232–1244.

[Davies 1995] P. F. Davies, "Flow-mediated endothelial mechanotransduction", *Physiol. Rev.* **75** (1995), 519–560.

[Deguchi et al. 2005] S. Deguchi, K. Maeda, T. Ohashi, and M. Sato, "Flow-induced hardening of endothelial nucleus as an intracellular stress-bearing organelle", *J. Biomech.* **38**:9 (2005), 1751–1759.

[Deshpande et al. 2006] V. S. Deshpande, R. M. McMeeking, and A. G. Evans, "A bio-chemo-mechanical model for cell contractility", *P. Natl. Acad. Sci. USA* **103**:38 (2006), 14015–14020.

[Deshpande et al. 2007a] V. S. Deshpande, R. M. McMeeking, and A. G. Evans, "A model for the contractility of the cytoskeleton including the effects of stress-fibre formation and dissociation", 2007.

[Deshpande et al. 2007b] V. S. Deshpande, M. Mrksich, R. M. McMeeking, and G. A. Evans, "A bio-mechanical model for coupling cell contractility with focal adhesion formation", 2007. submitted (2007b).

[Desprat et al. 2005] N. Desprat, A. Richert, J. Simeon, and A. Asnacios, "Creep function of a single living cell", *Biophys. J.* **88** (2005), 2224–2233.

[Discher et al. 1998] D. E. Discher, D. H. Boal, and S. K. Boey, "Simulations of the erythrocyte cytoskeleton at large deformation, II: micropipette aspiration", *Biophys. J.* **75**:3 (1998), 1584–1597.

[Fabry et al. 2001] B. Fabry, G. N. Maksym, J. P. Butler, M. Glogauer, D. Navajas, and J. J. Fredberg, "Scaling the microrheology of living cells", *Phys. Rev. Lett.* **87**:14 (2001), 148102.

[Fabry et al. 2003] B. Fabry, G. N. Maksym, J. P. Butler, M. Glogauer, D. Navajas, N. A. Taback, E. J. Millet, and J. J. Fredberg, "Time scale and other invariants of integrative mechanical behavior in living cell", *Phys. Rev. E* **68**:4 (2003), 041914.

[Ferko et al. 2007] M. C. Ferko, A. Bhatnagar, M. B. Garcia, and P. J. Butler, "Finite-element stress analysis of a multicomponent model of sheared and focally-adhered endothelial cells", 2007.

[Fredberg and Kamm 2006] J. J. Fredberg and R. D. Kamm, "Stress transmission in the lung: pathways from organ to molecule", *Annu. Rev. Physiol.* **68** (2006), 507–541.

[Gardel et al. 2006] M. L. Gardel, F. Nakamura, J. H. Hartwig, J. C. Crocker, T. P. Stossel, and D. A. Weitz, "Prestressed F-actin networks cross-linked by hinged filamins replicate mechanical properties of cells", *P. Natl. Acad. Sci. USA* **103**:6 (2006), 1762–1767.

[Guilak and Mow 2000] F. Guilak and V. C. Mow, "The mechanical environment of the chondrocyte: a biphasic finite element model of cell-matrix interactions in articular cartilage", *J. Biomech.* **33**:12 (2000), 1663–1673.

[Haider and Guilak 2000] M. A. Haider and F. Guilak, "An axisymmetric boundary integral model for incompressible linear viscoelasticity: application to the micropipette aspiration contact problem", *J. Biomech. Eng.* (*Trans. ASME*) **122**:3 (2000), 236–244.

[Haider and Guilak 2002] M. A. Haider and F. Guilak, "An axisymmetric boundary integral model for assessing elastic cell properties in the micropipette aspiration contact problem", *J. Biomech. Eng.* (*Trans. ASME*) **124**:5 (2002), 586–595.

[Hoffman et al. 2006] B. D. Hoffman, G. Massiera, K. M. Van Citters, and J. C. Crocker, "The consensus mechanics of cultured mammalian cells", *P. Natl. Acad. Sci. USA* **103**:27 (2006), 10259–10264.

[Howard 2001] J. Howard, *Mechanics of motor proteins and the cytoskeleton*, Sinauer Associates, Sunderland, MA, 2001.

[Hu et al. 2003] S. Hu, J. Chen, B. Fabry, Y. Numaguchi, A. Gouldstone, D. E. Ingber, J. J. Fredberg, J. P. Butler, and N. Wang, "Intracellular stress tomography reveals stress focusing and structural anisotropy in cytoskeleton of living cells", *Am. J. Physiol. Cell Ph.* **285** (2003), C1082–C1090.

[Huang et al. 2004] H. Huang, R. D. Kamm, and R. T. Lee, "Cell mechanics and mechanotransduction: pathways, probes, and physiology", *Am. J. Physiol. Cell Ph.* **287** (2004), C1–C11.

[Ingber 1997] D. E. Ingber, "Tensegrity: the architectural basis of cellular mechanotransduction", *Annu. Rev. Physiol.* **59** (1997), 575–599.

[Jadhav et al. 2005] S. Jadhav, C. D. Eggleton, and K. Konstantopoulos, "A 3-D computational model predicts that cell deformation affects selectin-mediated leukocyte rolling", *Biophys. J.* **88** (2005), 96–104.

[Kamm and Kaazempur-Mofrad 2004] R. D. Kamm and M. R. Kaazempur-Mofrad, "On the molecular basis for mechanotransduction", *Mech. Chem. Biosyst.* **1**:3 (2004), 201–210.

[Karcher et al. 2003] H. Karcher, J. Lammerding, H. Huang, R. T. Lee, R. D. Kamm, and M. R. Kaazempur-Mofrad, "A three-dimensional viscoelastic model for cell deformation with experimental verification", *Biophys. J.* **85** (2003), 3336–3349.

[Kaunas et al. 2005] R. Kaunas, P. Nguyen, S. Usami, and S. Chien, "Cooperative effects of Rho and mechanical stretch on stress fiber organization", *P. Natl. Acad. Sci. USA* **102**:44 (2005), 15895–15900.

[Kaunas et al. 2006] R. Kaunas, S. Usami, , and S. Chien, "Regulation of stretch-induced JNK activation by stress fiber orientation", *Cell. Signal.* **18**:11 (2006), 1924–1931.

[Khademhosseini and Langer 2006] A. Khademhosseini and R. Langer, "Nanobiotechnolgy for tissue engineering and drug delivery", *Chem. Eng. Prog.* **102** (2006), 38–42.

[Khademhosseini et al. 2006] A. Khademhosseini, R. Langer, J. Borenstein, and J. Vacanti, "Microscale technologies for tissue engineering and biology", *P. Natl. Acad. Sci. USA* **103**:8 (2006), 2480–2487.

[Kol et al. 2007] N. Kol, Y. Shi, M. Tsitov, D. Barlam, R. Z. Shneck, M. S. Kay, and I. Rousso, "Stiffness switch in human immunodeficiency virus", 2007.

[Kowalczyk 2006] P. Kowalczyk, "Orthotropic properties of cancellous bone modelled as parametrized cellular material", *Comput. Meth. Biomech. Biomed. Eng.* **9**:3 (2006), 135–147.

[Kruse and Julicher 2006] K. Kruse and F. Julicher, "Dynamics and mechanics of motor-filament systems", *Eur. Phys. J. E* **20** (2006), 459–465.

[Kumar et al. 2006] S. Kumar, I. Z. Maxwell, A. Heisterkamp, T. R. Polte, T. P. Lele, M. Salanga, E. Mazur, and D. E. Ingber, "Viscoelastic retraction of single living stress fibers and its impact on cell shape, cytoskeletal organization, and extracellular matrix mechanics", *Biophys. J.* **90** (2006), 3762–3773.

[Lammerding et al. 2004] J. Lammerding, P. C. Schulze, T. Takahashi, S. Kozlov, T. Sullivan, R. D. Kamm, C. Stewart, and R. T. Lee, "Lamin A/C deficiency causes defective nuclear mechanics and mechanotransduction", *J. Clin. Invest.* **113** (2004), 370–378.

[Lenormand et al. 2004] G. Lenormand, E. Millet, B. Fabry, J. P. Butler, and J. J. Fredberg, "Linearity and time-scale invariance of the creep function in living cells", *J. Roy. Soc. Interface* **1**:1 (2004), 91–97.

[Li et al. 2005] J. Li, M. Dao, C. T. Lim, and S. Suresh, "Spectrin-level modeling of the cytoskeleton and optical tweezers stretching of the erythrocyte", *Biophys. J.* **88** (2005), 3707–3719.

[Maniotis et al. 1997] A. J. Maniotis, C. S. Chen, and D. E. Ingber, "Demonstration of mechanical connections between integrins, cytoskeletal filaments, and nucleoplasm that stabilize nuclear structure", *P. Natl. Acad. Sci. USA* **94** (1997), 849–854.

[Mattout et al. 2006] A. Mattout, T. Dechat, S. A. Adam, R. D. Goldman, and Y. Gruenbaum, "Nuclear lamins, diseases and aging", *Curr. Opin. Cell Biol.* **18**:3 (2006), 335–341.

[McElfresh et al. 2002] M. McElfresh, E. Baesu, R. Balhorn, J. Belak, M. J. Allen, and R. E. Rudd, "Combining constitutive materials modeling with atomic force microscopy to understand the mechanical properties of living cells", *P. Natl. Acad. Sci. USA* **99**:Suppl. 2 (2002), 6493–6497.

[McGarry et al. 2005] J. P. McGarry, B. P. Murphy, and P. E. McHugh, "Computational mechanics modeling of cell–substrate contact during cyclic substrate deformation", *J. Mech. Phys. Solids* **53**:12 (2005), 2597–2637.

[McKeon et al. 1986] F. D. McKeon, M. W. Kirschner, and D. Caput, "Homologies in both primary and secondary structure between nuclear envelope and intermediate filament proteins", *Nature* **319**:6053 (1986), 463–468.

[Mijailovich et al. 2002] S. M. Mijailovich, M. Kojic, M. Zivkovic, B. Fabry, and J. J. Fredberg, "A finite element model of cell deformation during magnetic bead twisting", *J. Appl. Physiol.* **93** (2002), 1429–1436.

[Mills et al. 2004] J. P. Mills, L. Qie, M. Dao, C. T. Lim, and S. Suresh, "Nonlinear elastic and viscoelastic deformation of the human red blood cell with optical tweezers", *Mech. Chem. Biosyst.* **1**:3 (2004), 169–180.

[Mohrdieck et al. 2005] C. Mohrdieck, A. Wanner, W. Roos, A. Roth, E. Sackmann, J. P. Spatz, and E. Arzt, "A theoretical description of elastic pillar substrates n biophysical experiments", *ChemPhysChem* **6**:8 (2005), 1492–1498.

[Nelson et al. 2005] C. M. Nelson, R. P. Jean, J. L. Tan, W. F. Liu, N. J. Sniadecki, A. A. Spector, and C. S. Chen, "Emergent patterns of growth controlled by multicellular form and mechanics", *P. Natl. Acad. Sci. USA* **102**:33 (2005), 11594–11599.

[Ng et al. 2007] L. Ng, H. H. Hung, A. Sprunt, S. Chubinskaya, C. Ortiz, and A. Grodzinsky, "Nanomechanical properties of individual chondrocytes and their developing growth factor-stimulated pericellular matrix", 2007.

[Ohashi et al. 2002] T. Ohashi, Y. Ishii, Y. Ishikawa, T. Matsumoto, and M. Sato, "Experimental and numerical analyses of local mechanical properties measured by atomic force microscopy for sheared endothelial cells", *Biomed. Mater. Eng.* **12**:3 (2002), 319–327.

[Ohayon et al. 2004] J. Ohayon, P. Tracqui, R. Foldi, S. Fereol, V. M. Laurent, E. Planus, and D. Isabey, "Analysis of nonlinear responses of adherent epithelial cells probed by magnetic bead twisting: a finite element model based on homogenization approach", *J. Biomech. Eng.* (*Trans. ASME*) **126**:6 (2004), 685–698.

[Parker et al. 2002] K. K. Parker, A. L. Brock, C. Brangwynne, R. J. Mannix, N. Wang, E. Ostuni, N. A. Geisse, J. C. Adams, G. M. Whitesides, and D. E. Ingber, "Directional control of lamellipodia extension by constraining cell shape and orienting cell tractional forces", *FASEB J.* **16** (2002), 1195–1204.

[Pathak et al. 2007] A. Pathak, V. S. Deshpande, R. M. McMeeking, and A. G. Evans, "Analysis of stress fiber and focal adhesion distributions of cells on micro-patterned substrates", 2007. submitted (2007).

[Rivest et al. 2007] C. Rivest, D. W. G. Morrison, B. Ni, J. Rubin, V. Yadav, A. Mahdavi, J. M. Karp, and A. Khademhosseini, "Microscale hydrogels for medicine and biology: synthesis, characteristics and applications", 2007, Available at http://pjm.math.berkeley.edu/jomms/2007/2-6/p07.xhtml. J. Mech. Mater. Struct.

[Satcher and Dewey 1996] J. Satcher, R. L. and J. Dewey, C. F., "Theoretical estimates of mechanical properties of the endothelial cell cytoskeleton", *Biophys. J.* **71** (1996), 109–118.

[Shim et al. 2006] E. B. Shim, C. H. Leem, Y. Abe, and A. Noma, "A new multi-scale simulation model of the circulation: from cells to system", *Philos. T. Roy. Soc.* **364**:1843 (2006), 1483–1500.

[Shin and Athanasiou 1999] D. Shin and K. Athanasiou, "Cytoindentation for obtaining cell biomechanical properties", *J. Orthopaed. Res.* **17**:6 (1999), 880–890.

[Sinzinger et al. 1980] H. Sinzinger, K. Silberbauer, and W. Auerswald, "Quantitative investigation of sudanophilic lesions around the aortic ostia of human fetuses, newborn and children", *Blood Vessels* **17**:1 (1980), 44–52.

[Stamenovic et al. 2002] D. Stamenovic, Z. Liang, J. Chen, and N. Wang, "Effect of the cytoskeletal prestress on the mechanical impedance of cultured airway smooth muscle cells", *J. Appl. Physiol.* **92** (2002), 1443–1450.

[Stamenovic et al. 2004] D. Stamenovic, B. Suki, B. Fabry, N. Wang, J. J. Fredberg, and J. E. Buy, "Rheology of airway smooth muscle cells is associated with cytoskeletal contractile stress", *J. Appl. Physiol.* **96** (2004), 1600–1605.

[Stultz 2006] C. M. Stultz, "The folding mechanism of collagen-like model peptides explored through detailed molecular simulations", *Protein Sci.* **15** (2006), 2166–2177.

[Stultz and Edelman 2003] C. M. Stultz and E. R. Edelman, "A structural model that explains the effects of hyperglycemia on collagenolysis", *Biophys. J.* **85** (2003), 2198–2204.

[Suresh 2006] S. Suresh, "Mechanical response of human red blood cells in health and disease: some structure-property-function relationships", *J. Mater. Res.* **21**:8 (2006), 1871–1877.

[Suresh et al. 2005] S. Suresh, J. Spatz, J. P. Mills, A. Micoulet, M. Dao, C. T. Lim, M. Beil, and T. Seufferlein, "Connections between single-cell biomechanics and human disease states: gastrointestinal cancer and malaria", *Acta Biomater.* **1**:1 (2005), 15–30.

[Théry et al. 2006] M. Théry, A. Pépin, E. Dressaire, Y. Chen, and M. Bornens, "Cell distribution of stress fibres in response to the geometry of the adhesive environment", *Cell Motil. Cytoskel.* **63**:6 (2006), 341–355.

[Trickey et al. 2000] W. R. Trickey, G. M. Lee, and F. Guilak, "Viscoelastic properties of chondrocytes from normal and osteoarthritic human cartilage", *J. Orthopaed. Res.* **18**:6 (2000), 891–898.

[Trickey et al. 2006] W. R. Trickey, F. P. Baaijens, T. A. Laursen, L. G. Alexopoulos, and F. Guilak, "Determination of the Poisson's ratio of the cell: recovery properties of chondrocytes after release from complete micropipette aspiration", *J. Biomech.* **39**:1 (2006), 78–87.

[Tseng et al. 2004] Y. Tseng, J. S. Lee, T. P. Kole, I. Jiang, and D. Wirtz, "Micro-organization and visco-elasticity of the interphase nucleus revealed by particle nanotracking", *J. Cell Sci.* **117** (2004), 2159–2167.

[Van Vliet et al. 2003] K. J. Van Vliet, G. Bao, and S. Suresh, "The biomechanics toolbox: experimental approaches for living cells and biomolecules", *Acta Mater.* **51**:19 (2003), 5881–5905.

[Vaziri and Gopinath 2007] A. Vaziri and A. Gopinath, "Computational approaches in cell and biomolecular mechanics", 2007. in press.

[Vaziri and Kaazempur-Mofrad 2007] A. Vaziri and M. R. Kaazempur-Mofrad, "Mechanics and deformation of the nucleus in micropipette aspiration experiment", 2007. J. Biomech.

[Vaziri et al. 2006] A. Vaziri, H. Lee, and M. R. Kaazempur-Mofrad, "Deformation of the cell nucleus under indentation: mechanics and mechanisms", *J. Mater. Res.* **21**:8 (2006), 2126–2135.

[Vaziri et al. 2007] A. Vaziri, Z. Xue, R. D. Kamm, and M. R. Kaazempur-Mofrad, "A computational study on power-law rheology of soft glassy materials with application to cell mechanics", 2007.

[Wang and Suo 2005] N. Wang and Z. Suo, "Long-distance propagation of forces in a cell", *Biochem. Biophys. Res. Comm.* **328**:4 (2005), 1133–1138.

[Wang et al. 2000] J. C. Wang, P. Goldschmidt-Clermont, and F. C. P. Yin, "Contractility affects stress fiber remodeling and reorientation of endothelial cells subjected to cyclic mechanical stretching", *Ann. Biomed. Eng.* **28**:10 (2000), 1165–1171.

[Wei et al. 2007] Z. Wei, V. S. Deshpande, R. M. McMeeking, and A. G. Evans, "Analysis and interpretation of stress fiber organization in cells subjected to cyclic stretch", 2007. Submitted (2007).

[Wilson 2005] K. L. Wilson, "Integrity matters: linking nuclear architecture to lifespan", *P. Natl. Acad. Sci. USA* **102**:52 (2005), 18767–18768.

[Yang and Saif 2007] S. Yang and M. T. A. Saif, "Force response and actin remodeling (agglomeration) in fibroblasts due to lateral indentation", *Acta Biomater.* **3**:1 (2007), 77–87.

[Yeh et al. 2006] J. Yeh, Y. Ling, J. M. Karp, J. Gantz, A. Chandawarkar, G. Eng, J. Blumling, III, R. Langer, and A. Khademhosseini, "Micromolding of shape-controlled, harvestable cell-laden hydrogels", *Biomaterials* **27**:31 (2006), 5391–5398.

[Yu et al. 2006] J. Yu, J. Xiao, X. Ren, K. Lao, and X. S. Xie, "Probing gene expression in live cells, one protein molecule at a time", *Science* **311**:5767 (2006), 1600–1603.

[Zhou et al. 2005] E. H. Zhou, C. T. Lim, and S. T. Quek, "Finite element simulation of the micropipette aspiration of a living cell undergoing large viscoelastic deformation", *Mech. Adv. Mater. Struct.* **12**:6 (2005), 501–512.

[Zink et al. 2004] D. Zink, A. H. Fischer, and J. A. Nickerson, "Nuclear structure in cancer cells", *Nat. Rev. Cancer* **4**:9 (2004), 677–687.

ASHKAN VAZIRI: avaziri@deas.harvard.edu
*Division of Engineering and Applied Sciences, Harvard University, Cambridge, MA 02138, United States*
www.deas.harvard.edu/~avaziri

ARVIND GOPINATH: arvind.gopinath@gmail.com
*Division of Engineering and Applied Sciences, Harvard University, Cambridge, MA 02138, United States*

VIKRAM S. DESHPANDE: vsd@eng.cam.ac.uk
*Engineering Department, Cambridge University, Trumpington Street, Cambridge, CB2 1PZ, United Kingdom*

# QUANTITATIVE EVALUATION OF MECHANICAL PROPERTIES OF CELL MEMBRANES: AN EXACT SOLUTION

EVELINE BAESU, SUJATHA KALYANAM AND MARCELINA MOCANU

Properties of cell membranes are determined by means of a single mechanical experiment involving probing of the membrane with an atomic force microscope. The membrane is modeled as a two-dimensional medium with bending resistance whose energy has three contributions: from the strain energy of the membrane itself, from the internal pressure, and from the point load applied by the microscope. The problem is cast into a variational form and the emerging Euler–Lagrange equations are linearized and solved for the shape of the deformed cell, which can be readily compared with experimental data on the deformed shape to yield the mechanical properties of the membrane.

## 1. Preliminaries

Compliance of cell membranes has been observed to be correlated to the state of health of a cell; or more generally, mechanical properties of cell membranes can be important markers for diseases. For example, a correlation has been established between red blood cell membrane properties and diseases, such as sickle cell anemia, that result in diminished cell function [Evans and Mohandas 1987]. There is also evidence that a change in cell membrane compliance in a malignant tumor indicates the onset of metastasis, and the same change in compliance of neurons can indicate the presence of multiple sclerosis, long before the patient feels any symptoms. Therefore, there is a need to establish envelopes of normalcy for mechanical parameters of various cell membranes. An accurate quantitative understanding of cell membrane mechanical properties is key to attaining this goal.

The typical membrane of a mammalian cell consists of at least one bilayer composed primarily of lipid molecules, with hydrophilic and hydrophobic ends [Brock et al. 1994; Garrett and Grisham 1999; Alberts et al. 2002; Boal 2002]. In general, the membrane is connected to a protein network scaffold called the cytoskeleton. The cellular membrane has been modeled in the literature mostly as a solid thin shell, starting with the pioneering work of Fung [1966]. However, there is experimental evidence to suggest that the bilayers are fluid-like in nature, as the molecules do not oppose resistance when *shuffled* past each other—that is, there is no resistance to shear [Engelhardt and Sackmann 1988; Discher et al. 1994; Strey et al. 1995]. Thus, we propose to model the membrane as a *fluid* thin film endowed with bending resistance. We employ Noll's definition of a fluid: a material with a symmetry group (a set of deformations undetectable by subsequent mechanical experiments) coinciding with the unimodular group (tensors with the determinant equal to plus or minus one). In contrast, solids have as a symmetry group the orthogonal group (that is, with determinant equal to plus one). Further details about this important point may be found in [Steigmann 1999; Truesdell and Noll 1965; Naghdi 2002] and references cited

therein. Also, the molecules of the bilayer offer resistance to being taken apart due to the chemical interaction of the constituent molecules and to the hydrophobicity of the *inner heads*. As a result, we model the membrane as a fluid elastic medium endowed with bending resistance (characterized by an elastic constitutive equation satisfying invariance with respect to the unimodular group). The concept of a fluid elastic crystal medium is also treated in Ericksen's work on liquid crystals [Ericksen 1974] and by Jenkins [1977a; 1977b]. It is well known that cells undergo large deformations during their lifetime: for example, red blood cells with diameters of about 8 microns squeeze through capillaries only 3–4 microns in diameter. In the biomechanics literature, with few exceptions, models of red blood cells, as well as other cells, are primarily linear elastic. Extracting mechanical properties from global experiments on cells, helpful though they are in obtaining a general idea of membrane compliance, are not relevant for obtaining accurate mechanical parameters which would be useful as disease markers [Hochmuth et al. 1973; 1990; Skalak et al. 1973; Evans 1974; Evans and Hochmuth 1977; Evans and Skalak 1980; Evans 1983; 1992; Svetina et al. 1985; Chasis et al. 1988; Lim et al. 2002; Kuzman et al. 2004]. In the context of nonlinear theories, classical mechanical moduli such as Young's modulus and shear modulus have no meaning as they are not unique. New parameters, derived in the context of a robust mathematical treatment, are necessary for modeling this complicated medium.

From the experimental point of view, there is a plethora of chemical methods used to explore the constituency of cellular membranes. However, mechanical experiments (especially nondestructive ones) offer significant advantages for a program of in vitro and in vivo testing since soft, living matter has a higher degree of robustness with respect to mechanical forces compared to chemical manipulations.

In experimental techniques involving (nano)indentation of a solid material, the Hertzian theory [Johnson 1987; Morris et al. 1999] is conventionally employed to extract elastic constants of the material from force versus. penetration depth plots. This technique has been employed in experiments involving cells as well (for example, [Hassan et al. 1998]), but it has proven problematic and has been plagued by irreproducibility, primarily due to the presence of large deformations. Further, the finite size of the cell violates the mathematical assumptions of the Hertzian theory. Hertzian theory (see, for example, [Yin and Costa 1999]), assumes that the system undergoing indentation is a half-space, that is, a seminfinite system bounded by a surface (before indentation). This is, of course, not a good approximation for cells. In fact, the failure of the basic assumptions of the Hertzian theory renders the traditional output of an atomic force microscope (AFM) experiment—the force versus displacement at the tip of the cantilever—insufficient for characterizing the deformed shape of the cell. As such, new experiments are needed to determine the mechanical properties of cellular membranes. Indeed, we can have two very different shapes that coincide only in one point: the point of contact with the cantilever. This problem is not encountered in the testing of metals or generally hard materials that do not undergo large deformations and are nearly linear in their response.

New modeling of the contact mechanics, as well as a sequence of models for the membrane itself, is proposed in [Steigmann et al. 2003; Steigmann 2003] and [Baesu et al. 2004], which start from the most general constitutive equation for the strain energy of a two-dimensional fluid membrane with bending resistance. As linearization of this model is the subject of the current paper, we mention briefly the main features of the model. In [Baesu et al. 2004], an asymptotic analysis of this most general form yields as a first-order approximation a form of strain energy, which is traditionally referred to in the physics literature as the Canham–Helfrich strain energy [Helfrich 1973; Deuling and Helfrich 1976]. Moreover,
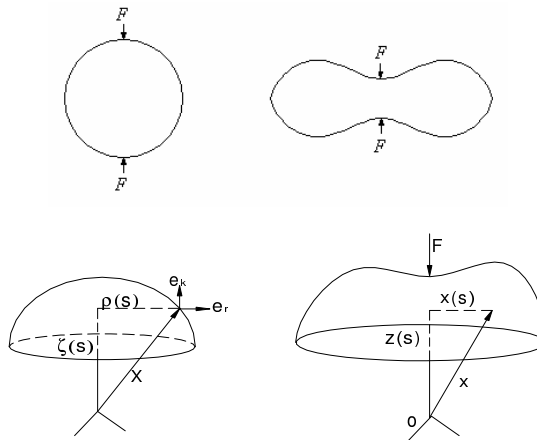
**Figure 1.** The geometry of deformation.

the framework presented in [Baesu et al. 2004] is more general and allows refinement of the model in ways compatible with mathematical requirements leading to the most general form. Variational methods are employed in [Baesu et al. 2004] to extract the deformed shape of a cell under an AFM experiment as a solution to the Euler–Lagrange equation. The interior of the cell is modeled as an incompressible material—a reasonable assumption as the cell is known to be made up of 50–55% water. Three new material parameters emerge as relevant for such a fluid medium: surface tension, and two bending moduli. The *shape equations* that describe the deformation of the cell under an AFM probe are highly nonlinear.

In this paper, we linearize the Canham–Helfrich model about small curvature and obtain an exact solution of the *poking problem* that describes an AFM experiment. We emphasize however that we use it only because it is the simplest model (first approximation) that satisfies the requirements of the most general model derived in [Baesu et al. 2004]. This general context is important especially for defining the theoretical envelope within which this simpler model can be further refined. For the sake of clarity, the general model, kinematics and constitutive aspects, including discussions concerning fluidity in the context of symmetry groups of a material, are briefly sketched in Section 2 and Section 3. Section 4 is concerned with Euler–Lagrange's equations and Section 5 with the linearized model and the exact solution.

## 2. Kinematics

We treat the case of an axisymmetric shape of the cell membrane, as illustrated in Figure 1, where the symbol $F$ stands for the force applied by the AFM tip, and $x$ and $X$ are the position vectors of an arbitrary particle on the membrane in the present and in the deformed configurations, respectively.

For clarification and more background on continuum mechanics we refer to the classic texts [Truesdell and Noll 1965; Green and Zerna 1968; Chandrasekharaiah and Debnath 1994; Chadwick 1999; Naghdi 2002]. For background on geometric methods in mechanics, especially membrane theory, see [Nitsche 1993; Ou-Yang et al. 1999].

The cylindrical coordinates of a point on the surface in the deformed configuration are given by

$$\boldsymbol{x} = r\boldsymbol{e}_r + z(r)\boldsymbol{k}. \tag{1}$$

The components of the surface metric tensor for the given coordinates are

$$a_{11} = a_1 \cdot a_1 = x_{,1} \cdot x_{,1} = (e_r + z'(r)k) \cdot (e_r + z'(r)k) = 1 + (z')^2,$$
$$a_{22} = a_2 \cdot a_2 = x_{,2} \cdot x_{,2} = re_\theta \cdot re_\theta = r^2. \tag{2}$$

Also, note that $a_{12} = a_{21} = 0$. Further, the normal to the deformed surface and the components of the curvature tensor are given by

$$\boldsymbol{n} = \frac{\boldsymbol{a}_1 \times \boldsymbol{a}_2}{\sqrt{a}} = \frac{1}{\sqrt{1-(z')^2}}(\boldsymbol{k} - z'\boldsymbol{e}_r),$$

$$b_{11} = n \cdot a_{1,1} = \frac{z''}{\sqrt{1-(z')^2}},$$

$$b_{22} = n \cdot a_{2,2} = \frac{rz'}{\sqrt{1-(z')^2}}, \tag{3}$$

$$b_{12} = b_{21} = 0,$$

where the second-order curvature tensor $\boldsymbol{b}$ is given by $\boldsymbol{b} = b_{11}\boldsymbol{a}^1 \otimes \boldsymbol{a}^1 + b_{22}\boldsymbol{a}^2 \otimes \boldsymbol{a}^2 + b_{12}\boldsymbol{a}^1 \otimes \boldsymbol{a}^2$. Consequently, the mean and Gaussian curvature, which appear in our constitutive equation, are calculated from (3) to be

$$2H = \operatorname{tr}\boldsymbol{b} = \operatorname{tr}\big[b_{11}\boldsymbol{a}^1 \otimes \boldsymbol{a}^1 + b_{22}\boldsymbol{a}^2 \otimes \boldsymbol{a}^2\big] = \frac{z''}{(1+(z')^2)^{\frac{3}{2}}} + \frac{z'}{(1+(z')^2)^{\frac{1}{2}}},$$

$$K = \det\boldsymbol{b} = \frac{z'rz''}{1-(z')^2}. \tag{4}$$

We linearize the model about small curvatures by taking $z' \ll 1$. Then, the linearization of the mean and Gaussian curvature, from (4) becomes

$$2H \approx z'' + \frac{z'}{r} = \frac{1}{r}(rz')',$$
$$K \approx 0. \tag{5}$$

## 3. Constitutive equation

The mechanical response of the cell membrane is described by a strain energy per unit area of the membrane surface dependent on $H$, the mean curvature $K$, the Gaussian curvature, and $J$, the local area stretch, in the present (deformed) configuration $\omega$. The most general form of the strain energy function for fluids, as shown in [Steigmann 1999; 2003; Steigmann et al. 2003], is represented by

$$w(H, K, J), \tag{6}$$

where $2H = \mathrm{tr}(\boldsymbol{b})$, $K = \det(\boldsymbol{b})$, and $J = \lambda\mu$, and where $\lambda$ and $\mu$ are the two principal stretches. An asymptotic expansion presented in [Baesu et al. 2004] in terms of a parameter representing the thickness/radius of curvature, indicates that the first approximation of (6) is

$$w = TJ + kH^2 + k_1 K, \tag{7}$$

where $T$, $k$, $k_1$ are the material moduli in this formulation. We emphasize that there is no connection whatsoever between these moduli and Young's modulus or Poisson's ratio, as this is a nonlinear theory employing completely different moduli.

## 4. Euler–Lagrange equations

The total potential energy of membrane described by (6), or its approximation (7), has three parts: one part due to the strain energy of the membrane itself, one from the applied point load, and one from the internal pressure. As we consider the material incompressible, the internal pressure is calculated as a Lagrange multiplier after the boundary conditions are enforced. For the sake of simplicity, we employ constant area and volume constraints. The energy functional for this problem was discussed in [Baesu et al. 2004] and [McElfresh et al. 2002], and for brevity we reproduce here only the final form:

$$E = \int_{\omega} w(H, K)\,da + \lambda S(\omega) - pV(\omega), \tag{8}$$

where $S(\gamma)$ is the total surface of the deformed configuration $\gamma$ , $V(\gamma)$ is its volume, $w$ is the strain energy of the membrane, and $p$ and $\lambda$ are the two Lagrange multipliers associated with the two constraints present in the problem (constant area and constant volume). The latter constraint is of particular interest as it allows us to calculate the pressure as a Lagrange multiplier without the need to know the pressure inside the cell a priori. In other words, a nondestructive experiment would suffice as there is no need to learn the pressure at some point inside the cell. It is shown in [Steigmann et al. 2003; Steigmann 2003] that the Euler–Lagrange equations for the energy (8) lead to the following shape equation:

$$\Delta\left(\frac{1}{2}w_H\right) + (w_K)_{;\alpha\beta}b^{\alpha\beta} + w_H(2H^2 - K) + 2H(Kw_K - w) - 2HT = p. \tag{9}$$

Employing the area constraint, the first approximation of the strain energy $w(H, K)$ (7) becomes

$$w = kH^2 + k_1 K, \tag{10}$$

where the coefficients are material constants to be determined. We remark that this approximation of $w(H, K)$ (see [Ou-Yang et al. 1999]) can be obtained though an asymptotic analysis conducted in terms of a parameter representing the ratio of the membrane thickness ($t$) to the infimum over the minimum of the radii of curvature over the whole deformed surface. Consequently, for the strain energy (10), the associated shape Equation (9) becomes

$$k[\Delta H + 2H(H^2 - K)] - 2\lambda H - p = 0, \tag{11}$$

where $\lambda$ is the Lagrange multiplier associated with the area constraint. We will be concerned next with the linearization of (11).

## 5. Linearized model

Using results from Section 2, the linearization of the shape Equation (11) leads to a new system of ordinary differential equations (ODE's) for the shape of the deformed surface. In what follows we consider only small curvatures; that is, we linearize the model about small curvatures. Once again, with the assumption that

$$(z')^2 \ll 1 \Rightarrow \sqrt{1 - (z')^2} \approx 1,$$

the expression for $H$ is given by Equation (5). Similarly, the Laplacian of $H$ is obtained in the following fashion

$$\Delta H = \frac{1}{\sqrt{a}} (\sqrt{a} a^{\alpha\beta} H_{,\beta})_{,\alpha} = \frac{1}{r\sqrt{1 - (z')^2}} \left( r\sqrt{1 - (z')^2} (1 + (z')^2)^{-1} H' \right)'. \tag{12}$$

The linearized expression for $\Delta H$ is given by

$$\Delta H \approx \frac{1}{r} (rH')'. \tag{13}$$

Consequently, the linearized form of the shape equation (11) is given by

$$H'' + \frac{1}{r} H' - \frac{2\lambda}{k} H = \frac{p}{k}, \tag{14}$$

where $\lambda$, $p$, $k$ are the constants as defined earlier. The net pressure across the membrane is very small and due to the linearization, the model is valid only for small curvatures. For what follows, we neglect $p$. Therefore, the shape equation takes the following form of a homogeneous equation:

$$H'' + \frac{1}{r} H' - \frac{2\lambda}{k} H = 0. \tag{15}$$

This equation is a modified Bessel equation of order zero whose general solution is given by

$$H(r) = B K_0(Ar) + C I_0(Ar), \tag{16}$$

where $I_0(Ar)$ and $K_0(Ar)$ are the Bessel functions of the first and second kind of order zero, respectively [Abramowitz and Stegun 1968], and $A = \sqrt{2\lambda/k}$. The integration constants $B$ and $C$ are to be found from the boundary conditions. The first boundary condition, is given by

$$\lim_{r \to 0} r H'(r) = \frac{-F}{2\pi k}, \tag{17}$$

where, again, $F$ is the value of the point load applied on the membrane. This boundary condition is obtained by integrating tractions along a small circle around the point of application of the point load and then taking the limit as the radius goes to zero. From (16) and (17) we obtain

$$r H' = -B Ar K_1(Ar) + C Ar I_1(Ar), \tag{18}$$

$$\lim_{r \to 0} Ar I_1(Ar) = 0, \tag{19}$$

$$\lim_{r \to 0} Ar K_1(Ar) = 1. \tag{20}$$

Since for $I_0' = I_1$ and $K_0' = -K_1$, $\lim_{r \to 0} I_1(Ar) = 0$, and $\lim_{r \to 0} Ar K_1(Ar) = 1$, it follows that (18) is satisfied if and only if $B = \frac{F}{2\pi k}$. The expression for $H(r)$ becomes

$$H(r) = \frac{F}{2\pi k} K_0(Ar) + C I_0(Ar). \tag{21}$$

Next, from (16) we get the ODE for $z(r)$:

$$\frac{1}{2r}(rz')' = \frac{F}{2\pi k} K_0(Ar) + C I_0(Ar), \tag{22}$$

with the solution

$$z(r) = \frac{F}{2\pi \lambda} K_0(Ar) + \frac{Ck}{\lambda} I_0(Ar) + D \ln(Ar) + E. \tag{23}$$

This equation is solved in a bounded domain with $r$ ranging from 0 to $5\,\mu\text{m}$ (approximately half the length of the cell measured from its pole, owing to axisymmetry). The boundary conditions for this equation, used to determine the constants $C$, $D$ and $E$, are given from geometrical conditions by

$$z'(0) = 0, \qquad z'(5) = 0, \qquad z(5) = 0, \tag{24}$$

where $z = z(r)$. These boundary conditions arise from the fact that at the point of application of the load, the slope of the membrane is zero due to the bending resistance. At the outer bound, the membrane is unaffected by the point load. As $r$ approaches zero, $x$ also approaches zero. The condition $(24)_1$ can be rewritten (with $x = Ar$) as

$$\lim_{x \to 0} \left( D - \frac{F}{2\pi \lambda} \right) \frac{1}{x} = 0. \tag{25}$$

From the properties of Bessel functions indicated above it is clear that a necessary and sufficient condition for (25) is:

$$D = \frac{F}{2\pi \lambda}.$$

Therefore, the equation for the slope is given by

$$\frac{dz}{dx} = \frac{F}{2\pi \lambda} \left( \frac{1}{x} - K_1(x) \right) + \frac{Ck}{\lambda} I_1(x). \tag{26}$$

Applying the second boundary condition, the constant $C$ is given by

$$C = \frac{-F}{20\pi k} \frac{\left( \sqrt{\frac{2k}{\lambda}} - 10 K_1(5A) \right)}{I_1(5A)}. \tag{27}$$

Substituting the final boundary condition in Equation (23), the constant $E$ is given by

$$E = \frac{F}{20\pi \lambda} \left[ \frac{I_0(5A)}{I_1(5A)} \left( \sqrt{\frac{2k}{\lambda}} - 10 K_1(5A) \right) - 10 \big( K_0(5A) + \ln(5A) \big) \right]. \tag{28}$$

Therefore, after substituting all the constants into Equation (23), the final solution is

$$z(r) = \frac{F}{2\pi\lambda}\big(K_0(Ar) + \ln(Ar)\big)$$

$$- \frac{F}{20\pi\lambda}\left[\frac{I_0(Ar) - I_0(5A)}{I_1(5A)}\left(\sqrt{\frac{2k}{\lambda}} - 10K_1(5A)\right) + 10\big(K_0(5A) + \ln(5A)\big)\right], \quad (29)$$

where, again, $A$ is expressed as $A = \sqrt{2\lambda/k}$. This equation can be used to find the values of the bending ($k$) and stretching ($\lambda$) moduli for a given point load and deflection of the membrane. The results of AFM imaging experiments performed by McElfresh et al. [2002] give the deflection of a bovine sperm cell membrane under the point of application of the load. The results for two different loads were used. However the values of the material constants $k$ and $\lambda$ cannot be uniquely obtained as the shape is not unique. The values of coordinates at two different points are required for solving the equations, and there is no experimental result available for this purpose. Since there are no experimental data to get an actual deformed shape under an AFM experiment, assumed values of bending and stretching moduli based on known values for other fluids are used to illustrate what the deformed shape might look like, using Equation (7). In particular, using material constants available in the literature for lipid bilayers (like surfactants), we were able to plot the deformed shape of the membrane (see Figure 2). Bending modulus ($k$) for surfactants is of the order $10^{-12}$ ergs (1 erg = 0.1 $\mu$J) [Ou-Yang et al. 1999; McElfresh et al. 2002] and the stretching or dilatation modulus ($\lambda$) for phospholipid bilayers is approximately equal to $10^{-1}$ N/m [Castro-Roman and Ligoure 2001]. The cell membrane is expected to offer a greater resistance to bending, hence it is expected to have a greater value for $k$. Assuming that the value of the bending modulus is of the order $10^{-7}$ ergs and an arbitrary value of the point load, $F = 6.6 \times 10^{-9}$ N [McElfresh et al. 2002], the deformed shape in Figure 2 was obtained where the length unit is $\mu$m. This is the expected shape of the deformed membrane. The order of magnitude of the bending modulus is
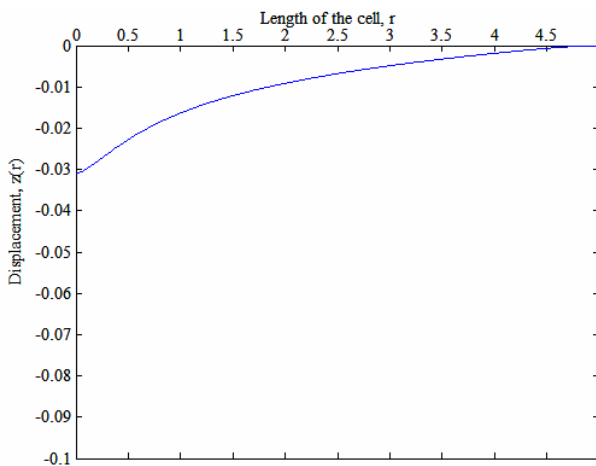


**Figure 2.** Plot of the deformed shape of the membrane.

reasonable because the order of magnitude of the displacement obtained here is the same as that of the actual displacement [McElfresh et al. 2002].

We remark that experiments to obtain the whole deformed shape are a great experimental challenge. Two different experimental set-ups to obtain the whole deformed shape of the cell membrane are in trial: one at the Lawrence Livermore National Laboratory and another at Prof. Turner's laboratory at the University of Nebraska. As experimental results become available, Equation (29) can be very easily used to obtain material constants for the membrane. Also, the exact solution (29) serves as a benchmark solution for comparison with future numerical simulations.

## References

[Abramowitz and Stegun 1968] M. Abramowitz and I. A. Stegun, *Handbook of Mathematical functions*, Dover Publications, New York, 1968.

[Alberts et al. 2002] B. Alberts, A. Johnson, J. Lewis, M. Raff, K. Roberts, and P. Walter, *Molecular biology of the cell*, Garland Science, London, 2002.

[Baesu et al. 2004] E. Baesu, R. E. Rudd, J. Belak, and M. McElfresh, "Continuum modeling of cell membranes", *Int. J. Non-Linear Mech.* **39** (2004), 369.

[Boal 2002] D. H. Boal, *Mechanics of cells*, Cambridge University Press, Cambridge, 2002.

[Brock et al. 1994] T. D. Brock, M. T. Madigan, J. H. Martinko, and J. Parker, *Biology of microorganisms*, Prentice Hall, New Jersey, 1994.

[Castro-Roman and Ligoure 2001] F. Castro-Roman and C. Ligoure, "Lateral stretching of fluid membranes by grafted polymer brushes", *Europhys. Lett.* **53** (2001), 483.

[Chadwick 1999] P. Chadwick, *Continuum mechanics: concise theory and problems*, Dover Publication, New York, 1999.

[Chandrasekharaiah and Debnath 1994] D. S. Chandrasekharaiah and L. Debnath, *Continuum mechanics*, Academic Press, Boston, 1994.

[Chasis et al. 1988] J. A. Chasis, P. Agre, and N. Mohandas, "Decreased membrane mechanical stability and in vivo loss of surface area reflect spectrin deficiencies in hereditary spherocytosis", *J. Clin. Invest.* **82** (1988), 617–623.

[Deuling and Helfrich 1976] H. J. Deuling and W. Helfrich, "The curvature elasticity of fluid membranes: a catalogue of vesicle shapes", *J. Phys.* **37** (1976), 1335.

[Discher et al. 1994] D. Discher, N. Mohandas, and E. A. Evans, "Molecular maps of red blood cell deformation: hidden elasticity and in situ connectivity", *Science* **266** (1994), 1032–1035.

[Engelhardt and Sackmann 1988] J. Engelhardt and E. Sackmann, "On the measurement of shear elastic moduli and viscosities of erythrocyte plasma membranes by transient deformation in high frequency electric fields", *Biophys. J.* **54** (1988), 941–965.

[Ericksen 1974] J. L. Ericksen, "Liquid crystals and cosserat surfaces", *Quart. J. Mech. Appl. Math.* **27** (1974), 213.

[Evans 1974] E. A. Evans, "Bending resistance and chemically induced moments in membrane bilayers", *Biophys. J.* **14** (1974), 923–931.

[Evans 1983] E. A. Evans, "Bending elastic modulus of red blood cell membrane derived from buckling instability in micropipette aspiration tests", *Biophys. J.* **43** (1983), 27–30.

[Evans 1992] E. A. Evans, "Physics of complex-biological membranes and cell interfaces", pp. 31–41 in *Materials research society symposium proceedings*, vol. 255, 1992.

[Evans and Hochmuth 1977] E. A. Evans and R. M. Hochmuth, "A solid-liquid composite model of the red cell membrane", *J. Membrane Biology* **30** (1977), 351–362.

[Evans and Mohandas 1987] E. A. Evans and N. Mohandas, "Membrane-associated sickle hemoglobin: a major determinant of sickle erythrocyte rigidity", *Blood* **70** (1987), 1443–1449.

[Evans and Skalak 1980] E. A. Evans and R. Skalak, *Mechanics and thermodynamics of biomembranes*, CRC Press, Boca Raton, FL, 1980.

[Fung 1966] Y. C. Fung, "Theoretical considerations of the elasticity of red blood cells", pp. 1761–1776 in *Proceedings of the federation of american society of experimental biology*, vol. 25, 1966.

[Garrett and Grisham 1999] R. H. Garrett and C. M. Grisham, *Biochemistry*, Saunders College Publishing, 1999.

[Green and Zerna 1968] A. E. Green and W. Zerna, *Theoretical elasticity*, Oxford University Press, 1968.

[Hassan et al. 1998] E. A. Hassan, W. F. Heinz, M. D. Antonik, N. P. D'Costa, S. Nageswaran, C. A. Schoenberger, and J. H. Hoh, "Relative microelastic mapping of living cells by atomic force microscopy", *Biophys. J.* **74** (1998), 1564–1578.

[Helfrich 1973] W. Helfrich, "Elastic properties of lipid bilayers: theory and possible experiments", *Z. Naturfresch* **280** (1973), 693–703.

[Hochmuth 1990] R. M. Hochmuth, "Cell biomechanics: a brief overview", *J. Biomech. Eng.-T ASME* **112** (1990), 233–234.

[Hochmuth et al. 1973] R. M. Hochmuth, N. Mohandas, and P. L. Blackshear, "Measurement of the elastic modulus for the red cell membrane using a fluid mechanical technique", *Biophys. J.* **13** (1973), 742–762.

[Jenkins 1977a] J. T. Jenkins, "The equations of mechanical equilibrium of a model membrane", *SIAM J. Appl. Math.* **32** (1977), 755.

[Jenkins 1977b] J. T. Jenkins, "Static equilibrium configurations of a model red blood cell", *J. Math. Biol.* **4** (1977), 149.

[Johnson 1987] K. L. Johnson, *Contact mechanics*, Cambridge University Press, Cambridge, 1987.

[Kuzman et al. 2004] D. Kuzman, S. Svetina, R. E. Waugh, and B. Zeks, "Elastic properties of the red blood cell membrane that determine echinocyte deformability", *Eur. Biophys. J.* **33** (2004), 1–15.

[Lim et al. 2002] H. W. Lim, M. Wortis, and R. Mukhopadhyay, "Stomatocyte-discocyteechinocyte sequence of the human red blood cell: evidence for the bilayer-couple hypothesis from membrane mechanics", pp. 16766–16769 in *Proceedings of the National Academy of Sciences*, vol. 99, 2002.

[McElfresh et al. 2002] M. McElfresh, E. Baesu, R. Balhorn, J. Belak, M. J. Allen, and R. E. Rudd, "Combining constitutive materials modeling with atomics force microscopy to understand the mechanical properties of living cells", pp. 6493 in *Proceedings of the national academy of sciences*, vol. 99, 2002.

[Morris et al. 1999] V. J. Morris, A. P. Gunning, and A. R. Kirby, *Atomic force microscopy for biologists*, Imperial College Press, London, 1999.

[Naghdi 2002] P. M. Naghdi, *ME 185 course notes*, University of California, Berkeley, 2002.

[Nitsche 1993] J. C. C. Nitsche, "Boundary value problems for variational integrals involving surface curvatures", *Quar. J. Appl. Math.* **51** (1993), 363.

[Ou-Yang et al. 1999] Z.-C. Ou-Yang, J.-X. Liu, and Y.-Z. Xie, *Geometric methods in the elastic theory of membranes in liquid crystal phases*, World Scientific Publishing, Singapore, 1999.

[Skalak et al. 1973] R. Skalak, A. Tozeren, R. P. Zarda, and C. S., "Strain energy function of red blood cell membranes", *Biophys. J.* **13** (1973), 245–264.

[Steigmann 1999] D. J. Steigmann, "Fluid films with curvature elasticity", *Arch. Ration. Mech. An.* **150** (1999), 127.

[Steigmann 2003] D. J. Steigmann, "Irreducible functions basis for liquid crystal films", *J. Appl. Math. Phys. (ZAMP)* **54** (2003), 462–477.

[Steigmann et al. 2003] D. J. Steigmann, E. Baesu, R. E. Rudd, M. McElfresh, and J. Belak, "On the variational theory of cell-membrane equilibria", *Interface Free Bound.* **5** (2003), 357.

[Strey et al. 1995] H. Strey, M. Peterson, and E. Sackmann, "Measurement of erythrocyte membrane elasticity by flicker eigenmode decomposition", *Biophys. J.* **69** (1995), 478–488.

[Svetina et al. 1985] S. Svetina, M. Brumen, and B. Zeks, "Lipid bilayer elasticity and the bilayer couple interpretation of the red cell shape transformations and lysis. Stud.", *Biophysics* **110** (1985), 177–184.

[Truesdell and Noll 1965] C. Truesdell and W. Noll, *The non-linear field theories of mechanics*, 3rd ed., Springer-Verlag, Berlin, 1965.

[Yin and Costa 1999] F. C. P. Yin and K. D. Costa, "Analysis of indentation: Implications for measuring mechanical properties with atomic force microscopy", *ASME J. Biomech. Eng.* **121** (1999), 462–471.

EVELINE BAESU: ebaesu@unl.edu
*W304 Nebraska Hall, Department of Engineering Mechanics, University of Nebraska, Lincoln, NE 68588, United States*
www.unl.edu/emhome/faculty/baesu.html

SUJATHA KALYANAM: sujatha.kalyanam@gmail.com
*W317 Nebraska Hall, Department of Engineering Mechanics, University of Nebraska, Lincoln, NE 68588, United States*

MARCELINA MOCANU: tiberium@easynet.ro
*Calea Mărăşeşti 157, Department of Mathematics, University of Bacău, Bacău 600115, Romania*

# SUBMISSION GUIDELINES

## ORIGINALITY

Authors may submit manuscripts in PDF format on-line. Submission of a manuscript acknowledges that the manuscript is *original and has neither previously, nor simultaneously, in whole or in part, been submitted elsewhere.* Information regarding the preparation of manuscripts is provided below. Correspondence by email is requested for convenience and speed. For further information, write to:

Marie-Louise Steele
Division of Mechanics and Computation
Durand Building, Room 262
Stanford University
Stanford CA 94305

## LANGUAGE

Manuscripts must be in English. A brief abstract of about 150 words or less must be included. The abstract should be self-contained and not make any reference to the bibliography. Also required are keywords and subject classification for the article, and, for each author, postal address, affiliation (if appropriate), and email address if available. A home-page URL is optional.

## FORMAT

Authors are encouraged to use LaTeX and the standard article class, but submissions in other varieties of TeX, and, exceptionally in other formats, are acceptable. Electronic submissions are strongly encouraged in PDF format only; after the refereeing process we will ask you to submit all source material.

## REFERENCES

Bibliographical references should be listed alphabetically at the end of the paper and include the title of the article. All references in the bibliography should be cited in the text. The use of BIBTeX is preferred but not required. Tags will be converted to the house format (see a current issue for examples), however, in the manuscript, the citation should be by first author's last name and year of publication, e.g. "as shown by Kramer, et al. (1994)". Links will be provided to all literature with known web locations and authors are encouraged to provide their own links on top of the ones provided by the editorial process.

## FIGURES

Figures prepared electronically should be submitted in Encapsulated PostScript (EPS) or in a form that can be converted to EPS, such as GnuPlot, Maple, or Mathematica. Many drawing tools such as Adobe Illustrator and Aldus FreeHand can produce EPS output. Figures containing bitmaps should be generated at the highest possible resolution. If there is doubt whether a particular figure is in an acceptable format, the authors should check with production by sending an email to:

production@mathscipub.org

Each figure should be captioned and numbered so that it can float. Small figures occupying no more than three lines of vertical space can be kept in the text ("the curve looks like this:"). It is acceptable to submit a manuscript with all figures at the end, if their placement is specified in the text by means of comments such as "Place Figure 1 here". The same considerations apply to tables.

## WHITE SPACE

Forced line breaks or page breaks should not be inserted in the document. There is no point in your trying to optimize line and page breaks in the original manuscript. The manuscript will be reformatted to use the journal's preferred fonts and layout.

## PROOFS

Page proofs will be made available to authors (or to the designated corresponding author) at a web site in PDF format. Failure to acknowledge the receipt of proofs or to return corrections within the requested deadline may cause publication to be postponed.